

BALTICA VII

Life Management and Maintenance
for Power Plants
Vol. 2

VTT SYMPOSIUM 247

Keywords:

power plant, maintenance, boilers,
machinery, equipment, inspection,
monitoring, condition, life, performance,
risk, reliability

BALTICA VII
Life Management and Maintenance
for Power Plants
Vol. 2

Helsinki–Stockholm–Helsinki
12–14 June, 2007

Edited by

Juha Veivo & Pertti Auerkari

Organised by

VTT



ISBN 978-951-38-6317-3 (soft back ed.)

ISSN 0357-9387 (soft back ed.)

ISBN 978-951-38-6318-0 (URL: <http://www.vtt.fi/publications/index.jsp>)

ISSN 1455-0873 (URL: <http://www.vtt.fi/publications/index.jsp>)

Copyright © VTT Technical Research Centre of Finland 2007

JULKAISIJA – UTGIVARE – PUBLISHER

VTT, Vuorimiehentie 3, PL 1000, 02044 VTT

puh. vaihde 020 722 111, faksi 020 722 4374

VTT, Bergsmansvägen 3, PB 1000, 02044 VTT

tel. växel 020 722 111, fax 020 722 4374

VTT Technical Research Centre of Finland

Vuorimiehentie 3, P.O.Box 1000, FI-02044 VTT, Finland

phone internat. +358 20 722 111, fax + 358 20 722 4374

VTT, Kemistintie 3, PL 1000, 02044 VTT

puh. vaihde 020 722 111, faksi 020 722 7002

VTT, Kemistvägen 3, PB 1000, 02044 VTT

tel. växel 020 722 111, fax 020 722 7002

VTT, Kemistintie 3, P.O. Box 1000, FI-02044 VTT, Finland

phone internat. +358 20 722 111, fax + 358 20 722 7002

Preface

The drivers in power technology, production and business are again shifting, this time towards zero carbon and other new solutions that aim to simultaneously answer the age-old questions on cost, availability and acceptability of different fuels and conversion processes. Only a part of the answer implies completely new technology, and much of the rest is likely to mean evolutionary development of existing principles. Even then, the common awareness on global warming is unprecedented and will have large scale consequences in decisions on investment. Tightly on the heels of new investment must follow the effort required for life management and maintenance, which need to take into account the peculiarities of new technology that may be very specific and suffer from lacking prior experience. However, the changes will also affect existing plant that may face new fuels, operational modes, and upgrading in some aspects at least.

The dash for biomass and other renewable fuels will not easily cover all power consumption any time soon, and also the base load plants will be affected by the change. It remains to be seen to what extent this implies e.g. ultrasupercritical efficiency, carbon sequestration, coal gasification, and/or new nuclear concepts. However, no single technology will cover all needs, and we probably have to live with an array of solutions that all need to be served and maintained for best performance. The BALTICA VII Conference aims to provide an updated and state-of-the-art experience on the essentials for life management and maintenance of power plants, and the conference papers of these proceedings will offer an excellent review on the current issues and solutions.

The editors wish to express their sincere gratitude to the authors, referees, organisers and the Board of the Conference for their invaluable contribution in preparing for the event and the proceedings. Financial and other contributions by the supporting and sponsoring organisations are also gratefully acknowledged.

Espoo, June 2007

Juha Veivo Pertti Auerkari

Editors

Contents

Contents of Volume 2

Preface	3
Session 3. Condition, life and risk management for power equipment	
Influence of coating quality on the service life of land-based gas turbine blades	7
<i>N.S. Cheruvu</i> <i>SWRI, San Antonio, USA</i>	
Evaluation of the operating conditions of gas turbine blades and vanes after long term service	25
<i>P. Auerkari, J. Salonen, T.E. Gustafsson, I. Karvonen*, H. Tanttari*, S. Mäkinen**</i> <i>VTT Technical Research Centre of Finland, Espoo, Finland</i> <i>*Lappeenranta Energia, Lappeenranta, Finland</i> <i>**Helsingin Energia, Helsinki, Finland</i>	
New concepts of RBI/RBM as applied in power plant practice	35
<i>J.M. Bareiß*, A.S. Jovanovic**, D. Balos**</i> <i>*EnBW Kraftwerke AG, Stuttgart, Germany</i> <i>**Steinbeis Advanced Risk Technologies, Stuttgart, Germany</i>	
Session 4. Living with damage	
Living with creep damage... outside the creep range	50
<i>J.M. Brear, P. Jarvis</i> <i>Stress Engineering Services (Europe) Ltd., Esher, UK</i>	
Predicting crack growth in high temperature plant	65
<i>I. Le May</i> <i>Metallurgical Consulting Services, Saskatoon, Canada</i>	
Creep resistance of steel weldments after long term operation	75
<i>J. Hakl, T. Vlasák, J. Pecha*, R. Pech**</i> <i>SVÚM a.s., Prague, Czech Republic</i> <i>*SES a.s., Tlmače, Slovakia</i> <i>**REMS, Prague, Czech Republic</i>	

Behaviour of coated and uncoated ferritic steels under isothermal and cyclic steam oxidation conditions	87
<i>A. Agüero, V. González, M. Gutiérrez</i>	
<i>Institute of Aerospace Technology, Metallic Materials Area, Torrejón de Ardoz, Spain</i>	
The hybrid coatings against hot corrosion: on-site and laboratory tests on P91 and carbon steels	98
<i>M. Danielewski, R. Gajerski, R. Filipek, S. Łabuś,</i>	
<i>E. Tyliczszak-Halibożek, A. Milewska</i>	
<i>AGH University of Science and Technology</i>	
<i>Kraków, Poland</i>	
Hot corrosion and erosion resistance of new coating alloys for biomass and waste boiler heat transfer surfaces	109
<i>S. Yli-Olli, S. Tuurna, M. Oksa, E. Turunen, T. Varis</i>	
<i>VTT Technical Research Centre of Finland, Espoo, Finland</i>	
Studying the effect of the elements Ce and Cr on the high-temperature oxidation behaviour of low-Cr steels	123
<i>V. B. Trindade, U. Krupp*, H.-J. Christ, S. Tuurna**,</i>	
<i>L. Heikinheimo**, M. Arponen***</i>	
<i>University of Siegen, Germany</i>	
<i>*University of Applied Sciences Osnabrück, Germany</i>	
<i>**VTT Technical Research Centre of Finland, Espoo, Finland</i>	
<i>***Rautaruukki Oyj, Raahе, Finland</i>	
Sulphidation behaviour of advanced materials for elevated kraft recovery boiler conditions	135
<i>S. Yli-Olli, P. Pohjanne, L. Heikinheimo,</i>	
<i>T. Kinnunen, P.H. Pankakoski</i>	
<i>VTT Technical Research Centre of Finland, Espoo, Finland</i>	
Application of an integrated risk management system for improved maintenance in industrial plants	147
<i>A. Jovanovic, D.T. Balos, G. Vinod, D. Balos, P. Stanojevic*</i>	
<i>Steinbeis Advanced Risk Technologies, Germany</i>	
<i>*NIS – Petroleum Industry of Serbia, Serbia</i>	

Session 6. Trends in monitoring and maintenance

- Coating integrated optical fibres for monitoring of boiler heat transfer surfaces 164
S. Sandlin, A. Hokkanen, T. Varis
VTT Technical Research Centre of Finland, Espoo, Finland
- Method of small samples for assessment of properties of power plant components: sampling devices and stress concentration in dimples 180
A. Dedov, I. Klevtsov, T. Lausmaa, D. Neshumayev
Tallinn University of Technology, Estonia
- NIMS structural materials databases and cross search engine – MatNavi 193
M. Yamazaki, Y. Xu, M. Murata, H. Tanaka, K. Kamihira, K. Kimura
National Institute for Materials Science, Tokyo, Japan
- Visualising creep exhaustion in a P22 girth weld 208
S. Holmström, A. Laukkanen, K. Calonijs
VTT Technical Research Centre of Finland, Espoo, Finland
- The LICON approach to life management 222
J.H. Rantala, P. Auerkari, S.R. Holdsworth, R.C. Hurst***
VTT Technical Research Centre of Finland, Espoo, Finland
**EMPA, Switzerland*
***EC-JRC-IE, The Netherlands*
- Experience on the ultrasonic inspection of control rod nozzles of reactor pressure vessel 235
P. Kauppinen, H. Jeskanen, R. Paussu, B. Elsing***
VTT Technical Research Centre of Finland, Espoo, Finland
**Fortum Nuclear Services, Helsinki, Finland*
***Fortum Power and Heat, Loviisa, Finland*

Influence of coating quality on the service life of land-based gas turbine blades

N. S. Cheruvu

Southwest Research Institute[®], San Antonio, USA

Abstract

The land-based gas turbine blades operate at severe operating conditions: higher metal temperatures and stresses, and severe duty cycles. Metallic coatings with or without a top ceramic coating have been used to protect the turbine blades. The durability of the coating system is one of the prime life-limiting factors of modern gas turbine blades. The quality of the coating plays a critical role on the coating life. This paper discusses the failure mechanisms of the coatings and describes how the quality of the coating affects the service life of a gas turbine blade. A few case studies are presented in the paper.

1. Introduction

In recent years, combustion turbines (CT) have become the equipment of choice for power generation by both electric utilities and independent power producers. The reasons for the popularity of CTs have been: availability of abundant low priced gas fuel, short construction lead times, ease of installation of CT plants, ability of CT plants to start up rapidly during peak power demand and substantial fuel cost savings due to increased efficiency in combined-cycle configuration. Combined-cycle plants exceeding 60% thermal efficiency (e.g., GE H series and Siemens-Westinghouse-G) have been installed.

Operation and Maintenance costs for newer, higher-firing-temperature gas turbines are more sensitive to replacement part costs than previous models. The replacement cost of the hot section components alone can exceed 35% of the cost of a new unit. The first-stage turbine blades are a major concern because of their short life and high replacement cost. Because of the higher operating temperatures encountered in these designs, the performance and durability of the coating system have become the prime life limiting factor of a CT blade. The turbine owners would like to extend the coating refurbishment intervals by being able to predict the remaining life of their coatings and to optimize the operating practices as necessary. The adverse consequences of non-optimal operation also need to be understood, since the economy of operation may often warrant rapid startup/shutdown procedures.

The coating failure modes vary with operating conditions and machine specific failure mechanisms and the specifics of coatings used and their quality need to be better understood. Failure of protective blade coatings represents a major profitability challenge for combustion turbine (CT) owners. Coating life usually dictates blade refurbishment intervals, which typically are shorter than desired for base-load units. Since most units are operated as combined-cycle units, there is a premium on their reliability, availability and maintainability.

Life consumption mechanisms of a coated blade include (a) coating degradation, (b) thermo-mechanical fatigue (TMF), and (c) creep. The mechanism of coating degradation and creep is a time dependent process, while TMF is a cycle dependent process. Failures of coatings both by degradation (i.e., losing protectivity under oxidation) at high temperature locations and by TMF at high strain locations have been observed [1]. The coating quality plays a significant role on the service life of a coating and poor quality coating lowers the coating life. The objective of this paper is to demonstrate the consequences of poor quality coating on the service life of a turbine blade.

2. In-Service Coating Degradation

Metallic coatings commonly used for CT blades such as CoCrAlY, CoNiCrAlY, NiCoCrAlYHfSi (PWA 286), and NiCoCrAlYSi (Sicoat 2231) exhibit a duplex microstructure containing fine β -phase particles [CoAl or (CoNi) Al] in a matrix of γ [2–6]. The β -phase and the matrix contain about 16 to 17 wt. % aluminum [3–4] and 3 to 5 wt. % aluminum, respectively. The microstructure of rhenium modified NiCoCrAlY (Sicoat 2453) exhibits a complex structure containing four different phases: α , β , and σ in matrix of γ [6–8]. The α -phase is a chromium-rich phase, while the σ -phase is rich in both chromium and rhenium and these phases contain no aluminum. The β - and γ -phases contain about 17 and 4 wt. % aluminum, respectively. The top aluminide on an MCrAlY coating or a stand-alone aluminide coating exhibits a single β -phase structure, containing approximately 20 to 25 wt. % aluminum [2]. The β -phase particles in these coatings act as reservoirs for aluminum and provide aluminum to form a protective surface oxide scale when the coated components are exposed to elevated temperatures in service. Typical microstructure of properly applied (good quality) MCrAlY and duplex coating on the blade external airfoil surfaces and an aluminide coating on the internal surface are shown in Fig. 1.

It is well known that both diffusion and overlay coatings degrade when they are exposed to elevated temperature for a long time [2, 4–6]. The mechanisms of in-service coating degradation include hot corrosion, oxidation, and degradation resulting from inward and outward diffusion of elements [9–11].

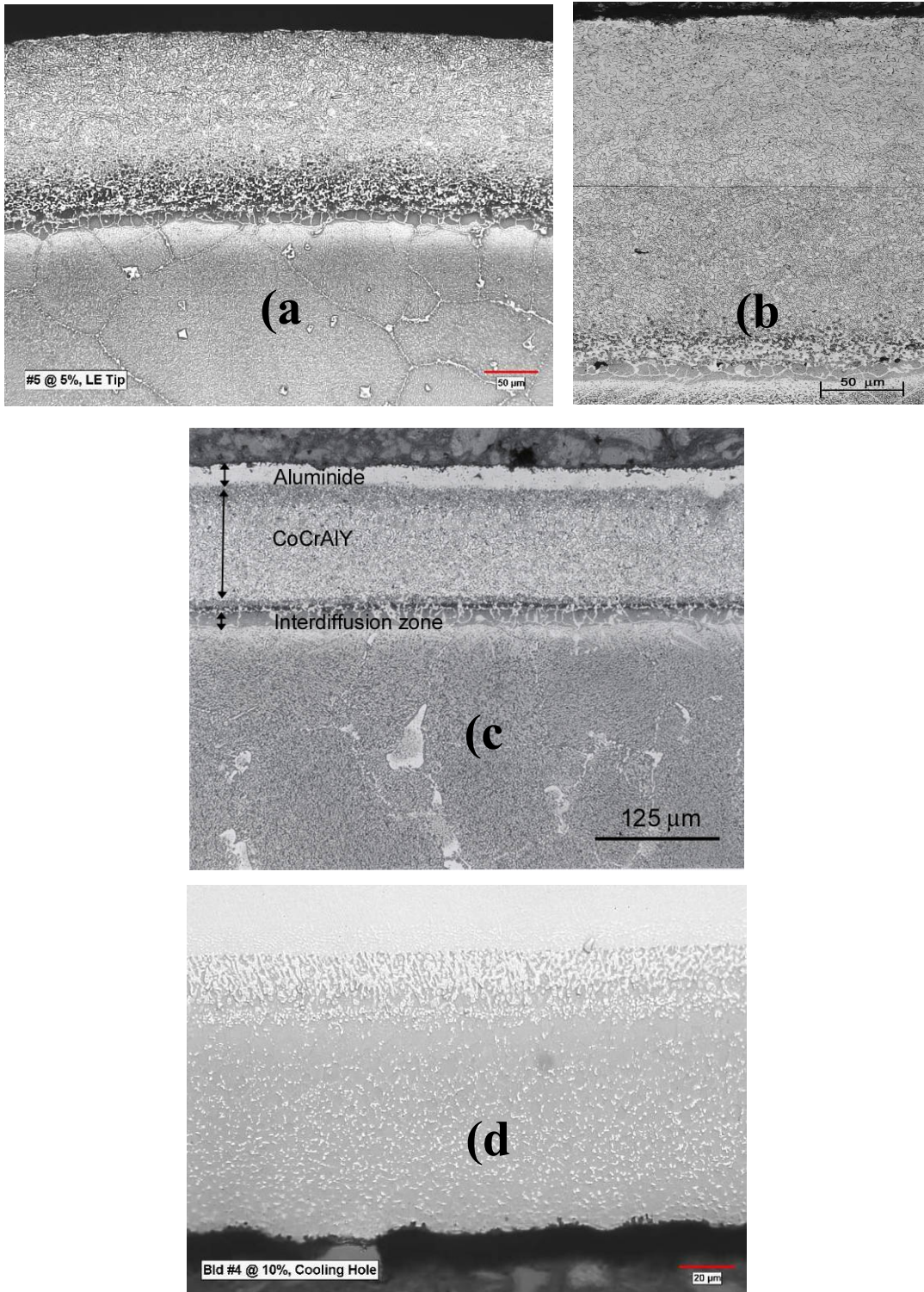


Figure 1. Typical microstructure of MCrAlY and aluminide coating on Row 1 blades: a) CoNiCrAlY on 501 D 5 blade, b) NiCoCrAlY (GT 33) on a 7EA blade, c) over aluminized CoCrAlY (GT 29Plus) coating on 7FA blade, and d) aluminide coating on a cooling hole of 7EA blade.

Advanced turbines are fired with clean natural gas and operate in a temperature range where oxidation supersedes hot corrosion. As a result, hot corrosion is not a concern in these turbines. The components in advanced turbines are more prone to oxidation and incidents dealing with oxidation of coating on F-Class turbine blades have been reported [12].

The results [4, 9, 13] published in the literature have shown that both diffusion (aluminide) and overlay (MCoCrAlY) coatings oxidize at the outer surface of the coating as a result of thermal exposure. Spallation and reformation of the protective oxide scale during long-term exposure lead to a loss of aluminum in the coating that promotes transformation of the β -phase into γ or γ' . The microstructural changes that occurred in the overlay coatings (CoCrAlY, NiCoCrAlY or NiCoCrAlY, NiCoCrAlHfSi) coatings after thermal exposure are similar. The coatings also degrade due to interdiffusion of elements from the coating into the substrate and vice versa, which is manifested by the interdiffusion zone growth.

A representative microstructure of a degraded duplex coating CoCrAlY (GT29+) after long-term service exposure is shown in Fig. 2. It is clear from the figure that the coating on the blade leading edge is severely degraded. The β -phase in the top aluminide coating decreased from 100% at the initial condition to approximately 25%. The β -phase in the CoCrAlY coating was almost consumed. These results indicate that in an over-aluminized CoCrAlY coating, the aluminide coating fails after complete degradation of the CoCrAlY coating.

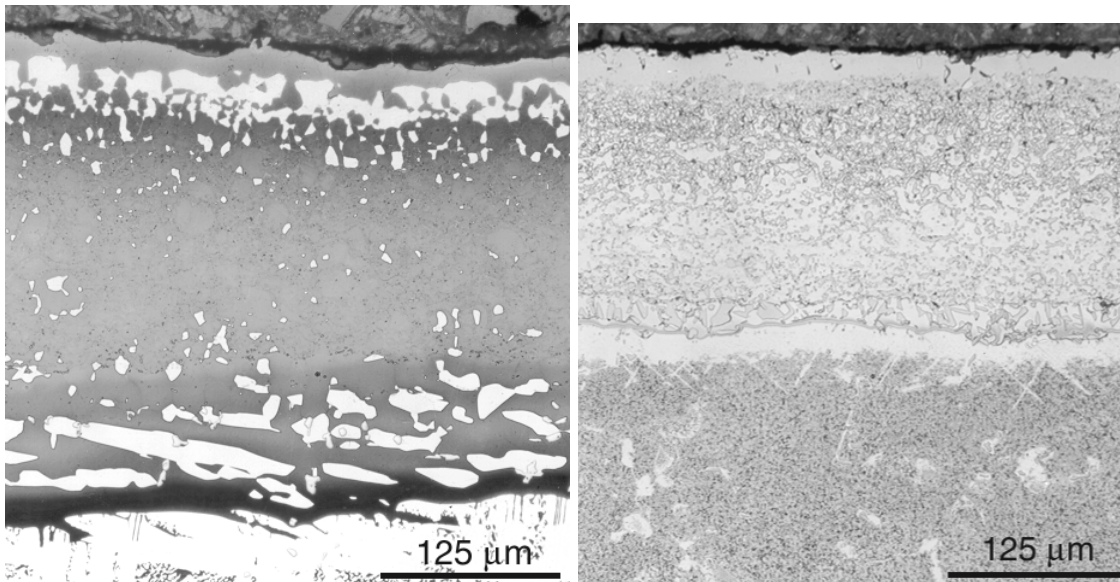


Figure 2. Optical micrographs showing microstructure of over aluminized CoCrAlY (GT 29Plus) coating on a) leading edge and b) trailing edge at 55% height of Frame 9FA blade after 17 188 hours of service.

In contrast to the coating condition on the leading edge, the coating on the trailing edge shows that it is in good condition. The volume fraction of β -phase in the top aluminide and CoCrAlY coatings on the trailing edge is almost comparable to the amount that is normally seen in an under graded coating (see Fig. 1). The interdiffusion zone width below the CoCrAlY coating on the trailing edge is significantly smaller than that at the leading edge (25 versus 115 μm). This indicates that the leading edge of the Frame 9000FA blade operated at a higher temperature than the trailing edge. The extent of in-service coating degradation also depends on the coating thickness as well chemical composition, particularly Al content in a given coating. Chemical composition and the quality of the coating (thickness and interface contamination) have a profound effect on the failure of coating by degradation owing to loss of protectivity under oxidation at high temperatures. Typically, thinner coating and a coating containing lower levels of aluminum degrades faster.

3. TMF Cracking

CT blades experience complex thermal and mechanical history during a typical cycle of operation, consisting of startup, steady state operation, and shut-down. Temperature gradients and mechanical constraints during cycling result in thermo-mechanical stresses, which can lead to TMF damage. Typically, TMF cracks are observed in the coating on the blade airfoil sections of 501 D5, Frame 7FA, and 9FA blades between the platform and approximately the 65% airfoil height [3, 14]. The extent and the location of cracking depend on the blade design including cooling flow and operating conditions. Typical morphology of TMF cracks in the GT29+ coated blades is presented in Fig. 3. The cracks in the coating were filled with oxide scale and a β -phase depleted zone was observed in the CoCrAlY coating in the vicinity of TMF cracks.

Many variables affect coating resistance to TMF cracking, but the most important ones are coating ductility which is closely related to composition as discussed earlier, the range of metal temperature and operational characteristics. The most important mechanical property of a coating is its resistance to thermo-fatigue cracking – a property closely related to their ductility characteristics. Selection of a coating on the basis of its ductility/temperature characteristics depends on the maximum strain levels likely to be experienced by the component over its operating temperature range. In general, selection of a coating with a low ductile brittle transition temperature (DBTT) and high toughness will be advantageous. The nominal composition of the overlay coatings is optimized to balance hot corrosion and oxidation resistance, DBTT, and toughness. An increase in the Al or Cr content of the CoCrAlY coating tends to increase the DBTT. Therefore to improve ductility, Al levels should be below 12 wt. % and sometimes as low as 5 wt. % are used. The addition of Ni to CoCrAlY coatings

has been found to decrease the DBTT and increase toughness. Addition of Si or Re (rhenium) to an overlay coating also increases the DBTT. The diffusion aluminides and high aluminum containing MCrAlY overlay coatings are brittle and are likely to exhibit lower resistance to TMF cracking compared to the coatings containing low aluminum. In general, NiCoCrAlY coatings are more ductile than CoCrAlY coatings and offer improved resistance to TMF. Maintaining quality (thickness and chemical composition etc.) of the coating is also important. For example, thicker over aluminized layer on a MCrAlY coating lowers the TMF cracking resistance.

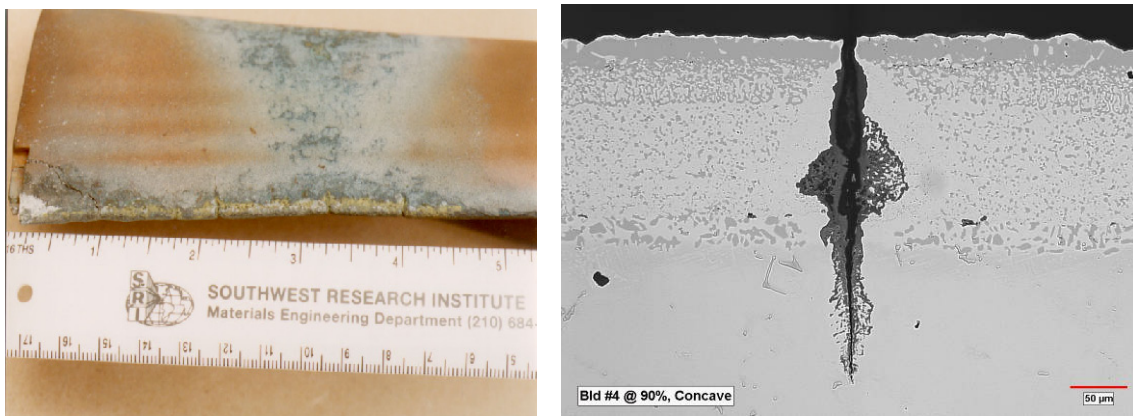


Figure 3. Photograph showing a) TMF cracks on the airfoil of a Frame 7EA Row 1 blade after 20 000 hours operation with 320 starts and b) typical morphology of a TMF crack in the over aluminized CoCrAlY coating on a Frame 9FA Row 1 blade after 26 000 hours operation with 630 starts.

4. Creep Damage

Typically, turbine blades do not fail by creep under normal operating conditions since they are designed with a good margin against creep rupture. The blades fail due to creep when they are not properly heat treated to the design high temperature strength or operate at a relatively high temperature due to improper cooling supply resulting from poor design or cooling hole blockage. Typically improper cleaning of the cooling passages and poor quality coating on the internal surface may contribute debris for the cooling hole blockage. Porous and delaminated coating on the internal surfaces is not durable for long-term operation. The debris generated due to spallation of poor quality coating on the internal surfaces blocks the cooling holes. Turbine blades fail in relatively short time when the cooling holes are blocked.

5. Case Studies

Three cases are presented in this section to demonstrate the importance of the quality of the coating on turbine blade life. In first two cases, the blades were replaced because of TMF cracks initiated in the coating and propagated into the substrate blade material. The premature failure was due to poor quality of the coating and the blades were replaced after a few months of service. In the third case the poor quality of the coating on internal cooling passages resulted in cooling blockage, which led to turbine outage due to Stage 1 blade failure. In all three cases the poor quality of the coating lead to premature blade failure.

5.1 TMF Cracking of 7FA Blades

Two Stage 1 blades (number 7 and 57) from a Frame 7FA engine were analyzed. The blades were operated on the same machine at different times. Blade 7 was a new blade and removed after 8286 hours with 670 start-stop cycles. Blade 57 was a re-furbished one and had seen about 2000 hours with 219 start-stop cycles. Both blades were made of GTD 111 DS and coated with GT 33+. Typical condition of the blades is shown in Fig. 4. Three transverse sections at the 25%, 50% and 75% airfoil heights were removed from each blade by electro discharge machining. Several metallurgical mounts were prepared from these sections for detailed metallurgical examination. Typical microstructure of the coating at the 25% airfoil height is shown in Fig. 5. The structure and chemical compositional measurements revealed that both blades had over aluminized NiCoCrAlY (GT 33 + type) coating. The thickness of top aluminide and NiCoCrAlY coating on Blade 7 was 40.6 and 234 μm and on Blade 57 it was 83 and 95 μm , respectively. Typical TMF cracking resistance is inversely related to the thickness of top aluminide. Contamination at the coating/substrate interface was observed on Blade 57, while the interface of Blade 7 was almost free from any contamination as illustrated in Fig. 5.

Chemical composition measurements were made on the NiCoCrAlY coating on the micro sections removed from both blades. The results are shown in Table 1. It is evident from the results shown in the table that the NiCoCrAlY coating on Blade 57 had about 2.5% more Al than the coating on Blade 7. As discussed in a previous section, the high Al content typically lowers coating ductility, toughness, and resistance to TMF cracking.

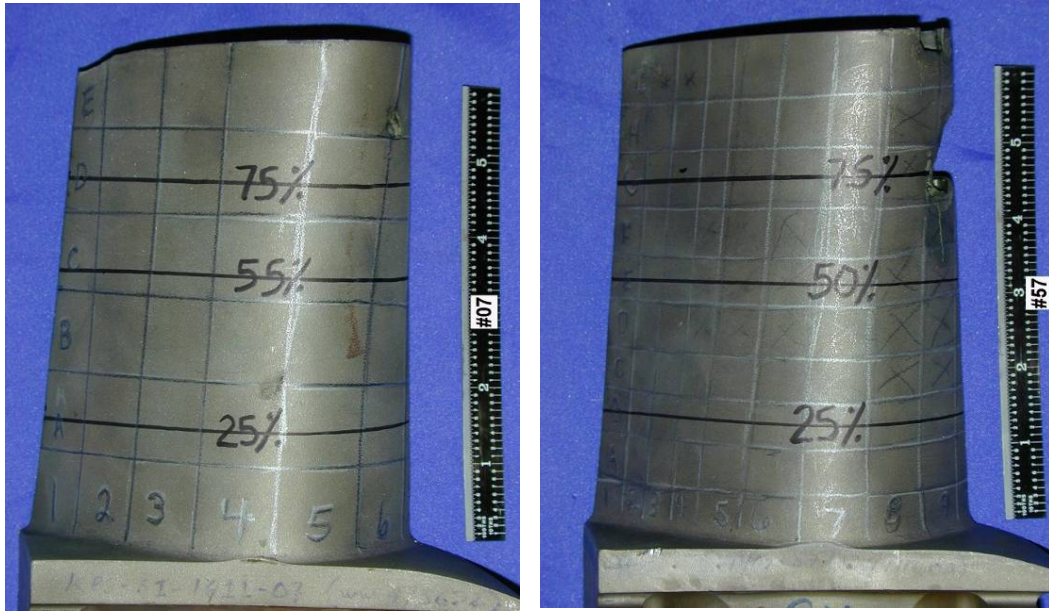


Figure 4. Photographs of as received Blade 7 and Blade 57. The transverse section locations at the 25, 50, and 75% are marked on the photographs.

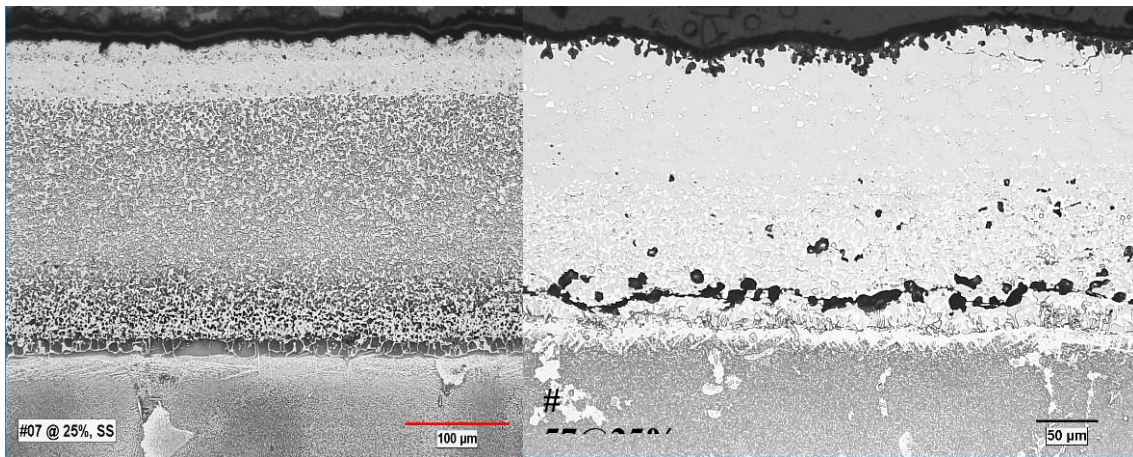


Figure 5. Microstructure of coating on Blade 7 and 57. Note thickness of CoCrAlY and aluminide coating variations between the blades and contamination at the coating/substrate interface of Blade 57.

Table 1. Chemical composition of NiCoCrAlY coating on Blade 7 and 57, wt%.

Blade #	Al	Ti	Cr	Co	Ni	Y
7	11.0	0.4	19.7	33.2	Balance	0.4
57	13.5	0.5	23.4	28.9	Balance	0.4

All micro sections prepared from the blades were examined for TMF cracking. The number of cracks observed on each blade at different airfoil height locations is shown in Table 2. Typical morphology of TMF cracking is shown in Fig. 6.

Several cracks on Blade 57 were extended in to the substrate, while Blade 7 all cracks but one were limited to the coating. Though Blade 57 had operated for a short time (2000 hours), it exhibited more TMF cracks compared Blade 7 that had operated for over 8286 hours. The extensive TMF cracking of Blade 57 can be attributed to the poor-quality of the coating, thicker top aluminide top coating and high Al content in the NiCoCrAlY. These results showed that the poor quality of the coating, i.e., thicker top aluminide coating and high aluminum content in the NiCoCrAlY lowered blade life at least by a factor of four.

Table 2. Variation of number of TMF cracking between Blade 7 and 57.

Blade Height, %	Blade 7		Blade 57	
	Pressure Side	Suction Side	Pressure Side	Suction Side
75	0	6	37	19
50	0	2	51	68
25	0	6	52	49
Totals	0	14	140	126

5.2 TMF Cracking of 501 D5 Blades

Two Stage 1 blades (number 47 and 10) from a 501 D5 engine were analyzed. The blades were operated on the same machine. The blades were new and removed after 5320 hours of service. The blades had seen 518 equivalent starts. The blades alloy was U 520 and coated with a bond coating of CoNiCrAlY and a thermal barrier coating (TBC). Two transverse sections at the 10 and 55% airfoil heights were removed from each blade for metallurgical evaluation. Typical condition of a blade and location of the two transverse sections are shown in Fig. 6.

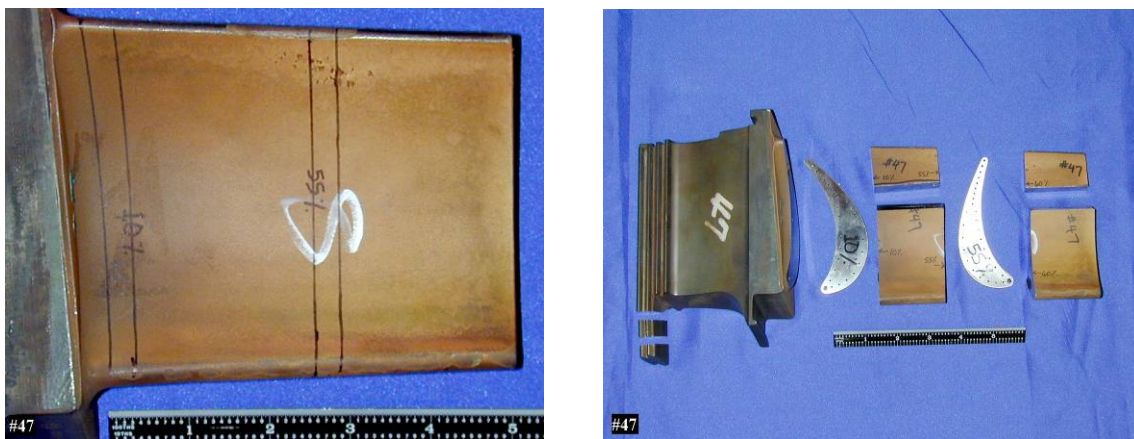


Figure 6. Photographs of as received 501 D5 blade showing the condition and locations of the transverse sections removed for metallurgical analysis.

Typical microstructures of the bond and the top ceramic coatings at the 10% blade height are shown in Fig. 7. Overall, thickness of the bond coating varied from 125 to 200 μm . The chemical composition of the bond coating on the airfoil was determined using energy dispersive spectroscopy (EDS). Compositional measurements were made at the 55% airfoil height. The results are presented in Table 3. The bond coating was found to be CoNiCrAlY on both blades.

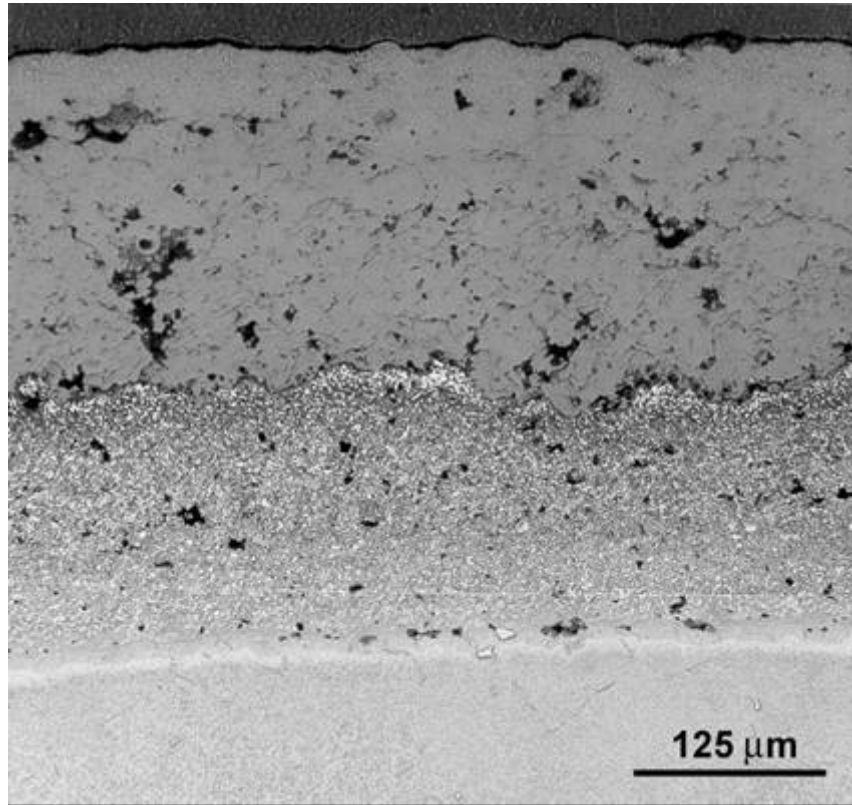


Figure 7. Optical micrograph of coating on the leading edge at the 10% airfoil height. Note porosity in the bond coating.

Table 3. Semi-quantitative composition of coating at the 55% blade height (in wt. %).

Blade Number	Al	Cr	Ni	Co	Y
47	8.1	20.0	34.9	36.7	0.3
10	8.5	19.8	35.5	35.7	0.4

As expected, microstructure of the coating on both blades at the 10% airfoil height was in good condition. No evidence of in-service coating degradation was seen. Microstructure of the CoNiCrAlY coating exhibited a duplex structure, consisting of β -phase ((Ni, Co)Al) in a matrix of γ -phase (solid solution of Ni-Co-Cr).

Extensive connected pores and voids were observed in the bond coating. The extent of porosity in the CoNiCrAlY bond coating was atypical. The outer surface of the bond coating was rough and exhibited hills and valleys. In some areas, the valleys did look like deep “pits” and were filled with TBC, suggesting that these valleys were formed during the original coating application. Thickness of the bond coating at some of these isolated valleys was measured to be 50 μm , as shown in Fig. 8. A discontinuous white layer was also observed at the outer surface of the bond coating as well as around the voids.

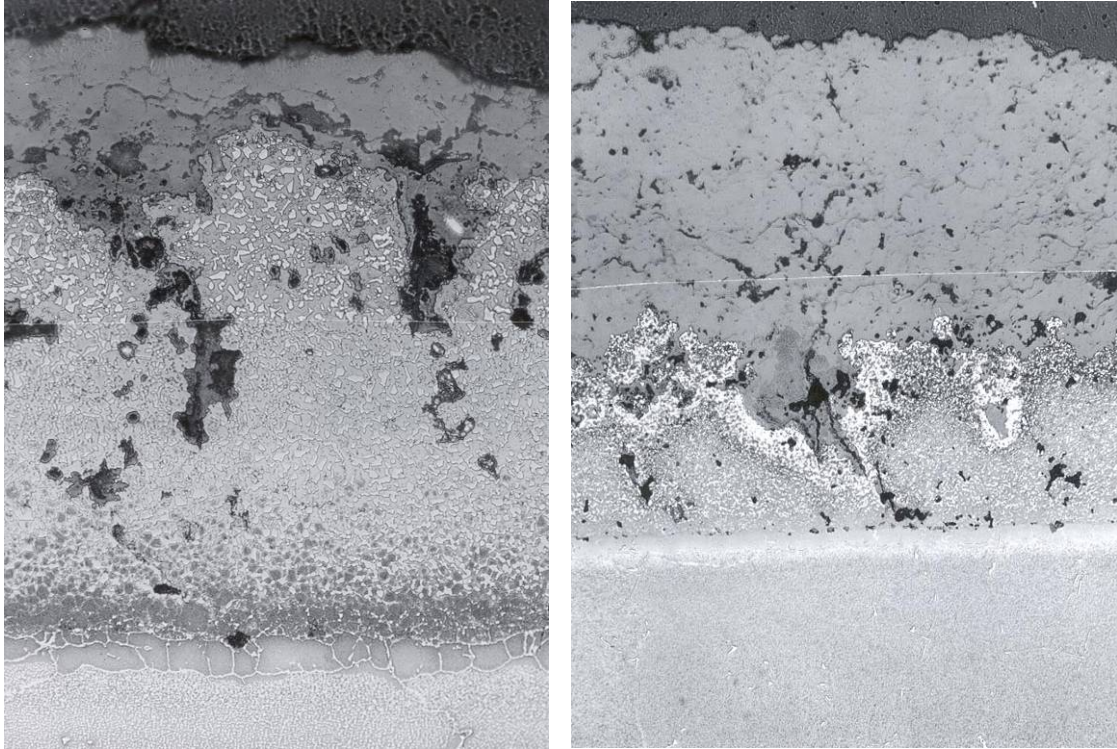


Figure 8. Optical micrographs of coating on the concave side of the airfoil showing voids and the white band of alloy depleted areas at the outer surface of bond coating and deep valleys.

The depletion of alloying elements such as chromium, aluminum, etc. leads to formation of the white layer. No oxide scale was observed in the proximity of the white layer. EDS analysis showed that chromium content in the white layer is lower than in a non-depleted area of the coating. The turbine blades operate at a relatively low temperature at the 10% airfoil height. Therefore, it is unlikely that the observed loss of chromium at the outer surface of the bond coating occurred during service. The white layer most likely formed during the post coating or diffusion heat treatment of these blades. The alloy depletion of the bond coating is not normally seen on properly processed turbine blades. The top coating on both blades was yttria stabilized zirconia (TBC). Thickness of the TBC varied from about 175 to 325 μm . No significant variation in the coating thickness was observed between the blades.

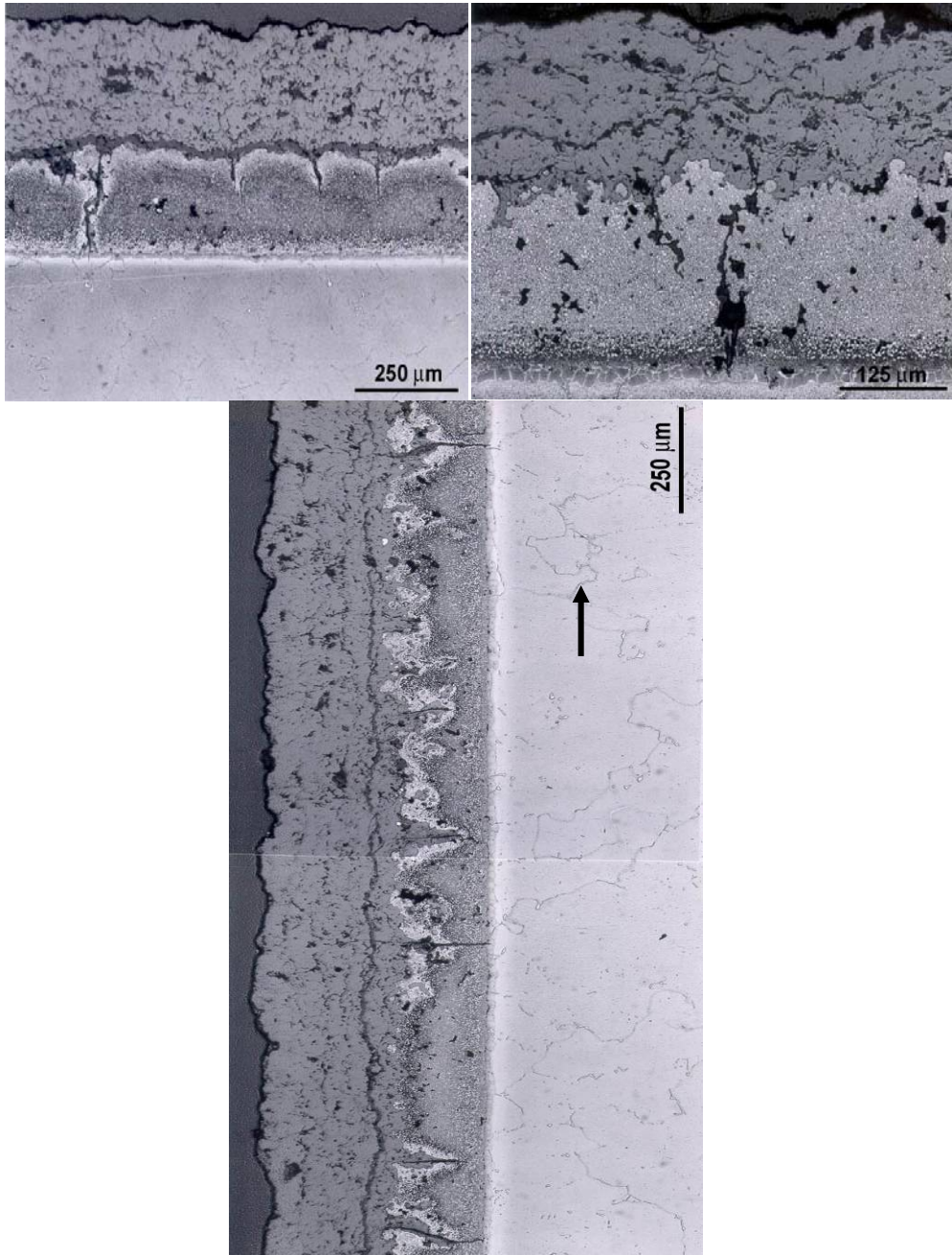


Figure 9. Optical micrographs of typical TMF cracks in the bond coating.

Fig. 9 shows typical cracks observed at the 10% and 55% airfoil heights. It is clear from the figures that most of these cracks are in the coating, but only few cracks extended into the substrate in both blades. Majority of cracks initiated from the outer surface of the bond coat and some were initiated from the pores/voids in the bond coating. The bond coat outer surface cracks initiated from “notch-like” defects in the coating. The notches are known to act as stress raisers and promote premature TMF crack initiation. The deepest cracks that were extended into the substrate in Blade 47 and Blade 10 propagated about 1 mil and 3 mils, respectively into the substrate below the bond coating.

The morphology of the cracks indicates that the cause of cracking is thermal-mechanical fatigue loading resulting from start-stop cycles of the turbine. The defects such as surface irregularities, alloy depletion, and excessive connected porosity in the bond coating are considered in part responsible for premature TMF cracking of these blades.

5.3 Creep Failure Frame 6 Blades

Ninety-two Stage 1 Frame 6 blades were received for evaluation. The turbine was fired with natural gas and fired at 1113°C (2035°F). The blade had operated for 6600 hours after refurbishment. The blades were made of GTD 111 DS and coated with GT 33 + like coating. The internal surfaces of cooling holes were coated aluminide. Blade No. 6 had airfoil fracture at 2.3 in. above the platform (at about 48% of the airfoil height) and Blade No 82 appeared to have a service induced crack at the trailing edge at approximately 68% of the airfoil height. Several other buckets had suffered different degree of consequential impact damage to the airfoil. The condition of the some of the blades is shown in Fig. 10. Visual examination revealed evidence of necking and secondary cracking on the concave and convex sides of the airfoil of Blade 6 as illustrated in Fig. 11. Examination of cooling holes revealed that cooling holes in 37 out of 92 blades were either partially or completely blocked. Deposit before and after removing from a blocked cooling hole of Blade 6 is shown in Fig. 12. The powder collected from the blocked cooling hole of Blade 6 was analyzed by EDS and the EDS spectrum is show in Fig. 13. The deposit contained predominantly Al, Cr, and oxygen. The X-ray diffraction results of cooling deposit showed that the deposit powder in the cooling hole of Blade 6 is a mixture of Al_2O_3 and Cr_2O_3 . In addition to these oxides, intermetallics of Al and Cr were also observed in the deposits collected from the cooling holes of other blades. These results indicate that the deposits in the cooling holes are most likely oxides of cooling hole coating and/or the slurry used for application of the aluminide coating on the internal surfaces.



Figure 10. Typical condition of as-received blades.

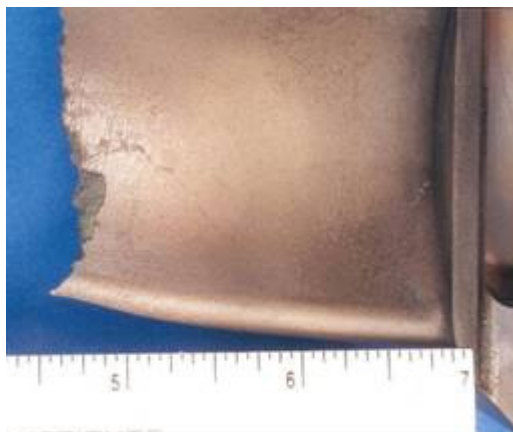


Figure 11. Photographs of Blade 6. Note necking at the leading edge.



Figure 12. Photographs of deposit in the cooling holes of Blade 6. Arrow on the photographs points to the deposit.

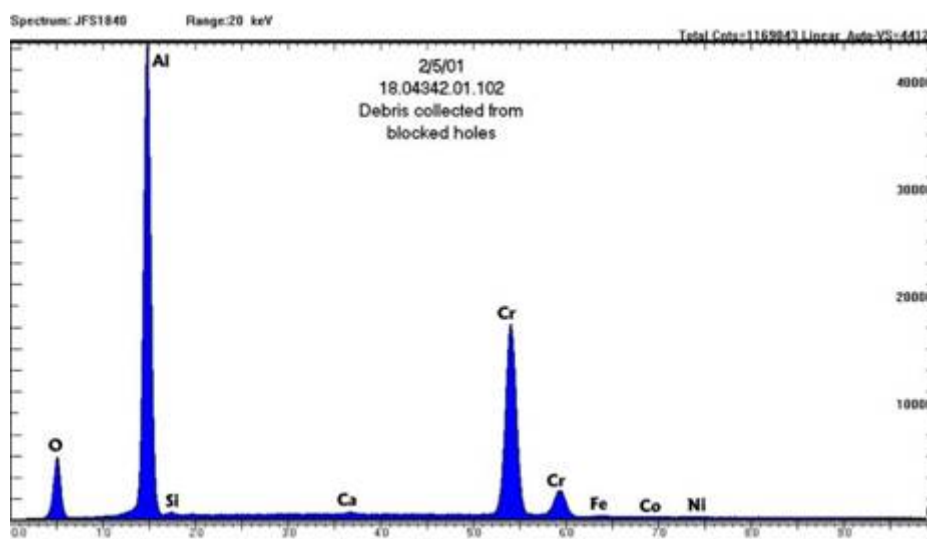


Figure 13. EDS spectrum obtained from the cooling deposit collected from Blade 6.

The coating on the internal surfaces (cooling holes) of three buckets was examined under a microscope. The examination showed that quality of the coating on the internal surfaces of all three was also poor. The aluminide coating on the internal surface exhibited a two layer coating and the top layer was porous as shown in Fig. 14. A two-layer coating structure or porous coating is not normally seen on the cooling-hole surfaces. This layer was not considered durable for long-term operation. Debris generated due to spallation of porous and/or the delaminated top layer was probably responsible for cooling-hole blockage. Consistent with the cooling hole blockage, the external coating and the base material at the leading edge of Blade 6 were severely degraded in a relatively short time. The severely degraded coating and the base material are shown in Fig. 15. These results indicate the blade 6 had seen very high temperature in excess of 1000°C (1832°F). In addition, creep cavities were observed on the grain boundaries of the base material of Blade 6 and 82 indicating that the mechanism of blade failure was creep. Cooling hole blockage resulting from the poor quality of the internal cooling surfaces was responsible for the premature creep failure of the blades.

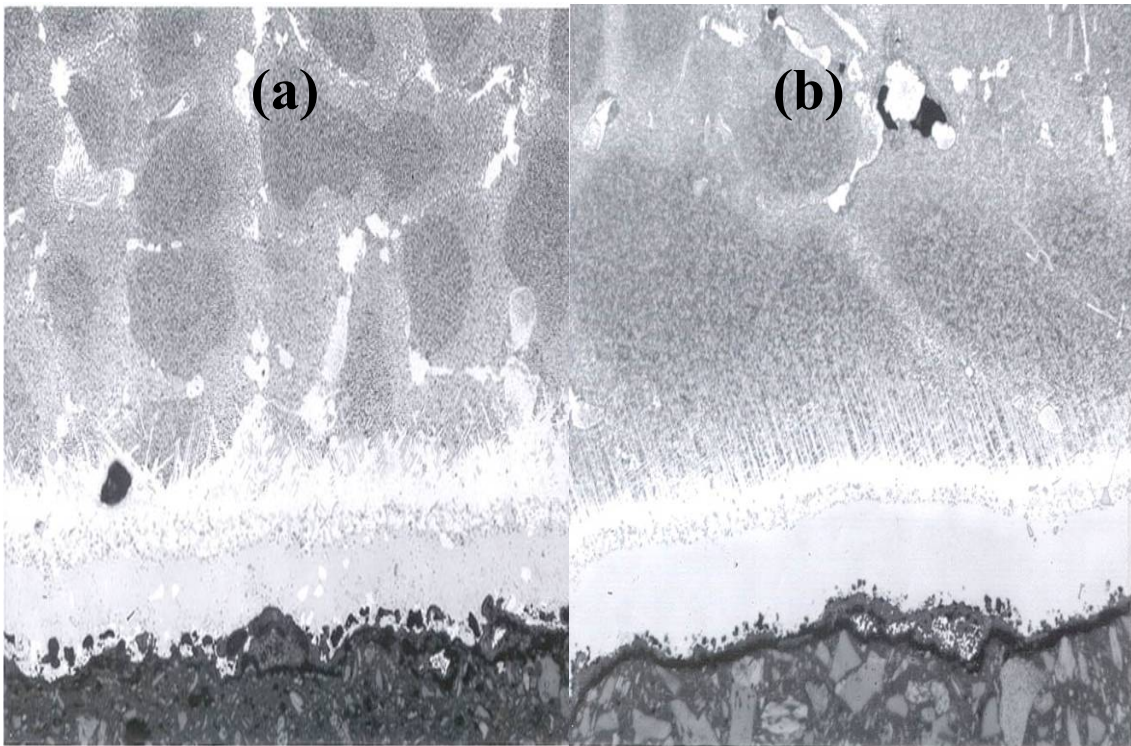


Figure 14. Optical micrographs showing aluminide coating on the cooling-hole surfaces. (a) Cooling Hole No. 11 of Bucket No. 5 and (b) Cooling Hole No. 12 of Bucket No. 82. Note porous and/or two-layered coating.

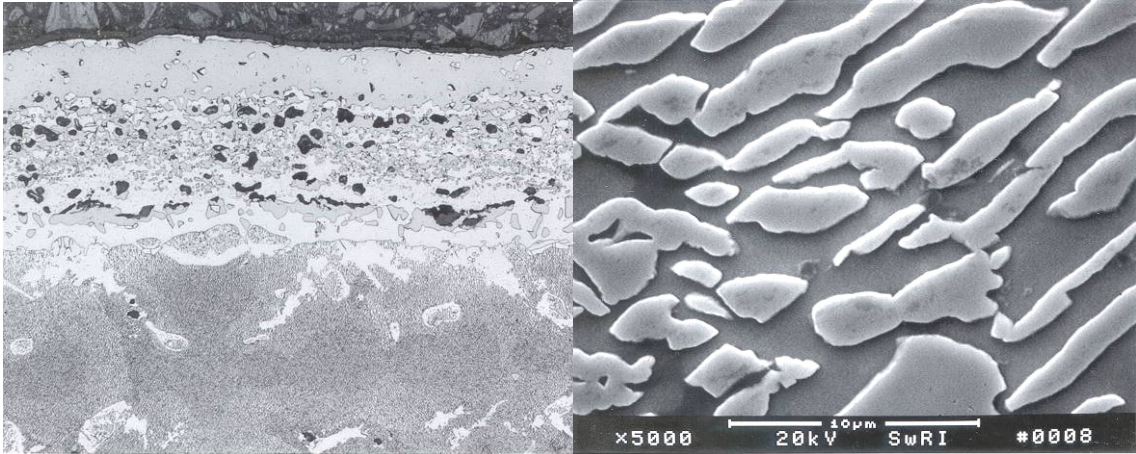


Figure 15. Degraded coating and gamma prime particles at the leading edge near the fracture.

6. Conclusions

From the evaluations conducted on the service run blades the following conclusions can be drawn:

- Coating quality is important for durability of turbine blades and availability of engines.
- Blade service life is controlled by the quality of the coating on the internal and external surfaces.
- Poor quality coating could lead to premature cracking or catastrophic turbine failure.
- Turbine repair and maintenance costs could be reduced by properly recoating the blades.
- To avoid premature failures, good quality control procedures need to be followed during manufacturing and refurbishment of turbine blades.

References

1. Cheruvu, N.S., Chan, K.S. and Leverant, G.R. "Combustion Turbine Hot Section Life Management: High Temperature Coating Systems," EPRI Report #1000432, Electric Power Research Institute, Palo Alto, California, 2000.

2. Cheruvu, N.S. and Leverant, G. R. "Influence of Metal Temperature on Base Material and Coating Degradation of GTD 111 Buckets," Proceedings of ASME International Gas Turbine and AeroEngine Congress and Exhibition, June 2–5, 1988, Stockholm, Sweden, Paper 98-GT-511.
3. Cheruvu, N.S., Carr, T.J., Dworak, J. and Coyle, J. "In-service Degradation of Corrosion Resistant Coatings," Proceedings of ASME International Gas Turbine and AeroEngine Congress and Exhibition, Birmingham, UK, 1996, Paper 96-GT-429.
4. Ellison, K.A., Daleo, J.A. and Boone, D.H. Proceedings of the Conference on "Life Assessment of Hot Section Gas Turbine Components," Edinburgh, The Institute of Materials, Edinburgh, London, UK, 1999. Pp. 311–327.
5. Cheruvu, N.S. et al. "Blade Life Management System for Frame 7FA/9FA Gas Turbine," 1998 Interim Report, EPRI, Palo Alto, KEMA Nederland B. V., Arnhem, The Netherlands, Florida Power & Light Co, Juno Beach, Florida, 1998, TR-111548.
6. Czech, N., Schmitz, F. and Stamm, W. "Microstructural Analysis of the Role of Rhenium in Advanced MCrAlY Coatings," *Surface & Coatings Technology*, 1995, 76–77, pp. 28–33.
7. Beele, W., Czech, N., Quadackers, W.J. and Stamm, W. "Long-term Oxidation Tests on a Re-containing MCrAlY Coating," *Surface & Coatings Technology*, 1997, 94–95, pp. 41–45.
8. Czech, N., Schmitz, F. and Stamm, W. "Improvement of MCrAlY Coatings by Addition of Rhenium," *Surface & Coatings Technology*, 1994, 68–69, pp. 7–21.
9. Cheruvu, N.S., Chan, K.S. and Leverant, G.R. "Condition Assessment and Life Prediction of Diffusion and Overlay Coatings," Presented at the EPRI/DOE Conference on Advances in Life Assessment and Optimization of Fossil Power Plants, March 11–13, 2002, Orlando, Florida.
10. Dallio, J.A. and Boone, D.H. "Failure Mechanisms of Coating Systems Applied to Advanced Turbines," Proceedings of ASME International Gas Turbine and Aero Engine Congress and Exhibition, Orlando, Florida, USA, June 1997, Paper 97-GT-486.
11. Srinivasan, V., Cheruvu, N.S., Carr, T.J. and O'Brien, C.M. *Materials and Manufacturing Processes*, 1995, 10, p. 955.

12. Dewey, R. and Hulshof, H. Blade Management Systems for Advanced F Class Turbines, Electric Power Research Institute, Palo Alto, California, TR-114312, 1999.
13. Cheruvu, N.S., Chan, K.S. and Leverant, G.R. "Blade Life Management: Coating Systems," EPRI Report #TR-113899, Electric Power Research Institute, Palo Alto, California, 1999.
14. Cheruvu, N.S., Chan, K.S. and Leverant, G.R. "Blade Life Management: Coating Systems," EPRI Report #1006608, Electric Power Research Institute, Palo Alto, California, 2002.

Evaluation of the operating conditions of gas turbine blades and vanes after long term service

Pertti Auerkari, Jorma Salonen and Tom E. Gustafsson
VTT Technical Research Centre of Finland, Espoo, Finland

Ilkka Karvonen and Heikki Tanttari
Lappeenrannan Energia, Lappeenranta, Finland

Sari Mäkinen
Helsingin Energia, Helsinki, Finland

Abstract

The combination of structural and materials performance together with the actual service conditions will determine the ideal timing for maintenance and the technical lifetime of gas turbine blades. While the designer aims to fit the process, structural and materials solutions together according to the foreseen service, some deviation is likely both in the manufactured components and in the actual service conditions. These deviations do not need to be large, as in particular a relatively small shift in local temperature can translate into large differences in life. The interest on the actual service temperatures often extends beyond the original supplier, but then the assumptions of design or original test data may not be available. Sacrificing one blade of a set for detailed inspection provides an opportunity to estimate the distributions of the effective service temperatures. In this paper, the principles of doing this are reviewed in brief, and few examples are given of evaluated blades. Although it is naturally possible that blades suffer from higher than expected thermal loads, quite often the evaluation will result in allowed life extension with or without refurbishment. The limitations of the approach are also discussed in brief.

1. Temperature estimation – principles

The designers and suppliers of gas turbines usually have a fairly good idea of the expected service temperatures in the turbine blades. This is not only because of good numerical tools for process and structural design but also because of the background experience and temperature measurements during the early development of the given type of turbine. However, actual service of any given machine will not follow such assumptions exactly, because of some likely differences in intake air, fuel, firing, operational modes, and possible modifications related to process, components or materials. Also, no early testing can fully reflect the influence of long term service that can involve a very wide

variation in the operational conditions in different machines. Because of the high temperature sensitivity of several damage mechanisms, it is nevertheless important that the service temperature is known and controlled within relatively narrow bounds.

A common principle of estimating the effective service temperature T for an in-service time t is based on the Slyozov-Lifshitz-Wagner-expression for particle coarsening by diffusion (originally for dilute mixtures). This expression can be expressed as [1]

$$(Kt/T)\exp(-Q/RT) = r^3 - r_0^3 \quad (1)$$

where K is a material dependent rate constant, Q is the apparent activation energy of the process, R is the gas constant, r is the effective mean diameter of the particles, and r_0 is their initial mean diameter. Measuring r and r_0 and knowing (or measuring) K and Q for the alloy will provide an estimate of the effective service temperature.

The in-service coarsening of the gamma'-particles of nickel-based gas turbine blade alloys are often suitable for such an assessment (Fig. 1).

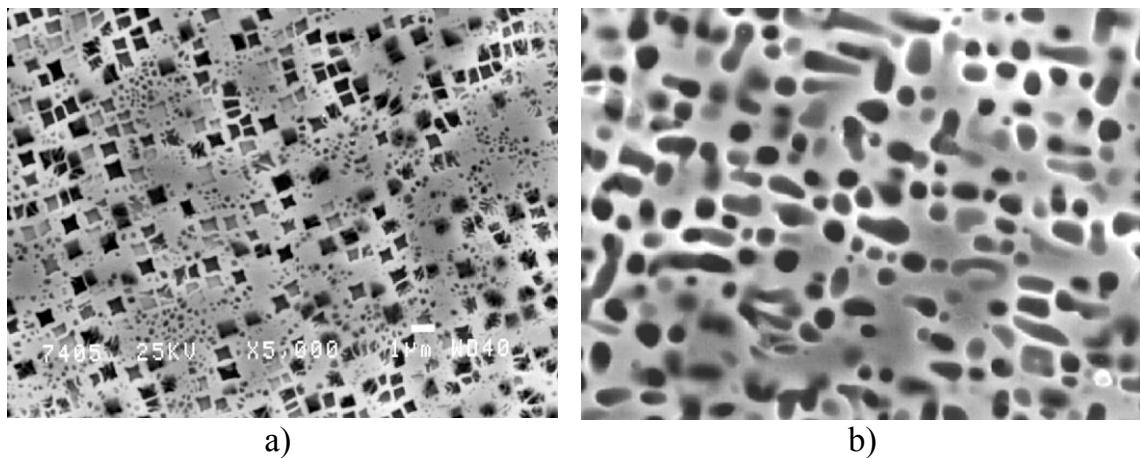


Figure 1. In-service changes of gamma'-particles in a blade alloy (GTD 111): a) as-new state (cooled blade root); b) hot blade midsection after 30 000 h of service.

These particles, however, usually show generally a distribution of sizes rather than a single uniform size. Therefore, a characteristic value needs to be selected for r and r_0 , and often some mean or peak value is selected for the purpose. It should be noted, however, that the size distribution of gamma'-particles can be wide and variable with more than one peak, and may not retain its original shape characteristics in time.

In the following, a few examples are taken of assessments where the thermal loads have been at clearly different levels, and where the strengthening gamma'-phase also shows originally differing appearance.

2. Example cases

Ex-service blades can exhibit very variable condition, from nearly as-new state to fully degraded and unrepairable scrap metal [2–4]. At the extremes, there may be little incentive for temperature estimation, but even in such cases the estimates may also help in e.g. analysis of possible deviation or failure. The examples below aim to cover some of the variation in different types of blades and materials.

Case 1: Vane of IN939

The coated ex-service first row vanes of a V64.3 gas turbine showed linear indications in surface inspections (FPI), and one vane was sacrificed for destructive inspection. The classical of Eq. (1) was applied for estimating the effective blade material temperatures at three cross-sections of the vane. The results near the mid-section of the vane are shown in Fig. 2.

Clearly, in this case the material temperature is far higher near the leading edge than elsewhere. The effects of thermal degradation were also evident in the MCrAlY coating of the vane and in surface cracking (not shown).

Case 2: Blade of GTD 111

This first row blade of a Frame 6 turbine had suffered from overheating to the extent that the protective coating has been consumed and the base material (GTD 111) shows severe oxidation (Fig. 3). The gamma'-particles had grown to very large size, at temperatures that had probably exceeded 1000°C. The base material has been weakened by oxidation to initiate and grow creep cracks between the outer surface and cooling holes. The blade was judged to have suffered irreparable damage.

Case 3: Blade of Udimet 500

The uncoated and uncooled blades in this case were from the second row of a W251 gas turbine, and made of the alloy Udimet 500 as confirmed by chemical analysis. The blades had been in service for 88 000 equivalent operating hours (eoh) without any notable damage indicated by NDE. One blade was destructively inspected, and the observed microstructures of the root and central blade sections are shown in Fig. 4. The corresponding size distributions of the gamma'-particles are shown in Fig. 5.

Comparing the mean size of the gamma'-particles to that at the cooler root region shows increasing mean size and widening size distribution of the gamma'-particles for the hottest blade section in service. Using Eq. (1) with the appropriate constants for Udimet 500 gives an effective service temperature of about 765°C. This is a credible level for the uncoated blade of the vintage turbine, and in this case the blade condition appeared to allow further service.

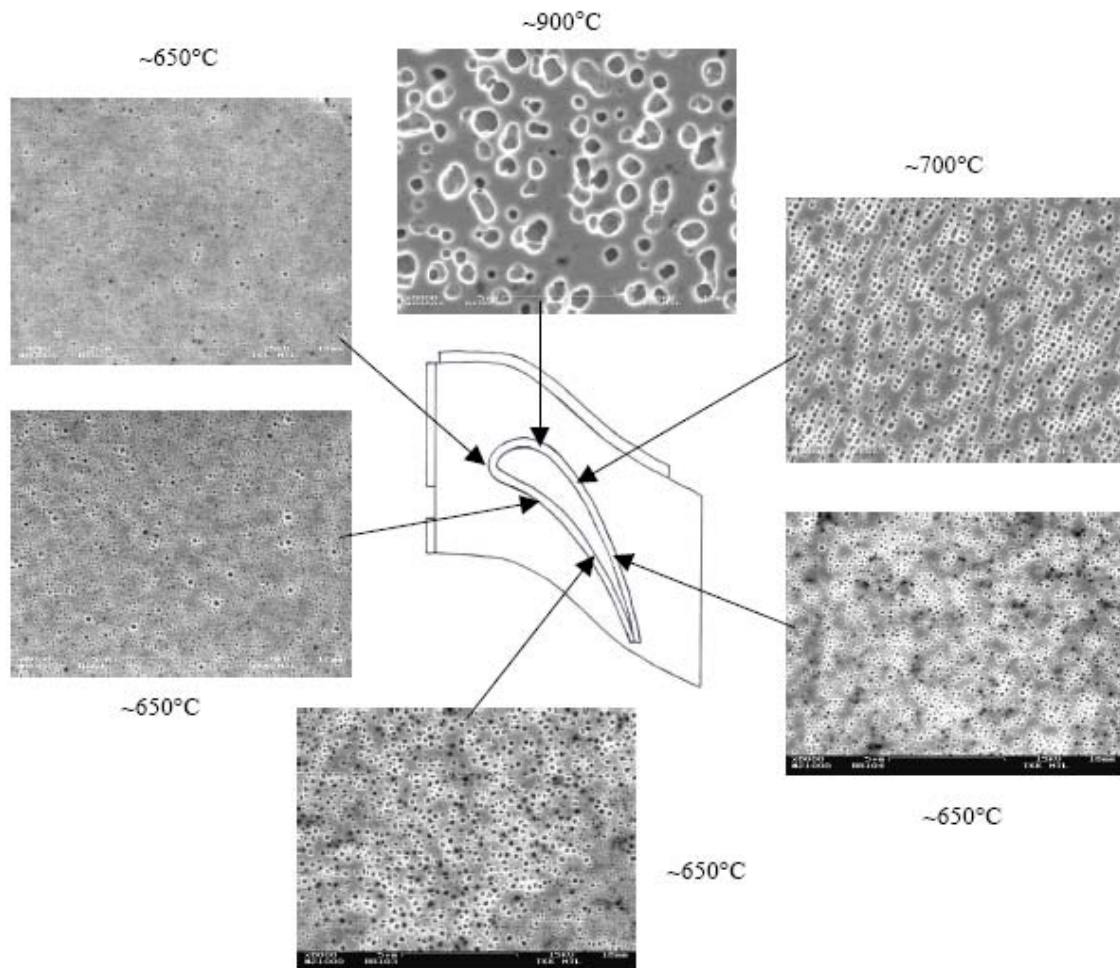


Figure 2. Observed gamma'-particles and the estimated service temperatures in a vane of IN 939 (near mid-vane cross-section) [2].

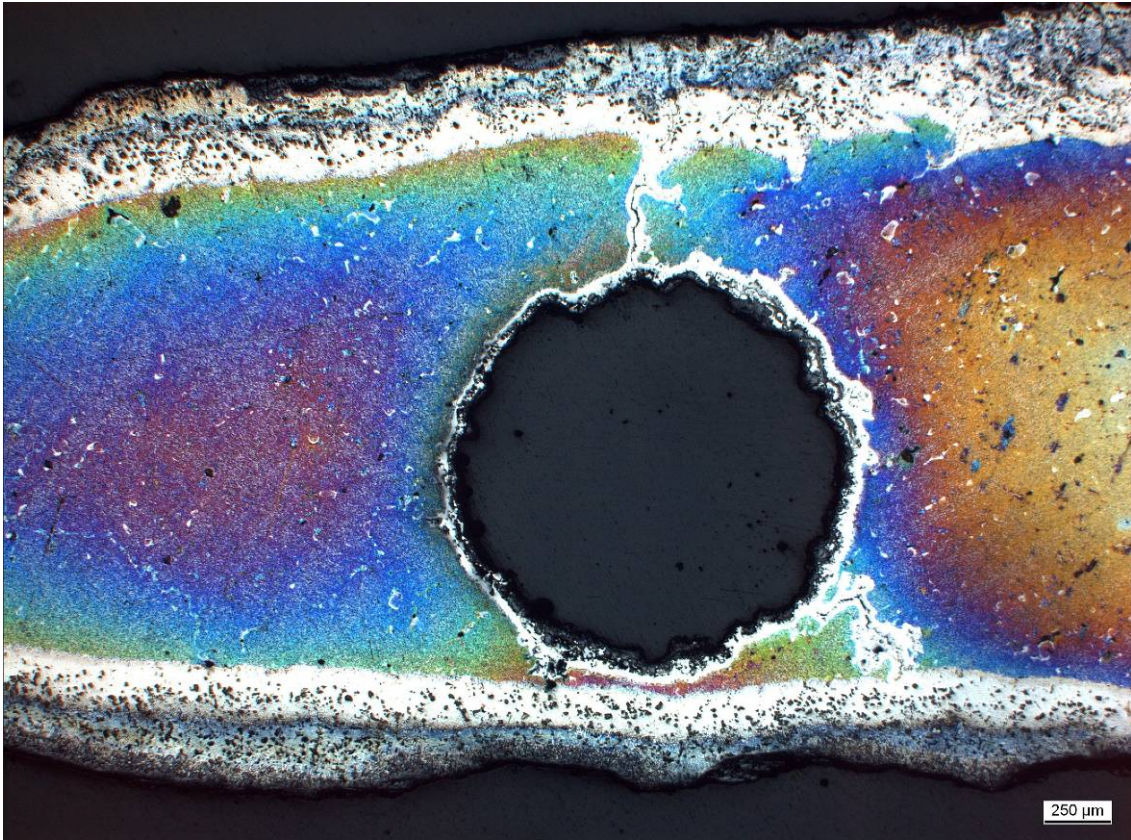


Figure 3. Cross-section of an overheated blade (GTD 111).

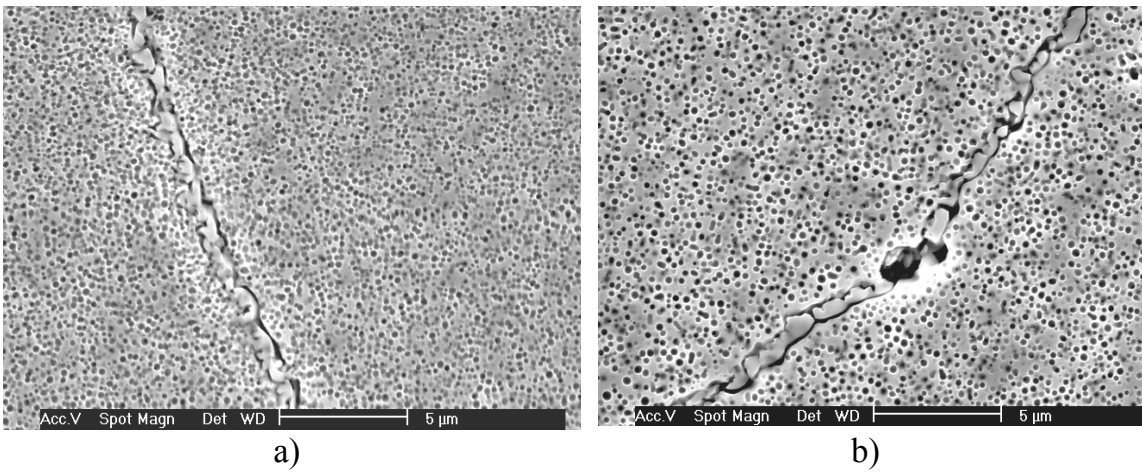


Figure 4. Gamma'-particles in Udimet 500: a) root section; b) blade section.

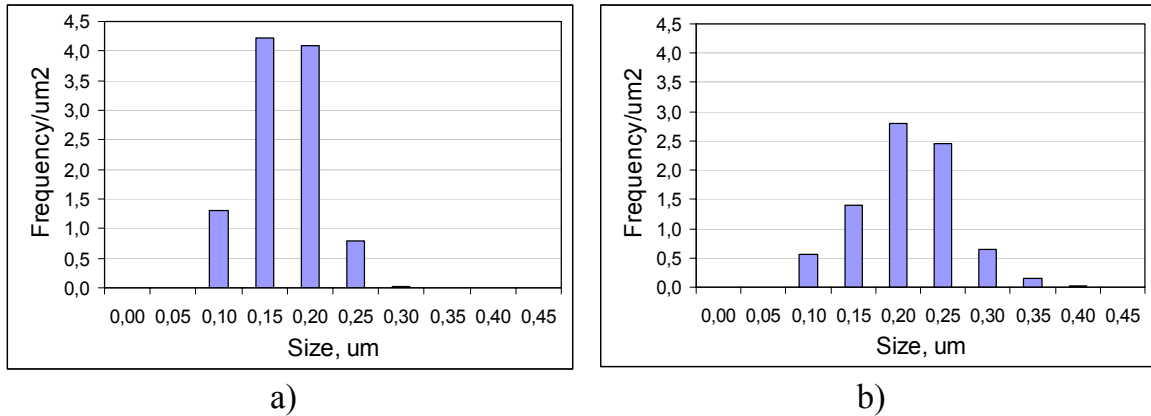


Figure 5. Size distributions of gamma'-particles, Udimet 500: a) root; b) blade.

Case 4: Blade of Udimet 720

The uncooled and uncoated blades in this example were from the fourth row of a V64.3 gas turbine, and made of an alloy corresponding to Udimet 720 according to the chemical analysis of sample blades, sacrificed after about 109 000 eoh. No significant damage was detected on the blade surfaces by NDE. The observed microstructures of the root and central blade sections of one blade are shown in Fig. 6 and corresponding size distributions of the gamma'-particles in Fig. 7.

In this case the comparison of the mean gamma' size at the cooler root region and at the blade midsection suggested that long term service had no significant thermal effect on the blades. The same was also shown by the similar and practically as-new shape of the gamma'-particles both at the root and in the blade section (Fig. 6).

Negligible or minimal thermal changes also mean that the microstructure does not indicate the actual service temperature but only suggests that it was less than 600–650°C. This is sufficient information so that with the exclusion of several competing mechanisms (creep, fatigue, wear etc) the blades could be returned to service without refurbishment.

3. Discussion: benefits and limitations

The principal benefit of the approach is of course the access to the actual effective service temperatures and temperature distributions along the blade. This information is often an essential element in evaluating the potential for further safe operation. In addition, the same microstructural assessment provides a general picture on the service condition of the blade, for example regarding coatings (if any), surface oxidation/corrosion, internal integrity, defects etc. With

experience on particular machines, blades and materials it may be possible to make a fair judgement on the blade condition and required action without further very detailed analysis.

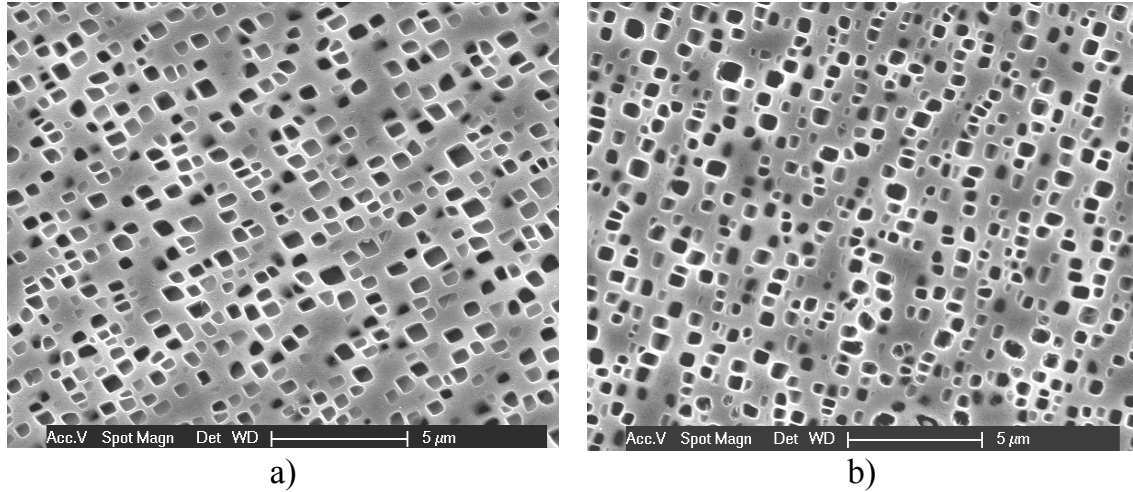


Figure 6. Gamma'-particles in Udimet 720: a) root section; b) blade section.

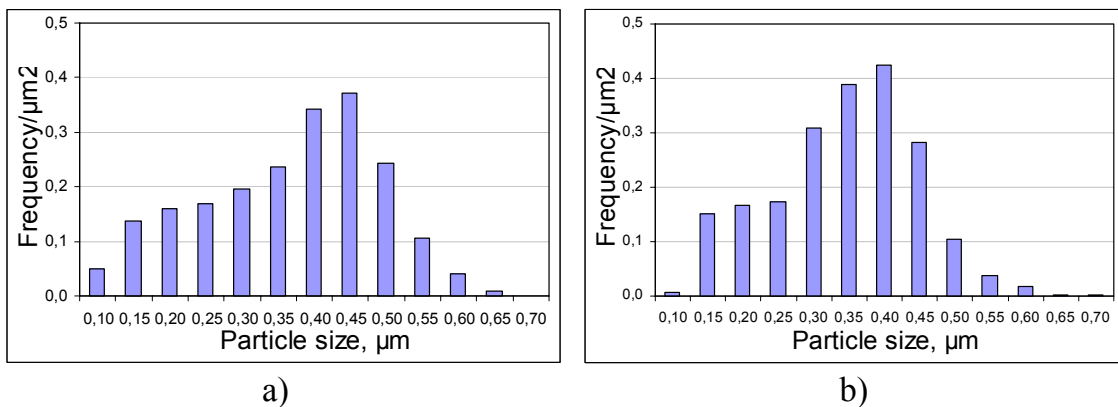


Figure 7. Size distributions of gamma'-particles, Udimet 720: a) root; b) blade.

The approach also has some limitations: for example, the indicated service temperature is effectively averaging the whole service history. Therefore, effects of short local peak temperatures are not easily distinguished from those of longer periods at somewhat lower temperatures. Nevertheless, such effects are generally not thought to set critical limits in blade life assessment.

Some limitations to the accuracy of the estimated temperatures arise from the variations in the observed microstructure and from the inaccuracies in evaluating the original initial microstructure. Such variation may be compounded by inaccuracy in supporting information, such as the history of heat treatments during fabrication or refurbishments. Even without such deviation, the inaccuracies e.g. in the material constants of Eq. (1) and the observed particle sizes can be a significant source of uncertainty. For some materials these

quantities are easier to obtain than for some others, for example because of available reference data or because of suitably sized and distributed gamma'-particles.

A potential source of uncertainty is the variation in the gamma'-particle distributions. These may vary quite significantly from one field of view to the next within the microstructure, and then it is necessary to sample a sufficient number of fields to obtain a representative combined distribution. Dependence on orientation can be expected, and it is not necessarily true that the root section represents the as-new distribution of the blade section, particularly if a thick-section area is selected for comparisons. As was also noted above, the size distribution can exhibit more than one peak, and may not retain its original shape characteristics in time.

There are alternative methods to estimate the local temperatures, for example using the width of the diffusion layers between the coating and base material of the blade [3]. Again, using such data requires not only a model for the thermally activated degradation processes but also data that is valid for the particular combination of coating and base material.

Also, in some cases the need for separate temperature estimates may be bypassed, for example when the coating condition alone is known to be life-limiting and the degradation rate of the coating can be independently estimated by using special NDT, for example [6]. However, even then if a blade is sacrificed for condition assessment of the coating, the service temperatures and the substrate condition are of interest.

However, limitations aside, the forensic evidence provided by the thermal processes in the microstructures of gas turbine blading is very useful and supports well the decisions on inspections and maintenance. With accumulating routines and experience from widening range of blades and vanes, the approach serves the users in managing the safe condition of ageing turbines.

4. Conclusive remarks

The service temperature is one of the most important factors that determine the degradation rate and life of gas turbine blades. This is mainly because several important damage mechanisms that can limit life, such as creep, oxidation and hot corrosion, are relatively sensitive to temperature. To assess the condition and residual life of turbine blades and vanes after a significant period of operation is often helped by estimates of the effective service temperature.

One way of to obtain such estimates is to rely on the observed coarsening of the gamma'-particles of the blade material, as observed from a sacrificed blade sample. The necessary comparison to as-new material is usually taken from the cooler root parts of the blades. The approach is demonstrated by examples covering coated (hot) and uncoated blades made of various Ni-based superalloys, and a range of turbine origins and designs.

The examples show that apart from some extreme cases, the resulting temperature estimates can provide a good basis for life assessment and extension. For this purpose, also the loads (stress levels) need to be assessed, as well as the environmental impact on surfaces and coatings. The actual condition and life assessment must necessarily consider a range of potential mechanisms that could become life limiting. The combination of structural and materials performance together with the actual service conditions will also determine the ideal timing for maintenance and eventual refurbishment of the blades. The limitations of the approach have been discussed in brief.

Acknowledgements

The materials and financial support through the partnership within the projects GT-MAT (1998–2000) and LC-Power (2004–2007) is gratefully acknowledged.

References

1. Hou, J.S., Guo, J.T., Zhou, L.Z., Li, Z.J., Qin, X.Z., Li, Y.L. and Ye, H.Q. Influence of solution heat treatment conditions on gamma prime characteristics in a hot corrosion resistant superalloy. Materials for advanced power engineering (Liege Conference), Part I. FZ Jülich 2006. Pp. 435–444.
2. Jauhiainen, P. Condition assessment and NDE of gas turbine blading materials. Graduate Thesis (in Finnish), Helsinki University of Technology, Espoo 2001. 161 p. + app.
3. Auerkari, P., Heikinheimo, L., Salonen, J., Lepistö, T. Materials implications for maintenance of gas turbines. Baltica V – Condition and life management for power plants, VTT Symposium 211, Vol. I. VTT, Espoo 2001. Pp. 89–98.
4. Cheruvu, N.S. Degradation of gas turbine coatings and life assessment. Baltica IV – Plant maintenance for managing life & performance. VTT Symposium 184, Vol. I. VTT, Espoo 1998. Pp. 79–91.
5. Reed, R.C. The Superalloys – fundamentals and applications. Cambridge University Press, Cambridge. 372 p.

6. Bicego, V., Lelait, L. Life prediction of gas turbine hot section components – an Italian-French cooperative project. Baltica VI – Life management and maintenance for power plants, VTT Symposium 233, Vol. 1. VTT, Espoo. Pp. 303–315.

New concepts of RBI/RBM as applied in power plant practice

Jörg M. Bareiß

EnBW Kraftwerke AG, Stuttgart, Germany

Aleksandar S. Jovanovic and D. Balos

Steinbeis Advanced Risk Technologies R-Tech, Stuttgart, Germany

Abstract

The paper presents results of application of two new approaches to risk-based inspection and reliability centered maintenance (RBI/RCM) applied to high temperature components in power plants. On the one hand the RIMAP procedure and on the other hand a safety-related evaluation based on Nondestructive Testing (NDT) results is used. The NDT-concept will be part of future, planned work of an Initiative from VGB PowerTech e.V.¹ to cluster the experience of periodic tests and test findings on boiler parts and steam piping from VGB-members. In the framework of new safety regulations this will help to concentrate onto systems, components and/or locations critical for safety, availability and reliability of power plants.

1. Introduction

The background for the paper is that current practice to inspection and maintenance planning in power plants as well as for most industries is nowadays still mostly time oriented and based on tradition/experience and prescriptive rules. Codes and standards related to inspection and maintenance are still exclusively national. Since late eighties there is a trend that risk-based approaches gain more and more importance and they are nowadays rapidly introduced into daily practice of inspection and maintenance planning in process and power plants.

These risk-based approaches are still allowed in all countries in Europe and help to concentrate onto systems, components and/or locations critical for safety, availability and reliability of industrial plants. However, the very process of finding the „most critical components“, generally denoted as prioritization, can be a challenge, especially if done under the time of pressure (e.g. deadlines, production targets, saving targets, etc.). Criticality can to be determined

¹ VGB PowerTech e.V. as a technical association for power and heat generation is a non-profit organisation and a voluntary association of companies of power plant operators and manufacturers.

according to different criteria, but in practice, the main criteria generally linked to the following aspects:

- state of component, that, combined with the probability profile of external load/factors, defines the probability that „an adverse event“ happens, and
- importance of the component practically usually expressed in terms of (e.g.) cost, safety consequences, environmental consequences and other consequences.

These aspects are the main elements of risk, defined as a combination (product) of probability of occurrence of certain (usually adverse) event and its consequences, for a given set of scenarios, can be used as basis for the critically-based ranking.

2. Results of RIMAP Application

The RIMAP procedure [1] is applicable to many industries and to different types of equipment (for example static equipment, rotating equipment, safety systems, and electrical/instrument equipment). The steps in the procedure are the same for all cases, even if the models and tools for assessing probability or consequence of failure may vary from one application to another.

One application of the RIMAP procedure takes place at a South German coal fired power plant, in operation since 1987 [8]. The demonstration has as main objectives the following issues:

- to demonstrate applicability and usefulness of the RIMAP-methodology on several practical cases focusing on high-temperature components of the plant (boiler parts and steam piping) and on the most common damage mechanisms (creep and fatigue)
- to demonstrate potential economic advantages
- to demonstrate the benefits of standardization
- to give input and feedback to further development/implementation of the methodology and standards for power related issues.

The assessment presented with emphasis on boiler parts, the main steam pipeline and the hot reheat pipeline of a 750MW coal-fired unit operating on 540°C/205 bar (overall 64 components). The risk analysis was performed on different levels regarding the depth of the required analysis and consequently the data base, starting with the screening level and generic data and ending for critical components with a detailed analysis (i.e. probabilistic high-temperature fracture mechanics and the fatigue-creep crack growth analysis) with all obtainable data for the component.

Data collected for the chosen 64 components (headers, t-pieces, elbows):

- Material properties (e.g. average creep rupture strength for the component material and fatigue strength at given temperature)
- Data from the on-line monitoring system (e.g. pressure, temperature)
- Test data (e.g. NDT), incl. previous inspection records
- Performed calculations data (e.g. TRD codes 300/301²) derived from
 - component geometry (e.g. inside diameter, wall thickness, design wall thickness, ...)
 - design temperature and pressure
 - operating temperature and pressure
 - service time of the component (operational hours).

For determination of consequence of failure (CoF), which was in this example considered from economical aspect, the following data was gathered for each of the components:

- Repair cost
- Replacement cost (purchasing/budget price)
- Additional repair/replacement cost
- Additional damage to other equipment cost
- Loss of production cost.

Systems/components planned for the risk analysis will be fully modeled and all data will be stored in a logical database. This will not only facilitate the assessment process itself but also the updating and auditing process that are an essential part of the process. In this application cases the identified component hierarchy was fully modeled in ALIAS Software System³, [9] (now commercially available as iRis-Power [10]) and the RIMAP Procedure flow was fully followed).

² Technical Rules for Steam Boilers TRD300/301 (1919), Vulkan-Verlag, Essen.

³ ALIAS – Advanced Life Assessment Software System, Copyright © 2002, MPA-Stuttgart, Germany.

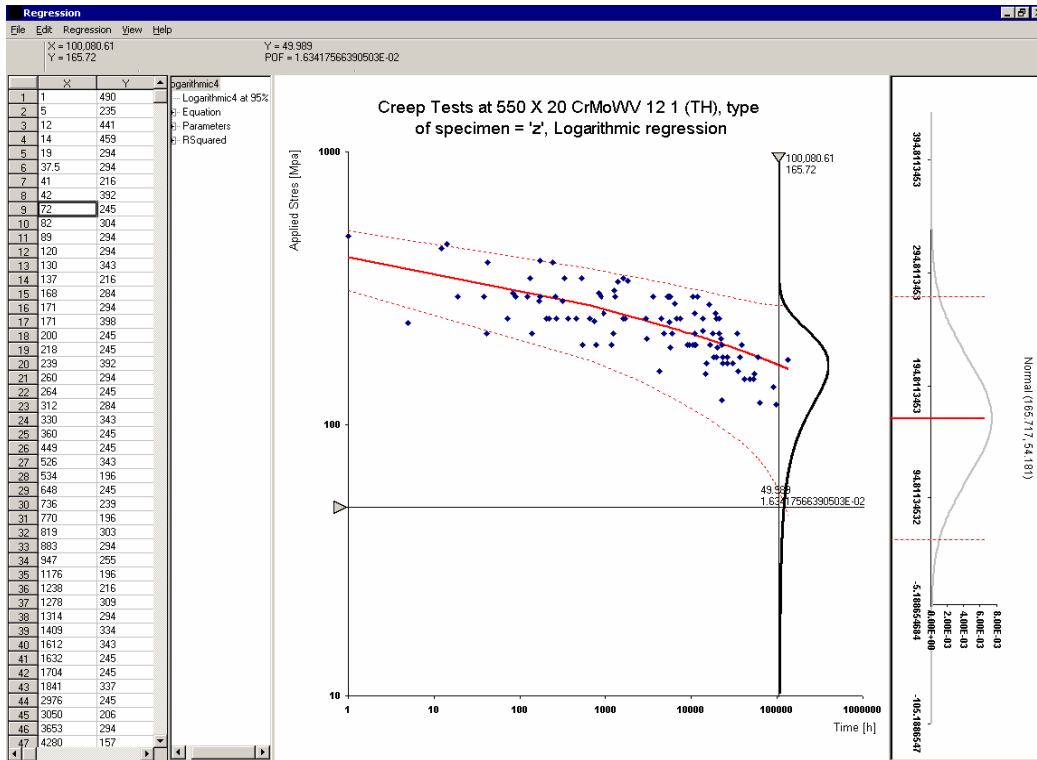


Figure 1. Example for PoF determination based on creep.

Since creep and fatigue are main damage mechanisms for components considered in this application cases, the PoF determination is based on creep exhaustion and fatigue exhaustion. Taking into account the uncertainties material data, load and geometries needed for calculation of exhaustion due to creep and fatigue, the risk of failure increasing with the operating can be assessed. This assessment was done according to the principles set in the EU project RIMAP [2]. It is assumed that average creep rupture strength and fatigue strength have a log-normal distribution like shown in the example of distribution for creep (12%Cr-steel at 550°C) for a given applied stress in Fig. 1.

For the screening level of the analysis only the general statistical data and the component design data was used. Based on this data and using TRD codes, service stress and exhaustion factors (e_z – creep exhaustion, e_w – fatigue exhaustion) were calculated. Based on PoF and CoF values, following the previously defined approach risk can be determined for each component and the defined failure scenarios (risk map see Fig. 2).

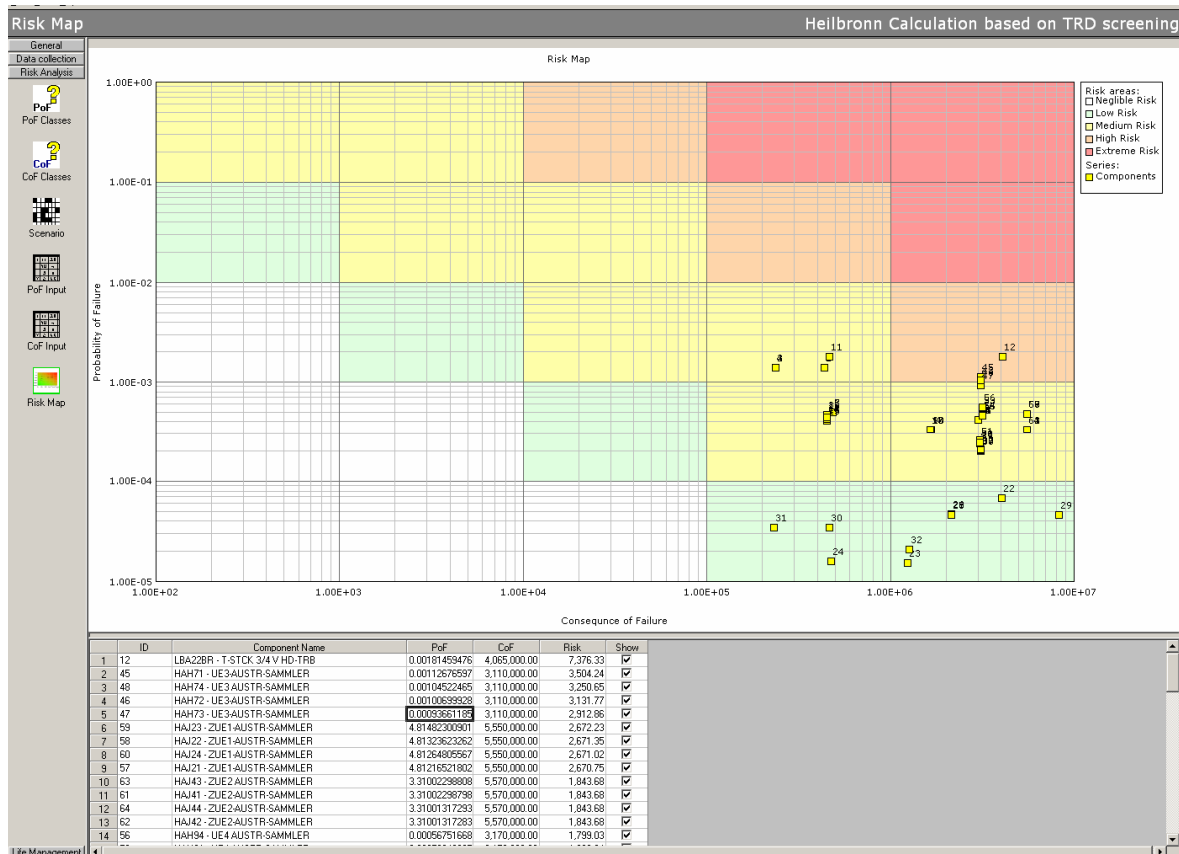


Figure 2. Risk map after screening level based on general/design data.

Since monitoring data was available for this sample application cases it was decided to perform analysis for all components taken on-line monitoring results into account. Because of seamless transition between analyses levels in proposed RIMAP approach it is not necessary to perform all steps performed already in previous (screening) level. Based on monitoring data, new values of exhaustion based on creep and fatigue (according to TRD code) could be calculated. Since PoF and CoF classes, as well as the scenarios were already done in the previous step, the only necessary step in this level is to calculate again the PoF values based on updated values of exhaustion (the methodology is the same like in the screening level, only more precise data is available). Newly calculated values were inputted into ALIAS-Risk and new risk map outlining the criticality of components was generated automatically (see Fig. 3).

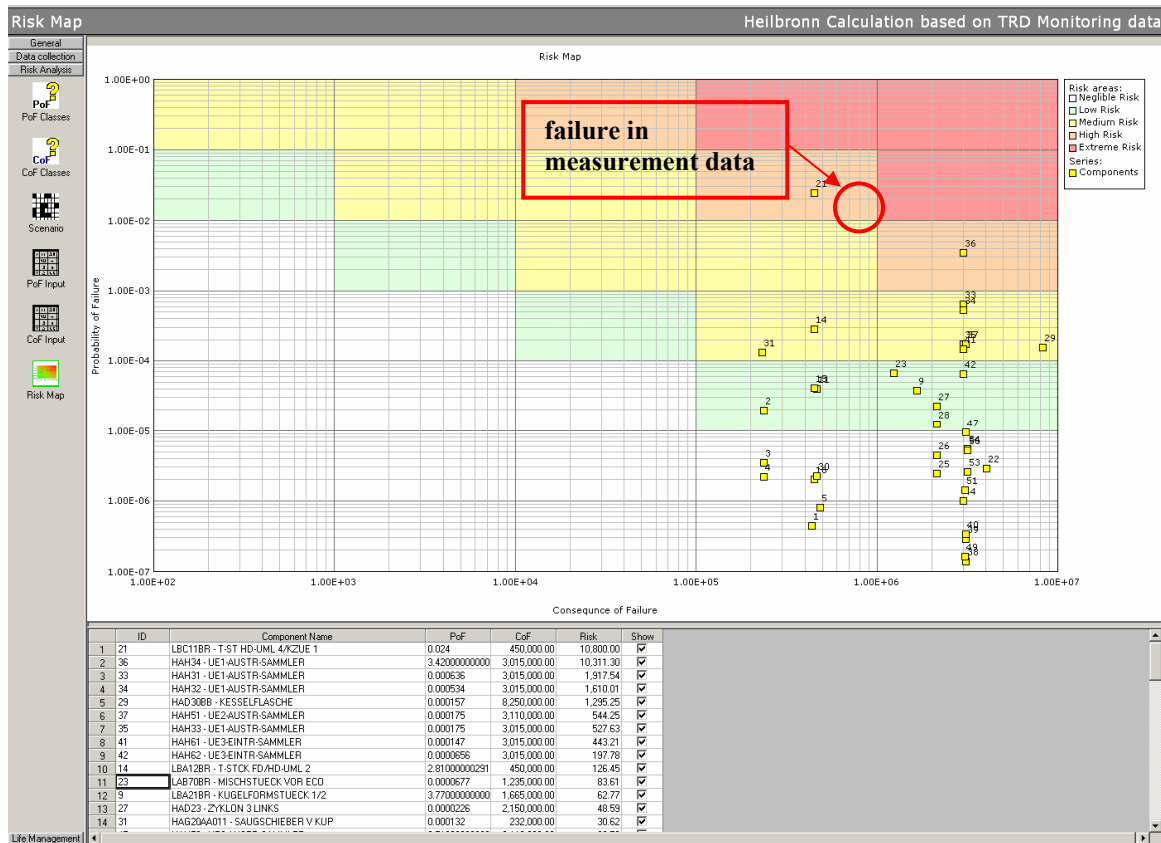


Figure 3. Risk map after intermediate analysis based on real operational data coming from on-line monitoring.

If the risk level of component/system isn't on an acceptable level after screening, on the level of intermediate analysis inspection results (e.g. replica) were introduced and probabilistic assessment of findings was done. Based on actions for different risk areas, which were defined by the plant owner (responsible person) inspection and maintenance (I&M) plan can be produced for each of the considered systems/components by assignment of different actions to corresponding risk levels and by definition of inspection effectiveness factors (like shown in Fig. 4). The type of inspection depends on the type of system/component and the damage mechanism. In our example NDT like UT, ET or PT/MT was chosen.

The optimization process includes comparison of value at risk before and after applying the inspection and maintenance actions suggested in the I&M plan. The improvement and decision making process should also be linked to legislation and other regulatory requirements, the PoF development over time and the accepted risk level defined by the plant owner (responsible person). The development of the PoF over time is an important parameter to consider when the maintenance/inspection strategies and intervals are determined in the analysis. The accepted risk level will define the minimum of components to be inspected like shown in Fig. 5.

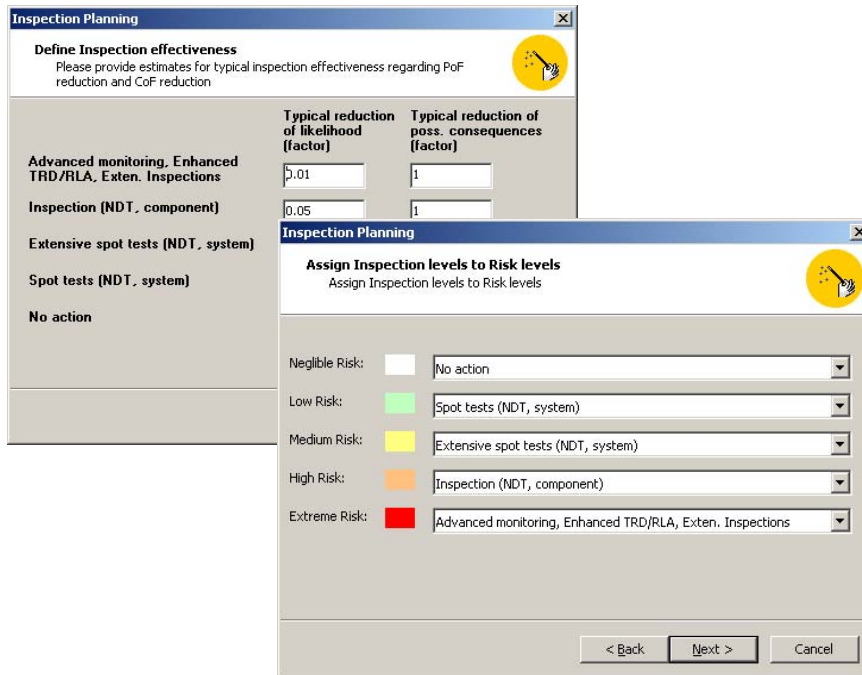


Figure 4. Assignment of inspection levels.

3. Results of NDT-concept

In respect to changes in national safety regulations for power plants put into operation before 01.01.2003 as well as changes in business targets (e.g. availability, maintenance costs, safety and environmental incidents, overall equipment effectiveness) the knowledge about the condition of monitoring-requiring plant gets more and more important for the decision making and the improvement process for inspection and maintenance plan through plant operator and plant management. In future the plant operator is responsible for the determination of appointed time of inspections on basis of a technical safety valuation of equipment and plant. Additional they have to define the method of inspection and quality level of inspector/responsible personnel.

For new power plants put into operation after 01.01.2003 the inspection plan and the interval of inspections has to be checked by authorities and inspectors. For older plants designed with TRD code the plant operator has only to notify the authorities about the appointed time of inspections if the planned dates of the inspection are inside the given limits of time frame (e.g. for boilers: 10 years for pressure test, 5 years for inner inspections/NDT).

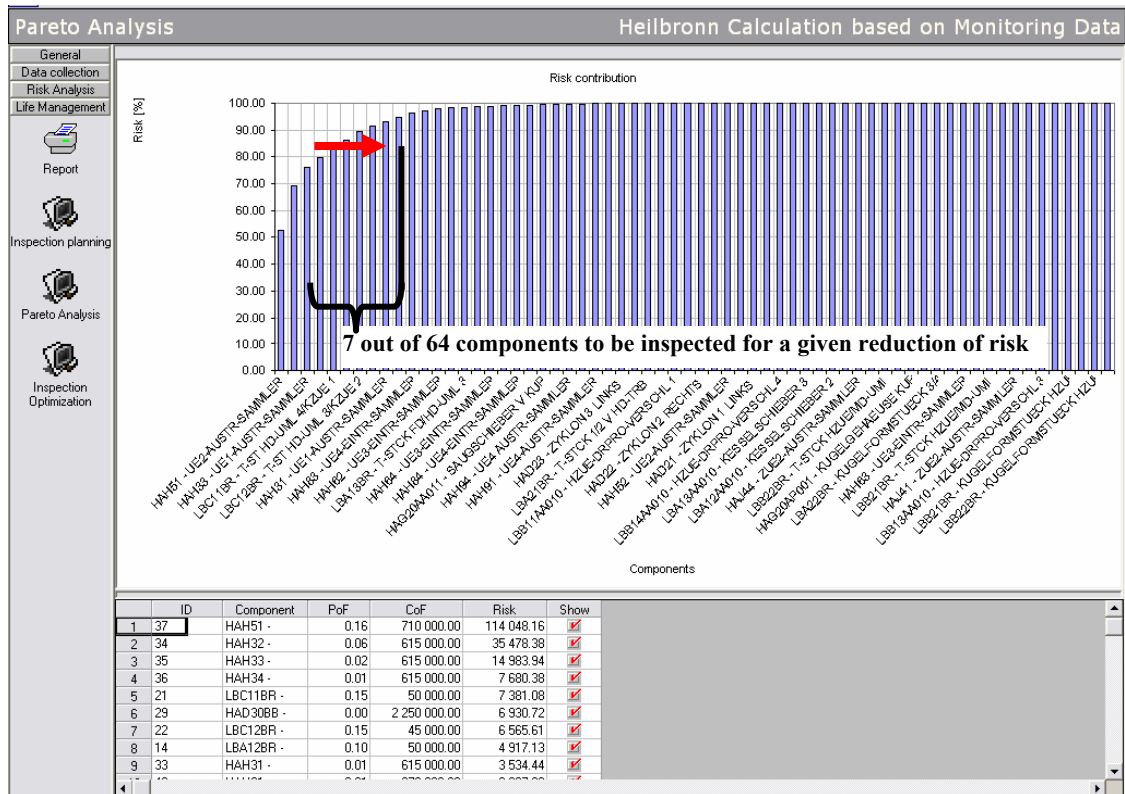


Figure 5. Optimization as function of accepted risk level.

However, manage through knowledge management will be the best way to fulfill the national regulations on the one hand and optimize the inspection plan (e.g. decreasing the number of planned days of plant shutdown for inspections or decreasing the number of extensive component inspections by spot tests on systems or by eliminating ineffective inspection) on the other.

A working group of members from the technical association VGB PowerTech e.V. describes in a document traditional and innovative concepts for condition monitoring with emphasis on pressurized components from boiler and steam pipelines. Beside risk-based/reliability-based approaches a safety-related evaluation based on NDT results is used for the inspection planning. The NDT-concept will be part of future, planned work of an Initiative from VGB Power Tech to cluster the experience of periodic tests and test findings on boiler parts and steam piping. In a first step the experience of 10–15 power plants (unit size: 300–1000 MW; operational time: 7–30 years) will be stored in one database. In the framework of new safety regulations this will help to concentrate onto systems, components and/or locations critical for safety, availability and reliability of power plants.

A first pre-study was done on the same place the RBI analysis was done (see chapter 3). The following data were collected for this example:

- Results of code based inspections (outer and inner inspections, pressure tests)
- Results of 430 inspection reports (NDT, calculations).

Fig. 6 shows the number of inspection reports over the time axis since start-up of the plant. Further the proportional allocation of the examinations to the systems is represented. Therefore the examinations took place to 80% at the systems HA (boiler parts) and L (feed water/boiler water systems) in accordance to the standard KKS⁴ (see Fig. 7). That means that for example the following components were regarded:

- Steam piping (main steam line, hot reheat line, cold reheat line, interconnecting piping)
- Boiler water transport (feed water piping, pumps, tank, deaerator, condenser)
- Feed water headers (HP, LP), preheater, injector
- Boiler parts (tubes, headers, drums, soot blowers).

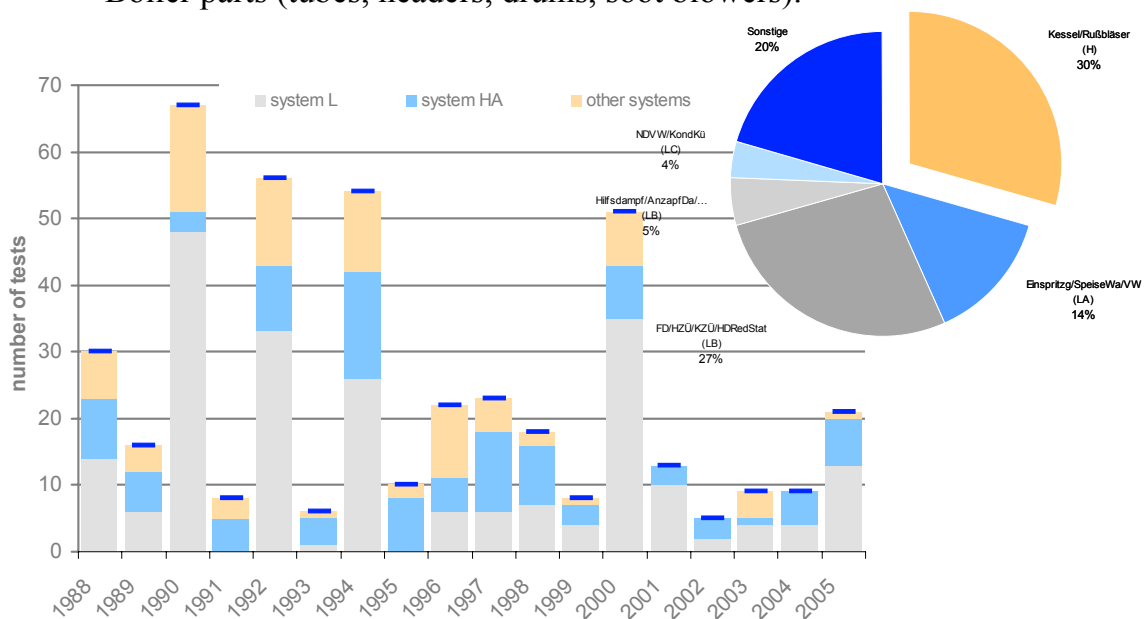


Figure 6. Number of tests (inspection reports) over the time axis since start-up of the plant and allocation to systems.

The NDT-concept is characterized by the following main steps

- Data collection and validation
- Determination of reliability of systems and analysis of test findings on component and system level (e.g. evaluation of effects on safety)
- Condition evaluation and classification of the systems
- Inspection planning (extent, contents and periods) in conformity with the inspection requirements of the national regulations
- Execution of the plan and continuous improvement.

⁴ KKS – Kraftwerk-Kennzeichensystem, VBG-KRAFTWERKSTECHNIK GmbH, December 1988.

The evaluation of the inspection reports shows that on more than 90% of the examined components no test findings were found. The test findings on boiler systems exclusively coming from leakage of tubes at the subsystems evaporator, super heater and economizer (HAD, HAJ and HAC). That means no safety related problem has been occurred (classification: damage tolerant systems).

Also in the subsystem L only a few test findings were present with exception to the well-known problem of injections (thermal shock).

All investigations of the NDT-concept show that a concentration of the condition-monitoring is possible on few components/systems by inclusion and consistent analysis of operational experience. Future investigations in further coal-fired power stations are to support this realization.

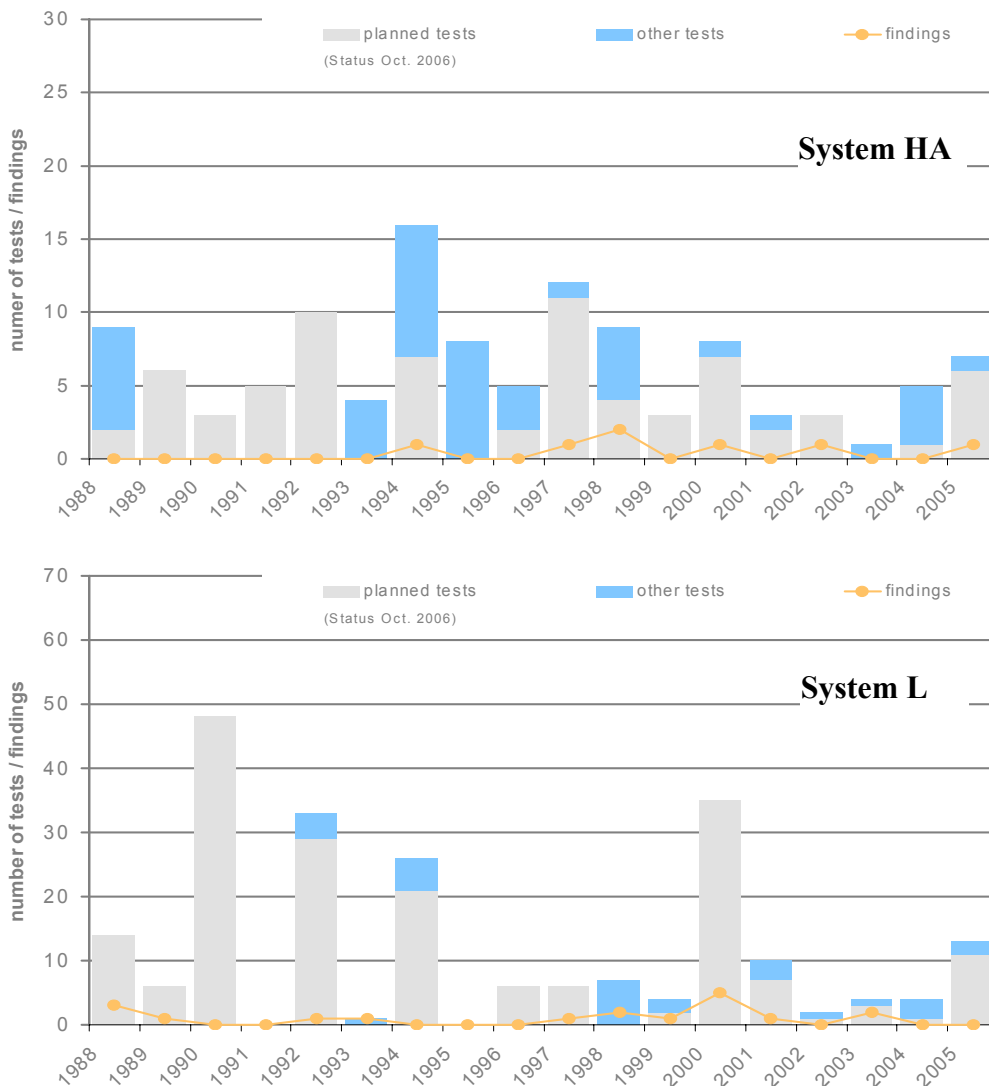


Figure 7. Number of tests (inspection reports) and test findings over the time axis since start-up of the plant for the systems HA and L.

4. Conclusions

From our experience with the application of the RIMAP methodology and the following conclusions can be drawn: The use of risk-based methods in inspection and maintenance of boiler parts and piping systems in power plant gives transparency to the decision making process and gives an optimized maintenance policy based on current state of component. In the framework of new safety regulations this will help to concentrate onto systems, components and/or locations critical for safety, availability and reliability of power plants. Future efforts and investigations are to be seen in the extension of the database for NDT-concept and in the combination of the presented concepts.

Acknowledgements

The authors wish to acknowledge the support provided for this work by the utility company EnBW HKW Heilbronn, Germany.

References

- [1] RIMAP CEN Workshop Document, CEN Workshop 24 "Risk-Based Inspection and Maintenance Procedures for European Industry", Jovanovic A., Main Editor, Final Draft Document in 60 days public discussion at CEN, April 200707.
- [2] RIMAP Project No, GROWTH Project GIRD-CT-2001-03008 "RIMAP", Risk Based Inspection and Maintenance Procedures for European Industry, Commission of the European Communities, Rev. of Oct. 4, 2000.
- [3] RIMAP WP2/D2.1, Generic RIMAP Procedure, GROWTH project GIRD-CT-2001-03008 "RIMAP", RIMAP RTD Consortium, Rev. 6, August 28, 2002.
- [4] Jovanovic, A.S., Auerkari, P. and Giribone, R. RIMAP WP3/I3.3: Assessment of Probability / likelihood of failure, GROWTH project GIRD-CT-2001-03008 "RIMAP", RIMAP RTD Consortium, version 10, 2004.
- [5] van Voren, R. RIMAP WP4/D4.3: RIMAP Application Workbook for the Chemical industry, GROWTH project GIRD-CT-2001-03008 "RIMAP", RIMAP RTD Consortium, version 0, 2003.
- [6] Winnik, S. Herring, A. and Gregory, R. RIMAP WP4/4.4: RIMAP Petrochemical workbook, GROWTH project GIRD-CT-2001-03008 "RIMAP", RIMAP RTD Consortium, version 1.1, 2003.

- [7] Jovanovic, A.S. and Auerkari, P. (2002). RIMAP WP4/4.1: RIMAP Application Workbook for Power Industry, Doc. Ref. No. 4-41-W-2002-01-5 (public) und Doc. Ref. No. 4-41-W-2002-02-5 (restricted), GROWTH project GIRD-CT-2001-03008 “RIMAP”, RIMAP RTD Consortium, 2002.
- [8] RIMAP Consortium, RIMAP WP4: Power Industry Demo Case, GROWTH project GIRD-CT-2001-03008 “RIMAP”, RIMAP RTD Consortium, Doc. Ref. No. 6-41-F-2004-01-1, 2004.
- [9] ALIAS Info Booklet, MPA Stuttgart, Rev. 15, Sept. 2004, MPA Stuttgart.
- [10] iRis Power Info Booklet, Steinbeis Advanced Risk Technologies, Rev. 1, April 2007, Steinbeis Stuttgart.

Annex: The RIMAP CEN Workshop Document [Ref. 1]

The RIMAP CEN Workshop Document [1] aims to provide guidance/framework for

- implementing risk-based inspection and maintenance (RBIM) and risk-based life management (RBLM) in industrial organizations and
- quality assurance and follow-up of activities, tasks and work processes.

by supporting optimal operations and maintenance (O&M) as well as asset management. “Risk” in RIMAP is understood as the combined effect of probability and consequence of failure. The RIMAP CEN Workshop Document consists of two parts:

- Section I – RIMAP Approach
(Scope, principles, requirements, RIMAP as part of overall management, limitations, compatibility with other approaches) and
- Section II – RIMAP Procedure
(General description and scope, requirements, inputs, procedure, output and warnings/applicability limits of each step of the procedure.

The RIMAP methodology for RBIM described in the RIMAP CEN Workshop Document is based on the development in the European project RIMAP – **R**isk-based **I**nspection and **M**aintenance **P**rocedures for European Industry [2] and is intended to be industry independent and addresses the following aspects:

- Inspection and maintenance planning
- All type of equipment, e.g. pressure containing, rotating, electrical, instruments and safety devices
- Technical and managerial aspects of maintenance and inspection planning

- Asset management related to inspection, maintenance and life assessment for plants, systems and components
- Production.

An overview of RIMAP procedure [1, 3] is shown in Fig. 1. As may be seen, it includes the following major five technical steps:

1. Initial analysis and planning
2. Data collection and validation
3. Multi-level risk analysis
4. Decision making and action planning
5. Executing and reporting

and additionally one techno-organizational (incl. economy-related aspects) step of overall management system, namely

6. Performance review.

Out of these steps, Multilevel Risk Analysis has one more dimension regarding the depth of the required analysis. Corresponding levels are:

- (a) screening (low level analysis)
- (b) intermediate level (levels of) analysis
- (c) detailed analysis.

A number of methods can be used to estimate the probability of failure (PoF) related to an event or a scenario. For introducing the PoF according to RIMAP procedure, three different types of sources can be used (see Fig. A2, [4]):

- One common reference source is taken from statistical analysis of historical data (H/S) on failures in comparable components.
- A second common source is based on forecasting or modeling (F/M) of the foreseen failure mode in the component considered.
- The third source is expert judgment (E/J), whereby human expertise is applied to extract the best estimate of PoF.

The individual sources for overall PoF determination are combined as outlined in Fig. A2. The elements from different kinds of sources can be modified according to factors related to source reliability and application.

Demonstrated applications of this methodology have been implemented in chemical, petrochemical, power (non-nuclear) and steel industries [5, 6, 7].

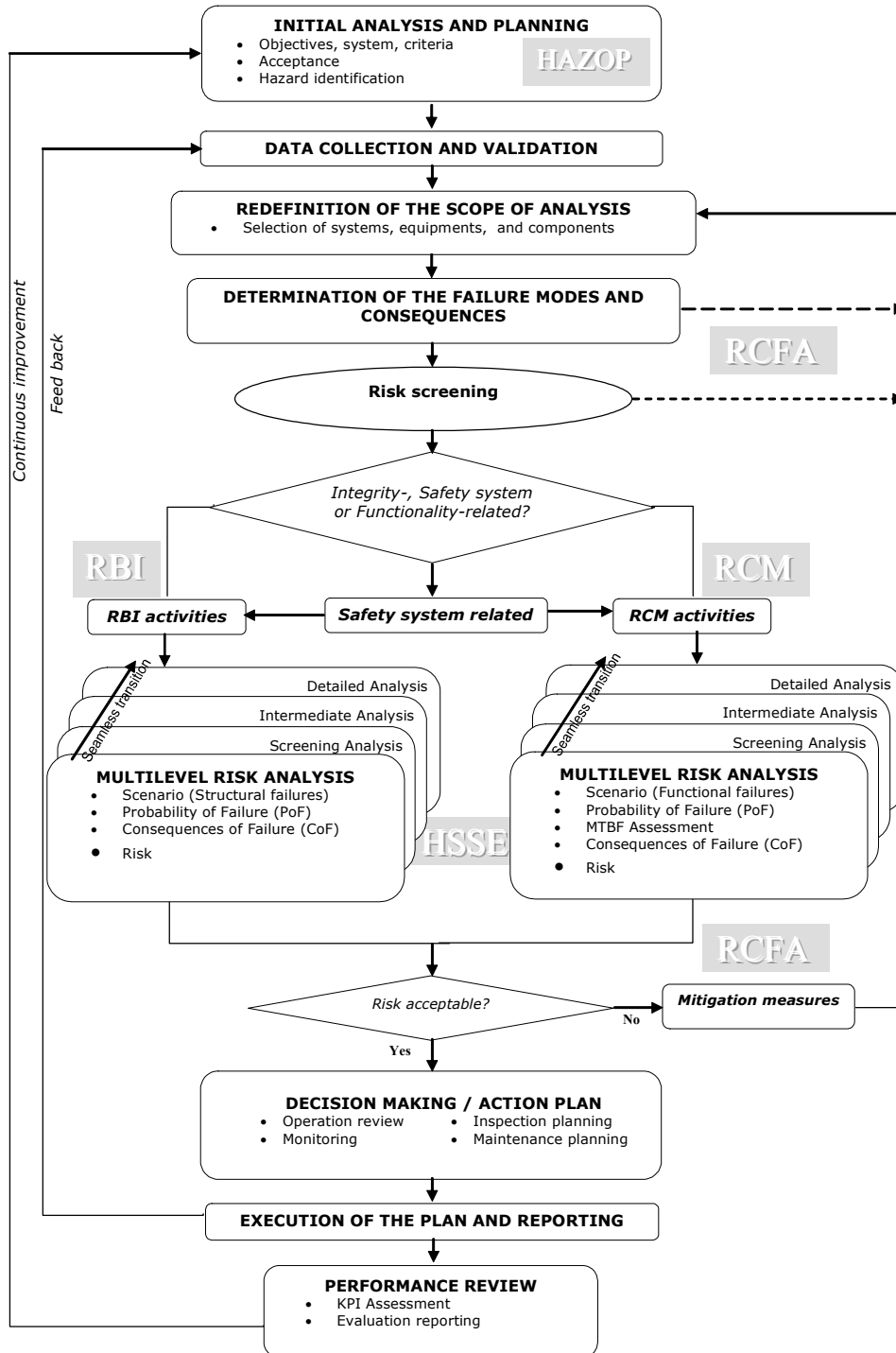


Figure A1. Framework of RIMAP procedure within overall management system

Acronyms referred in the figure for management systems:

- | | | |
|-------|----|---|
| HAZOP | := | Hazard and operability (study/analysis) |
| RCFA | := | Root Cause Failure Analysis |
| RBI | := | Risk Based Inspection |
| RBM | := | Risk-Based Maintenance |
| HSSE | := | Health, Safety, Security and Environment. |

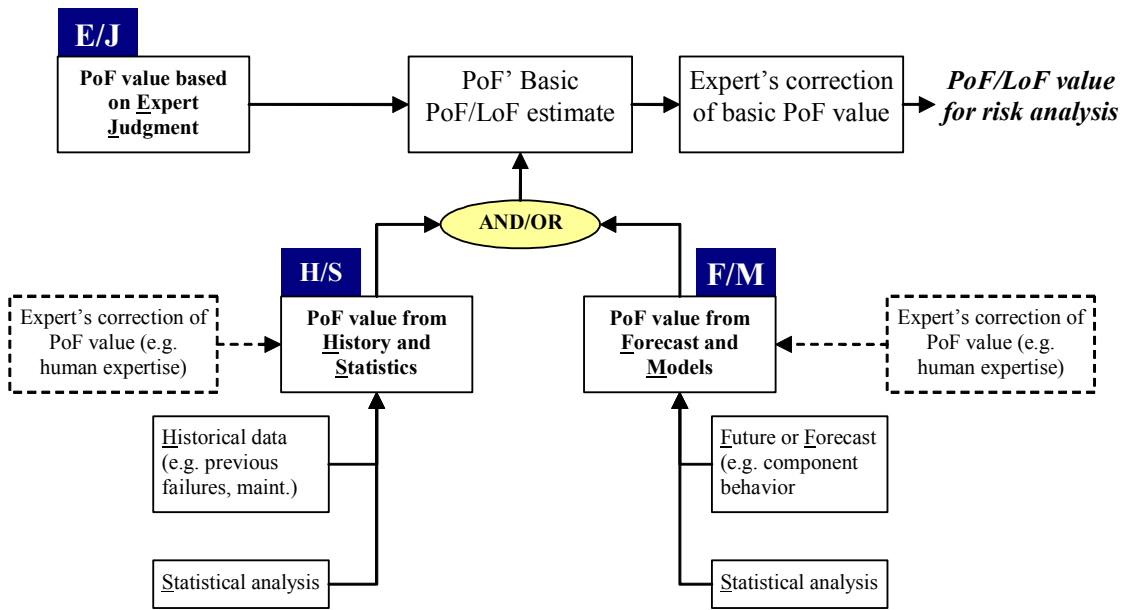


Figure A2. Elements of PoF determination in the RIMAP concept [4].

Living with creep damage... outside the creep range

John M. Brear and Paul Jarvis

Stress Engineering Services (Europe) Ltd., Esher, UK

Abstract

This paper addresses the effects of creep cavitation damage on other mechanical properties – chiefly those that affect behaviour outside the creep range. Such effects seem not to have been systematically studied, yet they are significant for the understanding and prediction of component integrity and life. The paper presents results obtained mainly as by-products of research programmes on low-alloy steels for both fossil and nuclear power plant and seeks to rationalise the findings to generate an overall picture of the effect. It is seen that a simple loss-of-effective-section model is adequate to describe many of the phenomena observed, but that other factors may also need consideration.

1. Introduction

The role of cavitation in the creep process is reasonably well understood, with theories of cavity nucleation and growth available that suit most engineering materials. Methods of determining the extent of creep cavitation by qualitative and quantitative non-destructive techniques have been developed. These, together with appropriate creep models, are regularly used both in the laboratory, to further the understanding of creep, and in the field, to assess component integrity and life.

The interactions of creep with other life limiting processes have also been studied extensively. Practical, validated models of the creep-fatigue and creep-corrosion interactions are available for component assessment. Similarly, a sufficient understanding of the role of creep cavitation in creep and creep-fatigue crack growth has been obtained such that it can be incorporated in the standard procedures for high-temperature defect assessment.

An area which has been less extensively investigated, and which is therefore less well understood, is the effect of creep cavitation on non-creep mechanical properties. It is this topic which is the subject of the present paper. Two fields of study have generated information that is relevant to this topic; otherwise, little systematic work has been done.

Historically, the first was the problem of stress relief embrittlement. In the United Kingdom, this affected many terminal welds on the main steam lines of the larger power generating units completed during the late 1960s and early 1970s. It resulted from the formation of creep cavities during the relaxation of welding residual stresses. Extensive studies elucidated the effects of impurity content, deoxidation practice, heat affected zone microstructure, weld design and weld procedure. Practical control of the problem was achieved by limiting the residual element content and modifying the weld design to control heat input and, therefore, microstructure. During the research, various mechanical test routes were employed to quantify the extent of embrittlement. In this work, the cavitation was generally produced by stress relaxation, rather than by forward creep. Even so, the results can be used to provide some indication of the non-creep properties of creep damaged material.

The second relevant field of study encompasses the work performed to develop methods of determining the remaining creep life of components. Mechanical tests, often on miniature specimens, and more-or-less non-destructive interrogation techniques have been investigated. Initially, programmes of work were conducted to investigate the validity of the life fraction rule in the context of post-exposure testing. Investigations into the effect of test acceleration led to exploration of the potential of using test routes other than creep or stress rupture to characterize ex-service material. In parallel, metallographic studies led to methods of damage classification and quantification that could be related to creep life consumption. Various non-destructive examination techniques were also applied to the problem of component assessment. The results of this work also contribute to an understanding of the effect of creep damage on non-creep properties.

The major problem in bringing all of this together into a coherent view is the lack, in much of the earlier work, of any systematic approach to cavity quantification. It is thus not always possible to determine which of the effects observed are purely due to cavitation and which are affected by other processes. During time at temperature, impurity segregation can lead to changes in grain-boundary properties besides those due to cavitation. The properties of the matrix are also changed by precipitation and coarsening sequences. Additionally, strain effects can contribute to both hardening and softening. Subsequent mechanical response is influenced by all of these processes, and in rationalising the available information, a considerable amount of inference has been necessary.

2. Effects within the creep range

Whilst this topic is well understood and needs no general treatment here, there are two issues within the authors' experience that are both interesting in their own right and serve as a useful introduction to the main topic.

2.1 Cavitation generated in non-standard mechanical contexts

It is usual to consider creep cavitation only in the context of forward creep tests, or occasionally stress relaxation tests. However, these simple situations are not always fully informative as to the behaviour of real components, where stress concentrations, multiaxiality and varying load and temperature histories can complicate the situation.

In the work of Batte *et al.* (1980), on the effects of deoxidation practice and residual element level on stress relief embrittlement, a wide range of tests was employed. The tests included short-term rupture, hot crack opening displacement, notched bend relaxation and plain and notched tensile relaxation, in all of which cavitation developed as the test progressed, besides tensile testing below the creep range, in which no cavitation was produced. The results of this work were not easy to interpret initially, due to the very wide range of grain sizes produced during the heat affected zone simulations. However, rationalisation of the data became possible when the key parameter ratio from each test was plotted against grain size and a square root relationship was seen (Brear, 1973–1985). The correlation between the different test types indicates that the effect of cavitation is consistent across the wide range of mechanical properties measured. It is unfortunate that no direct quantification of the cavitation was performed.

Whilst in this work the cavitation developed during the tests, the results do have bearing on this present study. The implication of the findings is that relatively simple models of the effect of cavitation should be sufficient to explain and predict a range of mechanical responses.

2.2 Creep cavitation and stress relaxation behaviour

Stress relaxation is normally effected by creep processes, and is thus slightly outside the scope of this review. However, there are some points deducible from the stress relaxation testing performed in the work on 0.5 CrMoV steels, described above, which are of wider import. During a stress relaxation test, creep cavitation may form progressively, thus influencing the subsequent relaxation rate through the change in effective cross section.

It has been suggested, by Hart *et al.* (1975) and others (e.g. Woodford, 1995), that a single, rapid stress relaxation test can be used to obtain a knowledge of creep response over a wide range of stresses. Such a test would thus have advantages over creep or rupture testing for the assessment of service exposed material.

Fig. 1 shows the instantaneous strain rates observed during stress relaxation testing of simulated coarse-grained and fine-grained heat affected zone microstructures

in 0.5 CrMoV steel, compared with the stress dependence of the minimum creep rate. It is seen that, for the heat which cavitates most readily in the coarse-grained condition (CMV-3), the instantaneous strain rate in the stress relaxation tests rises progressively above the corresponding minimum creep rates (Brear, 1973–1985, King, 1980). This relative increase in strain rate accompanies the development of creep cavitation during the relaxation process. The degree of strain rate acceleration is consistent with the effective stress concept of continuum damage mechanics and increases with the severity of the relaxation treatment. Neither the same heat in the fine-grained condition nor the purer heat in the coarse-grained condition shows this effect. These observations indicate that care would be needed to interpret the results of a relaxation test on material that already contained, or which developed, creep cavities.

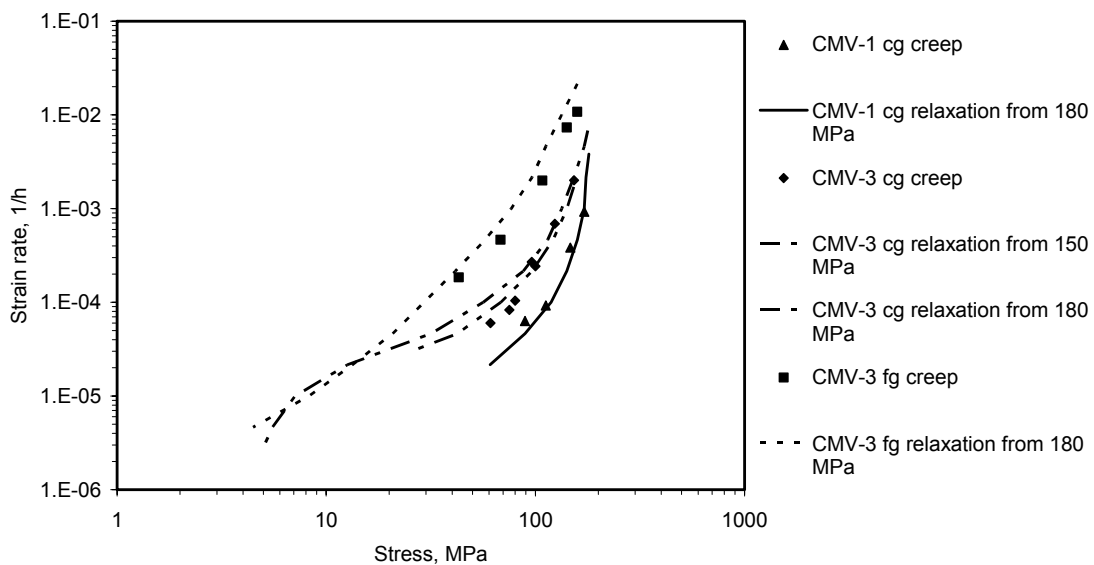


Figure 1. Strain rates in stress relaxation and creep, at 700°C, for two heats of 0.5 CrMoV steel in the coarse- and fine-grained heat affected zone conditions.

3. The effect of creep cavitation on subsequent processes

The situation envisaged here is that in which grain-boundary cavitation develops under creep conditions. A change in conditions then takes the component out of the creep regime, into a realm where other aspects of mechanical behaviour dominate. The question that arises concerns the influence of the pre-existing damage on the subsequent processes. In a realistic engineering context, the most likely changes in conditions are a decrease in temperature or an increase in strain rate.

The effect that creep cavitation might have on subsequent properties depends primarily on whether or not it remains stable or continues to develop. If the new conditions are outside the regime in which cavity nucleation or growth can occur,

then the existing cavity level is likely to remain constant. If the conditions allow, then further nucleation or growth might take place.

The operating mechanisms which underlie the subsequent properties should also be considered in respect of the extent to which they are controlled by matrix or grain-boundary processes. In the former case, it might be reasonable to expect the effect of the damage to be simply a stress increase related to the effective loss of section. In the latter case, additional effects might be observed. Flow and fracture properties may be affected differently.

The following sections address different groups of mechanical properties, considering what might be expected, under these guiding principles, and what has been observed.

3.1 Creep cavitation and density

It is normally assumed that plastic deformation conserves volume, having an effective Poisson's ratio of 0.5. The continuum damage hypothesis effectively assumes that this remains true in the presence of cavitation. However, it is evident that real cavities have a real volume, and must therefore affect the overall volume of the material and thus its effective density.

This idea formed the basis of attempts to use the measured density of small samples of ex-service material as a quantitative indicator of the degree of cavitation, and thus of life consumption. Though some successes have been claimed, it was found that the technique was insufficiently sensitive to give useful results.

3.2 Creep cavitation and elastic behaviour

3.2.1 Mechanical measurements of modulus

Elastic behaviour is primarily a matrix process, until the collapse limit. It is therefore to be expected that the influence of creep damage would be simply that of a stress increase governed by the effective loss of section. It was postulated by Kachanov (1990) that creep damage would lead to an apparent reduction in the value of Young's modulus obtained from conventional stress-strain data.

A major project was put in place to investigate the validity of the life fraction rule under simulated service followed by accelerated "post-exposure" rupture testing (EPRI 2253-4, see Viswanathan 1979; Brear et al. 1993). One of the materials studied was a 0.5 CrMoV turbine casing which, under the programme conditions, had a rupture life of around 60 000 h. This material showed classical grain-boundary cavitation, readily modelled using continuum damage concepts. Groups of specimens were crept to 30, 50, 70 and 90% of the known rupture life,

then reloaded at accelerated conditions. As part of the standard laboratory procedure, cold and hot tensile moduli were measured on reloading (somewhat approximately, being obtained from instantaneous strains recorded on successive additions of load to the test-pieces).

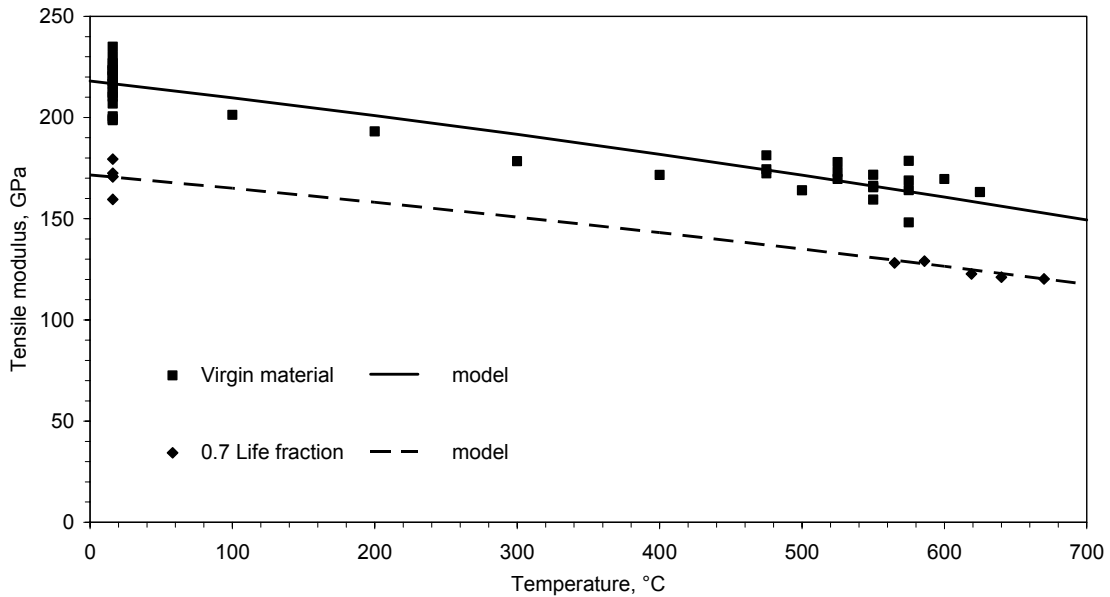


Figure 2. Observed Young's modulus for virgin and pre-crept 0.5% CrMo steel.

Fig. 2 shows the observed modulus as a function of temperature for virgin and pre-crept (0.7 life fraction) material. A consistent drop is seen. Fig. 3 shows room temperature modulus as a function of life fraction. Predictions based on a continuum damage mechanics model fit to the relationship between creep life and cavitation damage are included on both figures. These assume that the reduction in apparent modulus is directly proportional to the damage level. In both cases, the correlation between prediction and observation is good.

This effect of damage on structural compliance should be borne in mind when modelling displacement controlled phenomena, such as stress relaxation, or in formulating constitutive laws for finite element programs.

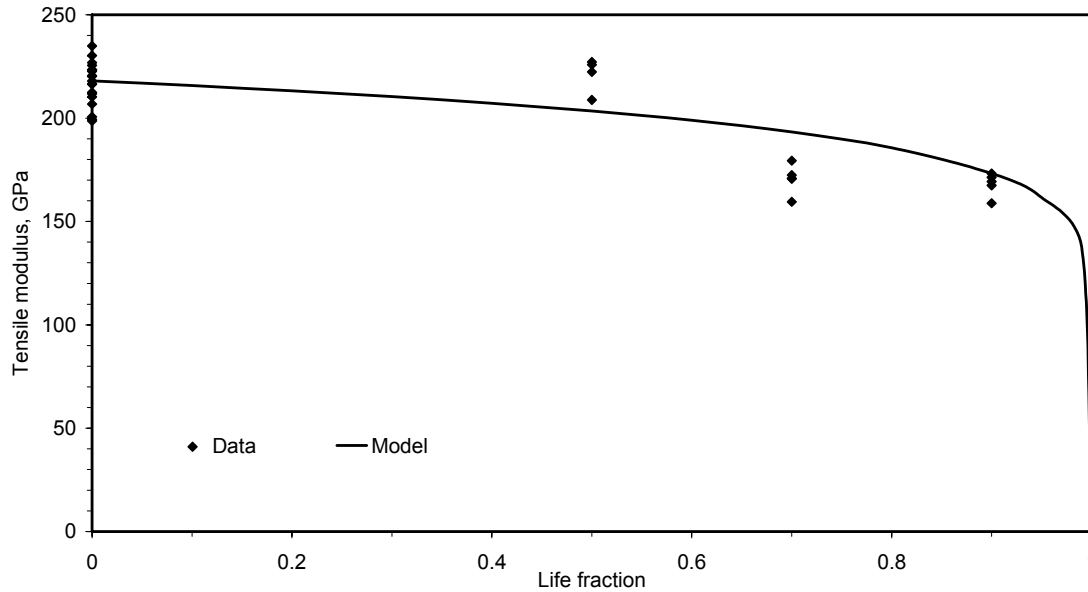


Figure 3. Observed and predicted room temperature Young's modulus as a function of creep life fraction for 0.5% CrMo steel.

3.2.2 Ultrasonic measurements of modulus

According to Kachanov's effective stress concept, damage effects should be independent of the physical form of the damage. It might equally be expected that, so long as the damage was uniformly distributed and of a fine scale compared with that of other microstructural features, the mechanical measurements of tensile modulus would also be insensitive to its precise form. Other methods of modulus determination may be more sensitive to the nature of the damage. It is, therefore, interesting to compare the above findings with the ultrasonic measurements reported by Eggeler *et al.* (1990) where a level of damage that would cause a 20 percent reduction in tensile modulus, at 0.9 life fraction, only generates a 1 percent decrease in ultrasonic velocity. Since the ratio of transverse and longitudinal ultrasonic velocities is related to the modulus, this apparent inconsistency implies that the mechanical and ultrasonic methods are measuring different physical phenomena.

The mechanical measurements reflect the global stress-strain response of the specimen, in other words – the compliance of a structure. For this, the effective stress concept should work well. The ultrasonic method, by contrast, measures the atomic-scale elastic properties of the lattice. Changes in velocity (and attenuation) are thus related to changes in signal path length due to progressive grain-boundary damage. On this basis, the two types of measurement can be reconciled. The observations of anisotropy in ultrasonic velocity in creep damaged material (Stamm and von Estorff, 1993) are consistent with this.

3.3 Creep cavitation and tensile behaviour

In addition to the effect on elastic loading, discussed above, it might be expected that creep damage would alter the plastic portion of the tensile stress-strain curve and the final strength and ductility. The effect is likely to depend on whether the subsequent tensile loading is within the creep range or not.

3.3.1 Tensile behaviour in the creep range

Various workers have considered the possibility of using short-term tensile tests as an alternative to creep or stress rupture tests for mechanically characterizing ex-service material (Nechtelberger *et al.*, 1972; Steen, 1983). Most of these methods have relied on an inversion of the relationship between stress and strain-rate implicit in the creep model. If successful, this should allow some correlation of the applied creep stress and resulting minimum creep rate in one test with the applied constant strain rate and attained maximum tensile stress in the other.

Unfortunately, in the present writer's view, the above studies were somewhat incomplete in their allowance for cavitation. None of them explicitly allows for it in their treatment of the creep model, nor do they record its presence or absence in the experimental work. The studies differ in their exact interpretations of the minimum creep rate and the maximum tensile stress, but none fully realises the effect of primary creep on the interpretation of these test-derived parameters (Brear *et al.* 1993).

The basic continuum damage mechanics equation set can be inverted in the manner required, under the assumption of strain hardening. This allows the constant strain rate behaviour of virgin material to be predicted using materials parameters derived from creep tests (Brear *et al.* 1993). However, the approach used in that paper makes some simplifying assumptions that do not remain valid when pre-existing damage is present. A more complete treatment is developed by Lian and Chen (1991) who found that creep cavitation behaves in a similar manner to the external loss of section and thus accelerates tensile instability. Before the onset of instability, the effect is simply to increase the effective stress at a given load.

3.3.2 Tensile behaviour below the creep range

Tensile tests have also been used extensively as a measure of stress relief embrittlement (Batte *et al.* 1980; Brear and King 1976, 1980; King 1980). In the earlier studies, on 0.5 CrMoV material, heat affected zone structures were simulated and then tempered for times at temperature comparable to commercial stress relief procedures. The subsequent ductility was then determined in an elevated temperature tensile test (King, 1980). A clear correlation was observed between ductility and residual element content in experimental alloys of

controlled purity. The results were found to be fully consistent with both the laboratory and the field behaviour of real welds. Though, in this procedure, no cavitation was present before the tensile test, nor did any develop during it, the pattern of results was fully consistent with that observed in tests where cavitation did develop. This may be explained by consideration of the embrittlement process. In the tempering range, segregation of impurity elements to grain boundaries occurs – as may be seen using appropriate analytical techniques such as auger electron spectroscopy or scanning transmission electron microscopy. The embrittled boundaries are susceptible to cleavage fracture in the impact and low temperature regimes, to reduced ductility tensile fracture at elevated temperatures and to cavity nucleation and growth in the creep regime.

Later work, on 0.5 CrMoV and A533B/A508 steels, improved the realism of the test route by replacing the tempering treatment with a period of stress relaxation from typical residual stress levels. The ductility difference between tempered and stress relieved specimens was taken as a measure of the degree of stress relief embrittlement (Brear and King 1976, 1980). The main benefit of this version of the test was that it compensated for those variations in ductility that were solely a result of tempering time. It is again unfortunate that no cavity quantification was undertaken in this work, though it must be remembered that this work antedated the metallographic methods of qualitative and quantitative damage assessment that are now in regular use. The metallography that was done certainly indicates consistent variation in the degree of cavitation with the amount of stress relaxed and the apparent susceptibility of the individual heats to embrittlement.

It was found that the subsequent tensile ductility provided a more sensitive and reproducible measure of embrittlement than did proof or ultimate tensile strength, and that the fracture strength was intermediate in usefulness. So far as cavitation is concerned, the stress values up to the ultimate strength seem to be simply affected by effective loss of section, though the picture is complicated by the strength changes due to tempering. The ductility, and to some extent the fracture strength, see a double effect, with the section loss effect being augmented by a change in fracture mode. Besides the correlation with residual element level and the effects of microstructure, the work on the nuclear pressure vessel steels also demonstrated a variation in stress relief embrittlement with the mechanical work done during the stress relaxation treatment (Brear, 1973–1985).

Figs. 4 and 5 present the variations in tensile ductility and fracture stress at 300°C, shown by a commercial heat of A533B in the coarse-grained heat affected zone condition after periods of tempering and stress relaxation at 615°C. The material was derived from a plate manufactured by Marrel Frères and delivered to the CEGB in 1974, after trial welding at Rotterdam Nuclear, for evaluation purposes and was fully described by Darbyshire *et al.* (1974). The heat-affected zone simulation, of 10s at 1300°C, resulted in a coarse-grained

(180 μ), fully bainitic microstructure. This material had a high impurity content and cavitared readily during stress relaxation (Brear and King, 1976).

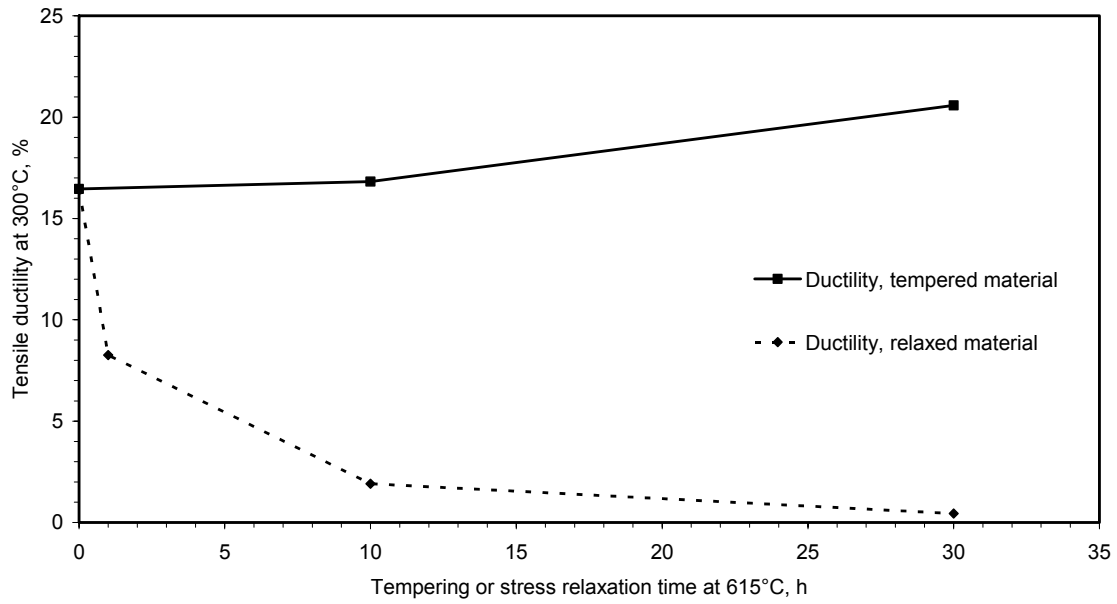


Figure 4. Variation in tensile ductility of a commercial cast of A533B after tempering and stress relaxation.

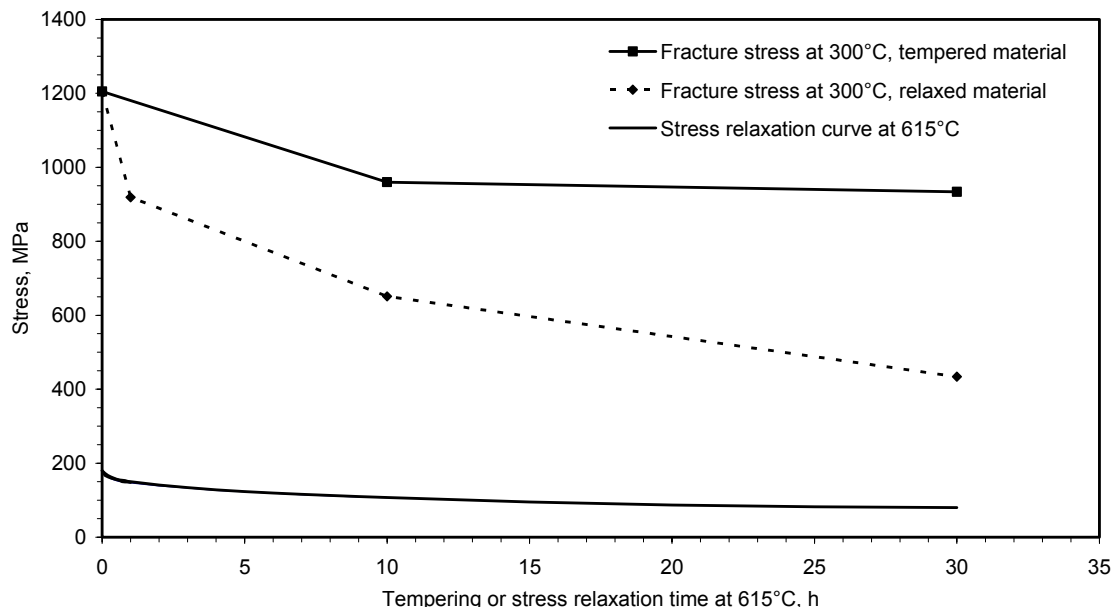


Figure 5. Variation in fracture strength of a commercial cast of A533B after tempering and stress relaxation.

3.4 Creep cavitation and fracture mechanics behaviour

The role of creep cavitation, forming progressively in the ligament ahead of a crack growing by creep, is well known. The accepted high temperature defect assessment procedures address this through extensions of the continuum damage mechanics approach (Webster and Ainsworth, 1994). A study of this is outside the scope of the present paper.

Here it is of interest to consider the role of pre-existing creep cavitation on classical, elastic-plastic fracture mechanics behaviour. Reasons of practicality have precluded the generation of uniform creep damage in conventional fracture mechanics specimens, however it has proved possible to generate a uniform distribution of creep cavities in Charpy impact specimens (Brear, 1973–1985).

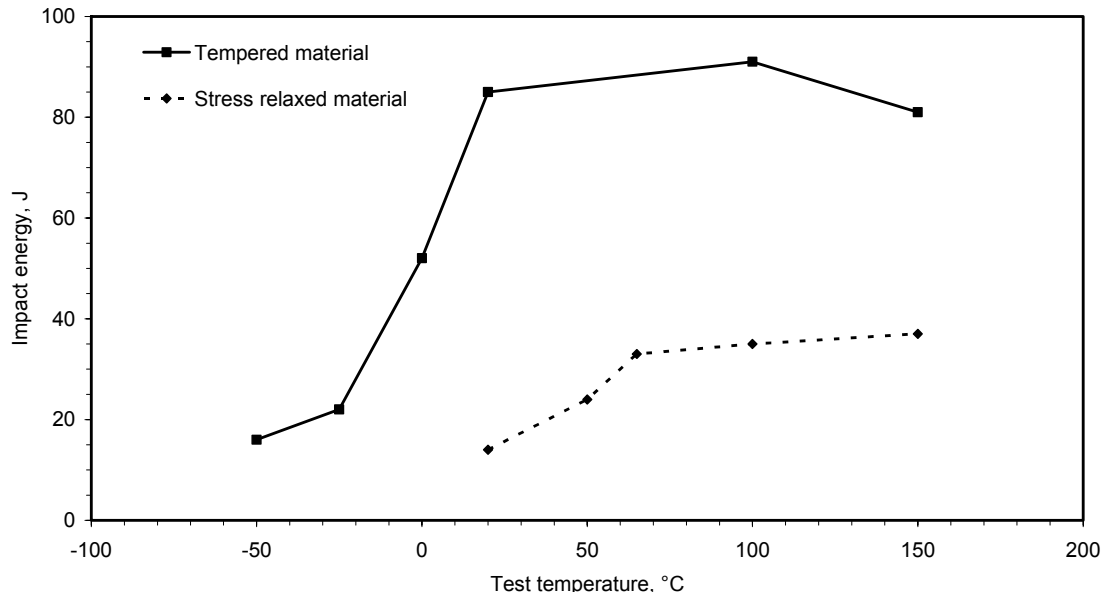


Figure 6. Impact energy transition curves for tempered and stress relaxed A533B.

Figs. 6 and 7 show impact energy and fracture appearance transition curves for the same heat of A533B material studied in the work presented in Figs. 4 and 5. Tensile specimens of simulated heat affected zone material, tempered or stress relaxed for 30 hours at 615°C, were then re-machined to create Charpy impact specimens. This generated impact test pieces whose major axis corresponded with the direction of the maximum principal stress during the tensile test. Thus, the plane of maximum cavity density coincided with that of impact crack propagation.

As mentioned earlier, this work was performed before the establishment of consistent cavity quantification methods; the degree of cavitation produced by the stress relaxation process cannot therefore be given definitively. However, the data reported for the same material in the preceding section show a 50%

reduction in fracture strength (at 300°C), which was accompanied by a reduction in tensile ductility from around 20% to about 2.5%. This represents a high level of damage, on any basis, and this should be borne in mind when considering the effect of creep cavitation on impact behaviour.

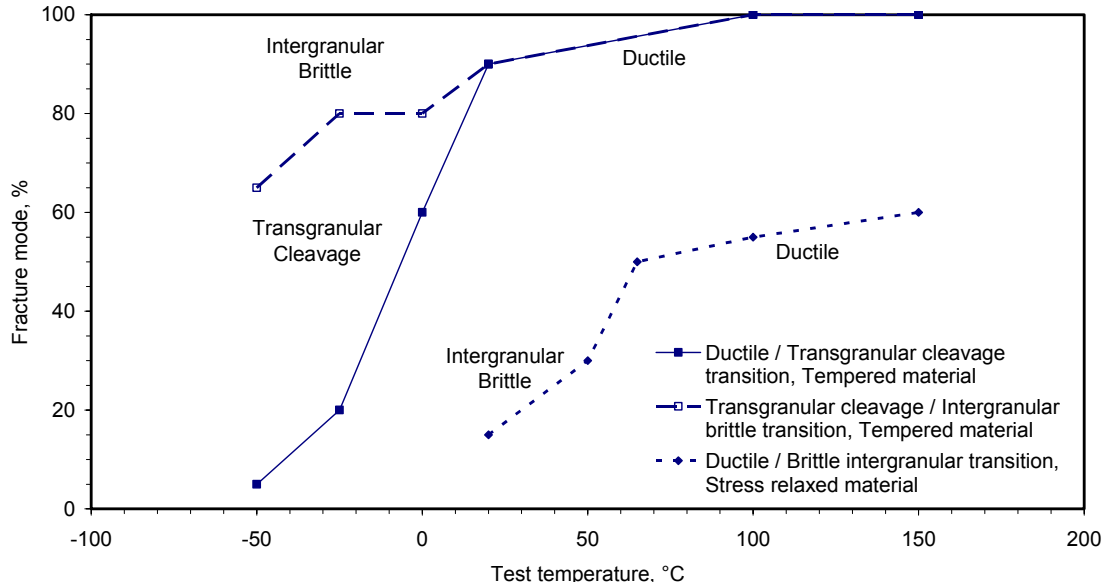


Figure 7. Fracture appearance transition curves for tempered and stress relaxed A533B.

Compared with the tempered material, the creep-damaged specimens show reduced impact energies, higher transition temperatures and a change to totally intergranular rather than predominantly transgranular failure in the brittle mode. The drop in upper-shelf impact energy is consistent with the change in tensile fracture stress (Fig. 4) and probably reflects the effective reduction in load-bearing area. The change in brittle fracture mode and increased transition temperature indicate an additional effect of the damage in initiating brittle cracks in this dynamic test. It is particularly notable that the stress relaxed material does not achieve a fully ductile upper shelf, but retains a significant intergranular brittle component of fracture. These steels were noted to be extremely sensitive to dynamic effects, with a very fine energy balance between cleavage crack initiation and propagation. In many cases of classically temper embrittled material, it was possible to observe large numbers of nucleated but stable cleavage cracks in the transition regime. This was not seen in the pre-cavitated specimens, where it is likely that local stress fields around the cavities ensured that sufficient driving force was available to propagate any brittle cracks that formed.

These observations imply that cavitation has a strong effect on fracture toughness and fracture mode. This should be borne in mind when using failure assessment diagrams.

4. Overview

It was postulated earlier that the effects of creep cavitation on subsequent properties would depend on:

- Whether the cavitation was expected to remain stable or continue to develop in the new mechanical environment
- Whether the critical properties in the new regime were dominated by matrix or grain boundary processes.

The results surveyed above confirm that these are the critical questions. Further, the work of Batte *et al.* (1980) implies that, subject to these broad principles, the effect of cavitation can be treated consistently across a wide range of mechanical properties. The general experiences of adherence to and departure from the life fraction rule and the effects, noted above, of cavitation on stress relaxation and tensile behaviour in the creep regime are consistent. Within regimes where a similar mix of deformation and damage processes occurs, the effects of cavitation on subsequent properties can readily be predicted using appropriate forms of the continuum damage model.

Outside this regime, but in conditions where matrix deformation processes dominate, the concept of damage being an effective loss of section appears to be a reasonable approximation. This is demonstrated by the effects of cavitation on elastic behaviour, on tensile properties below the creep regime, and on upper-shelf impact behaviour. Where grain boundary or other fracture processes are important, further effects of cavitation are seen, additional to the effective loss of cross section. This is observed in the tensile fracture behaviour below the creep range and in the transition and lower-shelf impact behaviour.

Given the above, it may be concluded that:

- Creep cavitation has an effect on elastic modulus, tensile strength and ductility (in and below the creep range), stress relaxation rate, fracture toughness and fracture mode.
- An allowance for cavitation as an effective loss of load bearing cross section should be made under all circumstances. This has implications for materials modelling in general, and for finite element models in particular.
- Special treatment is required for fracture processes in pre-cavitated material. Changes in fracture mode may occur. This has some implications for the development and use of failure assessment diagrams for creeping structures.
- Care should be applied when changing mechanical conditions between service and post-exposure testing. Tensile and stress relaxation tests may provide useful information on creep properties, but their interpretation is not straightforward when cavitation is present.

- It may be considered beneficial to carry out further research into the effects of cavitation on fracture under non-creep conditions

References

Batte, A.D., Brear, J.M., Holdsworth, S.R., Myers, J. and Reynolds, P.E. 'The effects of residual elements and deoxidation practice on the mechanical properties and stress relief cracking susceptibility of 0.5%CrMoV turbine castings'. Conf. 'Residuals, Additives and Materials Properties', London 1978. Phil Trans Roy Soc 1980, A295. Pp. 235–251.

Brear, J.M. Unpublished work performed at the Central Electricity Research Laboratories, Leatherhead, UK, 1973–1985, referenced here with thanks to the CEBG successor companies.

Brear, J.M., Aplin, P.F. and Timmins, R. 'The effect of primary creep on the Kachanov-Rabotnov Model – results on 0.5 CrMoV, 1CrMo, and Type 316 steels'. Conf 'Behaviour of Defects at High Temperatures' Sheffield 1992.ESIS Publication 15, eds. Ainsworth, R.A. and Skelton, R.P. Mechanical Engineering Publications, London, 1993. Pp. 401–422.

Brear, J.M. and King, B.L. 'Stress relief embrittlement in MnMoNi pressure vessel steels'. Conf 'Grain Boundaries', Jersey, 1976, Institution of Metallurgists, London, 1976. Pp. C13–18.

Brear, J.M. and King, B.L. 'An assessment of the embrittling effects of certain residual elements in two nuclear pressure vessel steels (A533B, A508). Conf. 'Residuals, Additives and Materials Properties', London 1978. Phil Trans Roy Soc 1980, A295. Pp. 252–264.

Darbyshire, J.M. et al. 'The Metallographic examination of two LWR pressure vessel procedure welds'. CERL Note RD/L/N188/74.

Eggeler, G. et al. 'Parameters for creep damage evaluation and their correlation with results from ultrasonic velocity, attenuation and energy evaluations' Fourth Int. Conf. 'Creep and fracture of Engineering Materials and Structures'. Swansea, 1990. Inst. Metals, London, 1990. Pp. 931–940.

Hart, E.W., Li, Y., Yamada, H. and Wire, G.L. In: 'Constitutive equations in Plasticity' ed. Argon, A.S. MIT Press, 1975. P. 149.

Kachanov, L.M. 'An Introduction to Continuum Damage Mechanics'. Kluwer Academic Publishing, The Netherlands, 1990.

King, B.L. 'Intergranular embrittlement in CrMoV steels: an assessment of the effects of residual impurity elements on high temperature ductility and crack growth'. Conf. 'Residuals, Additives and Materials Properties', London 1978. Phil Trans Roy Soc 1980, A295. Pp. 235–251.

Lian, J. and Chen, J. 'Plastic instability and strain to fracture for damaged materials'. Mater Sci Engng, A131, 1991, pp. 9–15.

Nechtelberger, E., Kreitner, F. and Krainer, E. 'Contribution of the rapid determination of the high temperature creep behaviour of steel using the method of Rajacovics'. 'Conf 'The Properties of Creep resistant Steels'. Dusseldorf, 1972.

Stamm, H. and von Estorff, U. 'Determination of damage parameters for microcrack formation under creep conditions'. Conf 'Behaviour of Defects at High Temperatures' Sheffield 1992. ESIS Publication 15, eds. Ainsworth, R.A. and Skelton, R.P. Mechanical Engineering Publications, London, 1993. Pp. 123–151.

Steen, M. 'Creep life assessment by slow strain rate tensile testing'. Int J Pres Ves and Piping, 14, 1983, pp. 201–225.

Viswanathan, R. 'Damage Mechanisms and Life Assessment of High-Temperature Components. ASM International, Ohio, 1979.

Webster, G. and Ainsworth, R.A. 'High Temperature Component Life Assessment'. Chapman and Hall, London, 1994.

Woodford, D.A. 'The design for performance concept applied to life management of gas turbine blades'. Conf Baltica III, Helsinki, 1995. VTT Symposium 150, VTT Technical Research Centre of Finland, Espoo, 1995. Pp. 319–332.

Predicting crack growth in high temperature plant

Iain Le May

Metallurgical Consulting Services, Saskatoon, Canada

Abstract

The detection of cracks in pressurized components operating at elevated temperature is a cause of concern because of the absence of proven yet robust methods of estimating crack growth and remaining safe life. The paper demonstrates a simplified, user-friendly procedure for the prediction of crack growth and remaining life of welded pipe containing crack at the welds the problem and various approaches to estimate crack growth and remaining life. For conditions where both creep deformation and cyclic loading are encountered.

1. Introduction

The specific problem on which this study is based involved a high temperature steam distribution system in which crack-like defects had been identified in many welds. An estimate of the probable safe life remaining in the pipes was required, however the information for each crack-like defect was incomplete, as only the depth from the exterior surface to the start of a circumferential crack had been recorded. This meant that only a worst case scenario in which the crack started at the location recorded and continued to the inner surface of the pipe could be considered. The effect on the predicted remaining safe life by considering the defects to be interior surface cracks as opposed to embedded cracks was evaluated to display the importance of complete data when describing the location and size of crack-like defects.

Crack growth was modelled using concepts time-dependent fracture mechanics concepts [1, 2], and both creep and fatigue were considered. The effect of cycling from hightemperature and pressure to atmospheric temperature and pressure, as occur during a plant shut down, was accounted for in creep crack growth by using the C_t parameter in the cyclic creep crack growth prediction component of the analysis. Traditional fatigue crack growth rates using ΔK were used in a cumulative damage law so both creep and fatigue effects were included in the analysis.

2. Modelling of crack growth

The program used was developed as an easy-to-use predictive method of evaluating the remaining safe life of pressurized components operating in the creep regime. The goal in creating the program was to allow non-expert personnel to use it as a first step to determine if more detailed analysis, such as finite element analysis (FEA), was warranted depending on the results of the analysis and the extent of cracking present.

The program calculates the required variables at an instant in time and determines the crack growth rate on a per cycle basis. It was created using creep-fatigue crack growth information and theory from many sources [1–5], all of which utilize a parameter to calculate creep crack growth. The validity of C^* as a creep crack growth parameter in the steady state creep regime is widely accepted, and is the parameter used in the R5 [5] flaw assessment procedure. The C_t parameter promoted by Saxena [1, 4] is equal to the C^* parameter in the steady state creep regime, however it accounts for small-scale and transition creep occurring at the start of each cycle. Crack growth due to creep is more rapid prior to the onset of steady state than during steady state creep, therefore the C_t parameter was used in this study. The R5 [5] assessment procedure uses ΔK and the Paris law to estimate the effects of cycling on crack growth, and then applies a linear accumulation damage law with the crack growth predicted using C^* . A similar approach was used in this study, with the crack growth due to creep calculated using C_t rather than C^* . The general calculation sequence was shown as follows.

1. The loading conditions are acquired: geometry, initial defect size, type and location.
2. The initial value of the stress intensity factor, K and the reference stress, σ_{ref} , are calculated.
3. σ_{ref} is used to calculate the non-linear fracture mechanics parameter, C^* .
4. C^* , the loading conditions and other information previously calculated are used to determine the value of C_t .
5. The power creep law is applied to C_t to determine the current crack growth rate, da/dt .
6. The current crack size is incremented by 0.1 mm (the value can be altered, but 0.1 mm was used in all calculations related to this work) and the required parameters, K , σ_{ref} , C^* , C_t , and da/dt are re-calculated. The time required to reach the current crack size, i.e. $a_o + 0.1$ mm is then determined. If this time is less than the hold time, the crack size is again incremented by 0.1 mm and the calculations are repeated until the time required to reach the crack size is equal to the hold time.

7. Once the hold time is reached the crack growth due to creep for the current cycle is determined by integrating da/dt over the hold time.
8. The Paris law is used to determine the crack growth due to fatigue for the current cycle.
9. The linear damage accumulation law is then applied and the crack growth calculated in step 7 is added to the crack growth calculated in step 8, which determines the total crack growth in the current cycle.
10. The initial crack size is then set to $(a_o + \text{growth calculated in step 9})$ and the procedure repeated until $\sigma_{ref} > \sigma_y$.

The stress intensity factors and reference stresses were calculated using the equations provided in API 579 [3]. Where influence coefficients were required in the calculations the tabulated values were curve fitted and the equations of the fitted curves were used to calculate the required influence coefficients.

For cracks that are initially embedded, the equations for calculating K have some limitations: for example if the centre of the crack is closer to the internal surface of the pipe than the external surface, the crack geometry is limited by the following equations.

$$\frac{d_1 - a}{t} \geq 0.2 \quad (1)$$

$$0.25 \leq \frac{d_1}{t} \leq 0.75 \quad (2)$$

and

$$\frac{R_i}{t} \geq 5 \quad (3)$$

where, d_1 is the distance from the centre of the flaw to the inner surface, a is the flaw size, R_i is the inner pipe radius and t is the pipe wall thickness.

Equations (2) and (3) must be satisfied at the beginning of calculations, and since flaws are assumed to grow equally in both radial directions and the pipe size is constant, they are held constant throughout the iterative calculations. Equation (1), however, must be checked after each increment, as the result of the left hand side changes as the crack grows. When the loading conditions and crack location are such that failure conditions are met while the crack is still an embedded flaw within the allowable limits of equations (1–3), there is no problem in the calculations. However, should the crack location be such that failure conditions are not met when equation (1) becomes invalid (the crack is too close to the surface for its size) the crack is then “moved” so that it becomes a surface crack

(either interior or exterior surface depending on which surface is closer). The total radial dimension of the flaw just prior to moving is $2a$: when the crack is moved to become a surface flaw, the total radial dimension used in the calculations is $a_o = 2a$, so that it is of equal size. By moving the crack in this manner the predicted life is slightly shorter than would be expected when using equations valid all the way until the crack is truly a surface flaw.

3. Modeling parameters

The growth of 360° circumferential cracks within the deposited weld metal of butt welded 2.25Cr-1Mo steel pressure tubing was chosen for the study. The material properties at the operating temperature (535°C) of the steam pipes are listed in Table 1. A pipe with a nominal diameter of 254 mm and wall thickness 21.4 mm was used in the evaluation, the complete pipe dimensions being listed in Table 2. The pipe corresponds to 10 in. Schedule 120. The dimension characterizing the flaw size (the crack depth) was not available and therefore an initial flaw size was assumed for each case considered.

Table 1. Material properties of 2.25Cr-1Mo weld metal at 535°C [4].

Yield strength, MPa	173 ^a	Ultimate tensile strength, MPa	350 ^a
Young's modulus, GPa	162	Plain strain fracture toughness	242
Creep crack growth law exponent	0.674	Creep crack growth law coefficient	10.767
Creep power law exponent	9.36	Creep power law coefficient	2.29E-23
Plasticity exponent	5.83	Plasticity coefficient	6.79E-16
Fatigue crack growth law exponent	3.1	Fatigue crack growth law coefficient	9.3E-9

^a2.25Cr-1Mo metal at 540°C [6]

Table 2. Dimensions of piping used in the analysis.

External radius, mm	Internal radius, mm	Wall thickness, mm
136.5	115.1	21.4

For surface flaws the initial flaw size corresponds to a_o , whereas for embedded flaws the initial flaw size corresponds to $2a_o$. Embedded flaws are assumed to grow towards the outer and inner surfaces at the same rate, and thus their centre location does not change throughout the calculations. Fig. 1 is a schematic representation of the three crack-like flaws considered.

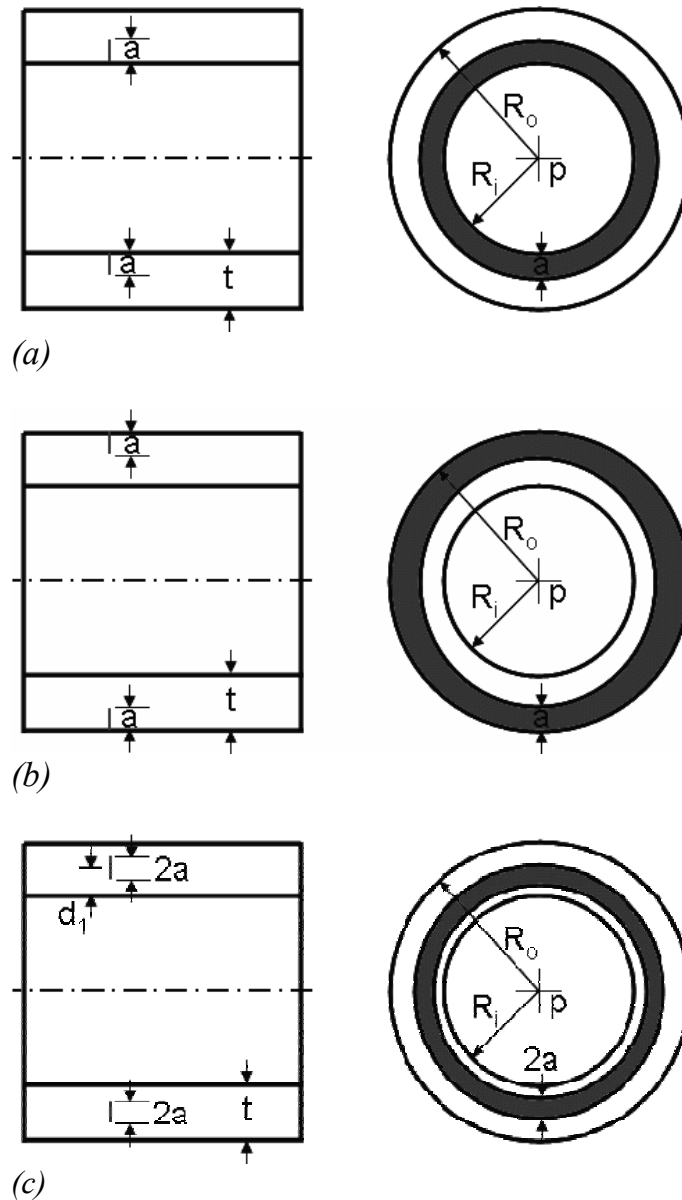


Figure 1. Geometry of 360° crack-like flaw: (a) at internal surface; (b) at external surface; and (c) embedded.

4. Results

A series of simulations with 360° circumferential cracks were completed with different variables held constant to display the effect of each variable on the remaining life prediction. When fatigue was accounted for the results were not significantly different from conditions of creep (including cyclic effects on creep) alone.

The effect of crack location on remaining life prediction is shown by holding all variables constant except for the distance from the inner surface of the pipe. The remaining life for a flaw with initial radial size $2a_o = 1.27$ mm was used in the

embedded calculations, while an initial radial size of $a_o = 1.27$ mm was used for surface defects. Fig. 2 is a plot of the number of cycles to failure versus the distance from the centre of the flaw to the internal surface, while Fig. 3 shows the remaining life in years as a function of the initial flaw location. The two end-points of the curves correspond to internal and external surface flaws respectively.

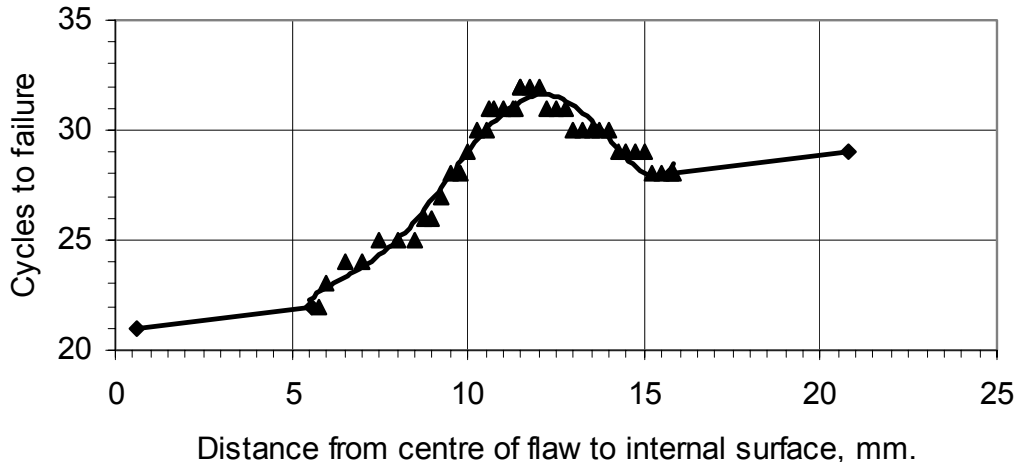


Figure 2. Number of cycles to failure as a function of the distance from the centre of the flaw to the interior surface of the pipe. End-points correspond to interior and exterior surface flaws. $p = 12$ MPa, $t_h = 4383$ h, and $2a_o = 1.27$ mm.

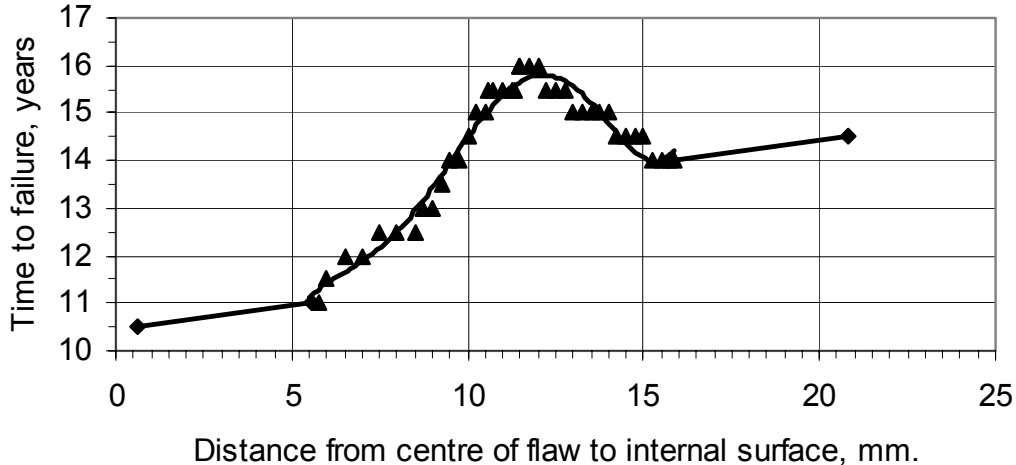


Figure 3. Time to failure as a function of the distance from the centre of the flaw to the interior surface of the pipe. Endpoints correspond to interior and exterior surface flaws. $p = 12$ MPa, $t_h = 4383$ h, and $2a_o = 1.27$ mm.

From Figs. 2 and 3 it is obvious that the flaw location is critical when remaining life is being predicted. An interior surface flaw represents the worst case scenario, as the internal pressure of the pipe is applied to the crack face, and the least critical location occurs close to the centre of the pipe, slightly towards the outside surface. The difference in expected remaining life from the worst case to

the best case is 11 cycles or 5.5 years, meaning that a best case flaw near the centre of the pipe would be expected to last over 50% longer than an internal surface flaw, a significant difference.

To show the importance of obtaining both the starting and ending radial dimension of a circumferential flaw, the effect of knowing only the distance from the outer surface to the start of a flaw was studied. This was completed by assuming the flaw start position to be 12.0 mm from the exterior surface and assuming different initial radial flaw dimensions $2a_o$. When the start position of the flaw is kept constant but the flaw size is altered the dimension d_1 also varies with flaw size. For the pipe and start depth chosen, flaw sizes ranging from $2a_o = 1.27$ mm to $2a_o = 5.10$ mm were examined. Initial flaw sizes larger than 5.10 mm were not valid according to equation (1). A flaw starting at a depth of 12 mm from the outer surface and extending to be an interior surface crack was also considered; however it was predicted to fail during the first cycle of operation and is not included in Fig. 4, which shows the effect of only knowing the defect start depth, and not its radial dimension.

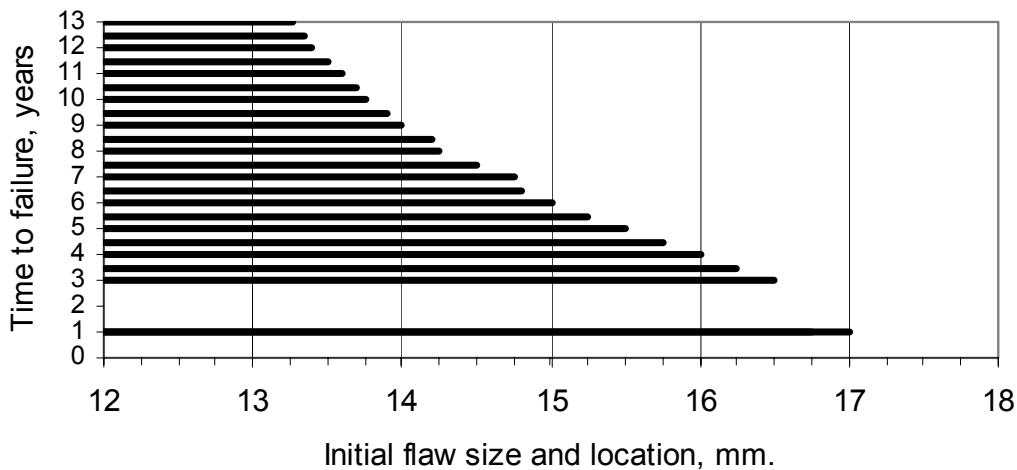


Figure 4. Predicted remaining life as a function of crack size. The size of the horizontal bars corresponds to the initial size of the crack, with all cracks starting 12.0 mm from the outside surface. The numbers on the x-axis correspond to the distance measured from the outside surface of the welded region of the pipe. A 360° circumferential crack was considered for the above figure. $p = 12$ MPa, and $t_h = 4383$ h.

From examining Fig. 4, it is obvious that knowing only the start depth does not provide adequate information for remaining life prediction, as with an initial flaw size of 1.27 mm the expected remaining life is 13 years, whereas for a flaw extending to the inner surface the remaining life is virtually nil. As would be expected, the remaining life expected decreases as the initial crack size increases.

As an additional component to the study the effect of varying the hold time between shut-downs was modeled, the effect of this having been previously discussed extensively by Saxena [1, 4], and our results are in agreement with the accepted trends, in that shorter hold times lead to shorter life expectancy. A flaw with an initial radial dimension of 1.27 mm was simulated for hold times of 730, 2922 and 4383 h. Fig. 5 shows the results of these simulations. All of the tests yielded curves of similar shape, with the maximum remaining life being 10.4 years for a hold time of 730 h, 15.33 years for a hold time of 2922 h and 16 years for a hold time of 4383 h.

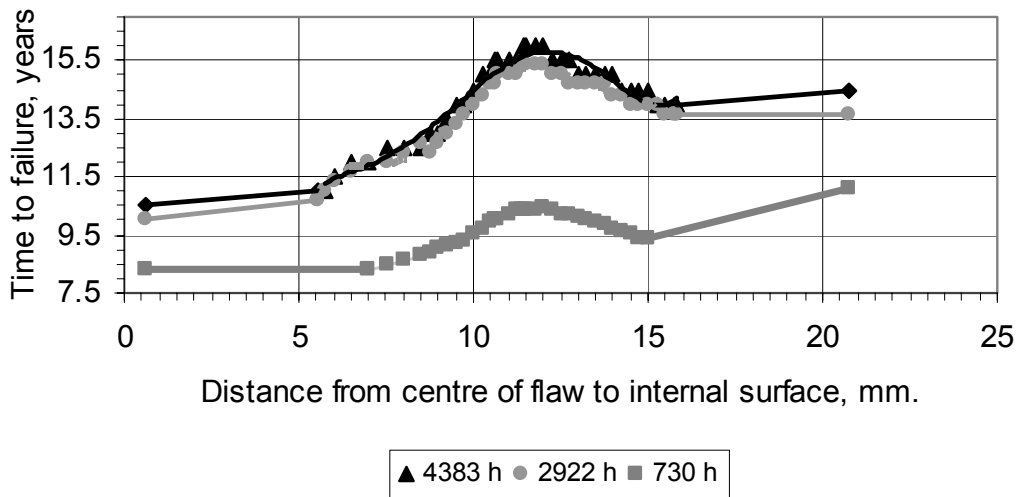


Figure 5. Variation of time to failure with hold time. $p = 12 \text{ MPa}$, $2a_o = 1.27 \text{ mm}$.

To verify that the shape of the curves shown in Figs. 2, 3, and 5 was consistent for different initial flaw sizes, an initial radial dimension of 2.54 mm was assumed and the analysis repeated. Fig. 6 shows the resulting curve for initial flaw sizes of 2.54 mm and 1.27 mm. It is clear that the curves are of similar shape, confirming that the location of a flaw to yield maximum life expectancy is size independent.

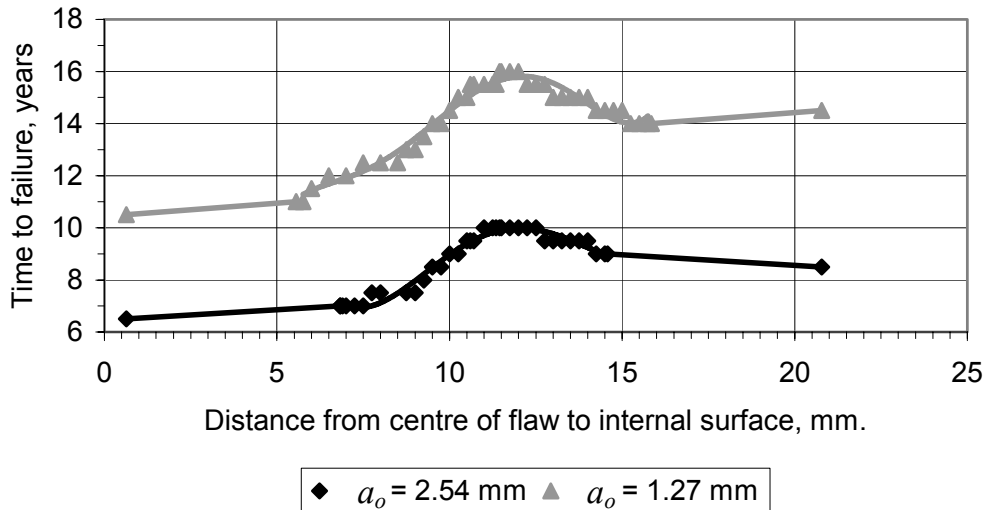


Figure 6. Effect of different initial crack size on trends. $p = 12$ MPa, $t_h = 4383$ h.

5. Conclusions

The effect of crack size and location within the butt welds of high pressure pipe operating in the creep regime has been studied by examining 360° circumferential flaws. Given an initial crack size a_o the remaining life predicted varies as the crack location changes, with the shortest life when the crack is an internal surface flaw, and the longest life when the centre of the crack is located slightly to the outer surface side of the centre of the pipe wall.

The location and complete geometric properties of a flaw are essential if a reasonable prediction of remaining life is to be made. Without this information the prediction could grossly over-or under-estimate the probable remaining life of welded pressurized pipes.

Additional studies are currently underway to evaluate other predictive methods, including the use of $(C_I)_{avg}$ to determine the average crack growth in a current cycle, $(da/dt)_{avg}$.

Acknowledgement

The contribution of Robert Peace, while he was employed at Metallurgical Consulting Services, to the development of the computer programme used in this study is gratefully acknowledged.

References

- [1] Saxena, A. Nonlinear Fracture Mechanics for Engineers. Boca Raton: CRC Press, 1998.
- [2] Webster, G.A. and Ainsworth R.A. High Temperature Component Life Assessment. London: Chapman & Hall, 1994.
- [3] Fitness-for-Service: API Recommended Practice 579 First Edition. Washington D.C: API Publishing Services, 2000.
- [4] Saxena, A. PCPIPE Version 3.0. A Computer Code for Integrity Analysis of Elevated Temperature Steam Pipes. Structural Integrity Associates, Inc., 1989.
- [5] Assessment procedure for the high temperature response of structures R5. Nuclear Electric.
- [6] Properties and Selection: Irons, Steels, and High-Performance Alloys. Metals Handbook 10th Edition, Vol. 1. ASM International, 1990.

Nomenclature

a	flaw size (depth)
a_o	initial flaw size for a surface defect
$2a_o$	initial flaw size for an embedded defect
C^*	creep crack growth rate parameter in extensive creep regime
C_t	creep crack growth rate parameter
$(C_t)_{avg}$	average value of C_t during the hold time of a cycle
d_1	distance from inner pipe surface to centre of embedded flaw
K	stress intensity factor
p	internal pressure
R_i	internal pipe radius
R_o	external pipe radius
t	wall thickness
t_h	hold time at elevated temperature and pressure
ΔK	stress intensity factor range
σ_{ref}	reference stress
σ_y	yield strength
da/dt	crack growth rate with respect to time
da/dN	crack growth rate with respect to cycles

Creep resistance of steel weldments after long term operation

Jan Hakl¹, Tomáš Vlasák¹, Jozef Pecha² and Radovan Pech³

¹SVÚM a.s., Prague, Czech Republic

²SES a.s., Tlmače, Slovakia

³REMS, Prague, Czech Republic

Abstract

Components in power generation plants, operating under creep conditions, are dimensioned for time limited operation. Except of moral obsolescence, the main reasons of limited life-time is the degradation of materials properties influenced by long term service and caused by temperature, stress and environment. Welded parts have the main requirement on the integrity of weldments. The contribution deals with creep resistance of 0.5Cr-0.5Mo-0.3V steel weldment after 162 kh operation.

1. Introduction

Parts of the power engineering facilities operated at increased temperatures are designed for a time-limited operation. Apart from moral obsolescence, the material degradation due to a long term action of temperature, stress and environment is the main reason of the limited lifetime. The integrity of the weld joints is the primary requirement for welded parts. The lifetime of weld joints has been investigated by a number of authors [1–6] in the course of years. Our contribution concerns these issues.

2. Experimental material

Steel according to ČSN 41 5128 was obtained in form of a segment of the linear part of the steam piping with the 219 mm outer diameter, a wall thickness of 25 mm and length of 295 mm. Chemical composition was as follows (wt%): 0.15 C; 0.53 Mn; 0.26 Si; 0.007 P; 0.005 S; 0.59 Cr; 0.42 Mo; 0.26 V; 0.013 Al. Prior to starting the operation, the steel properties were: yield strength $R_e = 410$ MPa, rupture strength $R_m = 561$ MPa, ductility $A_5 = 28.8\%$ and three values of impact strength: $KCU3 = 169, 190$ and 203 Jcm⁻². There was a circumferential weld in the middle of the obtained segment. The piping was in operation for 162 kh. The operation piping parameters were: steam temperature 540°C and pressure

13.52 MPa. The piping was designed for a service life of 10^5 h. At the end of the designed service life, the piping was examined for creep and material degradation in regular intervals.

3. The effect of the operation on the required piping thickness

For the estimation of the service life, first, the minimum thickness was determined of the piping wall, given by the operation parameters. According to the methodology described in [6], this quantity is given by the relation

$$s = \frac{p \cdot D_i}{(2\sigma_D - p) \cdot W_r} \quad (1)$$

where s is the piping thickness,
 p is the steam pressure,
 D_i is the internal diameter of the pipe,
 σ_D is the allowable stress at the service temperature.

$$W_r \leq W_r^{\max} = f(T, t_r) \leq 1 \quad (2)$$

where T is temperature,
 t_r is the creep life.

The W_r^{\max} parameter can be determined according to

$$W_r^{\max} = SRF = \frac{R_{mT}(W)}{R_{mT}(BM)} = f(T, t_r) \leq 1 \quad (3)$$

where SRF is the strength reduction factor,
 $R_{mT}(W)$ is the creep strength limit of the weld joint at temperature T and time to rupture t_r ,
 $R_{mT}(BM)$ is the creep strength limit of the base material at temperature T and time to rupture t_r .

We determined the strength reduction factor of the weld joint for steel 15 128.5 on the basis of data indicated in ref. [5, 6]. The graphical processing of the literature data of heat resistance and their evaluation for the determination of SRF is in Fig. 1. For the lifetime of 162 kh and temperature 540°C , the extrapolated value was $SRF = 0.791$.

It is still necessary to know the allowable stress for the determination of the wall thickness. In order to know σ_D , we must divide the value of 91.3 MPa (determined from ČSN 41 5128 [7] and valid for a given temperature and exploitation time) by coefficient 1.5 according to PN 13 1011 [8]. The value of the allowable stress is $\sigma_D = 60.87$ MPa for the given conditions.

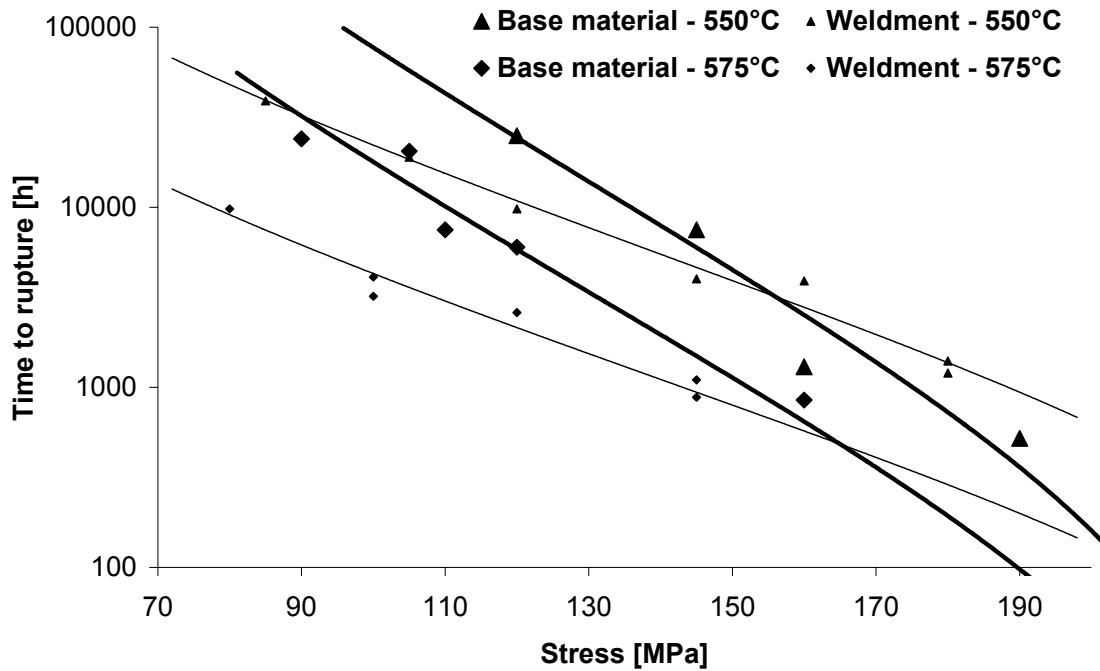


Figure 1a. Dependence of time to rupture on stress.

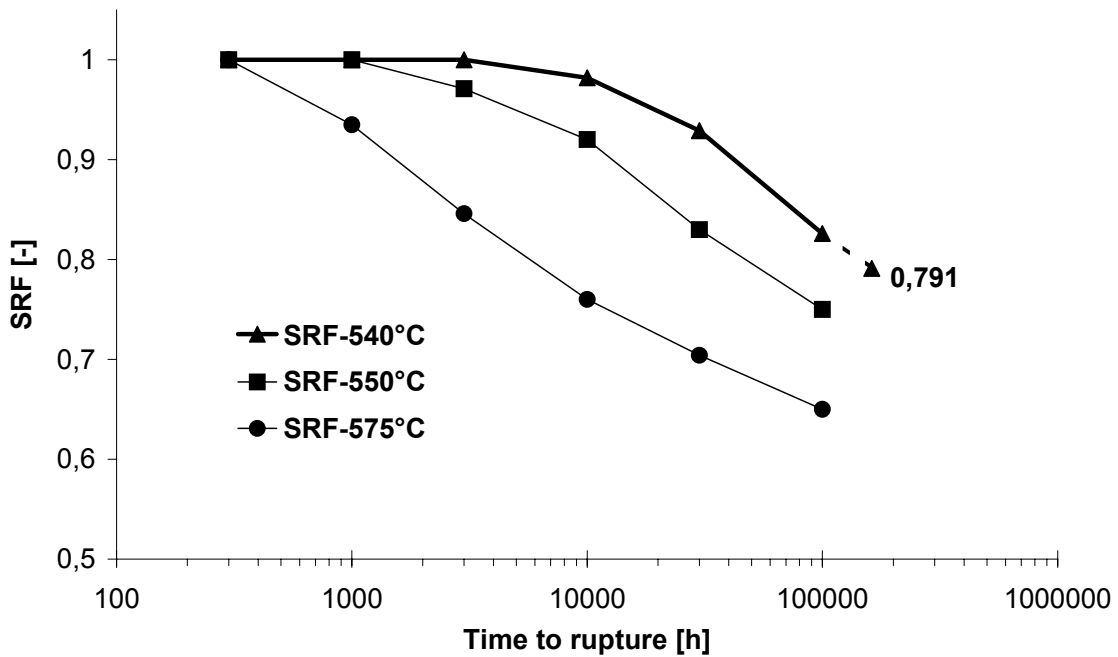


Figure 1b. Determination of the strength reduction factor of the weld joint for temperature 540°C and exposure 162 kh.

The minimum wall thickness is therefore

$$s = \frac{13.52 \cdot 169}{(2 \cdot 60.87 - 13.52) \cdot 0.791} = 26.69 \text{ mm}$$

which is a value greater than 25 mm. According to this method of calculation [8], the piping is already unsatisfactory.

However, the procedure of calculation that was routinely used when designing similar piping, considers the strength reduction factor of the weld joint $\text{SRF} = (0.85 \text{ to } 0.9)$ in dependence on the technology and type of weld. The design wall thickness had been 23.45 to 24.83 mm and therefore was satisfactory.

4. Material properties

4.1 Short term material characteristics

Specimens for studying mechanical properties were made so that their longitudinal axis was parallel with the pipe axis. The specimens for the determination of mechanical properties are of three kinds. The first kind characterized the material without a weld (state A); its gauge dimensions were $\text{Ø}6 \times 40$ mm. The second specimen represented the state after heat treatment $970^\circ\text{C}/1 \text{ h/air} + 700^\circ\text{C}/2 \text{ h/air}$ (state B), whose specimens were the same as in state A. The goal of state B was to regenerate the structure and approach the properties of the initial material. The third alternative corresponded to the material operated with the weld (state C). The gauge dimensions of this material were $\text{Ø}6 \times 60$ mm; the weld was in the middle of the length. Two specimens were evaluated from each state. Apart from this, state A and B was characterised by three tests of notch toughness.

The determined material properties of these states were compared with the standard [7] and the well-know initial properties (state D). The results are indicated in Table 1.

It is obvious that regenerated state B fully meets the requirements of the standard and the properties of initial state D. The yield limit R_e of the base material after operation (state A) and of the weldment after operation (state C) is below the requirement of the standard by 15% and 18%, respectively. It should be noted that the comparison of the yield limit and the ductility of the weld joint with the values of the basic material is only for information, due to the heterogeneity of the weld joint. For this reason, only strength limit R_m is evaluated during the tests of the weld joints. The R_m values are satisfactory in both states, however, narrowly above the minimum requirement of the standard. Ductility A_5 of state C

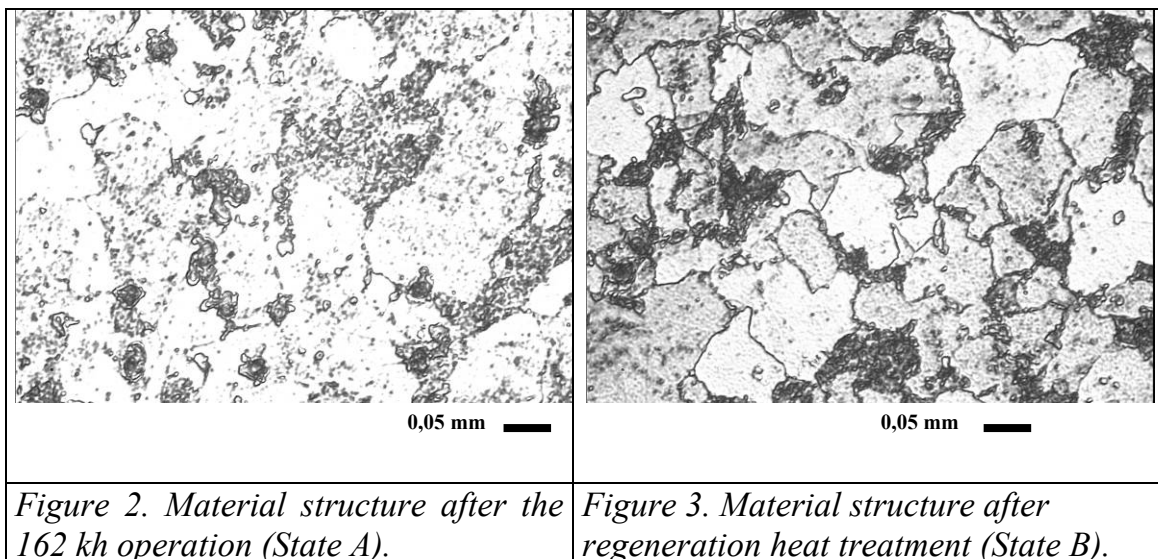
is below the admissible value of the standard approximately by 17%. Reductions of area Z are practically equivalent in states A, B, C. The notch toughness of state A also meets the requirement of the standard.

Table 1. Short term mechanical characteristics.

Property	State				
	15 128.5 [7]	D	A	B	C
R _e (MPa)	min 355	410	291 313	486 483	292 290
R _m (MPa)	Min 490 Max 690	561	502 516	630 625	504 505
A ₅ (%)	min 18	28,8	28,9 31,8	23,8 25,4	15,4 14,6
Z (%)			76,5 76,2	76,9 76,2	76,2 75,7
KCU 3 (Jcm ⁻²)	min 50	169 190 203	165 137 163	214 195 192	

4.2. Contribution of the regeneration annealing

During metallographic investigation, we first monitored possible occurrence of cavity damage. Cavities have not been found. This indicates that the creep damage did not reach a dangerous magnitude. The effect of the material heat treatment is obvious from Figs. 2 and 3. The structure after the 162 kh operation is illustrated in Fig. 2. The initial pearlitic areas changed to clusters of carbides in ferrite. The intensity of this reaction is obvious by comparison with Fig. 3 where is documented the structure changed into the initial state by heat treatment by procedure 970°C/1 h/air + 700°C/2 h/air. The short term characteristics of state B confirm this statement.



The second confirmation follows from Fig. 4, in which the creep strength is plotted at 540°C of the new material according to ČSN 41 5 128 [7] and the experimental points are plotted that characterise state B at the experimental temperature of 540°C. It is obvious that the normalised creep strength and the creep strength of state B belong to the same system.

The significance of this fact consists in that we can compare the creep properties of exposed states A and C with initial state B within one heat.

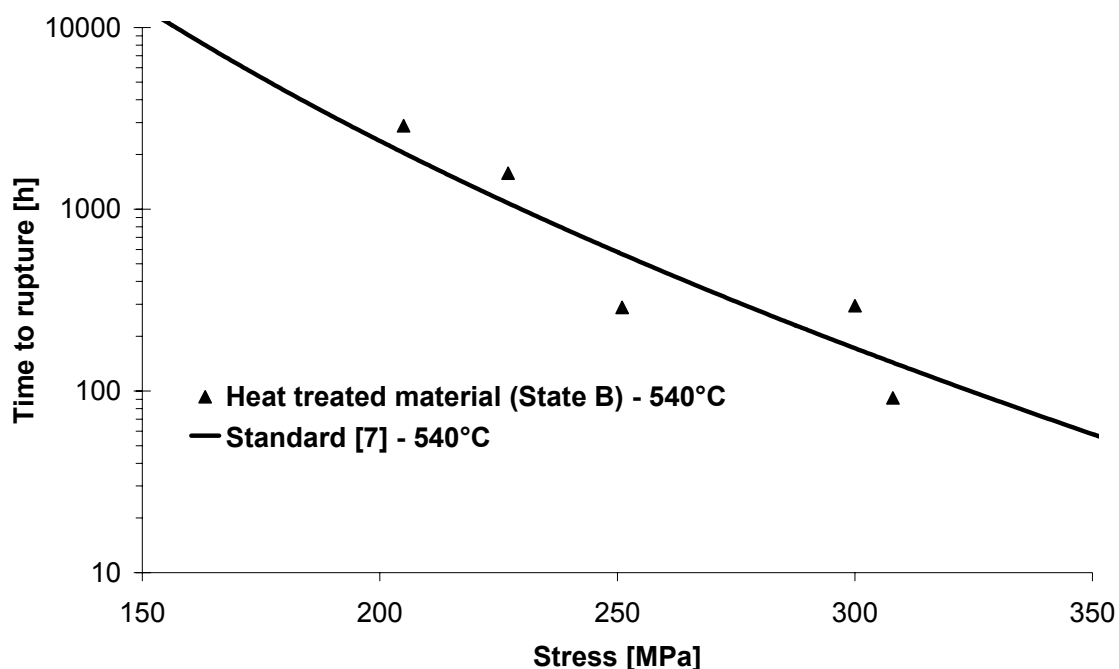


Figure 4. Normalised creep strength and the values corresponding to state B.

4.3 Creep properties

For the determination of the creep properties, specimens characterising state A and B had gauge dimensions $\varnothing 5 \times 25$ mm. State C was represented by specimens with specific gauge $\varnothing 7 \times 70$ mm; the single-V butt weld was in the middle of the gauge length. Schematic sampling procedure is shown on Fig. 5.

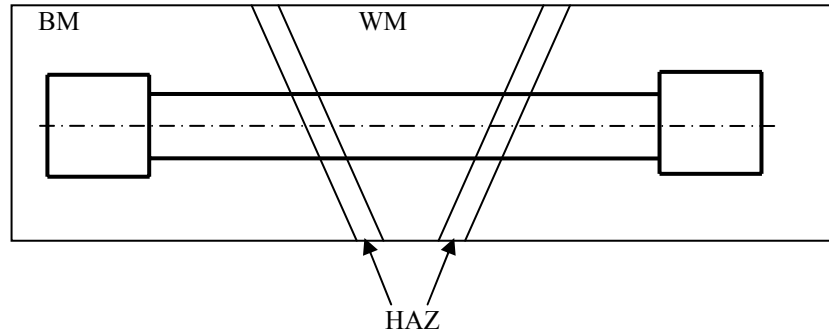


Figure 5. Sampling of specimen for test of circumferencial weld (State C).

A sufficient number of specimens was prepared for each state; they were tested at temperatures 540, 560 and 580°C. The orientation of the creep specimens was the same as that in specimens for the study of mechanical properties. The number of specimens for individual alternatives is obvious from Fig. 6, which is a plot of the dependence of stress on the Larson and Miller parameter P_{LM} in the following relation [9]

$$\log \sigma = A_1 + A_2 \cdot P_{LM} + A_3 \cdot P_{LM}^2, \quad (4)$$

where $P_{LM} = T \cdot (\log t_r + A_4)$,
 T is temperature,
 σ is stress,
 t_r is time to rupture,
 $A_1 - A_4$ are material constants.

The material constants are given in Table 2.

Table 2. Material constants.

State	A_1	A_2	A_3	A_4
A	-1,189778E+01	1,023446E-03	-1,825954E-08	3,500000E+01
B	-8,359059E+00	7,987391E-04	-1,458253E-08	3,500000E+01
C	-6,112795E+00	6,529468E-04	-1,239999E-08	3,500000E+01

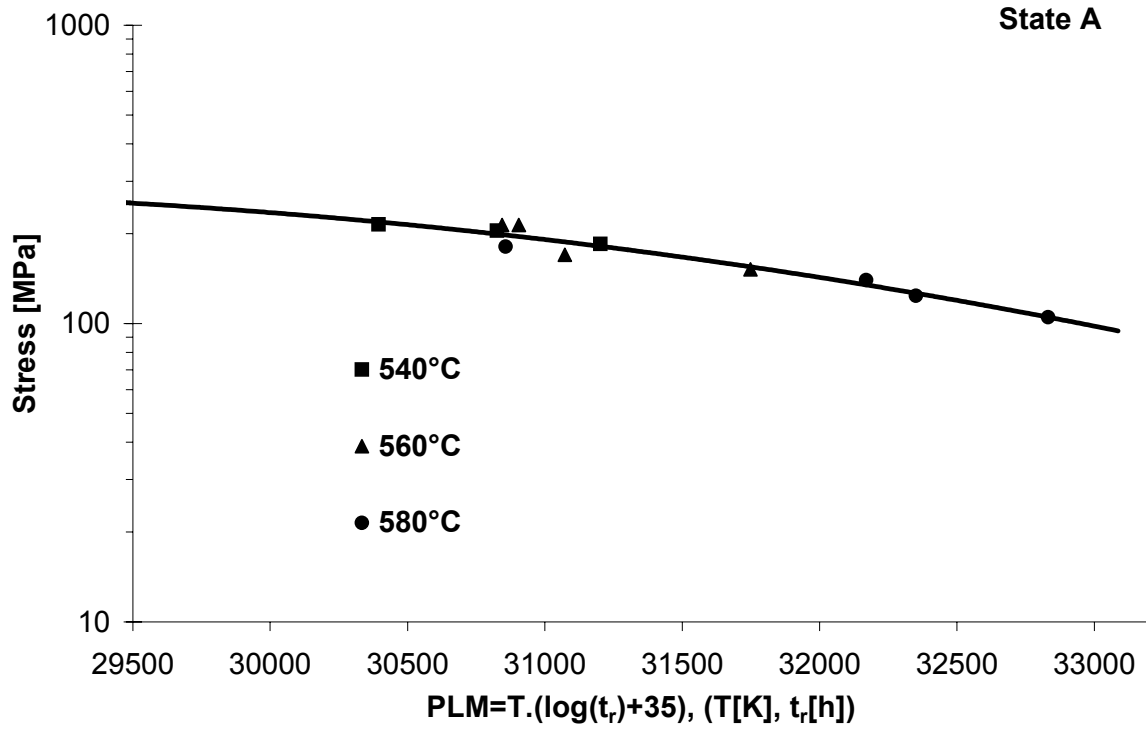


Figure 6a. Evaluation of creep strength for State A.

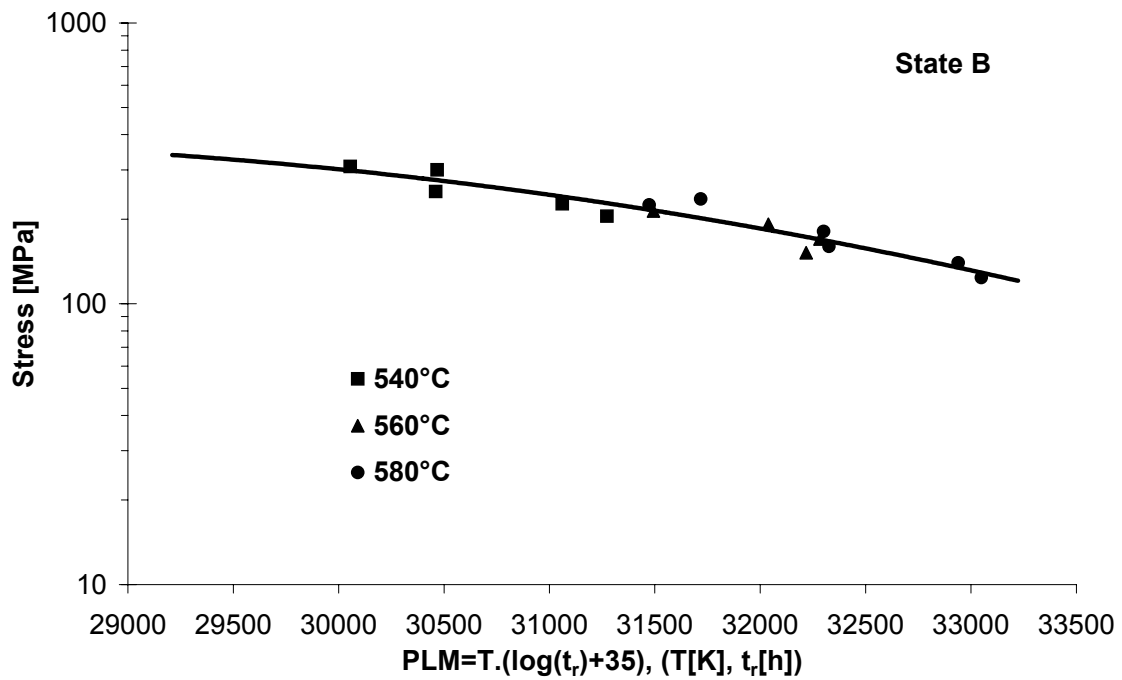


Figure 6b. Evaluation of creep strength for State B.

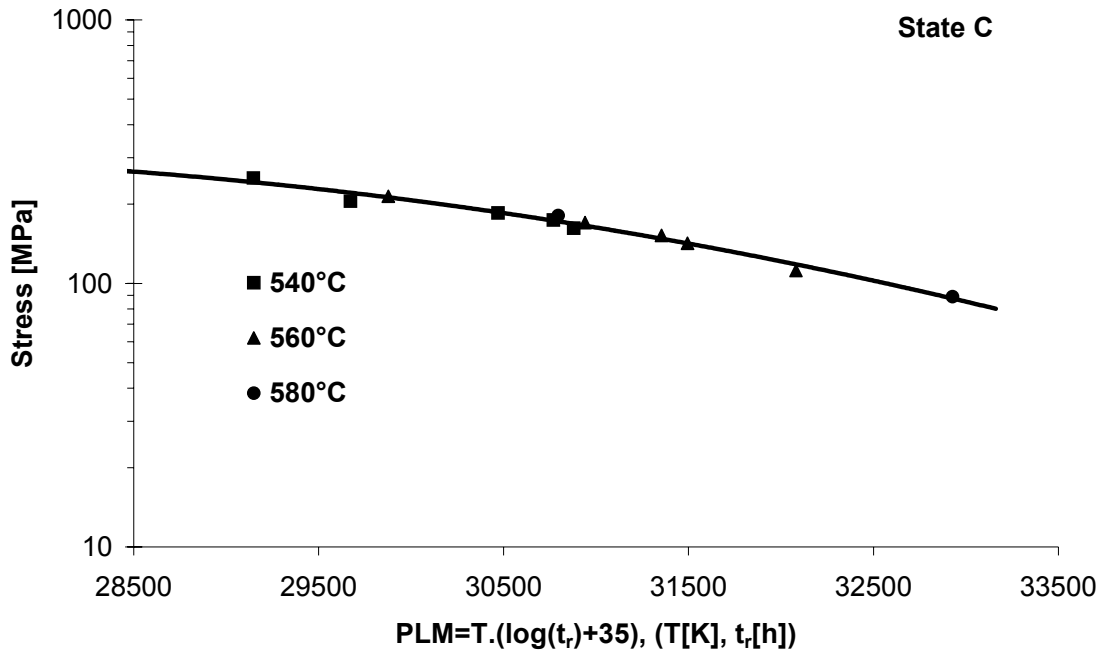


Figure 6c. Evaluation of creep strength for State C.

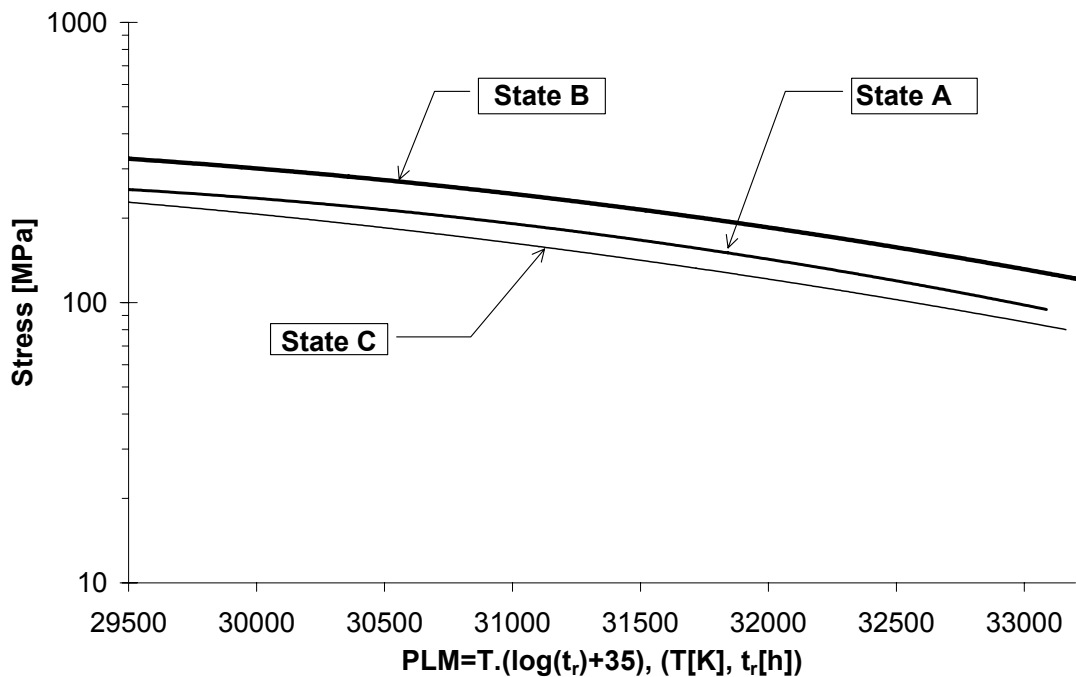


Figure 7. Comparison of creep strength for tested states.

It is obvious from Fig. 7 that the creep resistance of these material states is characterised by curves of three types. The regenerated material (state B) has the highest heat resistance; the material operated and containing the weld (state C) has the lowest resistance. Dominant rupture position of weldments (State C) was

visually localised in heat affected zone (HAZ). The state after operation but without the weld (state A), lies between these dependencies and it is therefore not dangerous. It is interesting for us to compare state C and B. Axis P_{LM} represents times from 162 078 to 544 753 h at a temperature of 540°C.

Therefore, the following relation corresponds to the indicated lifetime curves

$$SRF_{C/B} = \frac{R_{mT}(WC)}{R_{mT}(BMB)}, \quad (5)$$

where $SRF_{C/B}$ is the strength reduction factor of weld joint C in relation to the regenerated material B,

$R_{mT}(W)$ is the creep strength limit of the weld joint C at temperature T and time to rupture t_r

$R_{mT}(BM)$ is the creep strength limit of the regenerated material B at temperature T and time to rupture t_r .

The dependence of the strength reduction factor on the value of P_{LM} is indicated in Table 3. At $P_{LM} = 30\ 000$ (which essentially corresponds to 78 hours of further operation), the strength reduction factor of the weld joint assumes value $SRF_{C/B} = 0.69$. This value is similar to the value found in literature ($SRF = 0.791$).

With the increasing value of the parameter up to $P_{LM} = 31\ 000$, the $SRF_{C/B}$ value decreases up to 0.67. This state is achieved after approximately 1 300 hours of further operation. In this case, the required wall thickness is 31.5 mm according to relation (1). The service life of the piping is obviously already exhausted and further operation is not safe [8].

Table 3. Dependence of $SRF_{C/B}$ on P_{LM} .

Parameter P_{LM}	Correspond of time at 540°C (h)	Stress (MPa)		$SRF_{C/B}$
		State B	State C	
30 000	162 078	301	207	0.69
31 000	163 328	244	163	0.67
32 000	184 549	185	121	0.65
33 000	544 753	132	85	0.64

5. Conclusions

In the submitted paper, long term properties were followed of a part of steam piping and its weld joint after 162 kh operation at a temperature of 540°C. It was proved that the original properties of the pipe corresponded to the properties

according to ČSN 41 5128. It was also proved by testing that long term properties can be characterized by the strength reduction factor of the weld joint SRF, which assumes values 0.791 and less. It was determined during the application of this value to the calculation of the wall thickness that the steam piping does not meet the requirements determined in the PN 131011 company standard [8] that involves a binding proposal for the calculation of the piping systems stressed by internal overpressure at high temperatures. The service of steam piping was finalised with respect to requirements on safe operation.

Acknowledgements

This work was supported by Ministry of Education, Youth and Sports of Czech Republic – Project No.: VZ 257970001.

References

- [1] Auerkari, P. Assessment of residual creep life of a power plant steam piping. 8th congress of material testing, Vol. I., Budapest. Ed. Omikk – Technoinform, 1982. Pp. 117–121.
- [2] Pilous, V. and Stránský, K. Evaluation and estimation of residual service life of the steam line welded joint at the temperature of 540°C and under the pressure of 13,9 MPa. *Kovové materiály*, 23 (1985), No. 1, pp. 78–95. (In Czech)
- [3] Sklenička, V., Kuchařová, K., Čadek, J., Foldyna, V. and Sobotka, J. Creep properties of low alloy steel CrMoV after long term exploitation (in Czech). 7. Int. symposium on high temperature metallic materials. ČSVTS, Brno, 1986. Pp. 221–226.
- [4] Hakl, J., Bína, V. and Vlasák, T. Evaluation of long-term creep rupture strength of weld joints of low-alloy CrMo steel boiler tubes. Proc. Int. conference Integrity of High Temperature Welds. Ed. Institution of Mechanical Engineers, 1998. Pp. 65–75.
- [5] Sobotka, J. and Kuboň, Z. Contribution to evaluation of weldment creep strength with relation to dimensioning and estimation of steam boiler pipeline life. *Kotle a energetická zařízení 2003*. Ed. M.Ecler, Brno, 2003. Pp. 78–100. (In Czech).
- [6] Kuboň, Z. and Sobotka, J. Long-term creep rupture strength prediction and failure mechanisms of weld joints of boiler tubes. Int. Conf. Advanced Metallic Materials and their Joining, 25–27 Oct., 2004, Bratislava.

- [7] Standard ČSN 41 5128. Approved 1984.
- [8] Company standard PN 131011, Orgrez, Approved II. Issue in 1975.
- [9] Siefert, W. Warmfeste metallische Werkstoffe, Kamer der Technik, Zittau 1987.

Behaviour of coated and uncoated ferritic steels under isothermal and cyclic steam oxidation conditions

A. Agüero, V. González and M. Gutiérrez

Institute of Aerospace Technology, Metallic Materials Area,
Torrejón de Ardoz, Spain

Abstract

Next generation steam turbines are expected to operate at 600–650°C and at these temperatures, currently available high strength ferritic-martensitic steels need to be coated to prevent oxidation. Slurry deposited aluminide coatings have shown excellent performance up to 650°C under isothermal conditions. The behaviour of these coatings as well as that of uncoated P92 under thermal cycling conditions has been studied both in steam and in air at 650°C. The tested specimens were characterized by field emission scanning electron microscopy. A comparison with isothermal steam oxidation has been established. In cyclic oxidation, evidence of scale spallation from uncoated substrates was observed at shorter exposure times than for specimens tested under isothermal conditions. In the coated specimens, cracks originally present in the “as deposited” coating did not propagate or become sites of preferential oxidation during isothermal steam testing. However, the cracks widened and propagated causing substrate oxidation when the specimens were tested by thermal cycling in steam or in air.

1. Introduction

New generation steam turbines are expected to operate at 600–650°C and at these temperatures 8–10 wt. % Cr steels are attacked by steam, forming very thick scales in relatively short times [1, 2]. In recent studies carried out within the framework of COST actions 522 and 536, as well as in the European Project “Coatings for Supercritical Steam Cycles” (SUPERCOAT) the use of oxidation resistant coatings on these steels has been considered as an alternative to employing higher Cr alloys. Among the tested coatings, diffusion aluminides are very protective. These coatings are deposited by applying an Al slurry followed by a diffusion heat treatment at 700°C with thickness ranging from 40 to 100 µm [3–5]. Electron microprobe analysis as well as electron diffraction carried out in a Transmission Electron Microscope, confirmed the presence of an outer Fe₂Al₅ zone with Cr rich precipitates, and an inner and thinner FeAl layer on top of a zone containing acicular precipitates of AlN. The same zone shown in Fig. 1.

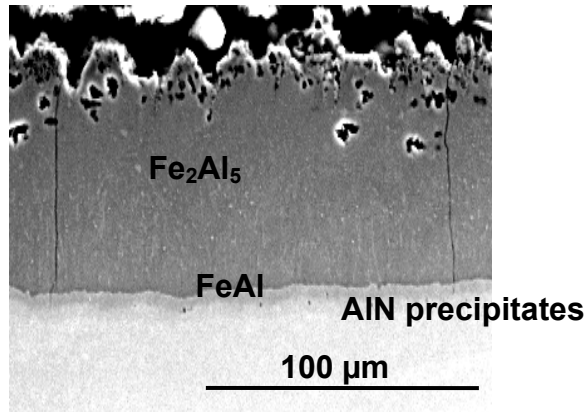


Figure 1. Microstructure of a slurry aluminide coating on P92.

The coating microstructure exhibit stress relieving cracks formed during cooling after the diffusion heat treatment. The behaviour of these coatings as well as that of uncoated P92 under thermal cycling conditions has been studied both under steam and under air at 650°C. The tested specimens were characterized by metallography, FESEM and XRD. A comparison with isothermal steam oxidation has been established.

2. Experiments

2.1 Materials

Ferritic steel P92 (C: 0.1, Mn: 0.5, Si: 0.03, Cr: 8.8, Ni: 0.06, Mo: 0.4, W: 1.8, V: 0.20 w%, Fe: bal) was obtained from Nippon Steel Corporation. The commercial Al slurry was obtained from Indestructible Paints Ltd.

2.2 Coating deposition

The coatings were deposited by applying the Al slurry by brush or spray gun. The commercial Al slurry required a “curing heat treatment” at 350°C for 30 minutes under air. The diffusion heat treatments were performed on a tubular furnace under flowing Ar.

2.3 Microstructural characterisation

The coated specimens were characterized by optical and field emission electron microscopy (JEOL JSM-6400 equipped with an Oxford EDS microanalyzer) of metallographic polished cross sections before and after exposure.

2.4 Steam oxidation laboratory testing

Isothermal Testing. The schematics of the closed loop laboratory rig employed at INTA is shown elsewhere [3]. Prior to testing, air is displaced from the chamber by means of N_2 which is kept flowing while heating up to 650°C (approximately at $600^\circ\text{C}/\text{h}$). Once the test temperature is achieved, the N_2 flow is cut and pure steam is introduced at a linear velocity of 8 cm/s . The steam temperature is measured and controlled by a thermocouple located inside the test chamber. To carry out weight measurements or to remove samples, they are furnace cooled to about 300°C under N_2 and subsequently removed. The reheat cycle is also carried out under N_2 . Samples were removed at different time intervals for metallographic analysis.

Thermal cycling in air. The test is carried out in a tubular furnace under laboratory air. Each cycle consists of heating in 5 min to 650°C , hold for 1 h followed by forced cooling in 5 minutes to 100°C (Fig. 2a). Samples are extracted a different intervals always at the end of a cycle to record the mass variation.

Thermal cycling in steam. The test is carried out under a 50% steam/Ar atmosphere in a tubular furnace. Each cycle consists of heating to 650°C at a rate of $6^\circ\text{C}/\text{min}$, hold for 5.5 h and cooling to 100°C at a rate of $2^\circ\text{C}/\text{min}$ (Fig. 2b). Samples are extracted a different intervals always at the end of a cycle to record the mass variation.

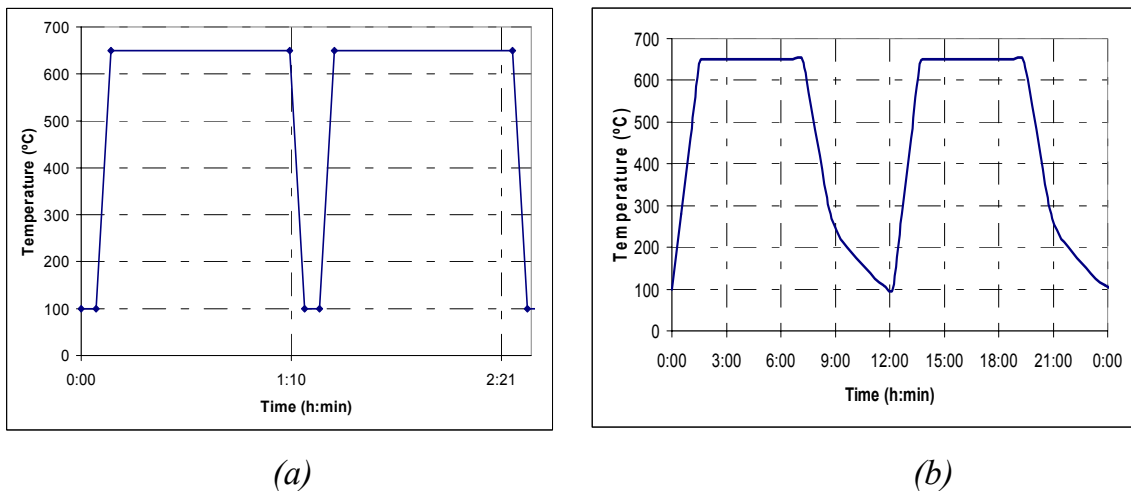


Figure 2. Thermal cycling: (a) in air, (b) in steam.

3. Results

3.1 Isothermal steam oxidation testing

The diffusive slurry aluminide coating protects P92 from steam oxidation for a period of up to 45 000 h at 650°C (test still ongoing) as shown in Fig. 3, where the weight variation of both coated and uncoated P92 is plotted as a function of time. The initial weight loss of the coated specimen is due to spalling of residual undiffused slurry. P92 experiences a large increase in weight as shown in Fig. 3, due to formation of a thick oxide scale composed of an outer Fe_3O_4 layer and inner Fe, Cr spinel.

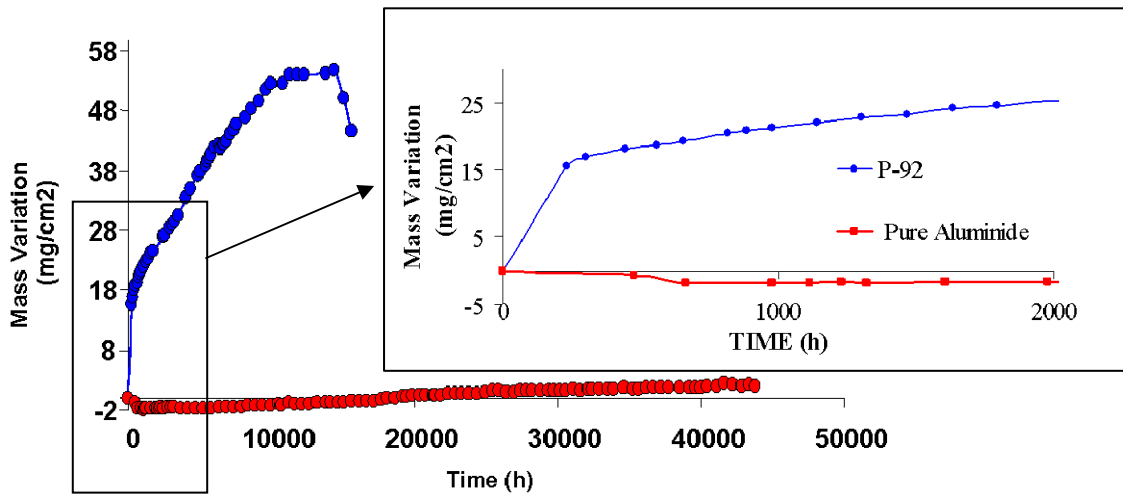


Figure 3. Isothermal steam oxidation at 650°C: mass change of aluminide coated and uncoated P92.

On exposure to steam at 650°C, the aluminide coatings form protective Al_2O_3 and degrade principally by Al inwards diffusion, resulting in a progressively lower Al content at the surface and an increment of the thickness of the AlN precipitation zone. Moreover, Kirkendall porosity develops at the coating-substrate interface as a result of a relatively higher Fe outwards diffusion rate once the Al concentration gradient has sufficiently decreased [6]. Cracks already present in the initial coating do not propagate into the substrate but are filled by the formation of aluminum oxide on the crack faces as shown in Figs. 4a and 4b where coating exposed for 8000 h is shown.

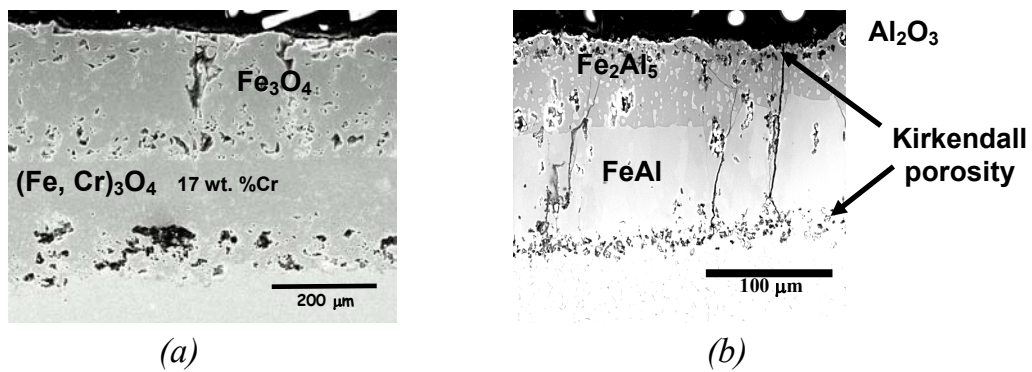


Figure 4. P92 exposed to steam at 650°C for 8000 h: (a) uncoated, (b) protected with a slurry aluminide coating.

3.2 Cyclic oxidation testing in air

The thermal cycling behavior of slurry aluminides has also been studied in air. Fig. 5 shows the weight variation of both coated and uncoated P92 as a function of time. The chosen cycle (see paragraph 2.4) is far too harsh for this application as a similar situation could only occur in a steam plant if boiler catastrophic failure would cause flooding of water into the turbine.

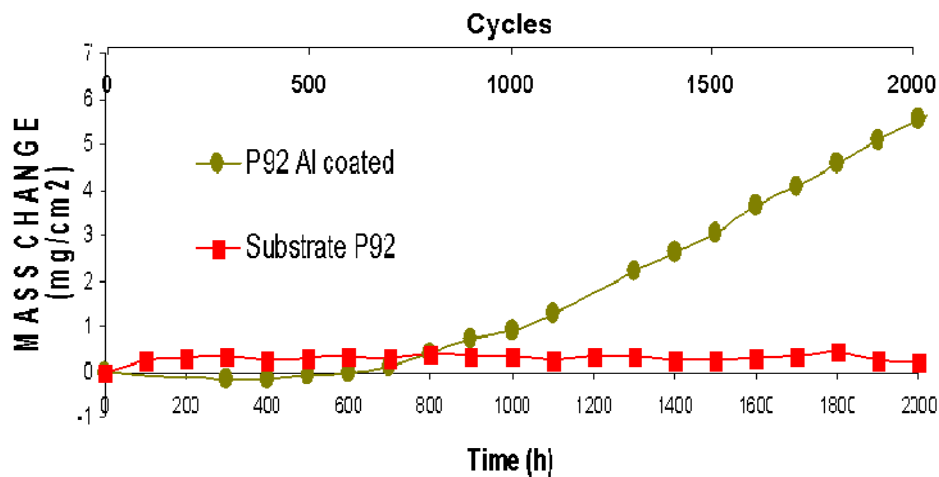


Figure 5. Cyclic air oxidation at 650°C: mass variation of aluminide coated and uncoated P92.

After 2000 h, uncoated P92 exposed to cyclic oxidation in air developed a very thin oxide layer rich in Cr and Mn as seen in Fig. 6. Other investigators have shown that uncoated P92 is quite resistant to oxidation at ambient air at 650°C, in agreement with the present results [7–10].

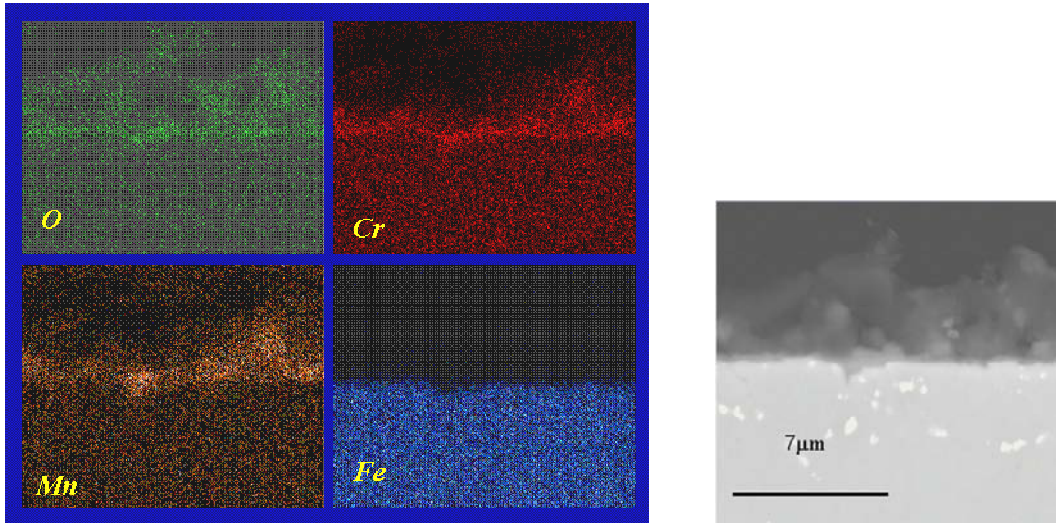
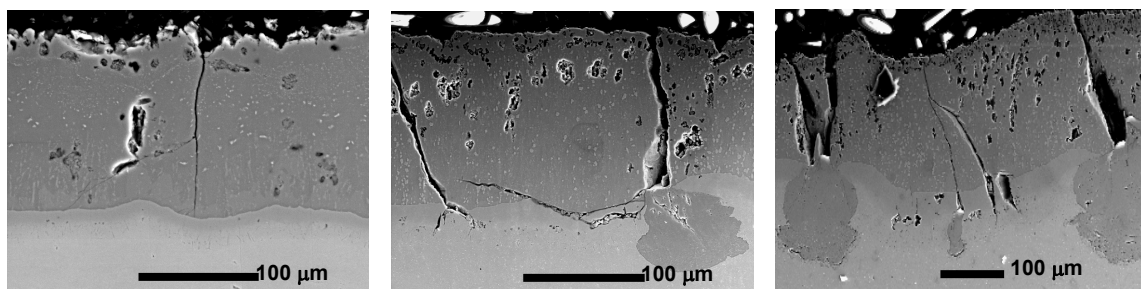


Figure 6. Uncoated P92 exposed to cyclic oxidation in air.

P92 aluminide coated samples showed no evidence of degradation or crack propagation after 100 cycles (Fig. 7). However, after 1000 cycles the cracks widened and propagated deflecting at the coating-substrate interface and the underlying substrate had started to oxidize. The cracks therefore have not healed by filling themselves with protective oxide because it grows very slowly under air at 650°C and/or because it spalls frequently, due to the thermal stresses originated by the fast heating and cooling rates.

A dual layer oxide consisting of Fe oxides on the top and Fe, Cr oxide adjacent to the substrate, formed at the cracks bottom below the coating-substrate interface as seen in Fig. 8. This oxide is quite similar to that formed on uncoated P92 when exposed to steam but under air this behaviour was unexpected.



100 cycles (h)

1000 cycles (h)

2000 cycles (h)

Figure 7. Slurry aluminide coated P92 exposed to cyclic oxidation in air.

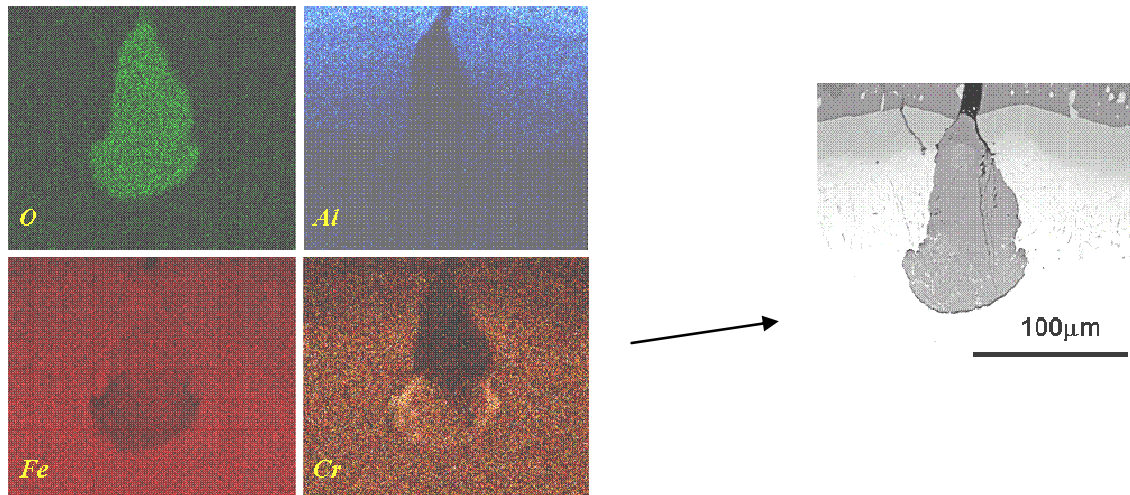


Figure 8. FESEM-EDS concentration mapping of the oxide developed at the coating-substrate interface after 1000 thermal cycles in air at 650°C.

As uncoated P92 experienced very low weight variation after the same exposure than the coated specimens. These observations may be explained as a result of significant modification of the substrate composition near the coating by interdiffusion with the coating, reducing the alloy's resistance to air oxidation. The levels of both Cr and Al are below the critical value required to form chromia and alumina respectively. The composition of the substrate near the coating interface was Cr: 6.5; Al: 3.0; Fe: 90.5 wt. %, whereas that of the unaffected substrate on the same specimen was Cr: 10.8; W: 1.6; Mo: 0.3, Fe: 87.3 wt. % (measured by EDS) indicating significant modification of the substrate composition near the coating probably by interdiffusion with the coating. The low Cr and Al content may well be the cause of the lower resistance of the alloy to air oxidation as they are both below the critical value required to form chromia and alumina, respectively.

3.3 Cyclic oxidation testing in steam

The thermal cycling behaviour of slurry aluminides has also been studied in steam. A smoother cycle was chosen in order to better simulate the heating and cooling stages in steam turbines. Fig. 9 shows the mass variation of both coated and uncoated P92 as a function of time and the number of cycles.

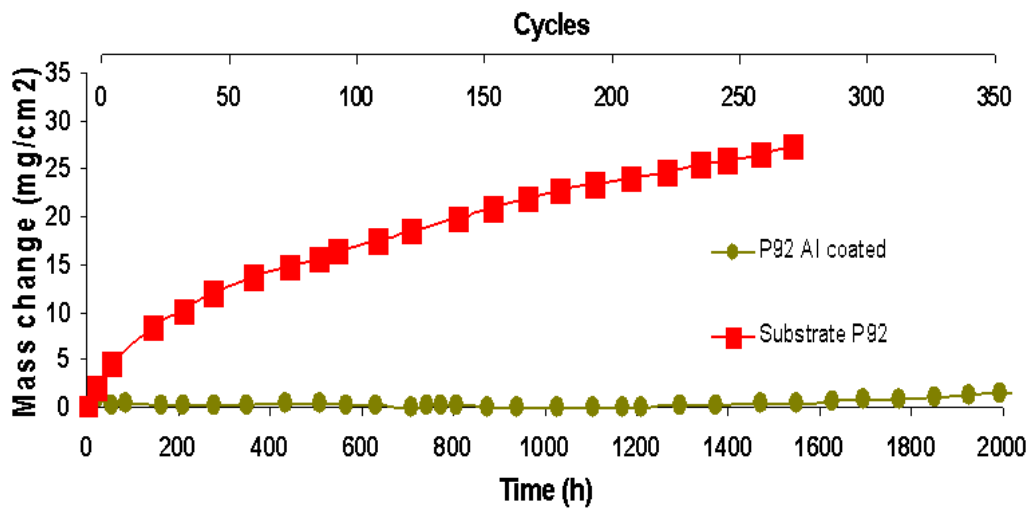


Figure 9. Cyclic steam oxidation at 650°C: mass change of aluminide coated and uncoated P92.

The uncoated specimens started to spall after first few cycles as shown in Fig. 10.

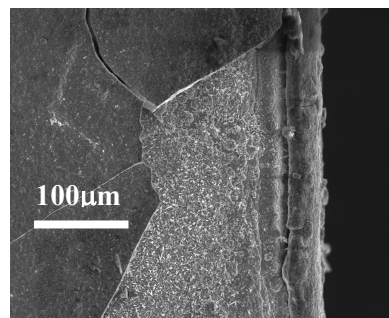
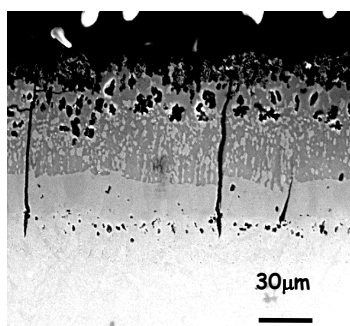
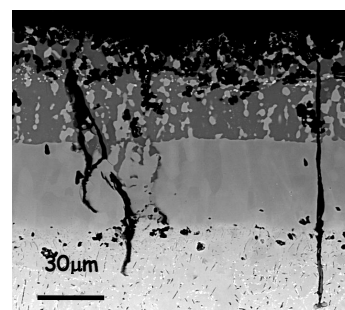


Figure 10. Uncoated P92 after 10 cycles of steam oxidation at 650°C.

Surprisingly, even at the chosen smoother cycles, the cracks originally present in the coating propagated into the substrate but after 2000 h of exposure (360 cycles) no evidence of substrate oxidation could be observed (Fig. 11).



100 cycles (550 h)



360 cycles (2000 h)

Figure 11. Slurry aluminide coated P92 exposed to cyclic steam oxidation at 650°C.

4. Discussion

Uncoated P92 exhibits very little oxidation under air even under very harsh cycles, however, in steam under both isothermal and cyclic oxidation conditions, P92 forms very thick oxide scales after short periods of exposure at 650°C, as expected. Under cycling conditions in steam, spalling was observed after very few cycles in contrast with the samples tested isothermally which did not exhibit spallation until after 10 000 h [6]. However, the mass variation data is not significantly different for the first 2000 h of exposure. This observation could be explained by a very fast oxide growth on spalled areas. Carefully designed experiments are required to verify this hypothesis. Test carried out in a bypass of an Alstom steam turbine [3] (Westfalen-Germany) have indicated that spalling of uncoated P91 samples occurs after very few hours of exposure and cycles as shown in Fig. 12. Despite having a lower oxidation resistance than P92 [8], extensive spallation has already occur after only 3300 h of exposure.



Figure 12. Uncoated P91 samples.

The aluminide coatings are very resistant to steam under isothermal conditions and cracks originally present do not propagate and heal by producing a protective Al_2O_3 scale. However, under air, substrate attack could be observed at the cracks bottom, indicating that air could reach the Cr impoverished substrate causing its oxidation. It therefore appears that under air the protective Al_2O_3 scale does not grow fast enough to “seal” the cracks or spalls frequently due to thermal expansion mismatch during cycling. In contrast, in the coated samples exposed to steam cyclic oxidation there was no evidence of substrate attack although the cracks widened and propagated. Therefore, it appears that steam contributes to a faster growth of the protective Al_2O_3 scale and/or that due to the lower heating and cooling rates, spalling is not significant. Aluminide coated samples tested in the Westfalen by-pass mentioned earlier did not exhibit crack propagation into the substrate after 3300 h and several cycles [3].

The expected life-time of a steam turbine is 300 000 h during which, around 3000 cycles are expected. Unless catastrophic failure occurs, these cycles are

very smooth with heating rates of around 2°C/min and cooling rates of 0.1°C/min. Results of the present experiments seem to indicate that the chosen cycles (for both air and steam thermal cycling experiments) are still too harsh and do not seem to adequately simulate the real operating conditions for coatings. Pint and collaborators found out that extending the constant temperature period of the cycle had a strong effect in reducing crack formation in aluminide coatings deposited by high temperature CVD [11]. They employed very fast cooling and heating rates but a hold time of 10 hours, almost twice that of the present experiments. On the other hand, it is clear that the on-set of spallation of uncoated substrates is accelerated by thermal cycling and in this case the results approach does obtained under real conditions.

5. Conclusions

P92 is quite resistant to air at 650°C and develops a protective Mn and Cr rich spinel. Under steam, a non-protective dual oxide is developed with a top Fe₃O₄ layer and an inner layer of (Fe, Cr)₃O₄. Under cyclic oxidation conditions in steam, scale spallation begins after the first few cycles whereas under isothermal conditions spallation begins after 10 000 h.

Slurry aluminide diffusion coatings are very resistant to steam at 650°C. Under isothermal conditions coating degradation mostly occurs by interdiffusion with the substrate as the Al concentration becomes depleted near the protective α -Al₂O₃ scale. However when the coatings are thermally cycled (with either steep or smooth ramps), stress relieving cracks initially present in the coating widen and propagate. In air, substrate oxidation takes place through the cracks that do not appear to form protective Al₂O₃ over their surface fast enough, for the cracks to heal and prevent air from reaching the unprotected and Cr impoverished substrate. In steam it appears that the growth of the protective scale is faster and/or the spallation slower and the resulting healing effect blocks steam from entering the crack. However, the cracks propagated into the substrate which could have very negative effects in the mechanical properties of the substrate.

Further investigations are required to determine the cycle that best simulates the operating conditions of a steam turbine for laboratory testing, as when slurry aluminide coated and uncoated specimens were tested in a steam by-pass of a power plant (Westfalen-Germany), coating crack propagation into the substrate was not observed after at least 6500 h.

References

- [1] Ennis, P.J. and Quadackers, W.J. *Materials for Advanced Power Engineering 2002*, pp. 1131–1142.
- [2] Quadackers, W.J., Ennis, P.J., Zurek, J. and Michalik, M. *Materials at High Temperature*, 22 (2005), pp. 47–60.
- [3] Agüero, A., Muelas, R., Scarlin, B. and Knödler, R. *Materials for Advanced Power Engineering 2002*, pp. 1143–1158.
- [4] Agüero, A., Muelas, R. and Gutiérrez, M. *Materials Science Forum*, 522–523 (2006), pp. 205–212.
- [5] Agüero, A., García de Blas, F.J., Muelas, R., Sánchez, A. and Tsipas, S. *Materials Science Forum*, 369–372 (2001), pp. 939–94.
- [6] Agüero, A., Muelas, R., Pastor, A. and Osgerby, S. *Surf. & Coat. Technol.* 200 (2005), pp. 1219–1224.
- [7] Vossen, P.T., Gawenda, P., Rahts, K., Röhig, M., Schorr, M. and Schütze, M. *Materials at High Temperature*, 14 (1997), pp. 387–401.
- [8] Ennis, P.J. and Quadackers, W.J. *Advanced Power Engineering 1998*, (1998), pp. 123–128.
- [9] Thiele, M., Teichmann, H., Schwarz, W., Quadackers, W.J. and Nickel, H. *VGB Power Technology*, 2/97 (1997), pp. 129–134.
- [10] Wright, I.G. and Pint, B.A. *NACE Corrosion*, Denver, CO, April (2002).
- [11] Pint, B.A., Zhang, Y., Tortorelli, P.F., Haynes, J.A. and Wright, I.G. *Materials at High Temperature* 18 (2001), pp. 185–191.

The hybrid coatings against hot corrosion: on-site and laboratory tests on P91 and carbon steels

M. Danielewski, R. Gajerski, R. Filipek, S. Łabuś,
E. Tyliczszak-Halibożek and A. Milewska

ewelinat@uci.agh.edu.pl

AGH University of Science and Technology, Faculty of Materials and Ceramics,
Al. Mickiewicza 30, 30-059 Kraków, Poland

Abstract

HybridMD is a mono- or multi-layer protective coating developed to extend the lifetime of boiler water walls and other equipment exposed to hot corrosion. The coating consists of the base layer(s) (30–80 μm thick) and the top layer(s) (25–60 μm). The base layer – HybridMDP consists of inorganic bonding agents and Al filler. The top layer – HybridMDN contains spherical and/or flake Al, Si and/or Al-Si fillers. The bonding is a mixture of organic resins. This coating was applied over sand blasted substrate of 16M and P91 steels. Prepared coupons of 16M and P91 steels were oxidized at 550°C and 620°C in air and to determine their oxidation behaviour. The results obtained for 16M steel at temperature 550°C show that coating provides active chemical and passive mechanical protection of the outer metal surface. It limits corrosive atmosphere access to the base metal, provides reduced rate of the oxides formation and reduces stresses in the growing oxide scale. The measured parabolic rate constants are in agreement with those predicted on the base Wagner theory. The results allow to explain an exceptional hot corrosion resistance of the HybridMD coating in coal fired boilers. At 620°C aluminium from coating reacts with P91 steel components, mainly iron, and forms intermetallic phases at the coating|steel interface. This aluminization process increases the hot corrosion resistance. The further tests are necessary to study the long time evolution of the diffusion zone and the effect of water vapour on P91 oxidation rate.

1. Introduction

Hot corrosion is an important problem in modern coal fired boilers. The introduction of the low NO_x burner systems significantly increased the corrosion rate. Nowadays hot corrosion often occurs in boilers in which low NO_x conditions are maintained and always when the low grade coal, organic materials, wood, waste etc. are burned. The reducing atmosphere combined with mineral matter, sulfur, chlorine and increased concentration of CO in the flue gas

causes high corrosion rates. The deposits destroy/disrupt the normally protective oxide scale. The hot corrosion mechanisms are complex and not fully understood. Protection against hot corrosion is an important issue in chemical industry and many others. Hot corrosion often results in boiler steels consumption of the order of ~1 mm/year and higher, while in pure air it does not exceed 100 $\mu\text{m}/\text{year}$ [1–6]. To reduce the corrosion rate, the highly alloyed steels and coatings are used.

HybridMD is a multilayer protective coating developed to extend the life-time of power plant boiler water walls or other equipment exposed to hot corrosion. Standard version of this coating consists of the base layer (30–80 μm thick) and the top layer (25–60 μm) (coating coated on P91 steel and oxidized at 650°C consisted only from base layer). The base layer consists of non-organic bonding agent and Al filler. The top layer contains spherical and/or flake Al, Si and/or Al-Si fillers. The bonding is a mixture of organic resins. HybridMD coating provides both active chemical and passive mechanical protection of outer metal surface. It limits corrosive atmosphere access to metallic surface and protects against erosion. HybridMD coating does not deteriorate due to the hot corrosion in both oxidizing and reducing atmospheres. In this paper we focus on the results of oxidation tests of 16M steel coated with HybridMD and P91 steel coated with HybridMDP in air at the temperature 550°C and 620°C.

2. Experiments

The materials, on which hybrid coating was tested were the steels 16M and P91. P91 was produced by Vallourec & Mannesmann Tubes in France according to ASME SA 335 norm. The composition of the steel P91 in wt. % is given by: C-0.097, Cr-8.780, Ni-0.270, Mn-0.470, Si-0.380, Mo-0.930, Nb-0.066, N-0.053, V-0.220, P-0.014, S-0.001, Al-0.006. In order to avoid the corner and other effects the large samples of the steels 16M and P91 were tested. The area of the coupons was in range from 250 up to 850 cm^2 .

Application procedure of HybridMD consisted of:

- sand blasting of the steels,
- air-less application of the base layer,
- thermal treatment at the temperature 350°C, 1 hour,
- air-less application of the top layer,
- thermal treatment at the temperature 350°C, 1 hour,
- measurement of coating thickness after 24 h.

The thickness of the coating was measured according to the standard PN-EN ISO 2178. Total thickness of HybridMD coating applied on 16M was between 58–76 μm . Thickness of the HybridMDP coating applied on P91 was between

66–80 μm . The oxidation tests of the coated and uncoated steel 16M were performed in air at the temperature 550°C for 450–650 h. The oxidation tests of the coated steel P91 were performed in air at the temperature 620°C for 350 h. In order to simulate the shut-down conditions, all coated samples were cooled down up to room temperature after \sim 200 h oxidation.

In oxidation tests original thermogravimetric apparatus (TG) was adopted. The thermogravimetric unit allows to examine the samples with the surface area up to 1000 cm^2 and mass up to 4 kg. The furnace is schematically shown in Fig. 1.

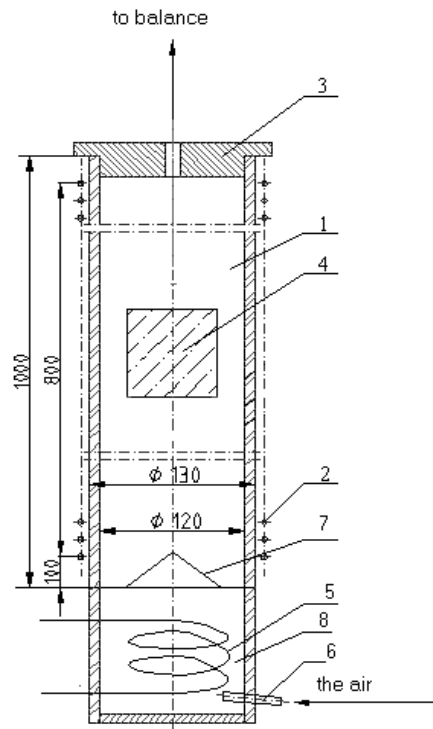


Figure 1. Cross-section of the heating chamber: 1 – vertical furnace tube, 2 – kanthal APM wires, 3 – top cover, 4 – sample, 5,8 – preheater, 6 – gas inlet, 7 – flow stabilizer.

The small samples were cut out from coated and uncoated areas of the steels after oxidation and were mounted in thermosetting organic resin. The optical examination of the oxidized steels and scanning microscopy observations for coated parts of the steel P91 (SEM and EDX) were performed.

3. Results

The results from the metallographic investigations of the oxidized coupons are shown in Figs. 2–5. Scanning microscopy observations with EDS analysis, are

presented in Fig. 6 and Table 1. The oxidation kinetics are shown in Figs. 7 and 8 for the steels 16M and P91, respectively.

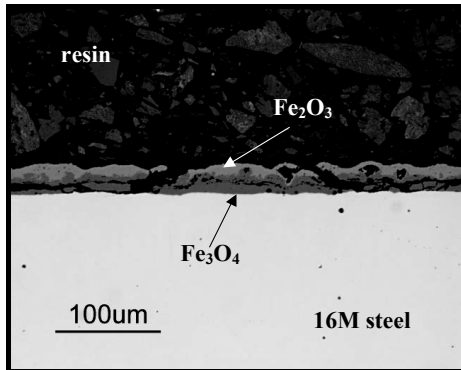


Figure 2. Cross section of oxide scale formed on uncoated 16M steel at 550°C, air, $t = 453$ h.

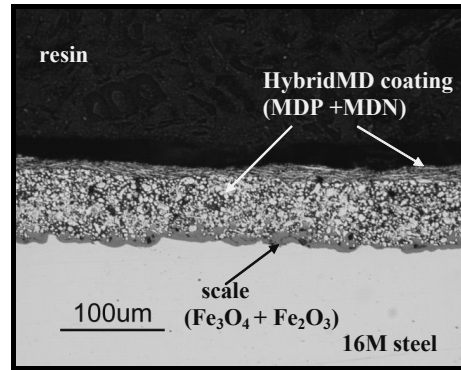


Figure 3. Cross section of coated 16M steel oxidized at 550°C, air, $t = 627$ h.

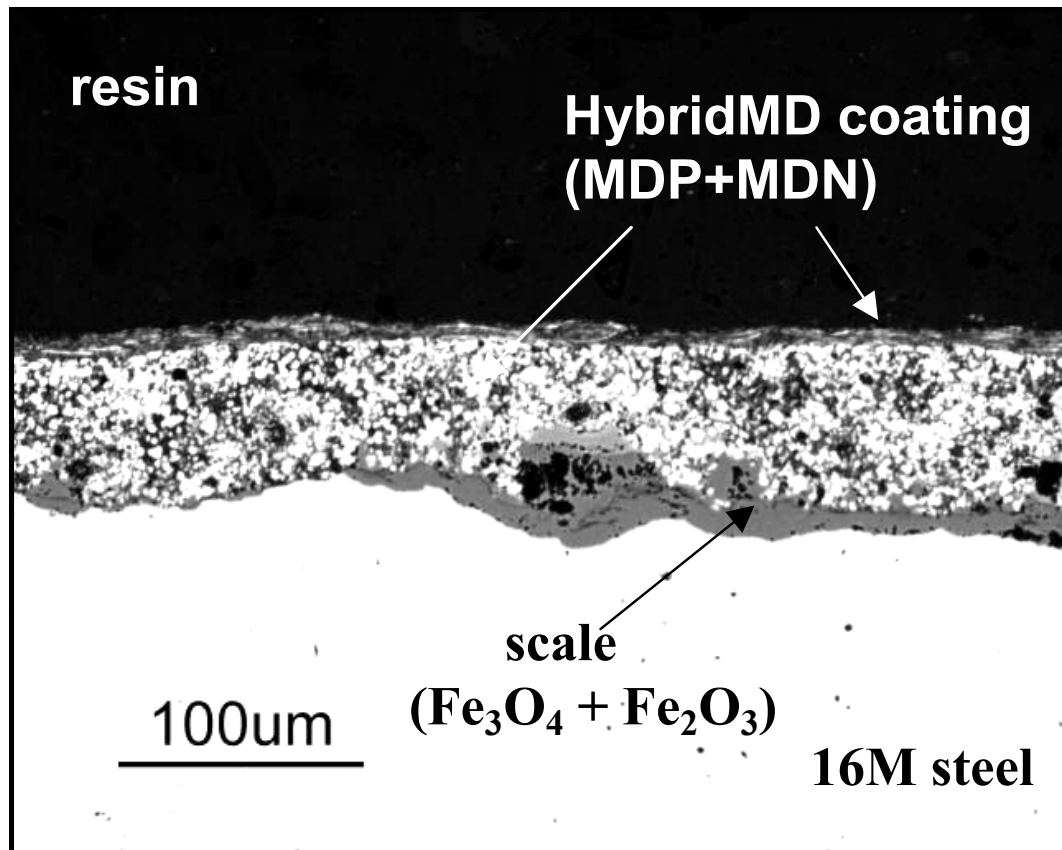


Figure 4. Cross section of coated 16M steel oxidized at 550°C, air, $t = 594$ h.

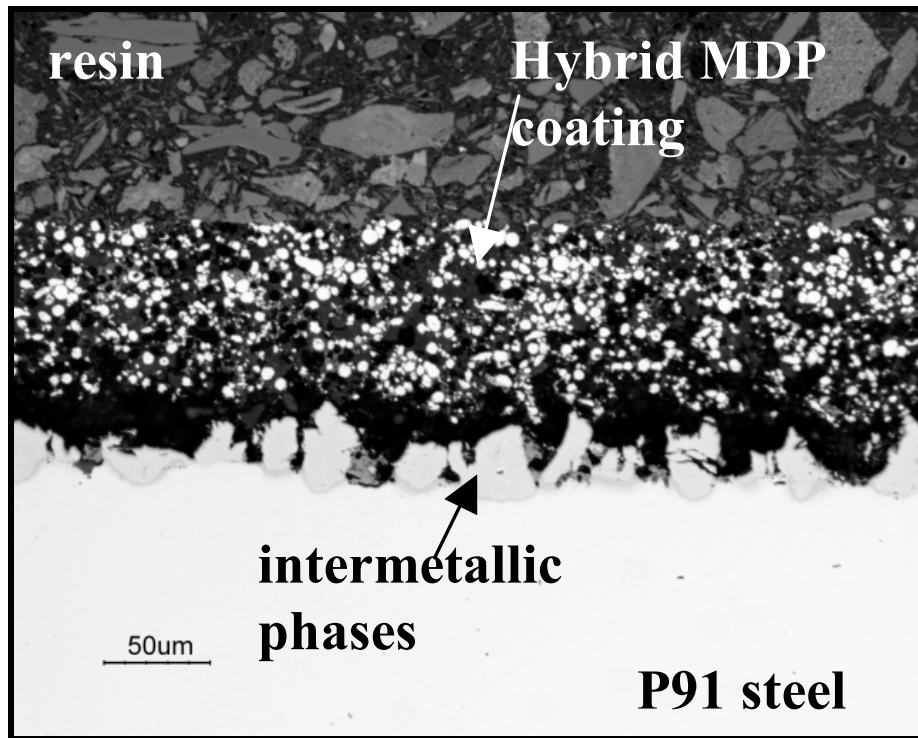


Figure 5. Cross section of coated P91 steel oxidized at 620°C, air, $t = 350$ h.

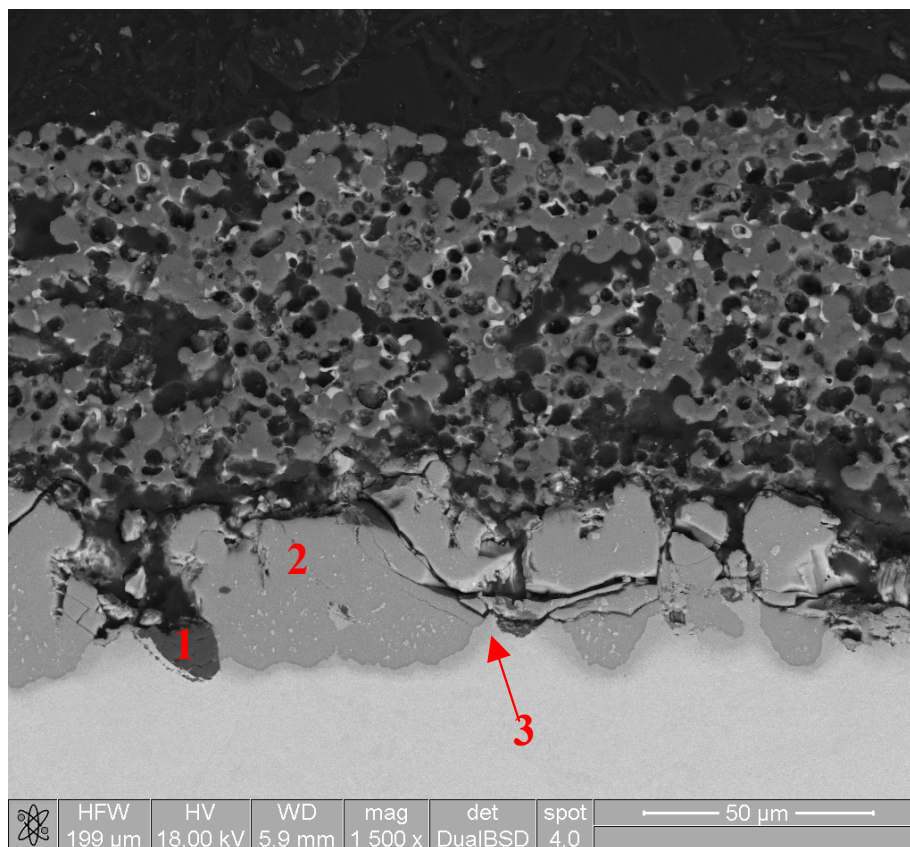


Figure 6. BSE image of coated P91 steel oxidized at 620°C, air, $t = 350$ h.

Table 1. Chemical composition from EDS analysis in at. % at points shown in Fig. 7.

Point	O	Al	Si	P	Cr	Fe
1	58.04	40.51	-	0.77	0.29	0.39
2	3.71	69.58	0.19	0.48	1.85	24.18
3	6.25	36.08	1.2	0.22	9.97	46.28

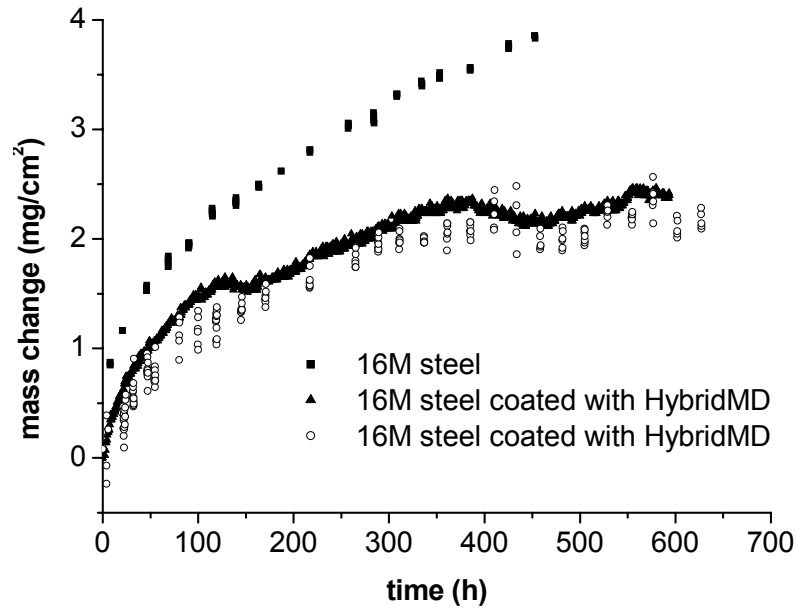


Figure 7. The kinetics of oxidation of 16M steel at 550°C in air.

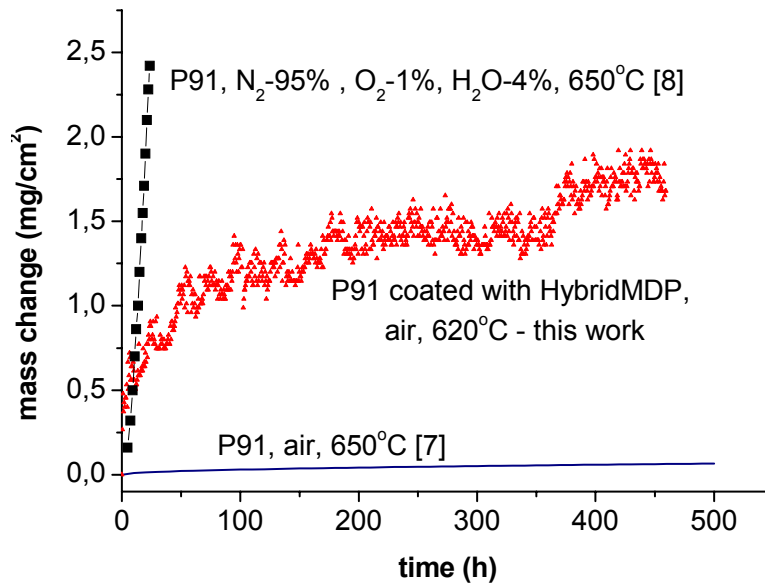


Figure 8. The kinetics of oxidation of steel P91 coated with HybridMDP at 620°C and uncoated steel P91 at 650°C in air [7]. Kinetic of initial stage oxidation of P91 steel at 650°C in N_2 -95%, O_2 -1%, H_2O -4% gas mixture [8].

3.1 Calculations of parabolic rate constant for 16M steel

The kinetics of the oxidation reaction for the 16M was approximated assuming the parabolic rate law:

$$\left(\frac{\Delta m}{S}\right)^2 = k_p'' t + A \quad (1)$$

where Δm denotes the mass change of the oxidized steel, S – surface of the sample, k_p'' – parabolic rate constant, t – oxidation time and A - constant. The calculated apparent parabolic rate constants are shown in Tables 1 and 2.

Table 2. Parabolic rate constants for oxidation of 16M steel at 550⁰C evaluated from thermogravimetric measurements.

The rate constant	0–650 h			Unit
	16M steel without coating	16M steel coated with HybridMD (t = 627 h)	16M steel coated with HybridMD (t = 594 h)	
k_p'' (mass gain)	$8,61 * 10^{-12}$	$2,39 * 10^{-12}$	$2,44 * 10^{-12}$	[g ² /cm ⁴ s]
k_p' (scale thickness)	$2,11 * 10^{-12}$	$5,85 * 10^{-13}$	$5,98 * 10^{-13}$	[cm ² /s]
k_c (metal loss)	$4,75 * 10^{-13}$	$1,32 * 10^{-13}$	$1,35 * 10^{-13}$	[cm ² /s]

Table 3. Oxidation rate constants, initial period excluded.

The constant rates	t > 200 h			Unit
	16M steel without coating	16M steel coated with HybridMD (t = 627 h)	16M steel coated with HybridMD (t = 594 h)	
k_p'' (mass gain)	$8,08 * 10^{-12}$	$1,19 * 10^{-12}$	$1,44 * 10^{-12}$	[g ² /cm ⁴ s]
k_p' (scale thickness)	$1,98 * 10^{-12}$	$2,91 * 10^{-13}$	$3,53 * 10^{-13}$	[cm ² /s]
k_c (metal loss)	$4,46 * 10^{-13}$	$6,57 * 10^{-14}$	$7,95 * 10^{-14}$	[cm ² /s]

Theoretical parabolic rate constant of the scale growth at 550⁰C was estimated on the base of the Wagner model [9]:

$$k_p' = \frac{1}{2} \int_{p_{O_2}'}^{p_{O_2}''} \left(\frac{z_c}{|z_a|} D_{Me}^* \right) d \ln \frac{p_{O_2}}{p_0} = 5,31 * 10^{-13} \text{ cm}^2/\text{s} \quad (2)$$

where: $p_0 = 1 \text{ atm}$ p_{O_2}' - magnetite dissociation pressure p_{O_2}'' - oxygen pressure, z_c, z_a – cation, anion valence D_{Me}^* - iron self-diffusion coefficient.

Dissociation pressure at the steel/oxide interface was calculated from thermodynamic data [10]:

$$p'_{O_2} = p_0 \exp\left(\frac{\Delta G^0}{2RT}\right) = 1,65 * 10^{-27} \text{ atm} \quad (3)$$

Self-diffusion coefficient of the iron was extrapolated from the formula [11]:

$$D = D_0 \exp\left(\frac{-E}{RT}\right) = 1,31 * 10^{-14} \text{ cm}^2/\text{s} \quad (4)$$

where: $D_0 = 5,2 \text{ cm}^2/\text{s}$ $E = 230 \text{ kJ/mol}$.

The thickness of scales formed on 16M steel at a temperature 550⁰C evaluated from kinetic measurements (TG) and determined on the basis of photomicrographs of cross sections of 16M steel is shown in Table 3.

Table 4. The thickness of the scales formed on 16M steel at 550⁰C evaluated from kinetic measurements (TG) and determined on the basis of photomicrographs of cross sections of 16M steel.

Sample	Scale thickness (TG) [μm]	Scale thickness (microsections) [μm]
16M steel coated with HybridMD (t = 627 h)	16	11 \pm 3
16M steel coated with HybridMD (t = 594 h)	16	13 \pm 3
16M steel uncoated (t = 453 h)	26	26 \pm 3

3.2 Calculations of parabolic rate constant for coated P91 steel

The kinetics of the oxidation reaction for the coated P91 steel was approximated assuming the parabolic rate law, Eq. 1. Parabolic rate constants for oxidation of coated P91 steel at a temperature 620⁰C, excluding initial period averages $1,29 * 10^{-12} \text{ g}^2/\text{cm}^4\text{s}$.

4. Discussion and conclusions

Oxidation of coated and uncoated 16M and P91 steels follows the parabolic rate law, Figs. 7 and 8. The initial mass gain during the oxidation of coated P91 and M16 steels is affected by the reaction between coating and oxygen. At 620°C aluminium from coating reacts with P91 steel components, mainly iron, and forms intermetallic phases at the coating|steel interface, Fig. 6. This aluminization process increases the hot corrosion resistance. The further tests are necessary to study the long time evolution of the diffusion zone and the effect of water on P91 oxidation rate.

The laboratory studies on 16M, reported here, together with several observations and the full scale industrial tests, all indicate the stability and protective properties of HybridMD coating, Figs. 9–10.



Figure 9. Photograph of the waterwall tubes coated with HybridMD (two central tubes) after exposure during 8000 h, after washing of deposits.

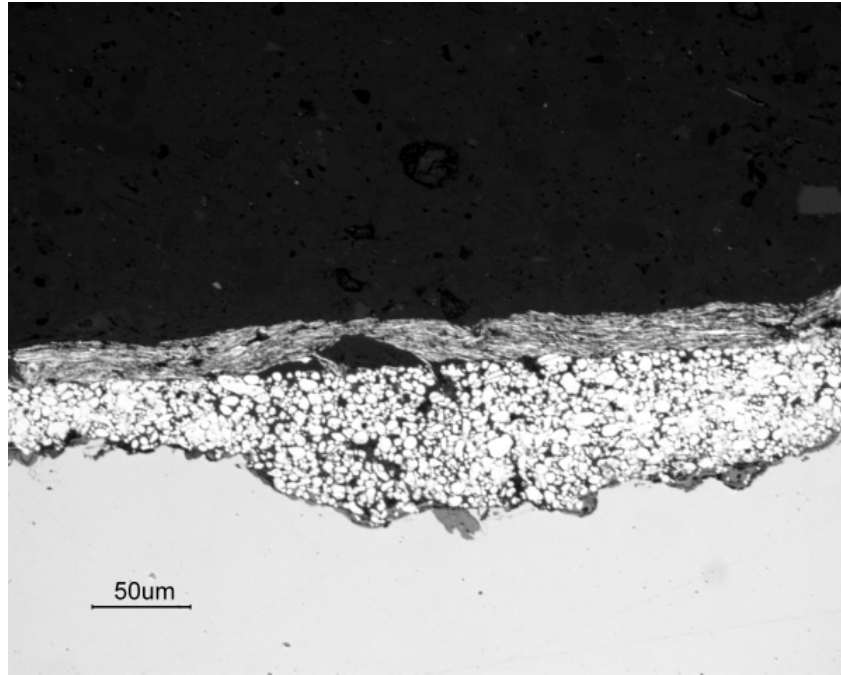


Figure 10. Cross section of HybridMD coated tube after operating time ~ 8000 h in the power station.

The coating reduces rate of magnetite formation on the steel. A good agreement obtained, between the parabolic rate constants values calculated from Wagner model and determined in direct measurements (TG) for 16M steel with HybridMD coating shows that coating provides the stability of the magnetite layer. The oxides growing during the both laboratory tests and during the service form the single-phase, compact scales on metals. The HybridMD coating improves the mechanical properties of the oxide scale (decreases stresses at the Fe/Fe₃O₄ interface).

Acknowledgements

The present work was financially supported by grant no. 28.160.7003, 18.18.160.385.

References

1. Liu, S. i Zhu Z., “Case of Waterwall-Fire-Side Corrosion”, Corros. Sci. Prot. Techn., 11, 1999, 189.
2. Viswanathan R. “Materials technology for coal-fired power plants”, Adv. Mat. and Proc., August 2004, 73.

3. Lepingue V., Louis G., Petelot D., Lefebvre B. and Vaillant J.C., "High temperature corrosion behaviour of some boiler steels in pure water vapour", *Mat. Sci. Forum*, 239, 2001, 369.
4. Lai G., Hulsizer, P. and Brooks R. "Life Extension of Boilers Using Weld Overlay Protection", *Baltica IV*, Techn. Res. Centre of Finland, 1998, 319.
5. Kung S. and Bakker W. "Waterwall corrosion in coal-fired boilers – a new culprit: FeS", *NACE Corrosion 2000*, March 26–31, 2000, Orlando, Florida.
6. Korozja niskiemisyjna, opracowanie dla EDF, 6 maja 2004, Wrocław.
7. Vossen J.P.T., Gawenda P., Rahts K., Rohrig M., Schorr M. and Schutze M. "Limit of oxidation resistance of several heat-resistant steels under isothermal and cyclic oxidation as well as under creep in air at 650°C", *Materials at High Temperature*, 14 (4), 1997, 387.
8. Ehlers J., Young D.J., Smaardijk E.J., Tyagi A.K., Penkalla H.J., Singheiser L., Quadackers, W.J. "Enhanced oxidation of the 9% Cr steel P91 in water vapour containing environments", *Corrosion Science*, 48, 2006, 3428.
9. Wagner C., "Contributions to the Theory of the Tarnishing Process", *Z. Phys. Chem.*, B21, 1933, 25.
10. Barin I., Knaohe O., "Thermochemical Properties of Inorganic Substances", Springer-Verlag, Berlin Heidelberg New York, Verlag Stahleisen m.b.H. Dusseldorf, 1973 oraz suplement z 1977.
11. Danielewski M., "Kinetics of Gaseous Corrosion Processes" w *ASM Handbook Vol. 13A, "Corrosion: Fundamentals, Testing, and Protection"*, S.S. Cramer and B.S. Covino, Eds. (ASM, Materials Park, Ohio 2003), 97.

Hot corrosion and erosion resistance of new coating alloys for biomass and waste boiler heat transfer surfaces

S. Yli-Olli, S. Tuurna, M. Oksa, E. Turunen and T. Varis

VTT Technical Research Centre of Finland, Espoo, Finland

Abstract

In the present work new coating materials have been tested in laboratory conditions simulating high temperature corrosion in biomass boilers and waste incinerators with molten salt deposits. The work also included some thermodynamic modelling and high temperature erosion testing. In the deposit corrosion tests the dense Ni- and Cr-based materials performed somewhat better than iron-based materials in means of corrosion. In the porous coatings corrosion had propagated into the coating through the pores. Inconel 625, as well as some of the other high Ni-materials, had good corrosion resistance, but the coating detached from the low alloy steel substrate material in many cases. Welded materials (MIG, laser) formed a very dense coating and therefore reacted like bulk materials and HVOF coatings were denser than arc sprayed coatings. It can be concluded that tough and dense coatings succeed best in the erosion conditions. However, due to their lamellar structure coatings are very sensitive to the size of erosive particles and the impact angle. The thermodynamic modelling supported quite well the corrosion test results, in spite of some weaknesses in the databases, e.g. content of boron. The new salt database used in some modelling cases gave good results, but should be applied with some caution.

1. Introduction

Problems in power plant boilers, which use biomass and waste as fuel, are often caused by high temperature corrosion especially due to alkali metals and chlorine, and erosion especially in the case of fluidized bed boilers. Fuels used in biomass boilers contain for example wood, straw, agricultural waste, and crops, which may contain high contents of chlorine. Also waste fuel is heterogeneous and causes aggressive corrosion conditions in boilers. High temperature corrosion limits the effective use of both the biomass combustion and waste incineration boilers due to lower steam temperatures. Material wastage is mainly caused by chlorine induced high temperature corrosion and erosion depending on the fuel and boiler type. Critical components for corrosion are heat exchanger surfaces, such as water walls and superheaters. In order to minimize material

related risks, normally used low alloy steels have been replaced with high alloy steels in more aggressive conditions. These alloys normally contain high amount of nickel and chromium for enhancing high temperature corrosion resistance. The high cost and sometimes hard to manufacture bulk materials could be replaced with coatings, which can be applied on the more economical low alloy steel.

Thermal spraying is one possibility to manufacture protective coatings on boiler components. Suitable methods are arc spraying and HVOF, high velocity oxy-fuel spraying. Benefits of the thermal spray coatings are typically lower cost, improved engineering performance, and increased component life. Coating properties can be tailored in order to achieve desired material properties, such as corrosion resistance, erosion resistance, hardness, low friction. Most potential material combinations based on present knowledge are chromium and nickel by good corrosion protection properties mixed with different carbides, which have good properties against erosion. However, as economic point of coatings has to be considered, also iron based materials with chromium alloying were chosen for testing.

The aim of this work was to find durable new coating materials for extreme boiler conditions.

2. Materials and methods

2.1 Test materials

To select right materials a literature survey was made to find out the most suitable candidate alloys for these environments. On the basis of this survey test materials were selected from three different coating materials types iron based materials, nickel based materials and carbide-containing hard metal coatings, they are presented in more detail in Table 1. A short basis for the material selection is described in the following.

For highly corrosive boiler applications iron based coatings need to be alloyed with oxide forming materials, e.g. aluminium or chromium. To improve erosion resistance carbide or boride forming elements are usually added. Typically these coatings are based on 15–25% chromium containing iron matrix with hard chromium, tungsten or boride containing phases. The high hardness of these coatings is based on complex nanoscale or amorphous boride or carbon phases. Commercially known trade marks for iron based boiler coatings with boride or carbide alloying are Armacor and Duocor. These materials have been reported to be promising [2, 3, 4].

Table 1. Tested materials in corrosion and/or erosion tests.

Material	Tech.	Composition [w.%]
TAFA 45CT	Arc	Cr 45, Ti 5, Ni bal.
TAFA/Armacor 95MXC	Arc	Cr 43–46, Si 1.75–2.25, Fe bal.
Nanosteel SHS717	Arc, HVOF	Fe (bal.), Cr <20, Mo <5, W <10, C <2, Mn <5, Si <2, B <5
Durum 580	HVOF	Cr 27.2, Ni 10.7, Mo 3.9, Si 1.4, C 2, Fe bal.
Inconel 625	Arc, HVOF	Ni 58, Cr 21.5, Mo 9, Fe 5, Co 1, Si 0.5, Mn 0.5, Nb 3.65
Amperit 568.1	HVOF	Cr ₃ C ₂ -20NiCr
TiC-Alloy 59	HVOF	Cr 23, Mo 16, Fe < 1, Ni bal.
NiCr	Arc, HVOF	Ni45Cr5Ti
Durmat XDU	Arc	Cr 30; Ni 10; Mo 4; C 2; Fe-bal.
Suna-1	Arc	C 0.9, B 2.8, Cr 22, Mo 1.5, W 1-2
Suna-2	Arc	C 0.9, B 2.8, Cr 22, W 1-2, Mo 1.5
T22	Bulk	Cr 2.5, Mo 1, Mn 0.5, Si 0.3, Fe bal.

Nickel based materials with at least 20% of chromium have been reported to be resistant to high temperature oxidation up to 800°C. To improve the corrosion and erosion resistance of the Ni-20%Cr for boiler applications, are three possibilities [4, 6, 7]:

- a) Increase of the chromium content up to 55%, which improves the corrosion resistance against sulphur and chlorine containing gases and the erosion resistance.
- b) NiCrBSiFe self fluxing alloys. With silicon and boron additions the melting temperature of the alloy is decreased and particle adhesion is improving. The hardness of the coating is increased by formation of chromium boride CrB and complex (Fe, Ni, Cr)-carbo-borides in the alloy. Also other hard phases like WC or Cr₃C₂ can be added to improve hardness.
- c) Alloying with other phase constituents like molybdenum or aluminium. Molybdenum improves the stiffness and aluminium improves oxidation resistance and self fluxing properties of the alloy.

NiCr-coatings have been reported to protect of the base material against molten salts and chlorine gases with good results. In very high chloride containing environments the thermally sprayed coatings can suffer from chloride attack through oxides and voids at the splat boundaries and the coating can be destroyed

rapidly. Fusing treatment might improve the corrosion resistance, but then the alloying should be optimised for fusing [2].

The erosion resistance of NiCr-coatings is limited. The erosion resistance can be improved by two different ways: adding hard particles e.g. WC in the NiCr-matrix, or increase the stiffness of coating by adding molybdenum. For high bed particle impact energy the increase of stiffness seems to be the more effective. This method is in other way also better since by adding hard particles the cracking tendency of coating is increases.

The carbide coatings containing Cr_3C_2 , WC or TiC are defined as hard metal coatings. WC-CoCr and Cr_3C_2 -NiCr are standard HVOF sprayed coatings against erosion. TiC is often mentioned as an option for oxidation resistant carbide but the actual solutions are rare. There are several factors affecting the properties of hard metal coatings e.g:

- Size of the carbides and how evenly the carbides are distributed in matrix.
- Matrix composition and content, especially chromium.
- Density and adhesion of splats.

Although the erosion resistance of WC-Co -coatings is excellent, the material has poor high temperature resistance. WC-CoCr -coatings are not recommended for use over about 500°C , because of possible oxidation and decarburisation. The oxidation resistance of WC-coatings is strongly dependent on matrix.

It is reported that HVOF-sprayed Cr_3C_2 -NiCr has the best wear resistance at boiler tubes if the amount of chlorine in ash is low [8]. Normally Cr_3C_2 -NiCr coatings are brittle and therefore erode by cracking and chipping. The predominant development trend, to overcome the consequences resulting from coating brittleness, is carbide size reduction. Chlorine has found to accelerate strongly the wear rate of Cr_3C_2 -coatings comparison with the NiCr-coatings. Cr_3C_2 -coatings are not recommended against high chlorine environment, which often occurs in biomass burning boilers. Cr_3C_2 -coatings could be suitable for boilers with erosive but low (especially Cl) corrosion environments.

2.2 Coating techniques

2.2.1 Arc

Arc sprayed coatings were manufactured by Sulzer Metco, Smart Arc equipment. Coatings were sprayed onto a 5 mm thick 10CrMo substrate. Parameters were optimized in order to produce relatively fine lamella size. In arc spraying the feedstock material is in the form of wire and material is melted in electric arc. Melted material is blown to the surface by atomising air. The spray particle temperature is therefore controlled by combination of arc voltage and current.

Particle velocity is affected by atomising air velocity, which is controlled by the nozzle shape and atomising air pressure. In arc spraying selected parameters (arc, voltage and atomising air pressure) determine also the size distribution of spray particles which affects on coating properties. The main goal for parameters selection was to achieve constant arc burning, but fine tuning of parameters were performed to produce relatively fine lamella size. In arc spraying spray particle velocity is relatively low, which means relatively high porosity level on produced coating.

2.2.2 HVOF

HVOF spraying were done by Sulzer Metco, Diamond Jet Hybrid spray equipment by using propane or hydrogen as a fuel gas. Main advantage by using HVOF is the improved coating density compared to arc spraying. In coating production the parameters were selected to minimize oxidation of spray particle during coating.

2.2.3 Laser treatment

Arc spraying was used for manufacturing of the coating for laser glazing. The manufactured coating was Ni20%Cr. Laser treatment was performed with 3kW diode laser with 22 x 5 mm optics. The goal of the laser glazing was to remelt the surface of the coating and eliminate any open porosity.

2.3 High temperature corrosion and erosion tests

The high temperature corrosion tests were made at VTT's high temperature corrosion test furnaces with and without deposits. The tests were made to simulate an actual situation in boilers, where molten salt deposits corrode the tubes. The tests cycles that lasted for 168 h are illustrated in Table 2. Test conditions 1 and 2 are taken from the EFC 14 [9] testing standards for high corrosion testing in waste incinerator conditions.

Table 2. The test conditions for high temperature screening tests.

No.	Temp.	Gases	Water vapour
1	400°C	1000 ppm HCl + N ₂ , 1% SO ₂ + air	2.5% H ₂ O
2	550°C	1000 ppm HCl + N ₂ , 1% SO ₂ + air	2.5% H ₂ O
3	550°C	2000 ppm SO ₂ + air	15% H ₂ O
4	550°C	2000 ppm HCl + air	15% H ₂ O

The deposit tests were made in the same atmosphere as tests 1 and 2 (2.5% H₂O + 1% SO₂ + 0.1% HCl + air), at 550°C. Test durations were 168 h and 504 h. The applied deposit was alkali chloride – alkali sulphate salt mixture of eutectic composition, which forms molten phase in 520–530°C:

6.5 w-% NaCl; 59 w-% Na₂SO₄; 34.5 w-% KCl.

Erosion tests were performed in two different test arrangements, the other pure erosion (tests 1 & 2) and the other simulating erosion conditions in fluidized bed boiler (test 3). The used test conditions are presented in Table 3.

Table 3. Performed erosion tests.

No.	Temp.	Abrasive	Gas	Impact angle	Velocity
1	20°C	3 kg aluminium oxide, particle size 100–300 µm	Air	30° and 90°	80 m/s
2	650°C	3 kg aluminium oxide, particle size 100–300 µm	Air	30° and 90°	80 m/s
3	550°C	Quartz sand	Air		

2.4 Thermodynamic modelling

Modelling was carried out with the FactSage program. The time for reaching the equilibrium cannot be told from thermodynamic calculations, but they give an idea of what to expect when the reaction has reached a stable state. The predicted corrosion products of the selected materials can be read from these stability diagrams.

3. Results and discussion

In the high temperature corrosion tests without deposits, no significant differences were observed between the testes coating materials. The high temperature deposit corrosion test simulated very aggressive conditions, which may occur in biomass boilers or waste incinerators, especially in the superheater area. Quantitative comparison between different coatings could not be performed, because mass loss or gain could not be measured since only one side of the samples had been coated.

The surface of the iron-based Suna-1 material had reacted slightly in the deposit tests. Approximately a 25 µm thick reaction layer could be detected that consisted of iron, sulphur, sodium, potassium, chromium and oxygen. The higher

Cr and Ni containing materials Suna-2, Durmat XDU, Armacor M and Nanosteel SHS717 reacted in similar way (Figure 1 and 2).

The substrate material, low alloy steel T22, had corroded quite strongly under exposure, as can be seen in Figure 1c). The linear corrosion rate for 10CrMo would be approximately 3.3 mm/a. The oxide layer on 10CrMo consisted of iron, chromium, sulphur and chlorine. This proved that the conditions were extremely corrosive.

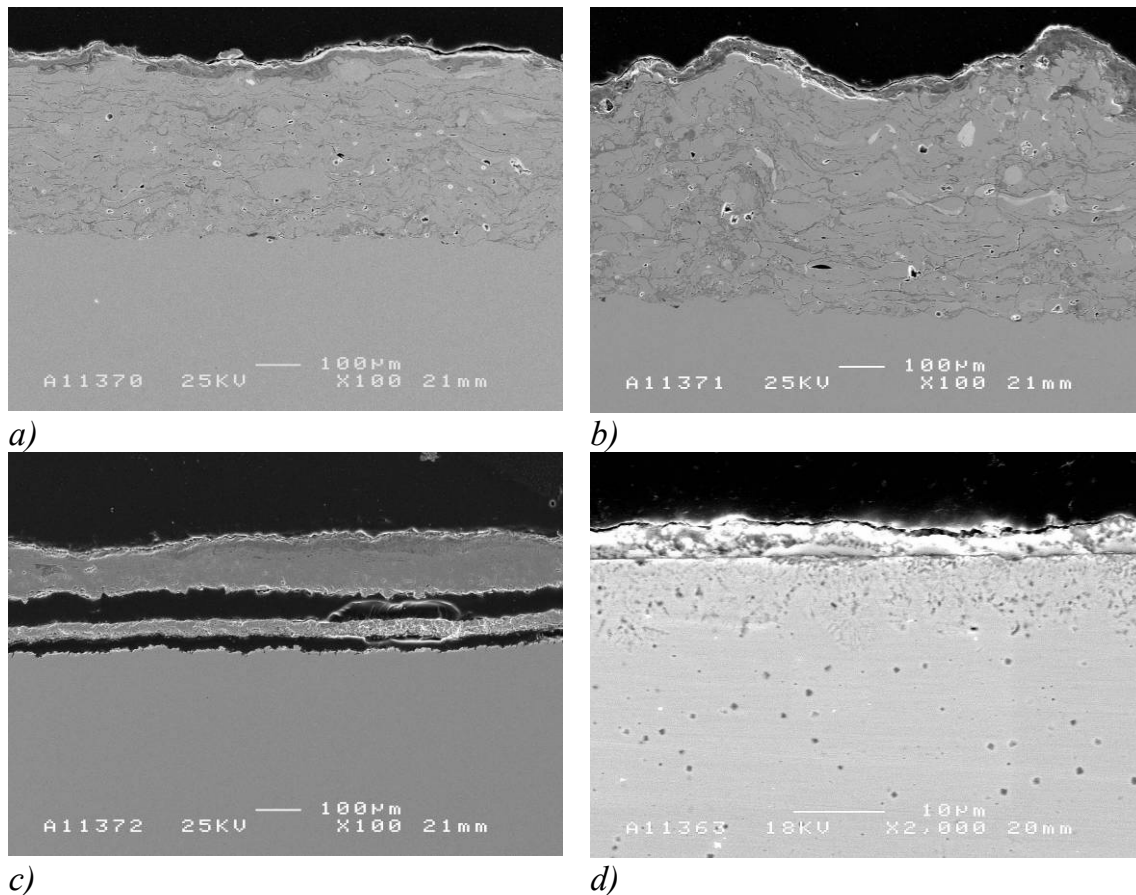


Figure 1. Scanning electron micrographs of cross-sections of the tested samples. a) Suna-2; b) Durmat XDU-2005238; c) substrate material 10CrMo after 168 h; and d) surface of NiCr laser coating after 504 h exposure.

In the NiCr laser coating some selective corrosion was detected on the coating surface. Chromium oxide layer, about 5 µm thick, containing also sulphur was formed on the surface, see Figure 1 d) and Figure 2 a). Chromium depletion can also be seen to a depth of 15 µm from the coating surface, this makes the coating more vulnerable for corrosion (Figure 1 d). Depletion is dangerous if the protective oxide on the surface detaches or cracks for some reason the weakened zone will be under attack and it will not have the same ability to form a protective layer. It is also possible the when the oxide grows thick the temperature at the metal oxide interface increases so that molten corrosion

products may form. These molten phases might lead to internal corrosion. Figure 2 shows the influence of the coating mechanism on the lamellar structure. From the arc sprayed coating chlorine was detected from the coating substrate interface, which in this case has led to delamination of the coating.

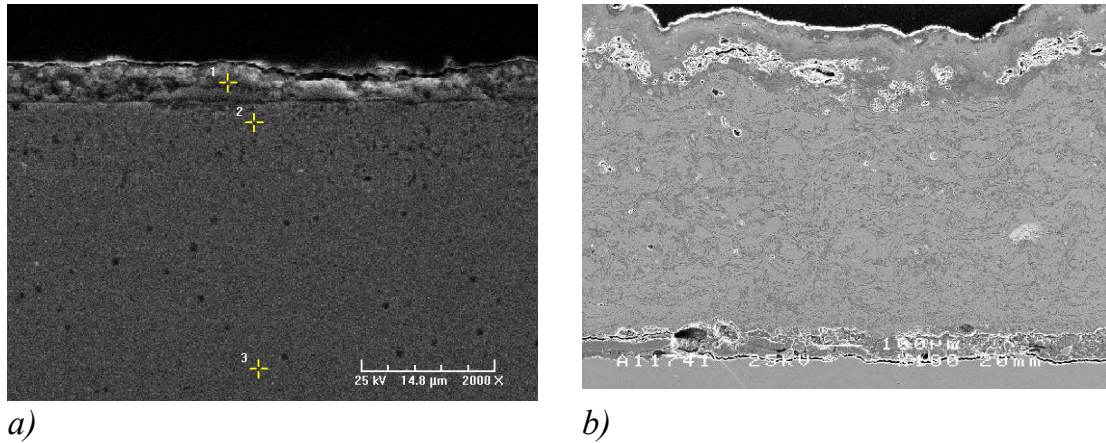


Figure 2. a) Outer surface of NiCr laser coating after 504 hours deposit exposure. b) Arc sprayed NiCr coating analysis from the coating substrate interface.

Inconel 625 had a thin reaction layer in the coating surface containing Cr, S, Ni and O. The problem with Inconel 625 was delamination of the coating from the substrate (Figure 3), which could also be seen in the previous tests. In some cases an iron oxide layer was detected from the coating and substrate interface, but in most cases no corrosion products were found. The delamination can be caused by thermal stresses, a CTE difference of the coating and the substrate or by formation of corrosion product on the interface.

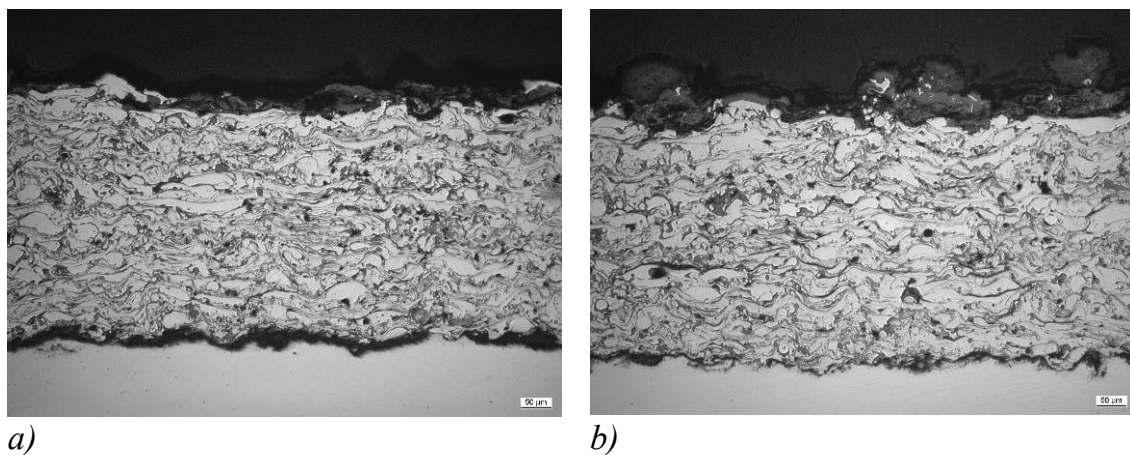


Figure 3. Arc sprayed Inconel 625 after a) 168 h and b) the 504 h deposit test.

The carbide containing materials had a thin, 10–20 μm, reaction layer of Cr, S, Na, K and Ni (if present in the coating) on the surface. Some of the coatings were

also porous and corrosive agents had infiltrated the structure through the pores on the surface of the coating (Figure 4).

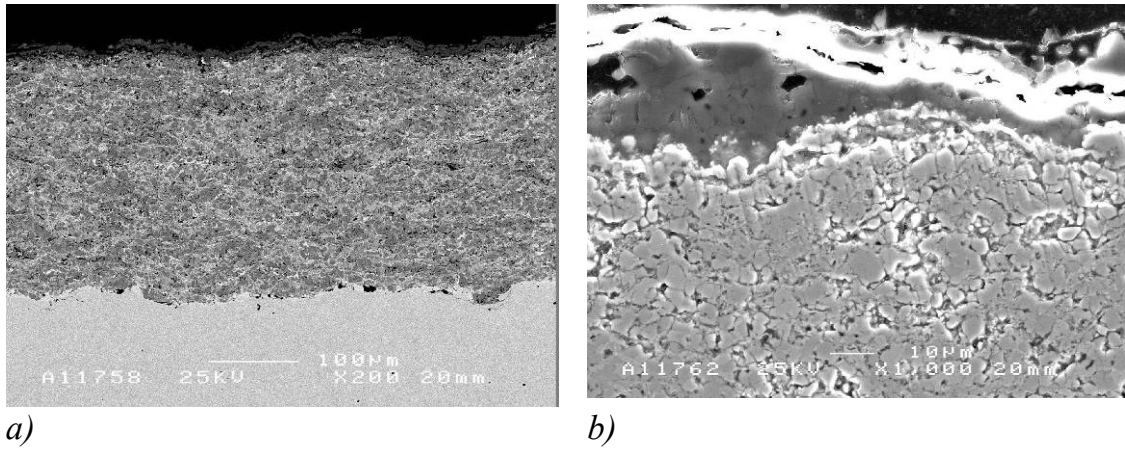


Figure 4. HVOF sprayed Cr_3C_2-NiCr after the 504 h deposit test a) x20 and b) x1000 magnification.

The iron based materials endured corrosion surprisingly well (Figure 5) although the coating structure wasn't as good as it could have been. There was an approximately 10–15 μm reaction layer on top of the coating but similar and even thicker layers were observed on the other materials.

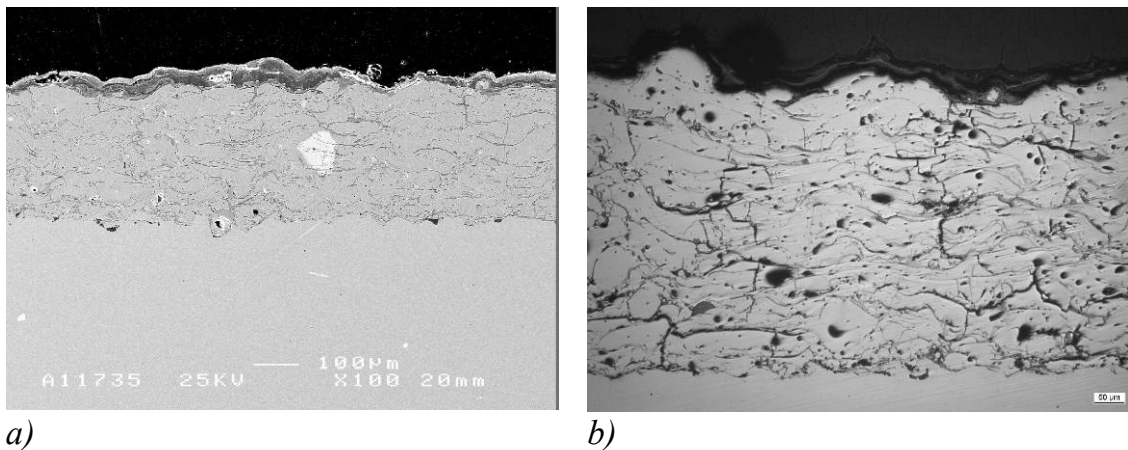


Figure 5. Arc sprayed a) Armacor M and b) Nanosteel SHS 717.

In erosion tests the mass change of the samples was detected. The results are presented in Table 4 and Table 5. The hardness of the coatings was measured before and after the testing. The measured average hardness's of the tested materials are presented in Table 6. Some of the coatings were very hard and brittle before the testing (marked with * in the table). The hardness of the tested samples changed during the testing, apparently due to densification caused by high temperature.

Table 4. Results of erosion tests 1 and 2 in room temperature and in 650 °C (WL = weight loss).

Material	Spray	Thickness [μm]	20°C/30° WL [μg]	20°C/90° WL [μg]	650°C/30° WL [μg]	650°C/90° WL [μg]
NiCr45CT	Arc	450	28.57	36.47	28.20	36.80
Suna-1	Arc	400–450	36.00	103.47	25.23	49.10
Armacor 95MXC	Arc	400–450	47.8	141.97	23.87	28.37
Durmat XDU	Arc	400–450	40.03	109.33	42.27	87.70
Inconel 625	Arc	450	22.30	34.43	36.80	51.50
Durum 580	HVOF	260	25.50	59.40	23.53	43.10
Cr ₃ C ₂ -NiCr	HVOF	280	17.30	51.30	14.37	55.20
Ref. St. 45	Bulk	-	18.63	10.73	-	-
Ref. St. 35	Bulk	-	18.93	9.73	-	-
Ref. Al.316	Bulk	-	-	-	26.70	10.53

Table 5. Results of the fluidized bed erosion test 3 in 550 °C (WL = weight loss).

Material	Spray	Thickness [μm]	550°C WL 1 [μg]	550°C WL 2 [μg]	Average WL [μg]
NiCr45CT	Arc	450	0.0660	0.1254	0.0957
Suna-1	Arc	400–450	0.0427	0.0723	0.0575
Armacor 95MXC	Arc	400–450	0.0531	0.0901	0.0716
Durmat XDU	Arc	400–450	0.1753	0.2524	0.21385
Inconel 625	Arc	450	0.0538	0.0796	0.0667
Durum 580	HVOF	200	0.0060	0.0158	0.0109
Cr ₃ C ₂ -NiCr	HVOF	290	0.0147	0.0158	0.01525
Durum 580	HVOF	260	0.0232	0.0161	0.01965

Table 6. Hardness (Vickers, 300 g) before and after erosion testing in 650 °C.

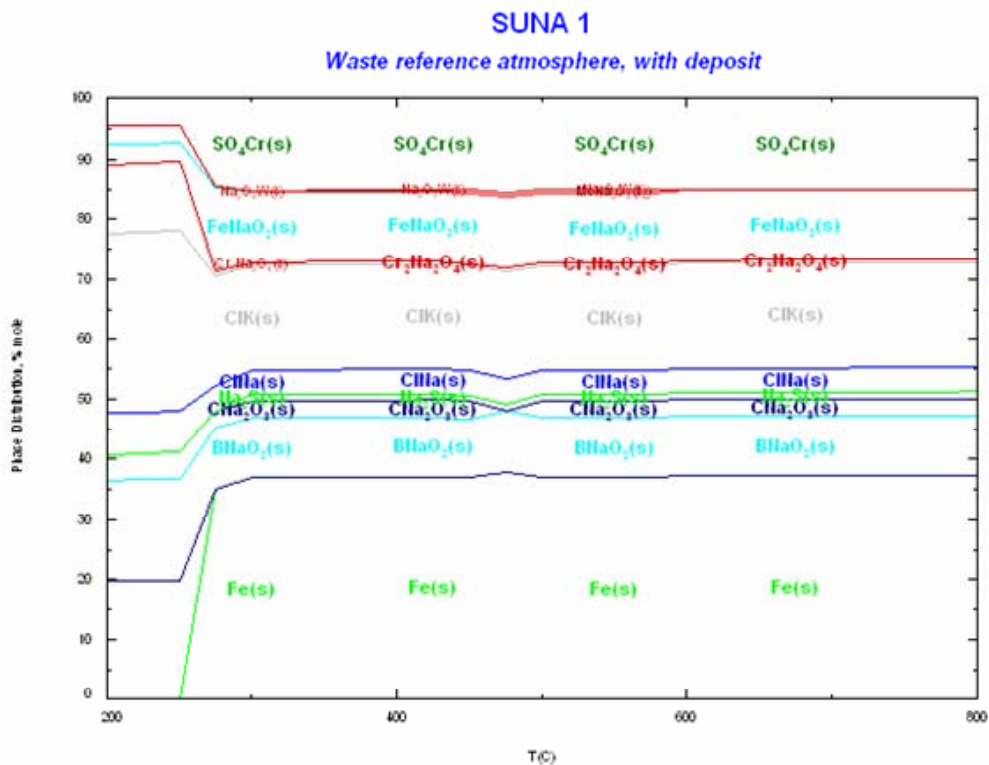
Material	HV Before	HV After	HV Change	Hardness
NiCr45CT	387	506	-119	Increased
Suna-1	1152	833	319	Decreased
Armacor 95MXC	1011*	789	222	Decreased
Durmat XDU	1194*	1093	101	Decreased
Inconel 625	432	449	-17	Increased
Durum 580	699*	700	-1	Increased
Cr ₃ C ₂ -NiCr	907	921	-14	Increased

* a brittle coating

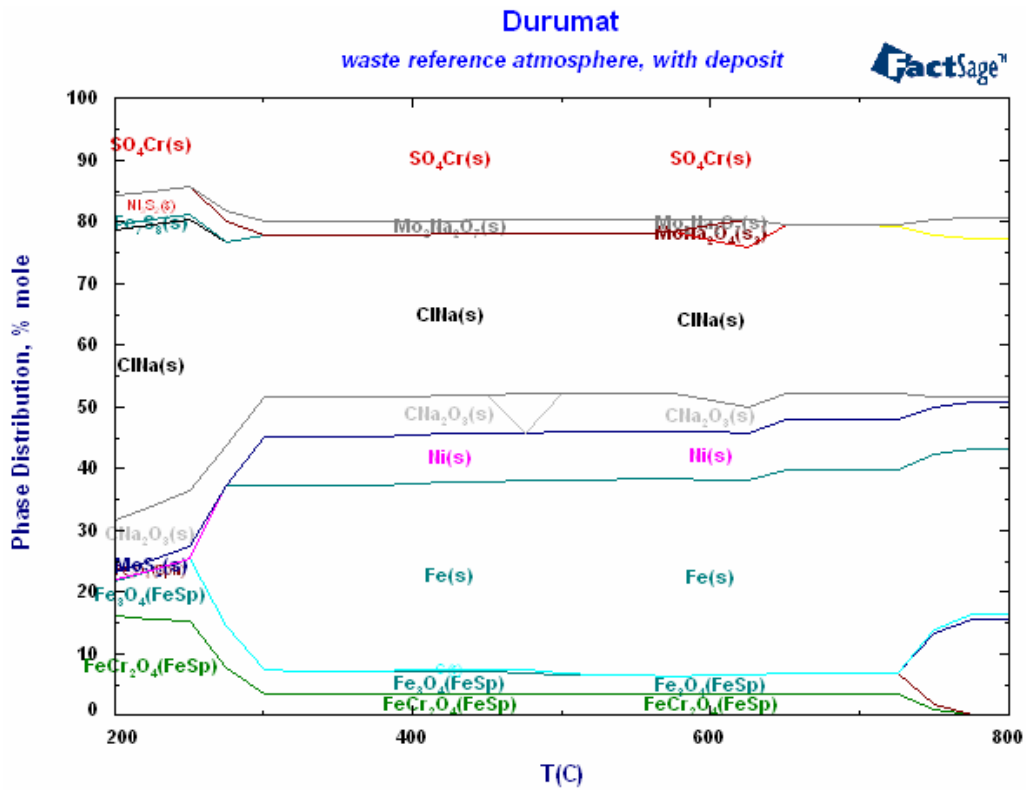
It could be seen that the coatings performed better when the impact angle was indirect, but the bulk reference was better with a direct angle. This is mainly due to the lamellar structure of the coatings. During the tests at high temperatures some of the iron based coatings toughened, which improved the materials erosion resistance. Open question remains, whether the toughening of the iron-based materials is sufficient enough in the lower temperatures (than 650°C), as is case in waste incinerators.

In all tests Durum 580 was in the best five materials, especially it performed well in the fluidized bed erosion test. High chromium steel Armacor M had good high temperature erosion resistance, as it apparently toughened due to temperature. Coating NiCr45CT succeeded uniformly in the erosion tests, but didn't stand out in any one of them. The carbide material (Cr₃C₂-20NiCr) had excellent resistance in fluidized bed erosion test, but it is very sensitive to the erosion angle.

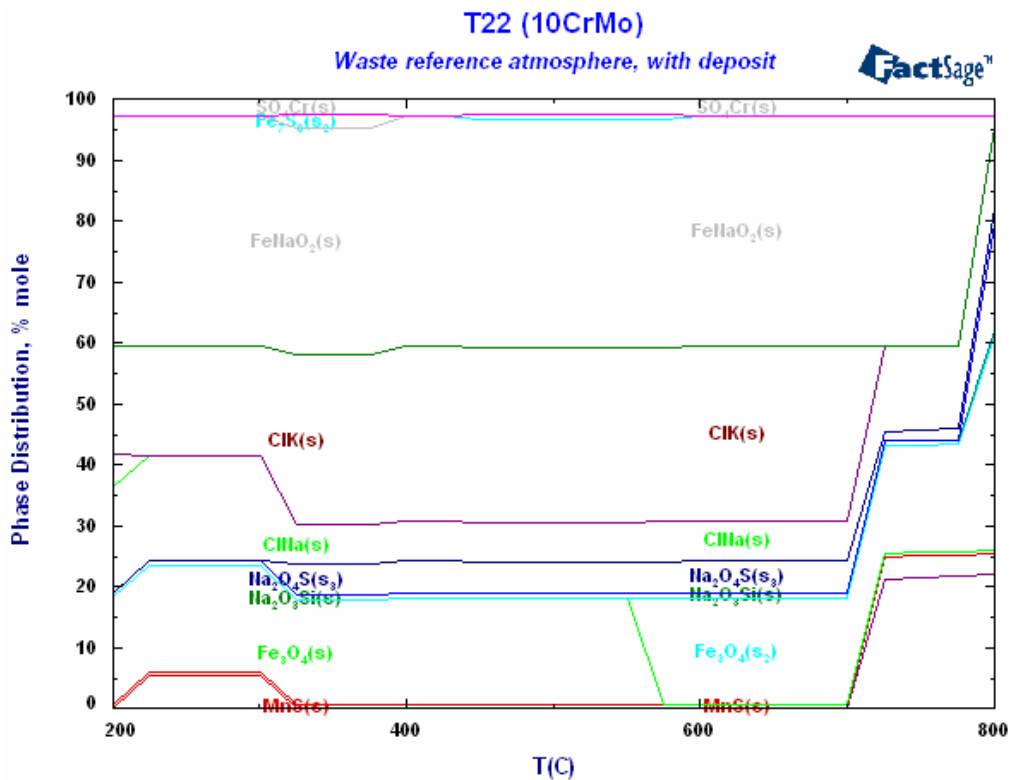
In Figure 6 are presented thermodynamic calculations made by FactSage, with the test deposit (Eq. 1) in the waste reference atmosphere (test condition 1, Table 1) of materials SUNA 1, DURMAT and T22 as reference. The figures show the phases at stable state. As can be seen alkali metals (especially sodium) are very reactive, but the large amount of FeNaO₂ in T22 raises a doubt of the reliability of the calculations when sodium is present. Otherwise the calculations seem adequate also when compared to results from the corresponding laboratory tests. The formations order of the compounds can not be seen from these calculations.



a)



b)



c)

Figure 6. Phase distribution diagrams of selected materials in the waste reference atmosphere with deposit.

4. Conclusions

In the deposit corrosion testing the dense Ni- and Cr-based materials performed slightly better than iron-based materials in terms of corrosion resistance. In the longest deposit test a clear corrosion reaction layer formed on the surface of the iron-based materials. The formed corrosion product layer was thinner on the Ni-, Cr-, and carbide based materials, but the structures were more often porous. In the porous coatings corrosion had propagated into the coating through the pores. Particularly strong deterioration occurs when chlorine is trapped in these pores, as was seen with some of the carbide containing coatings.

Inconel 625, as well as some of the other high Ni-materials, showed good corrosion resistance, but the coating detached from the low alloy steel substrate material in many cases, probably because of the differences in coefficients of thermal expansion. Welded (MIG, laser) materials formed a very dense coating and therefore reacted like bulk materials. HVOF coatings were denser than arc sprayed coatings, but both thermal sprayed coating types had superior corrosion resistance in comparison with the low alloy steel T22 (10CrMo910) used as reference material. More work is needed to be done to better understand these corrosion mechanisms of different types of coatings.

In the erosion tests HVOF sprayed Durum 580 was the best coating material. Also Armacor M and NiCr coatings had good erosion resistance. Iron-based coatings softened and toughened at the test temperature, which explains their improved erosion resistance. In conclusion tough and dense coatings succeeded best in the erosion conditions. However, due to their lamellar structure coatings are very sensitive to the size of erosive particles and the impact angle.

The thermodynamic modelling supported quite well the corrosion test results, in spite of some weaknesses in the databases, like with high contents of boron. The new salt database used in some modelling cases gave good results, but should be applied with some caution. To conclude, at the present the thermodynamic modelling tools can assist in screen testing, planning of test conditions, life assessment and analysis of test results. With improved databases these tools could also be used to assist in materials selection. The tools should be developed to take the kinetics of the studied reaction to account, so that also the corrosion rates and material lifetime could be predicted.

Acknowledgements

The work has been done in the EU project Protective coatings with combined monitoring system to control process conditions in boilers PROCOMO 1.

References

1. EU project 513023 “Protective coatings with combined monitoring system to control process conditions in boilers” PROCOMO, 1.9.2004–31.12.2006.
2. Uusitalo, M.A., Vuoristo, P.M.J. and Mäntylä, T.A. Elevated temperature erosion-corrosion of thermal sprayed coatings in chlorine containing environments. *Wear* 9069 (2002), pp. 1–9.
3. Totemeier, T.C., Wright, R.N. and Swank, W.D. Microstructure and Stresses in HVOF Sprayed Iron Aluminide Coatings. *Journal of Thermal Spray Technology*, 11(3) September (2002), pp. 400–408.
4. Wang, B.Q. and Seitz, M.W. Comparison in erosion behavior of iron-base coatings sprayed by three different arc-spray process. *Wear* 250 (2001), pp. 755–761.
5. Higuera Hidalgo, V., Belzunce Varela, J., Carriles Menéndez, A. and Poveda Martínez, S. High temperature erosion wear of flame and plasma-sprayed nickel-chromium coatings under simulated coal-fired boiler atmospheres. *Wear* 247 (2001), pp. 214–222.
6. Uusitalo, M.A., Vuoristo, P.M.J. and Mäntylä, T.A. High temperature corrosion of coatings and boiler steels in oxidizing chlorine-containing atmosphere. *Materials Science and Engineering A346* (2003), pp. 168–177.
7. Sidhu, B.S. and Prakash, S. Evaluation of the corrosion behaviour of plasma-sprayed Ni₃Al coatings on steel in oxidation and molten salt environments at 900°C. *Surface and Coatings Technology* 166 (2003), pp. 89–100.
8. Wang, B.-Q. and Verstak, A. Elevated temperature erosion of HVOF Cr₃C₂/TiC-NiCrMo cermet coating. *Wear* 233–235 (1999), pp. 342–351.
9. Guidelines for methods of testing and research in high temperature corrosion, European Federation of Corrosion Publications (EFC) Number 14, H.J. Grabke and D.B. Meadowcroft (Eds.). The Institute of Materials 1995. 224 p.

Studying the effect of the elements Ce and Cr on the high-temperature oxidation behavior of low-Cr steels

V.B. Trindade^{1*}, U. Krupp², H.-J. Christ¹, S. Tuurna³,
L. Heikinheimo³ and M. Arponen⁴

¹Institute for Materials Science, University of Siegen, Germany

²Faculty of Engineering and Computer Sciences, University of Applied Sciences
Osnabrück, Germany

³Materials Performance, VTT Technical Research Centre of Finland, Espoo, Finland

⁴Rautaruukki Oyj, Finland

* corresponding author: vicente@ifwt.mb.uni-siegen.de

Abstract

The oxidation behavior of steels containing low-Cr concentrations (0.5–2.25 wt.%) has been studied in laboratory air in the temperature range of 400–550°C. The oxidation rate of the steels were lower than that of pure iron, but higher than that of pure iron when a small amount of rare earth element cerium (0.03 wt.%) is added to the steel 2.25Cr1Mo. The mass change follows a nearly parabolic law for the case of pure iron and the steel without Ce addition, while linear behavior describes the oxygen uptake for the case of the steel 2.25Cr1Mo+0.03Ce. SEM cross section observations and thermodynamic calculations confirm that there is no wustite (FeO) formation during oxidation of pure iron and low-Cr steels at 550°C, whereas FeO might be formed in the oxide scale of 2.25Cr1Mo+0.03Ce at the same oxidation conditions (temperature, atmosphere and exposure time). By investigating the temperature for FeO stability, this study reveals that the temperature for FeO formation on pure iron is 568°C, for the steel 2.25Cr1Mo 589°C, and 471°C for the steel 2.25Cr1Mo+0.03Ce. This low value for the FeO stability temperature found for the steel 2.25Cr1Mo+0.03Ce explains why this steel oxidizes very fast at 550°C.

1. Introduction

The global pressure for recycling and ecological energy production increases steadily in combination with the demand of cost-effective application of materials. However, some severe corrosion problems, associated with the high internal/intergranular corrosion rates in boiler components, need to be avoided.

For high-temperature applications in power plants, Fe-base alloys, normally containing the alloying elements Cr and Ni, are mainly used for boiler components, e.g. high-alloy steels for super-heaters and low-alloy steels for exhaust systems, because they provide a reasonable combination of mechanical properties, corrosion performance and the corresponding cost as compared to other high-temperature materials.

Low-alloy steels are used as part of boiler components for non-heated exit areas in superheater tubes and reheater tubes. The external surface of these tubes are exposed to air at temperatures between 500–600°C, which lead to a thickness loss of the tubes as a consequence of oxide formation. In spite of the numerous investigations on the oxidation of iron-alloys, basic questions concerning the oxidation mechanisms are still open. Some studies reported that oxides on low-alloy steels grow mainly by outward Fe diffusion [1–3], because the diffusion coefficient of Fe in iron oxides is much higher than that of oxygen [4–6]. Even with lower diffusivity of oxygen within the bulk oxide, some investigations [7–10] pointed out that inward oxidation may take place due to fast oxygen diffusion along grain boundaries of oxides. Others studies [11–14] proposed the possibility of molecular oxygen permeation through microcracks and/or pores within the oxide scale, which leads to inward oxide growth.

Some classical investigations have been performed on the high temperature oxidation of pure Fe in air or oxygen [15–17], Chen *et al.* [18] give a detailed review. It is well established that the high temperature oxidation kinetics of Fe follows basically the parabolic rate law. A two-layer scale composed of magnetite (Fe_3O_4) and hematite (Fe_2O_3), with the thickness ratio being about 4:1, forms up to about 570°C, and a three-layer scale composed of Wustite (FeO), magnetite and hematite, with thickness ration being 95:4:1, is observed at higher temperatures. The formation of the thick wustite layer upon higher temperature exposure is due to the higher diffusion coefficient of Fe and O in FeO as a consequence of a high vacancy concentration compared with hematite and magnetite [19–22].

The main objectives of the present study are to understand and quantify the effect of the grain size of the substrate on the oxidation behaviour of pure iron and low-alloy ferritic steels, and to investigate the effect of cold working, thermal cycling and the addition of Ce on the oxidation kinetics of low-Cr steels.

2. Materials and Experimental Procedure

In this study the oxidation behavior of three low-Cr steels and pure iron at high temperature was investigated. In addition of the standard compositions listed in Table 1, steel 2.25Cr1Mo was modified through the addition of 0.03 wt.% of the rare earth element cerium.

Table 1. Nominal chemical composition (in wt. %) of the low-Cr steels used.

Steel	Cr	C	Si	Ni	Mn	Mo	Al	Cu	Fe
71518	0,55	0,07	0,36	0,21	1,01	---	0,04	0,39	Rest
X60	1,43	0,06	0,22	0,04	0,69	---	0,05	0,01	Rest
2.25Cr1Mo	2,25	0,09	0,23	0,44	0,59	0,96	0,01	0,15	Rest

The grain sizes of the three commercial steels were modified by applying a heat treatment at 1050°C in inert gas atmosphere for different time. Fig. 1 shows the change of the grain size with heat treatment for the steel 2.25Cr1Mo. The microstructure consists basically of ferrite. Carbides are also present, but the volume is small due to the low carbon content. The grain size was measured using the mean linear intercept technique.

In order to investigate the effect of cold working on the oxidation behaviour of the low-alloy steel 2.25Cr1Mo, different rolling steps were performed on annealed specimens. Four cold working states were studied (thickness reduction: 4%, 12%, 20% and 70%).

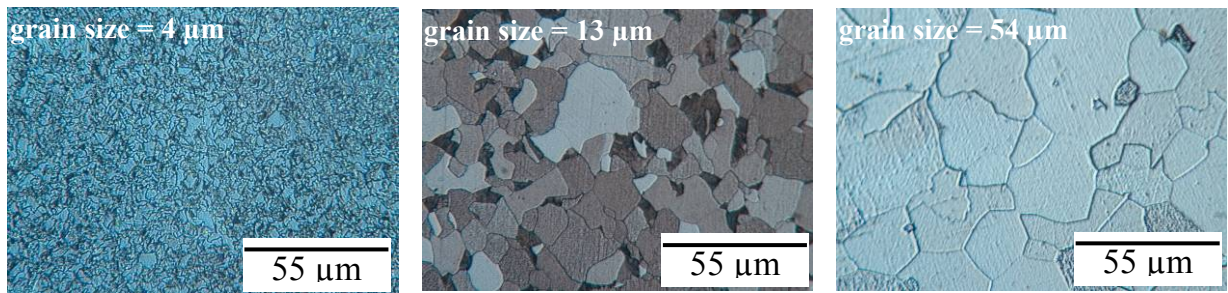


Figure 1. Optical microscopy observation of the microstructure of the 2.25Cr1Mo before and after annealing in inert atmosphere for grain size change.

Samples with dimensions 10 x 10 x 3 mm³ were used for the thermogravimetric study. The samples were ground using SiC paper down to 1200 grid. They were finally cleaned ultrasonically in ethanol prior to oxidation. A hole of 1 mm diameter served for hanging the samples in a thermobalance by means of a quartz thread. Isothermal and thermal cycling thermogravimetry was carried out using a microbalance of a sensibility of 10⁻⁵ g in combination with an alumina chamber and a SiC furnace. The exposure temperature varied from 400°C to 800°C. After oxidation, the specimens were embedded in epoxy and carefully polished using diamond paste down to 1 μm and cleaned ultrasonically in ethanol. Analysis of the oxide structure and thickness measurements of oxide layers were performed using scanning electron microscopy (SEM) in combination with energy-dispersive X-ray spectroscopy (EDX) and X-ray diffraction (XRD).

3. Results and Discussions

Fig. 2a shows the oxidation kinetics of pure iron exposed at 550°C to laboratory air. The oxides formed on pure iron at 550°C are those expected by the thermodynamic calculation, i.e. Fe₃O₄ in contact with the substrate and Fe₂O₃ in the outer region. Fig. 2b shows a scanning electron micrograph of the two layers on the sample surface.

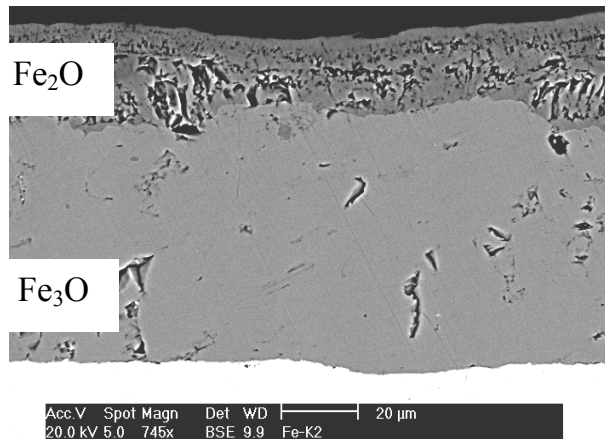
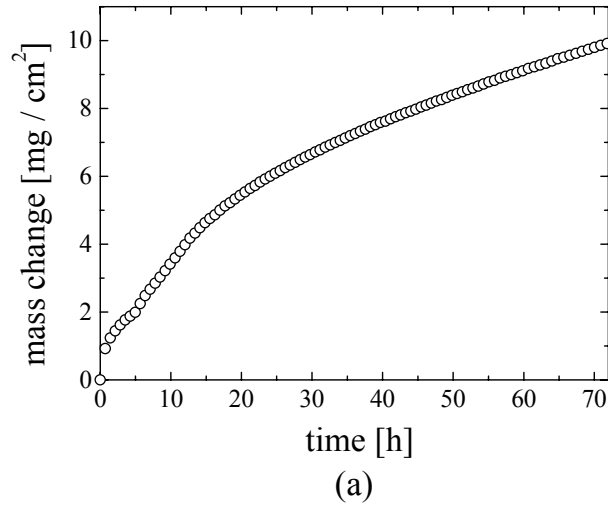
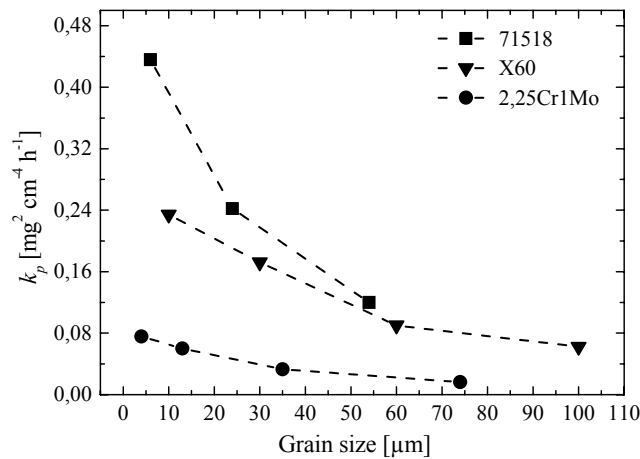


Figure 2. (a) Mass change as a function of time for pure iron at 550°C for 72 h; (b) cross-section of the scale formed on the surface of pure iron at 550°C for 72 h.

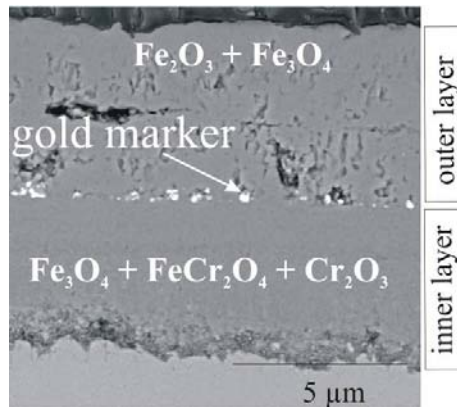
The effect of Cr content and grain size of the steels are shown in Fig. 3. The parabolic rate constant (k_p) was calculated from thermogravimetric measurements using Eq. 1.

$$\left(\frac{\Delta m}{A}\right)^2 = k_p t \quad (1)$$

As shown in Fig. 3a the oxidation kinetics decreases strongly as the grain size of the substrate increases. The decrease in the oxidation kinetics can be attributed to the reduction of the inner oxide layer growth kinetics (see Fig. 3b) [23, 24]. For the three low-Cr steels the thickness of the inner scale differs considerably after 72 h of oxidation in laboratory air at 550°C as a function of the grain size of the substrate changing from 4 μm to 100 μm. Measurements of the total scale thickness revealed a very small change in the thickness of the outer layer. The increase in Cr-content from 0.5 wt.% (steel 71518) to 2.25wt.% (steel 2.25Cr1Mo) has a strong beneficial effect on the oxidation resistance.



(a)



(b)

Figure 3. (a) Effect of the grain size of the substrate and the Cr content on the oxidation kinetics of the low-Cr steels oxidized at 550°C in laboratory air for 72 h, (b) oxide scale structure showing the gold marker within the scale separating the outer and the inner layer.

Fig. 4 shows the effect of cold working on the oxidation kinetics of 2.25Cr1Mo after oxidation in laboratory air at 550°C for 24 h. The oxidation kinetics decreases obviously with increasing degree of cold working. Cold working increases the dislocation density and therefore increases the amount of faster diffusion paths (dislocation pipes) in the sample [25, 26]. Consequently, fast

diffusion of chromium to the inner scale can be expected. It was shown [27] that the increase of chromium concentration in the spinel phase decreases the diffusion coefficient of iron and oxygen in this spinel phase considerably, and therefore reduces the growth kinetics of the outer and the inner oxide layer.

For samples submitted to cold working higher than 42%, recrystallization took place, which causes a reduction in the dislocation density and the formation of very small new grains giving rise to a high inward transport of oxygen into the substrate and therefore higher oxidation kinetics was observed.

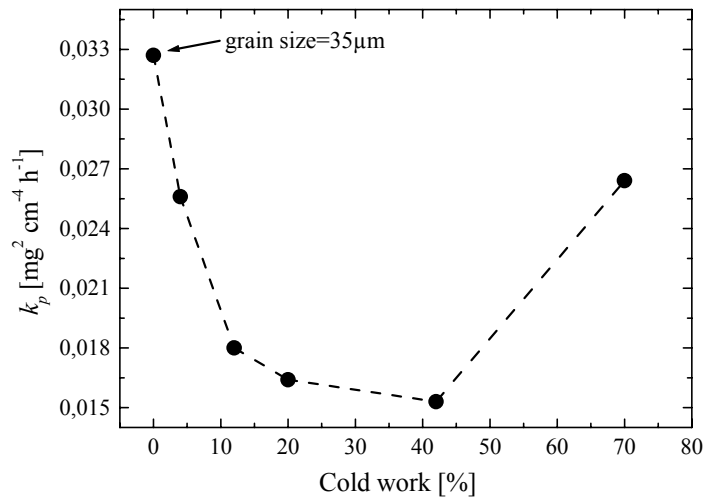


Figure 4. Effect of the cold working on the oxidation kinetics of the 2.25Cr1Mo oxidized in laboratory air at 550°C for 24 h.

Under thermal cycling oxidation conditions, the oxidation kinetics of the steel 2.25Cr1Mo is dramatically accelerated as shown in Fig. 5. No spallation was observed as usually occurs for NiCrAl alloys. The formation of the inner oxide scale and the preferential oxidation along grain boundaries (see [10, 23]) probably works as a pegging, increasing the oxide scale adherence. However, the formed oxide scales have a high tendency of cracking during cooling permitting easy access of oxygen to the substrate/oxide interface leading to higher oxidation kinetics during the next hot cycle.

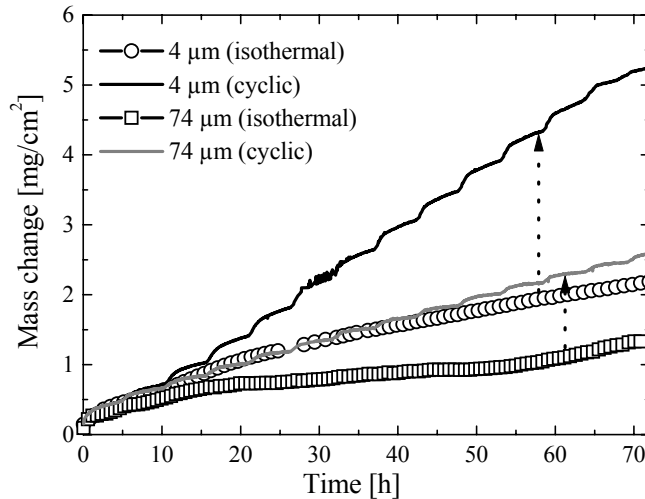


Figure 5. Oxidation of the steel 2.25Cr1Mo with two different grain sizes at 550°C in laboratory air under isothermal and thermal cycling conditions.

A small addition of Ce (0.03wt.%) in the steel 2.25Cr1Mo affects oxidation kinetics strongly. The evidence is presented in Fig. 6a, showing that the mass change of the sample during exposure to laboratory air at 550°C reached a very high value of 15mg/cm² after 72 hours. This value is even higher than that of pure iron oxidation (ca. 10mg/cm²). Oxygen uptake follows a linear behavior with time exhibiting a constant oxidation rate k_1 ($k_1 = 6.3 \times 10^{-5} \text{mg/cm}^2\text{s}$), whereas in the previous cases (pure iron and the low-Cr steels) the mass change followed a nearly parabolic behavior. The oxide scale formed on 2.25Cr1Mo+Ce in laboratory air is shown in Fig. 6b. Chromium is present in the FeO layer and in a small concentration in the Fe₃O₄ layer.

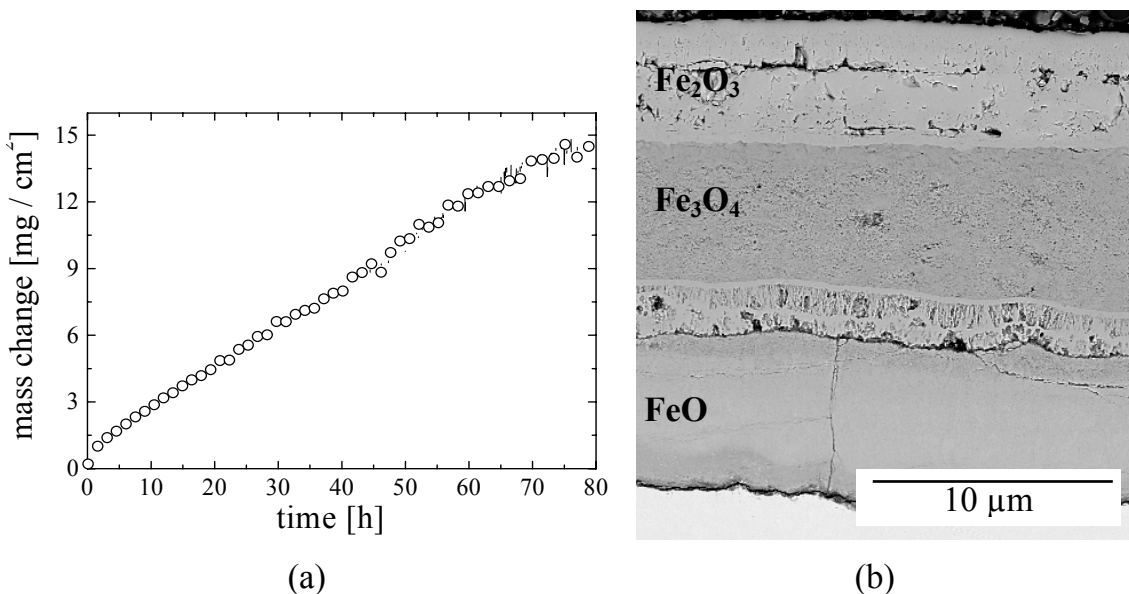


Figure 6. (a) Oxidation kinetics of the steel 2.25Cr1Mo+Ce at 550°C exposed to laboratory air and (b) structure of the oxide scale after 72 h.

The presence of FeO in the steel 2.25Cr1Mo+Ce is responsible for the linear oxidation kinetics observed (see Fig. 6a). It is well known in the literature that due to the high defect concentration in FeO, iron diffuses very fast through this oxide [12, 13, 17]. However, according to the thermodynamic equilibrium, FeO is stable only at temperature higher than 570°C for pure iron and this temperature increases when the Cr-content increases (see Fig. 7). Since FeO forms already at 550°C on the steel 2.25Cr1Mo+Ce, Ce can be assumed to reduce the minimum temperature of FeO stability.

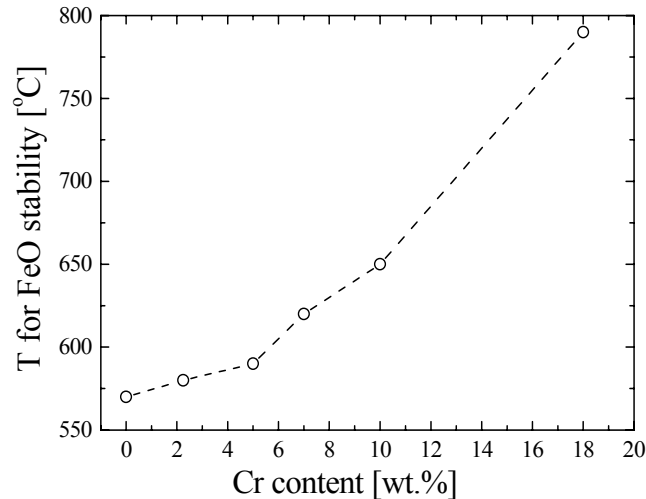


Figure 7. Calculation of the minimum temperature for FeO (wustite temperature) stability using the thermochemistry software FactSage.

In order to understand the influence of Ce on the stability of FeO (temperature for FeO formation) in the system Fe-Cr-Ce-O better, experiments were carried out, in which the oxidation of samples were performed at different temperatures and the mass change as well as microstructural changes were determined. The oxidation constants measured for the three materials investigated (pure Fe, the steel 2.25Cr1Mo and steel 2.25Cr1Mo+Ce) showed that FeO is formed at (i) 568°C on pure Fe, (ii) 580°C on the steel 2.25Cr1Mo and (iii) 471°C on the steel 2.25Cr1Mo+0.03Ce. Figure 8 shows the experimentally observed and the calculated temperatures for the beginning of FeO formation. An excellent agreement exists between the simulated values and those obtained in laboratory tests. Unfortunately, thermodynamic data for Ce is not included in the thermochemistry databank used in this work.

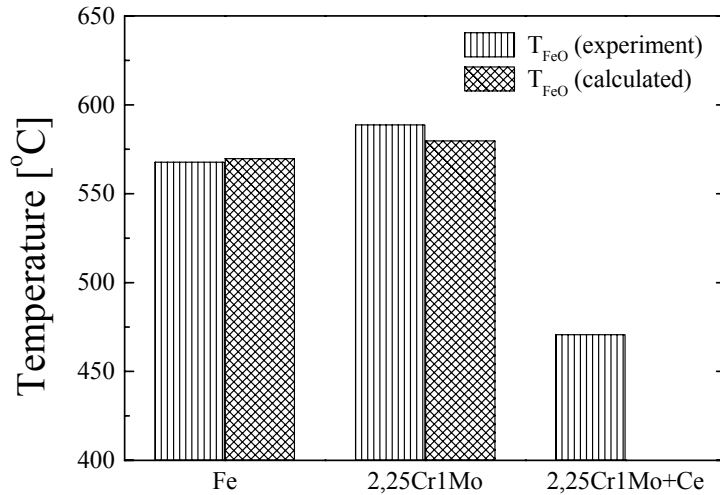


Figure 8. Experimental and calculated temperature for FeO stability during oxidation of pure iron, the steel 2.25Cr1Mo, and the modified steel 2.25Cr1Mo+0.03Ce.

These results confirm the effect of Cr as to increase the temperature of FeO formation, and Ce seems to decrease the temperature of FeO stability down to a minimum temperature of 471°C. Hence, the use of steels containing Ce to temperatures higher than this value is strongly restricted, since FeO grows very fast.

The steel 2.25Cr1Mo with and without Ce addition were exposed to atmosphere containing SO₂ (8% O₂ - 200 ppm SO₂ - 15% H₂O - N₂) and HCl in combination with SO₂ (8% O₂ - 2000 ppm HCl - 200 ppm SO₂ - 15% H₂O - N₂) at 550°C. The corrosion attack in presence of SO₂ was higher for the steel containing Ce (see Fig. 9a), showing that the rare earth element Ce decreases the corrosion resistance of low-Cr steels to SO₂-containing atmospheres. The corrosion behavior of the low-Cr steel in the atmosphere containing additionally HCl, shows that the addition of Ce in the steel 2.25Cr1Mo is beneficial (see Fig. 9b). The steel with Ce addition, reduces at least for a long exposure time (360 h) the corrosion rate (scale thickness) by a factor of 2.5.

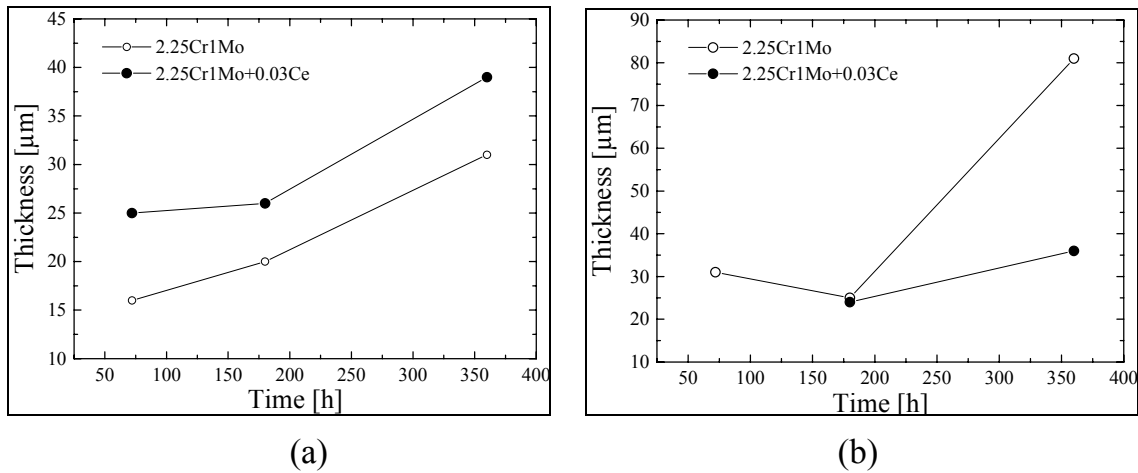


Figure 9. Corrosion behaviour of the steels 2.25Cr1Mo and 2.25Cr1Mo+0.03Ce at 550° C in atmospheres containing (a) 8% O₂ - 200 ppm SO₂ -15% H₂O - N₂ and (b) 8% O₂ - 2000 ppm HCl - 200 ppm SO₂ - 15% H₂O - N₂.

4. Conclusions

This study revealed that oxide scales on pure iron and on the low-alloy ferritic steel 2.25Cr1Mo grow outward as well as inward at 550°C. An increased oxidation attack was observed with decreasing grain size due to higher oxygen transport along substrate grain boundaries. The decrease in the oxidation kinetics for steel samples cold worked up to 42% can be explained by the higher Cr pipe diffusion along dislocation-pipes leading to a higher Cr-concentration within the inner oxide layer. This reduces the outward iron diffusion and the inward oxygen diffusion. For samples cold worked, recrystallization took place causing a reduction in the dislocation density and for very high deformation degrees a very small new grain size. Therefore, high degrees of cold work accelerate oxidation kinetics of low-alloy steels. Thermal cycling strongly increases the oxidation kinetics of the steel 2.25Cr1Mo due to the formation of cracks within the oxide scale during cooling.

The FeO stability was experimentally determined in the present study for each material. For pure iron the minimum temperature of FeO stability was found to be 568°C, for the steel 2.25Cr1Mo 589°C and for the steel 2.25Cr1Mo+Ce only 471°C. Experimental observation and thermochemistry calculation show an excellent agreement for the cases of pure iron and 2.25Cr1Mo steel, while the experimental result for the steel 2.25Cr1Mo+Ce indicated a strong reduction of the FeO stability temperature.

In material research for boiler development, Ce is intended to be used as an element which is able to enhance mechanical strength of low alloy steel. However, with respect to oxidation resistance it might have an opposite effect.

The corrosion attack in steel containing Ce also increased in atmospheres containing SO₂, but might be decreased in atmospheres containing additionally HCl.

References

- [1] Granaud, G. and Rapp, R.A. *Oxidation of Metals*, 11(4), (1977) 193.
- [2] Castle, J.E. and Surman, P.L. *The Journal of Physical Chemistry* 71 (1967) 4255.
- [3] Himmel, L., Mehl, R.T. and Birchenall, C.E. *Journal of Metals* 5 (1953) 827.
- [4] Millot, F. and Niu, Y. *Journal of Physics and Chemistry of Solids* 58 (1997) 63.
- [5] Reddy, K.P.R. and Cooper, A.R. *Journal of American Ceramic Society* 66 (1983) 664.
- [6] Heumann, T. *Diffusion in Metallen*, Springer-Verlag, Berlin Heidelberg, Germany, 1992.
- [7] Wagner, C. *Journal of Electrochemical Society*, 99 (1952) 369.
- [8] Megusar, J. and Meier, G.H. *Metallurgical Transaction*, 7A (1976) 1133.
- [9] Pickering, H.R. *Journal of Electrochemical Society*, 119 (1972) 64.
- [10] Trindade, V.B., Krupp, U. and Christ, H.-J. InCorr-Software for Simulation of Internal/Inwards Corrosion at High Temperatures (chapter 3.1, 36–46) / Modeling of Internal Oxidation/Corrosion (Chapter 3.1 and 4.2). In: OPTICORR Guide Book (D. Baxter, L. Heikinheimo, Hrsg.) Espoo, Finland, 2005.
- [11] Carter, R.E. and Richardson, F.D. *Journal of Metals*, 6, 1244, 1954.
- [12] Bürgel, R. *Handbuch der Hochtemperaturwerkstofftechnik*, 2. Auflage, Vieweg-Verlag, Braunschweig/Wiesbaden, Deutschland, 2001.
- [13] Hauffe, K. *Reaktionen in und an festen Stoffen*, 2 Band, Springer-Verlag, Berlin, Deutschland, 1996.
- [14] Wagner, C. *Zeitschrift für physikalische Chemie*, 21 (1933) 25.

- [15] Hussey, R.J., Sproule, G.I., Caplan, D. and Graham, M.J. *Oxidation of Metals* 11 (1977) 65.
- [16] Goursat, A.G. and Smeltzer, W.W. *Oxidation of Metals* 6 (1973) 101.
- [17] Kubaschewski, O. and Hopkins, B.E. *Oxidation of Metals and Alloys*, Butterworths, London, 1962.
- [18] Chen, R.Y. and Yuen, W.Y.D. *Oxidation of Metals* 57 (2002) 53.
- [19] De' Ans, J. *Taschenbuch für Chemiker und Physiker Band I – Physikalisch-chemische Daten*, 4. Auflage, Sprunge-Verlag, Berlin, Deutschland, 1992.
- [20] Millot, F. and Niu, Y. *Journal of Physics Chemistry Solids*, 58 (1997) 63.
- [21] Castle, J.E. and Surman, P.L. *Journal of Physics Chemistry*, 73 (1969) 632.
- [22] Chen, W.K. and Peterson, N.L. *Journal of Physical Chemistry of Solids*, 36 (1975) 1097.
- [23] Trindade, V.B. Hochtemperaturoxidation chromlegierter Stähle und von Nickel-Basislegierungen: Experimentelle Untersuchung und Computersimulation, PhD thesis, Univesität Siegen, Berichte aus der Materialwissenschaft, Shaker Verlag, Aachen, 2006.
- [24] Trindade, V.B., Krupp, U., Wagenhuber, P.G. and Christ, H.-J. *Materials and Corrosion*, 56 (2005) 785.
- [25] Trindade, V.B., Borin, R., Yang, S., Krupp, U. and Christ, H.-J. *Materials Research*, 8 (2005) 365.
- [26] Kofstad, P. *High Temperature Oxidation of Metals*, Wiley, New York, 1966.
- [27] Birks, N. and Meier, G.H. *Introduction to High Temperature Oxidation of Metals*, Edward Arnold, 1983.

Sulphidation behaviour of advanced materials for elevated kraft recovery boiler conditions

Sanni Yli-Olli, Pekka Pohjanne, Liisa Heikinheimo,
Tuomo Kinnunen and Pekka H. Pankakoski

VTT Technical Research Centre of Finland, Espoo, Finland

Abstract

The behaviour of new kraft recovery boiler materials in reducing conditions has been evaluated in this study. Sanicro 38, Sanicro 36Mo, Sanicro 65, 4C54 and HR11N were tested in gas mixtures containing hydrogen sulphide (H_2S) and carbon monoxide (CO) with and without water vapour. Steel 304L and a basic carbon steel were used as reference materials. A thin (max. 1 μm) oxide layer, probably a spinel ($FeCr_2O_4$), was observed on some of the exposed materials in the tests with 15% water vapour. This layer protected the materials from sulphidation. The protective effect of water vapour was not eliminated by the increase in temperature from 400°C to 440°C or in H_2S concentration from 500 to 5000 ppm. However, water vapour did not protect carbon steel. Without water vapour, sulphidation started at low levels of H_2S and was accelerated by increasing H_2S concentration. The reference material 304L and Sanicro 36 Mo showed the best sulphidation resistance. The formed layers of corrosion products were analysed with EDS and compared to thermodynamic modelling by FactSage. In most cases the thermodynamic predictions agreed very well with the EDS analyses. The results suggest that alloying with molybdenum will restrain sulphidation.

1. Introduction

The growing need for clean energy also requires improved efficiency of kraft recovery boilers. This leads to higher gas temperatures and pressures, and it is predicted that the tube temperatures at the lower furnace will rise to 400–440°C, which will increase sulphidation risk. Then the traditional materials cannot be safely used or their corrosion rates are no more within the economically tolerable levels. Therefore, there is need for new durable materials with verified performance in the new and more severe conditions. Sulphidation caused by reducing hydrogen sulphide containing mixed gases has been studied extensively at higher temperatures (>700°C) than the ones presently of interest [1–6]. These investigations indicate that chromium (>25 wt-%) and molybdenum improve sulphidation resistance, and nickel at high amounts enhances sulphidation. Sulphidation of many elements used in typical furnace wall tube materials may start already at much lower temperatures, as shown in DCS measurements [7]. These results (Table 1) indicate that sulphidation of nickel, iron

and manganese starts at lower temperatures than sulphidation of chromium and molybdenum. Sulphidation problems may appear in the lower furnace of the new high pressure kraft recovery boilers, when the tube temperatures are increased over 400°C. The risk should be highest in high nickel or nickel base alloys with relatively low chromium and molybdenum content.

Table 1. Sulphidation temperatures of selected elements.

Element	Sulphidation temp.
Cr	400–700°C
Mo	550–650°C
Mn	250–550°C
Fe	250–400°C
Ni	250–450°C

2. Materials and methods

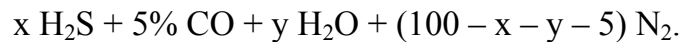
To study the sulphidation resistance of new alternative lower furnace materials, Sanicro 38 (UNS N08825), Sanicro 36Mo (UNS N08036-2), Sanicro 65 (UNS N06625 mod.), 4C54 (UNS S446600) and HR11N were evaluated with AISI 304L and a carbon steel as reference materials. The compositions of the test materials are presented in Table 2.

Table 2. The chemical composition (wt-%) of the test materials.

	C	Si	Mn	Cr	Ni	Mo	V	Cu	Al	Fe	Others
San 36Mo	0.01	0.27	4.9	27	33.8	5.35	0.06	0.08	0.02	bal	W, Ti, Nb
San 38	0.02	0.16	0.66	19.9	38.3	2.54	0.05	1.58	0.07	bal	W, Ti, Nb
San 65	0.03	0.23	0.27	23.7	63.8	8.6			0.19	2.8	Ti, N
San 65X-1	0.0001	0.49	0.49	21.3	66.4	10.7			0.01	0.31	Ti, N
4C54	0.19	0.47	0.69	26.6	0.28	0.03	0.06	0.02		bal	W, Ti, Nb
HR11N	0.02	0.18	0.36	27.2	39.5	0.83	0.05	0.16	0.02	31.5	W, Ti, Co
Reference material											
304L	0.01	0.35	1.23	18.3	10.2	0.43	0.06	0.22		bal	W, Ti, Nb

Alloy HR11N was delivered by Sumitomo Metals and other materials by Sandvik. Sanicro 65 was changed in the middle of the test program to Sanicro 65X-1.

The tests were conducted using 15 x 15 x 2 mm coupons cut from the test materials. The test coupons were then ground to 1200 grit and carefully ultrasonically cleaned with acetone and ethanol. In every test duplicate samples were tested to get more reliable data. The tests were performed at the VTT's high temperature testing facilities under controlled atmospheres of gas mixtures with the following formulation:



The test gases, times and temperatures are given in more detail in the test matrix Table 3.

Table 3. The test matrix: test gases, temperatures and durations.

Concentration		Temperature, duration	
H ₂ S	H ₂ O	400°C	440°C
500 ppm	0%		288 h
500 ppm	15%	144 h, 288 h	144 h, 288 h
1000 ppm	0%		288 h
1000 ppm	15%	288 h, 432 h	144 h, 288 h
2500 ppm	0%		288 h
2500 ppm	15%		288 h
5000 ppm	0%		288 h
5000 ppm	15%		288 h

After the high temperature corrosion tests the samples and the possible spalled corrosion products were weighed (Mettler balance AT261 ± 0.015 mg). After this the samples were analysed with an optical and a scanning electron microscope (OM, SEM). Semi qualitative electron dispersive spectroscopy (EDS) was used to analyse the corrosion products. Thermodynamic calculations were made with the FactSage program to validate the formed corrosion products.

3. Results

In the tests with 15% water vapour no significant weight changes could be seen from any of the test materials or in the 304L reference material. An oxide scale of approximately 1 μm was formed on all the test materials, as can be seen from Fig. 1a. On the sample surfaces small scattered areas containing some oxygen and sulphur were found (Fig. 1b). The carbon steel reference material suffered from intense sulphidation, shown as severe spallation of the oxide scale in all tests containing 15% water vapour.

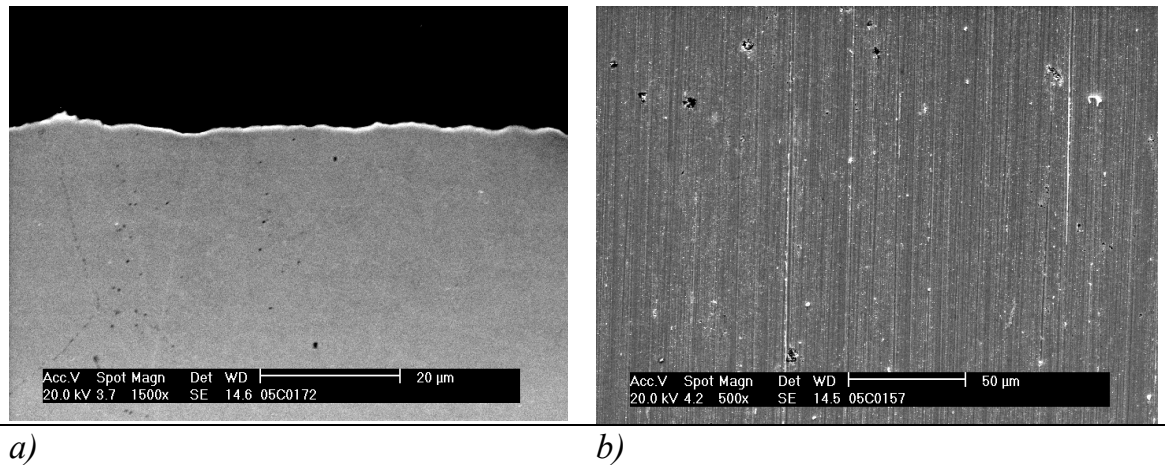


Figure 1. a) The cross-section and b) the surface of Sanicro 38 after the 288 h corrosion test in 1000 ppm H_2S , 5% CO , 15% H_2O at 440°C.

In the tests without water vapour significant weight change could be detected from all materials even with only 500 ppm of H_2S (Fig. 2). Sanicro 38, Sanicro 36 Mo, 304L and HR11N showed some also scale spallation in these tests, which was taken into account into the weight change. The thicknesses of the formed scales varied between 0 to 25 μm (Fig. 3). From the figure can also be seen that at 5000 ppm the corrosion scale of 304L had all spalled off. Again the resistance of the carbon steel reference material was inferior to the others; scales spalled tremendously, and the weight changes were decades higher than of the other test materials.

Examples of the corrosion scales formed during the tests are shown Fig. 4. From the micrograph of Sanicro 65 (Fig. 4a) can be seen starting inward corrosion and three different corrosion product layers. The EDS analyses showed that the inner scale was a chromium sulphur compound, with a sulphur chromium oxide scale on top of this and the outer scale was a compound of nickel and sulphur.

From the micrograph of HR11N (Fig. 4b) can be seen even corrosion and two different corrosion product layers. The EDS analyses showed that the inner scale was a chromium sulphur compound, and the outer scale was a compound of nickel, iron and sulphur. The micrograph of Sanicro 38 (Fig. 4c) showed starting

inward corrosion and at least two different corrosion product layers. The EDS analyses showed that the inner scale was a chromium sulphur compound with a hint of oxygen and iron, the outer scale was a compound of nickel, iron and sulphur.

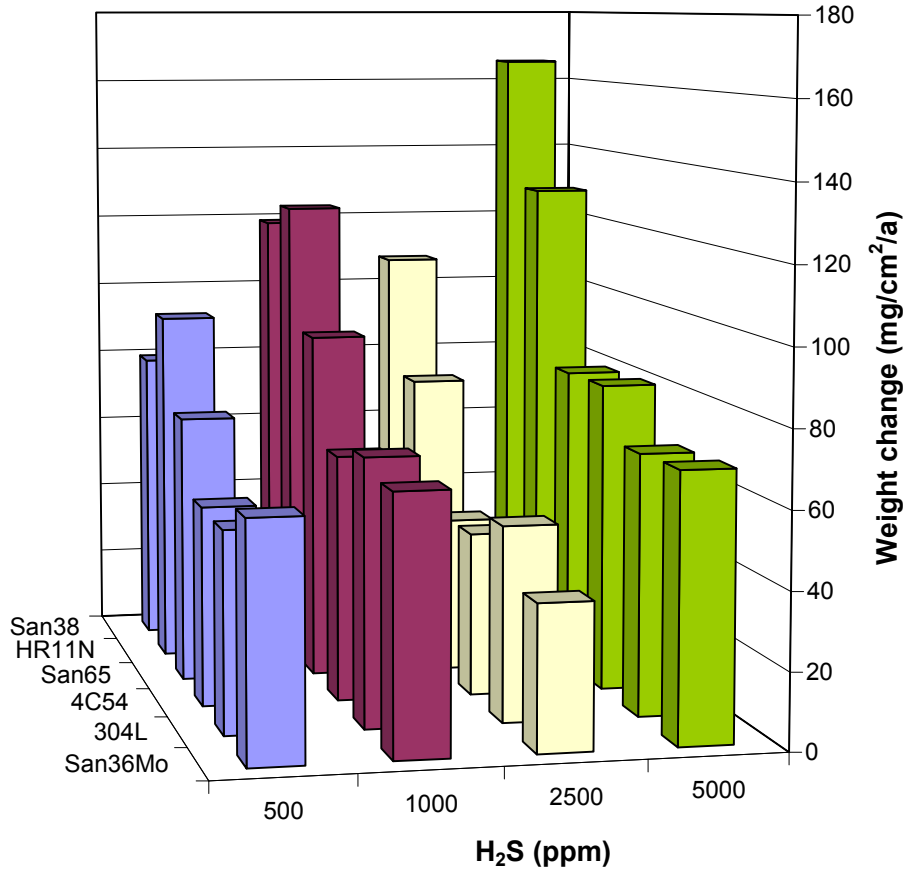


Figure 2. Weight change ($\text{mg}/\text{cm}^2/\text{a}$) of the tested materials in the tests without water vapour at 440°C .

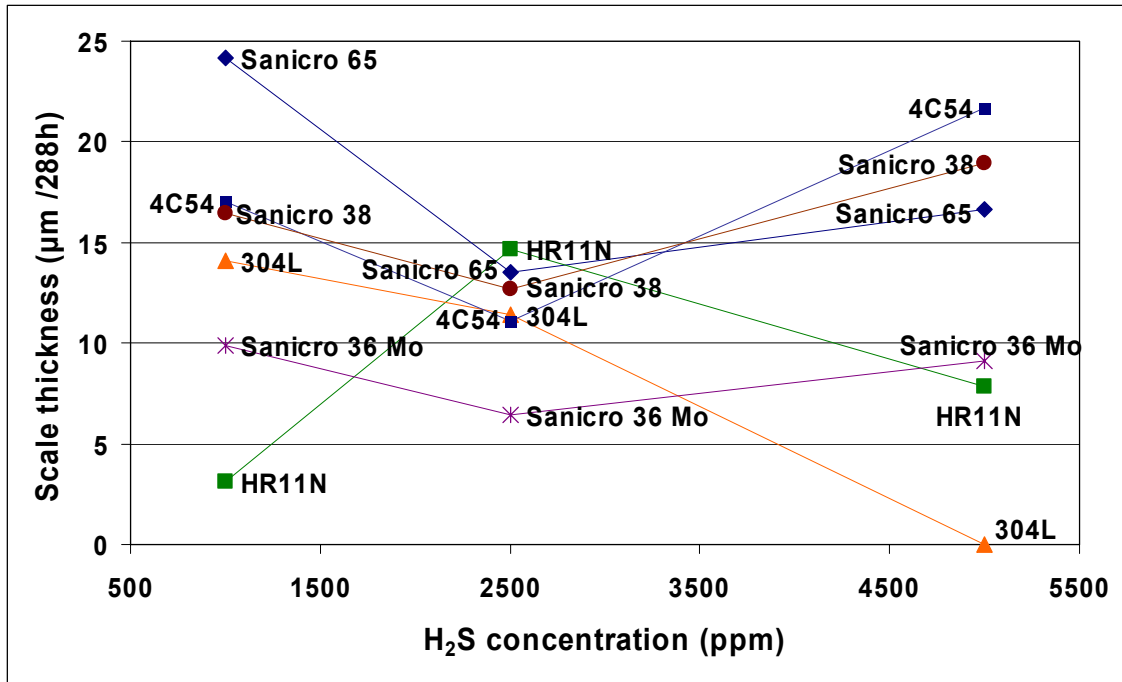


Figure 3. The corrosion scale thicknesses of the tested samples at 440°C without water vapour.

From the micrograph of Sanicro 36 Mo (Fig. 4d) can be seen even corrosion and two different corrosion product layers. The EDS analyses showed that the inner scale was a chromium sulphur compound with a hint of oxygen and iron, the outer scale was a compound of nickel, iron and sulphur. The micrograph of 304L (Fig. 4e) showed even corrosion and at least two different corrosion product layers. The EDS analyses showed that the inner scale was a chromium sulphur compound, and the outer scale a compound of nickel, iron and sulphur. From the micrograph of 4C54 (Fig. 4f) can be seen starting inward corrosion and at least two different corrosion product layers. The EDS analyses showed that the inner scale was a chromium sulphur compound with a hint of oxygen and the outer scale was a compound of iron and sulphur.

Fig. 5 shows calculated thermodynamic stability diagrams of Sanicro 36Mo with 15% water vapour (Fig. 5a) and without water vapour (Fig. 5b).

In general calculations gave similar stability diagrams to all test materials. When water vapour was present the first formed scale was an iron, chromium spinell oxide FeCr_2O_4 (Fig. 5a), the following scales depended on the composition of the material. When water vapour was not present the first formed scale was chromium oxide Cr_2O_3 with lower hydrogen sulphide concentrations, with 5000 ppm of H_2S the first formed scale was some kind of a sulphide (Fig. 5b).

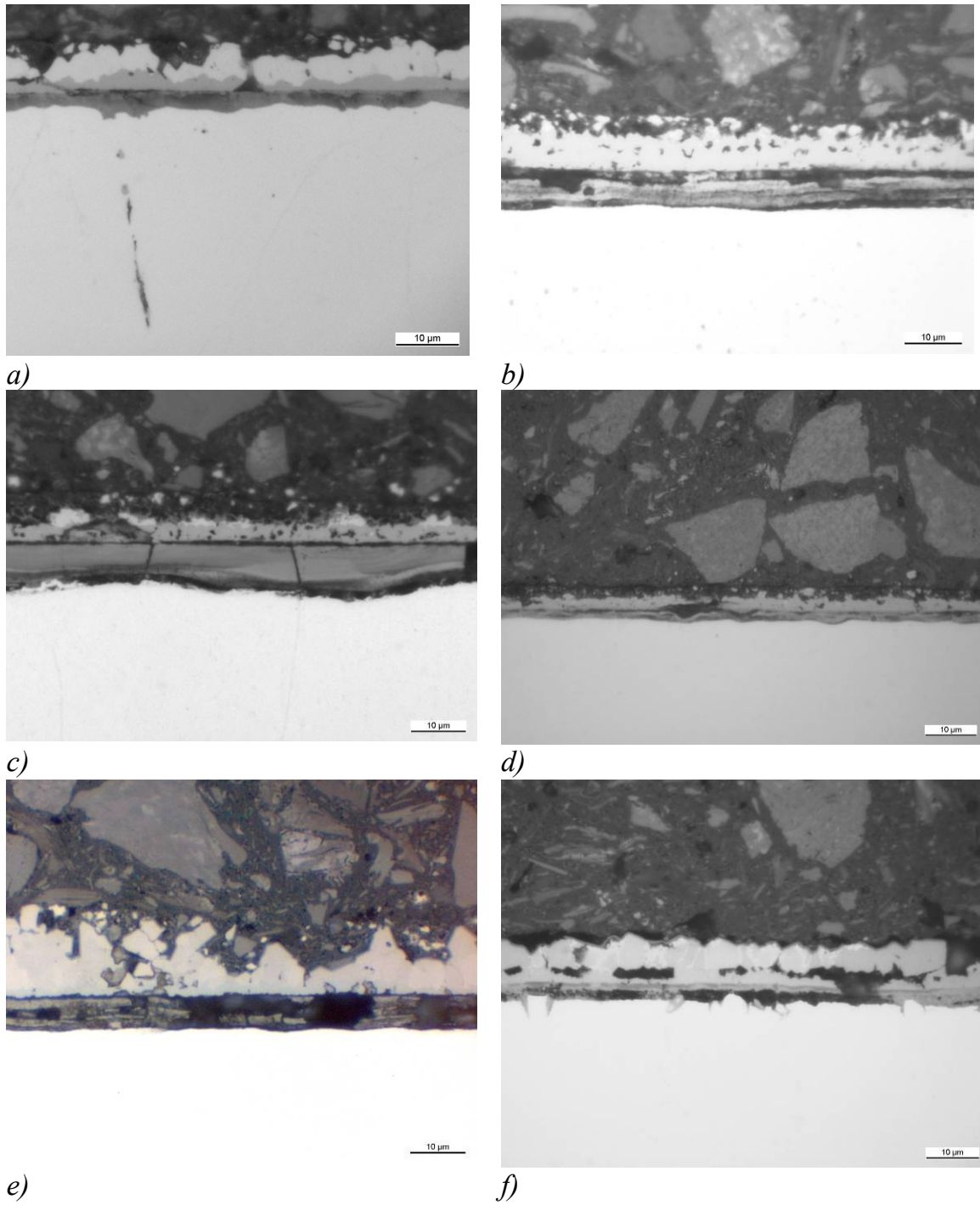
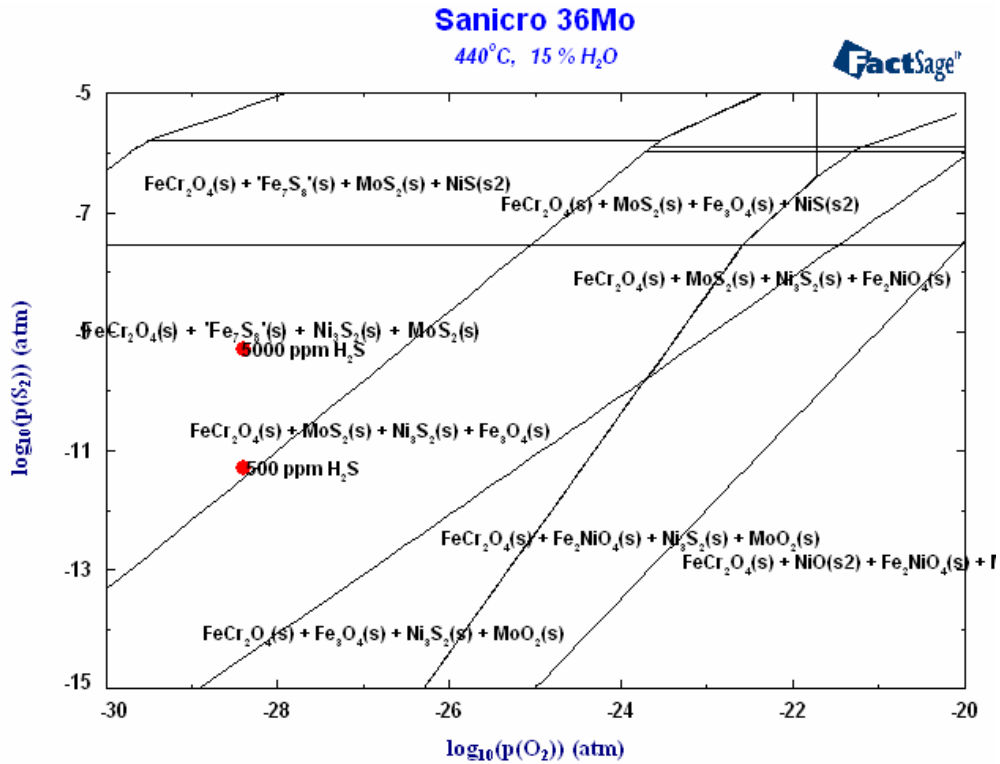
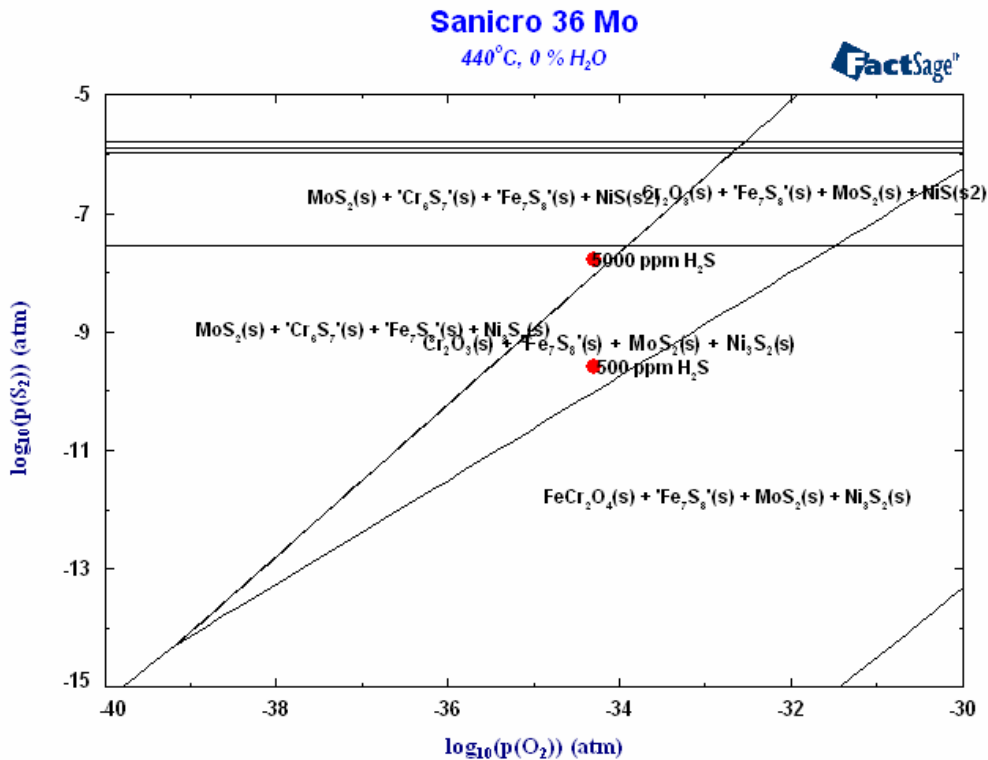


Figure 4. The cross section of a) Sanicro 65 b) HR11N c) Sanicro 38 d) Sanicro 36 Mo e) 304L and f) 4C54 after 288 h at 440°C, 2500 ppm H_2S , 5% CO and 0% H_2O .



a)



b)

Figure 5. Thermodynamic calculations of Sanicro 36 Mo at 440°C a) with 15% water vapour and b) without water vapour.

4. Discussion

Water vapour influences on the sulphidation of new recovery boiler materials. The obtained results showed that 15% of water vapour restrained sulphidation in the 288 h tests. The increase of hydrogen sulphide (H_2S) from 500 ppm to 5000 ppm did not override the protective influence of the water vapour; neither did the increase of temperature from $400^\circ C$ to $440^\circ C$. A thin (max. $1\mu m$) spinell oxide ($FeCr_2O_4$) was observed on the tested materials and on the 304L reference material, and this protected the materials from sulphidation (Fig. 5a). When compared to previous results [8] it was seen that water vapour has a protective influence even at higher H_2S concentrations (6000 ppm) at slightly lower temperatures. Water vapour did not protect the carbon steel from sulphidation.

In tests without water vapour sulphidation resistance of all test materials decreased when hydrogen sulphide concentration was increased. Exception to this behaviour was the H_2S concentration of 2500 ppm where a downswing on the mass change curve was observed in all materials. This partially is explained by the formation of different corrosion products at different H_2S concentrations, this was partially supported by the thermodynamic calculations. The temperature dependency of sulphidation was not investigated in this study, but earlier studies indicate that an increase in temperature will increase the sulphidation rate [8]. When water vapour was not present the first formed scale was chromium oxide Cr_2O_3 with lower hydrogen sulphide concentrations, with 5000 ppm of H_2S the first formed scale was some kind of a sulphide (Fig. 5b).

Normally in terms of pure oxidation the chromium oxide scale is more desirable than any spinell oxide phase. In case of sulphidation the situation is different since the spinell phase seems to be more protective than chromium oxide scale. At higher temperatures the failure of the protective chromium oxide scale has also been observed [1–6]. Some transition metals (e.g. Ni, Fe and Mo) can diffuse through the Cr_2O_3 scale and react on top of it forming sulphides. This was also seen in the corrosion scale analyses of the test materials, a chromium compound was observed at the metal – sulphide interface, and an iron and/or nickel sulfide scale on top of it. In some of the materials also an incipient internal corrosion was observed. This might be due to the penetration of gaseous sulphur through the oxide to the oxide – metal interface, where the sulphur reacts with the chromium of the metal forming chromium sulphides (Fig. 6).

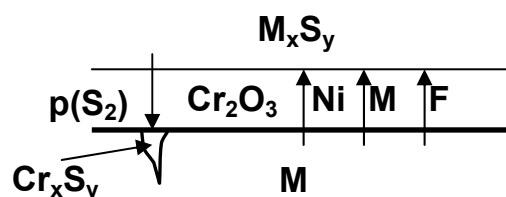


Figure 6. Sulphidation of high chromium metals.

The thermodynamic calculations (Fig. 5b) indicate that even 5% H₂O would be sufficient to form a protective spinell phase on the metal surface. This as well as the reason for the protective function of the spinell scale should be examined in more detail in future studies.

In the tests without water vapour differences in weight change between materials could be seen (Fig. 2) and on the basis of mass change a following list from the worst to the best was obtained.

Carbon steel <<< Sanicro 38 < HR11N < Sanicro 65 ≤ 4C54 < Sanicro 36 Mo ≤ 304L.

The alloys Sanicro 38, HR11N and Sanicro 36 Mo spalled the most. Of these Sanicro 36 Mo performed the best indicating that alloying with molybdenum protects against sulphidation. The good influence of molybdenum alloying has also been reported earlier [1–6]. It is proposed that the formed molybdenum sulphite grows first relatively fast but when it reaches a stabile state it restrains the further sulphidation of the material. This has only been reported at higher temperature (~700°C), but the present results indicate that molybdenum alloying has also a positive effect at lower temperatures in restraining sulphidation. Sulphidation resistance was also improved by chromium alloying as expected. The amount of alloyed nickel didn't have a major effect on the sulphidation rate, which was predicted by earlier results [1–6]. Some grain boundary corrosion was detected in the ferritic stainless steel 4C54. Therefore although this material performed well in the tests it must be noticed that grain boundary corrosion is more dangerous than evenly progressing corrosion.

In most cases the thermodynamic calculations were supported by the EDS cross section analyses. By combining these two methods good approximations of the formed corrosion products could be made. Defects and faults were still found in some calculations, therefore thermodynamic modelling can not be used independently to predict sulphidation. The modelling can still be used as a supporting tool in analyses and it can also help in e.g. planning of test programs.

5. Conclusions

The objective of the project was to evaluate the sulphidation behaviour of new kraft recovery boiler materials in reducing conditions. The following materials were selected as test materials: Sanicro 38, Sanicro 36 Mo, Sanicro 65, 4C54 and HR11N. The common stainless steel 304L and a basic carbon steel were used as reference materials. The materials were tested in four different hydrogen sulphide (H₂S) concentrations mixed with 5% of CO, with and without water vapour.

The results showed that 15% of water vapour protected the test materials from sulphidation, by forming a FeCr_2O_4 spinel. This positive effect was not eliminated by increase in temperature (400°C to 440°C) or in H_2S concentration (500 to 5000 ppm). Without water vapour, sulphidation started at low H_2S concentrations and was accelerated by increasing concentration.

Best sulphidation resistance was observed in the reference material 304L and in alloy Sanicro 36 Mo. The alloys Sanicro 38 and HR11N had lower sulphidation resistance than the nickel base alloy Sanicro 65. In particular, Sanicro 38 had a mass change over 160 $\text{mg}/\text{cm}^2/\text{a}$, which is approximately 80 $\text{mg}/\text{cm}^2/\text{a}$ more than any other alloy. The results are consistent with the general observation that alloying with molybdenum and chromium restrains high temperature sulphidation.

Acknowledgements

The authors wish to thank the Finnish Recovery Boiler Committee and the Finnish Funding Agency for Technology and Innovation (Tekes) for financial and technological support for the project.

References

1. Lai, G.Y. High-temperature corrosion of engineering alloys, ASM international, USA, 1990.
2. Norton, J.F., Hodge, F.G. and Lai, G.Y. A study of the corrosion behaviour of some Fe-Cr-Ni and advanced Ni-based alloys exposed to sulphidising/oxidising/carburising atmosphere at 700°C, High temperature materials for power engineering, Proceedings Part I, 1990. Pp. 167–176.
3. Lai, G.Y. and Hodge, F.G. The corrosion behaviour of a new sulphidation-resistant alloy in a sulphidizing/oxidizing/carburizing atmosphere, Heat-resistant materials, Proceedings of the First International Conference, Wisconsin, USA, 1991. Pp. 211–223.
4. Natesan, K. and Wang, D.Y. Developments of weldments for sulphur-containing combustion environments, Heat-resistant materials, Proceedings of the First International Conference, Wisconsin, USA, 1991. Pp. 395–414.
5. Gesmundo, F., Niu, Y., Viani, F. and Rande, G. The sulphidation behaviour of Fe-Nb, Co-Nb and Ni-Nb alloys in H_2 - H_2S mixtures at 700°C, Progress in the understanding of corrosion, Vol. 1, The Institute of Materials, London, UK, 1993. Pp. 742–749.

6. Schulte, M. and Schülte, M. The behaviour of protective sulfide scales on various steels in H₂S-containing atmospheres during temperature changes, *Progress in the understanding of corrosion*, Vol. 1, The Institute of Materials, London, UK, 1993. Pp. 750–757.
7. Wada, H., Takada, K. and Sasaki, T. DSC studies on reactions of the elements with sulphur, *Solid state ionics*, 172 (2004), pp. 421–424
8. Mäkipää, M., Oksa, M. and Pohjanne, P. Corrosion testing of high-nickel alloy composite tube materials in simulated recovery boiler lower furnace conditions, *VTT Symposium 214, 10th International Symposium on Corrosion in the Pulp and Paper Industry (10th ISCPPI)*, Helsinki, 21–24 August 2001, Vol. 1, Hakkarainen, Tero (ed.), VTT Technical Research Centre of Finland, Espoo (2001). Pp. 73–88.

Application of an integrated risk management system for improved maintenance in industrial plants

A. Jovanovic, D. T. Balos, G. Vinod and D. Balos

Steinbeis Advanced Risk Technologies, Stuttgart, Germany

P. Stanojevic

NIS – Petroleum Industry of Serbia, Novi Sad, Serbia

Abstract

The paper presents the application of the Integrated Risk Management System (iRis) and its application to the areas of Risk Based Inspection (RBI), Reliability Centered Maintenance (RCM), Root Cause Failure Analysis (RCFA) and Health, Safety and Environment (HSE). The web-based system integrates also the aspects of risk management related to data acquisition and management and interactive reporting and controlled use of single parts of the system by various individual users and/or user levels. A complementing part of the system is a tool for project management including the documentation and activity management, as well as scheduling and e-education and e-training.

The complementing parts of the system are the CMMS part (maintenance management), the extension of HSE to HSSE (including the “security” aspects and providing links to the disaster management system) and further interfacing towards general management system and process modeling and management systems. Experiences from the applications of system in Hungary (at over 60 units) and in Serbia, for several refineries and further units in upstream and downstream, are presented in the paper.

1. Introduction – Integrated Risk Management

The world-wide experience clearly shows [1] that integration and defragmentation of knowledge, approaches, regulation and R&D are the prerequisites for the successful management of risks. This integration is needed along the following main lines:

- EU-wide, geographical integration: approaches of different states / regions to risks are often completely different;
- Integration over different stakeholders groups: the 60+ most important EU stakeholders in the area of emerging risks, major industry, SMEs, leading R&D, academia, associations and organizations...

- Cross-sectorial integration: the approaches to emerging risks across different application areas and branches (not within single sectors, but cross-sectorial – following the risks!);
- Interdisciplinary integration: Different disciplines and methods dealing with risk science; in particular the interdependence between (a) technology and society and (b) technology and nature will be tackled;
- Integration of methods and tools: Different solutions and tools should be integrated;
- Integration over all aspects of emerging risks along the life cycle of technologies and products (Fig. 1);
- Integration of existing and new technologies.

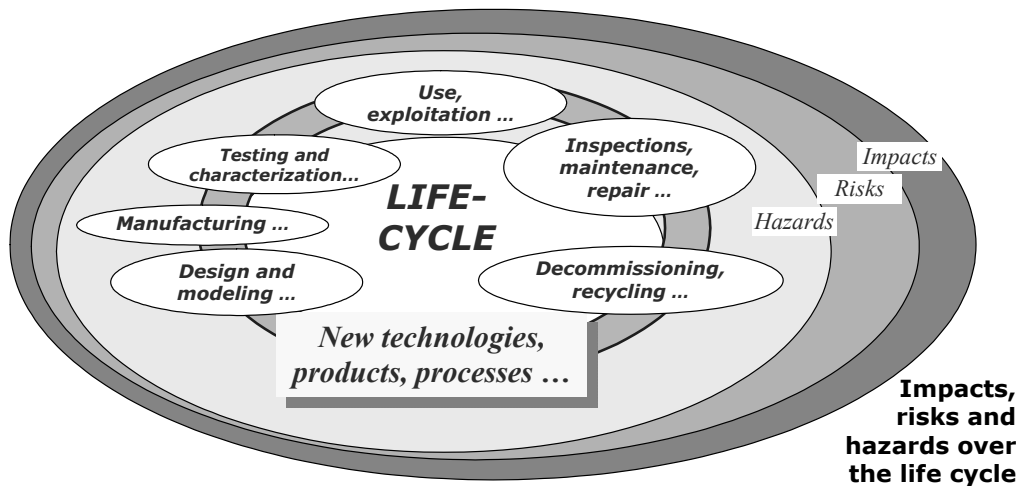


Figure 1. Integrated approach to risk – a key of successful risk management.

In this paper primarily the integration

- of approaches over the branches (power, process, petrochemical)
- of methods and tools, and
- RBI (risk-based inspection), RCM (reliability centered maintenance), RCFA (root-cause failure analysis) and HSSE (health, safety, security, environment) aspects (Fig. 2).

is considered and it is described how the integration is done within the iRiS system (Integrated Risks Management System – in the subsystems iRiS-Petro and iRiS-Power) of Steinbeis Advanced Risk Technologies.

The basis for the integration is given by

- shared principles of integration provided in ETPIS [2], RIMAP [3–4] and CEN WA24 [5] approaches, as well as in the relevant codes and guidelines [6–9] and [10], and
- common IT infrastructure based on the web (dot.net) technology.

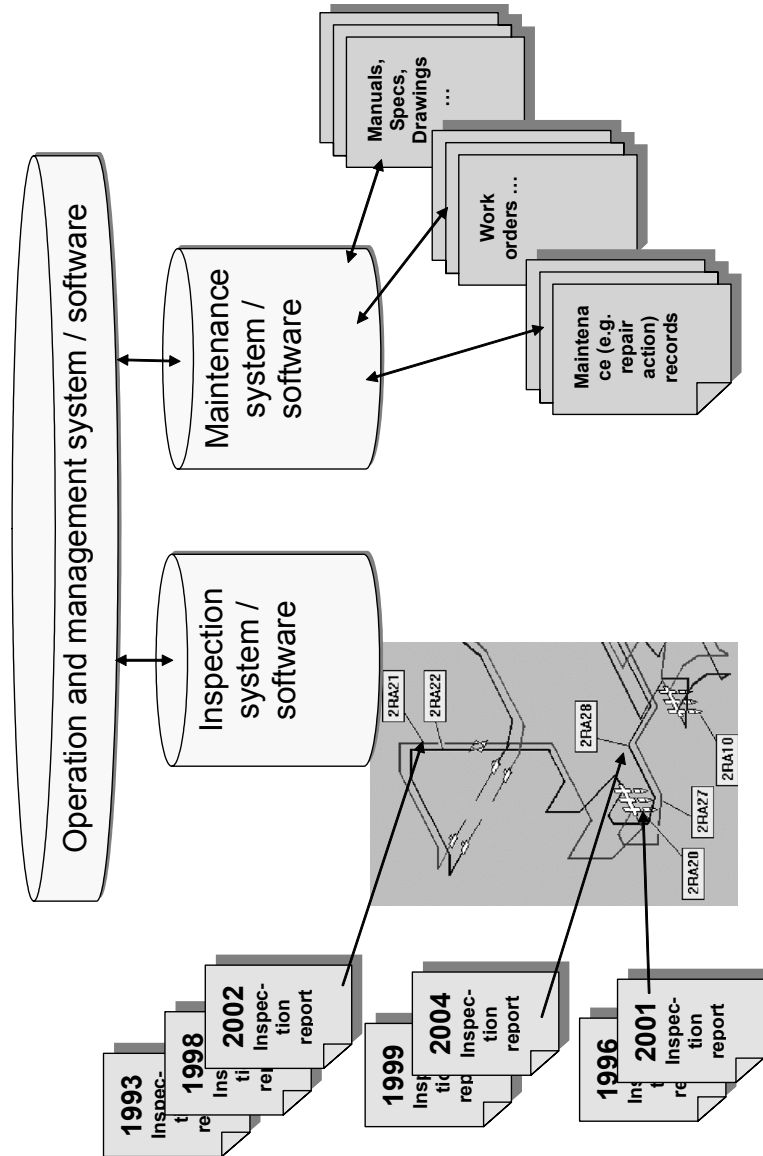


Figure 2. Integrated approach to RBI/RCM/RCFA.

2. iRiS-System

The system has currently two main parts: one for petrochemical plants (iRiS-Petro) and one for power plants (iRiS-Power). Further industrial modules are

considered (e.g. paper, steel, palm-oil refineries, ...) and will be realized, just like the first two ones based on market-demand only. The considered modules preceding market demands are those related to emerging risks.

2.2 Common paradigm

Common paradigm for both iRiS main parts is given by approach and the procedure RIMAP CEN WA 24 and the main modules of the system cover the main steps in the procedure (Fig. 3).

2.3 Common Modules and modules of iRiS Petro

2.2.1 Data/Asset Management

The software allows a web-based 3D view of your complete assets, starting from geographical distribution of the assets using predefined or GIS-based maps, towards true 2D or 3D models of your units, equipments and components. The models are based on 2D drawings and 3D models from your existing CAD software. Furthermore, the models allow the users to visually identify the equipment, components and locations where certain actions are performed. The 3D model allows the users to get all the information needed (be it design information, performed analyses and inspections or planned ones) from one central point.

Each piece of equipment in the system gets an appropriate data sheet for the given type of equipment that can hold all the information as required per standard specification (i.e. EN, API or ASME). This way, the engineering and asset knowledge is centralized in one single point. Directly from the data sheets, the information can be used at the same time as equipment specification (i.e. as replacement order). For each piece of equipment, the appropriate records of performed inspections are kept. This way, it is traceable how the equipment state has changed through time, and the early signs of problems can be easily identified and pinpointed.

Furthermore, the inspection records can be directly used in RBI and RCM evaluations. RBI software suite consists of the following software modules:

- Management System Evaluation Module (MSEQ)
- API 581 qualitative analysis system for unit-based approach (screening)
- API 581 qualitative (component-based) – Level 1, semi-quantitative – Level 2 and quantitative – Level 3 analysis modules
- RIMAP-based assessment (option to be agreed with the end-user in each particular case)

2.2.1 RBI

The Management System Evaluation Module (MSEQ) is a questionnaire based software for evaluation of management systems according to the Appendix D in API581.

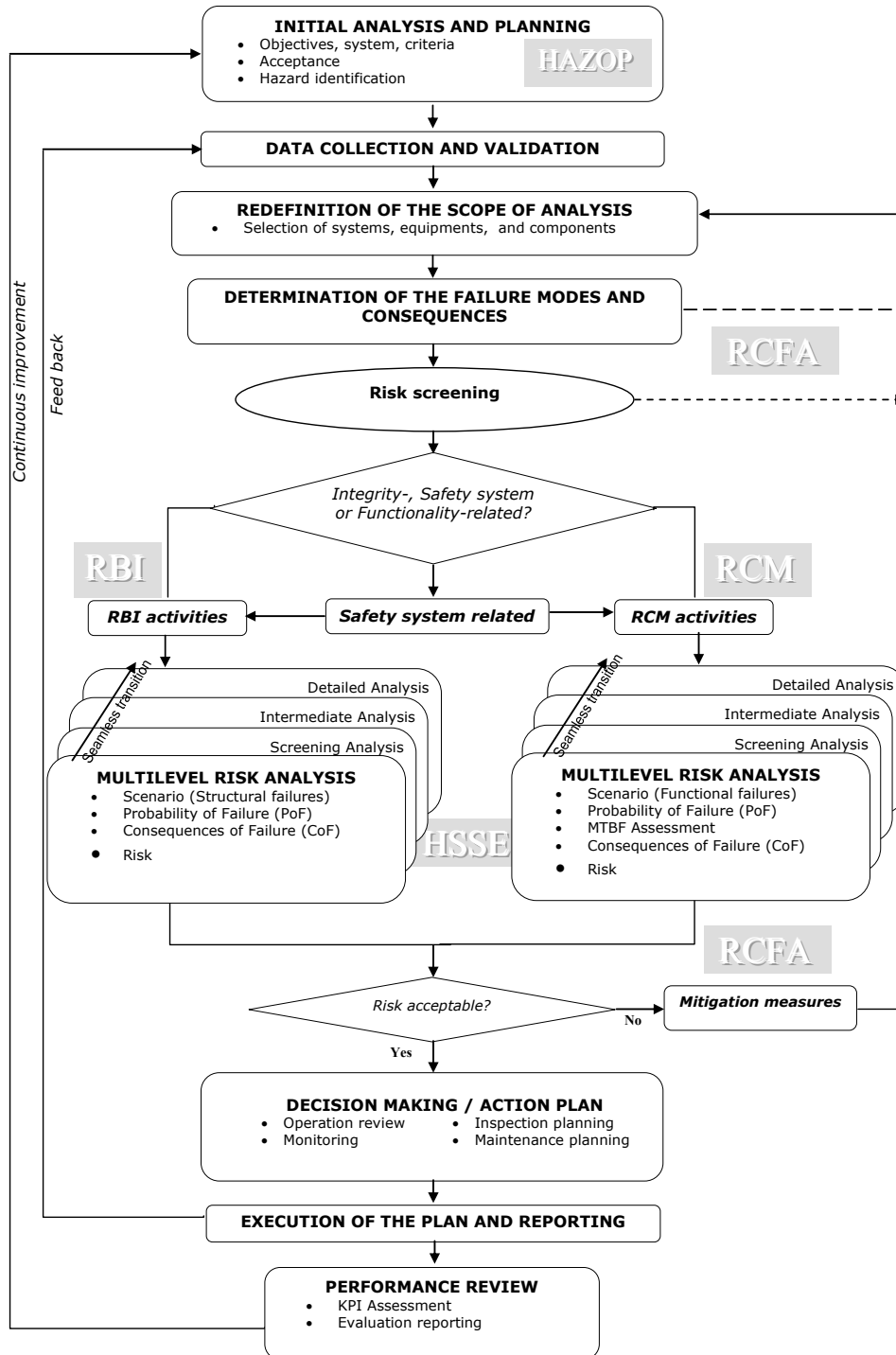


Figure 3. Framework of RIMAP procedure of CEN WA 24 [5].

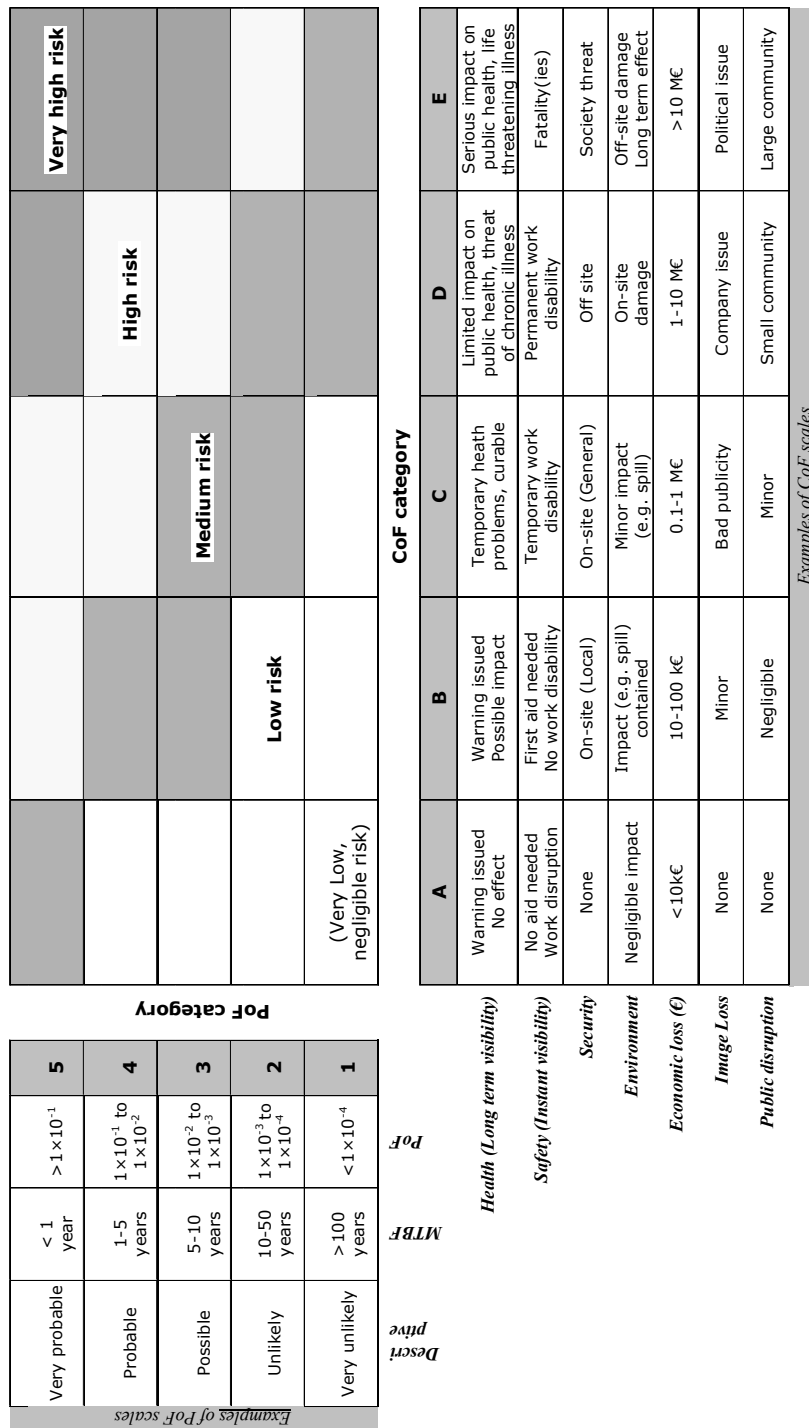


Figure 4. CEN WA 24 Risk Matrix: example of the risk matrix for detailed assessment, involving HSE and economic risks with four risk limit categories.

The module for API 581 qualitative analysis system for unit-based approach (screening – QLTA, Fig. 6) is based on the Workbook for Qualitative Risk Analysis given in Appendix A of the API581 Base Resource Document. It is used to determine the Likelihood and Consequence Category for a given unit. Depending on the nature of the chemicals in a unit, the Consequence Category

can be determined based on the flammable or toxic hazards for the unit. Flammable consequences are represented by the Damage Consequence Category, since the primary impact of a flammable event (fire or explosion) is to damage equipment. Toxic consequences fall under the Health Consequence Category, since their impact is usually limited to adverse health effects. The RBI (component-based) – level 1, semi-quantitative – level 2 and quantitative – level 3 analysis module (Fig. 7), based on the API581, performs the tasks necessary to determine the risk rank of the equipment and optimize the inspection plan for the equipment based on either qualitative approach (level 1), semi-quantitative approach (level 2) or quantitative approach (level 3).

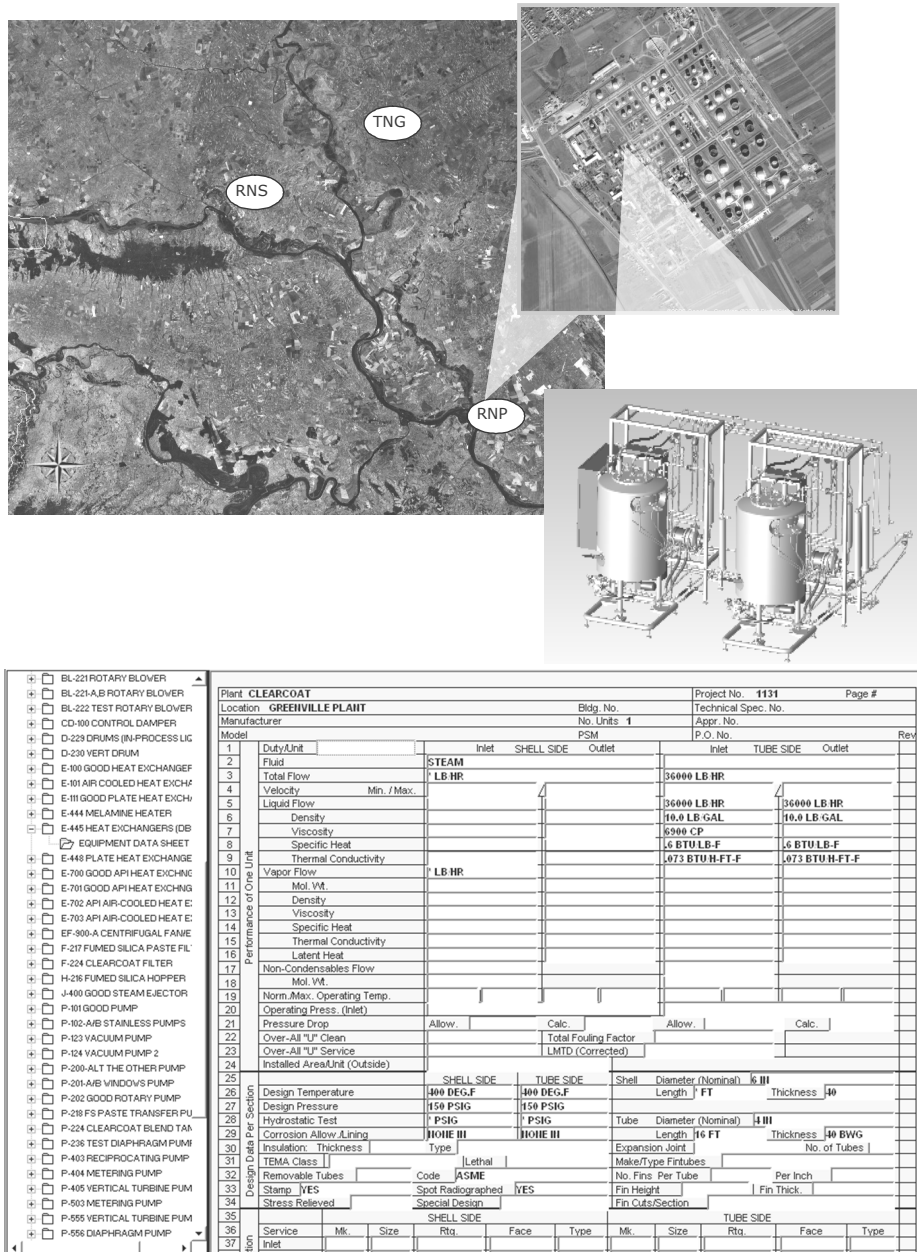


Figure 5. Asset and inspection data and records in iRis.

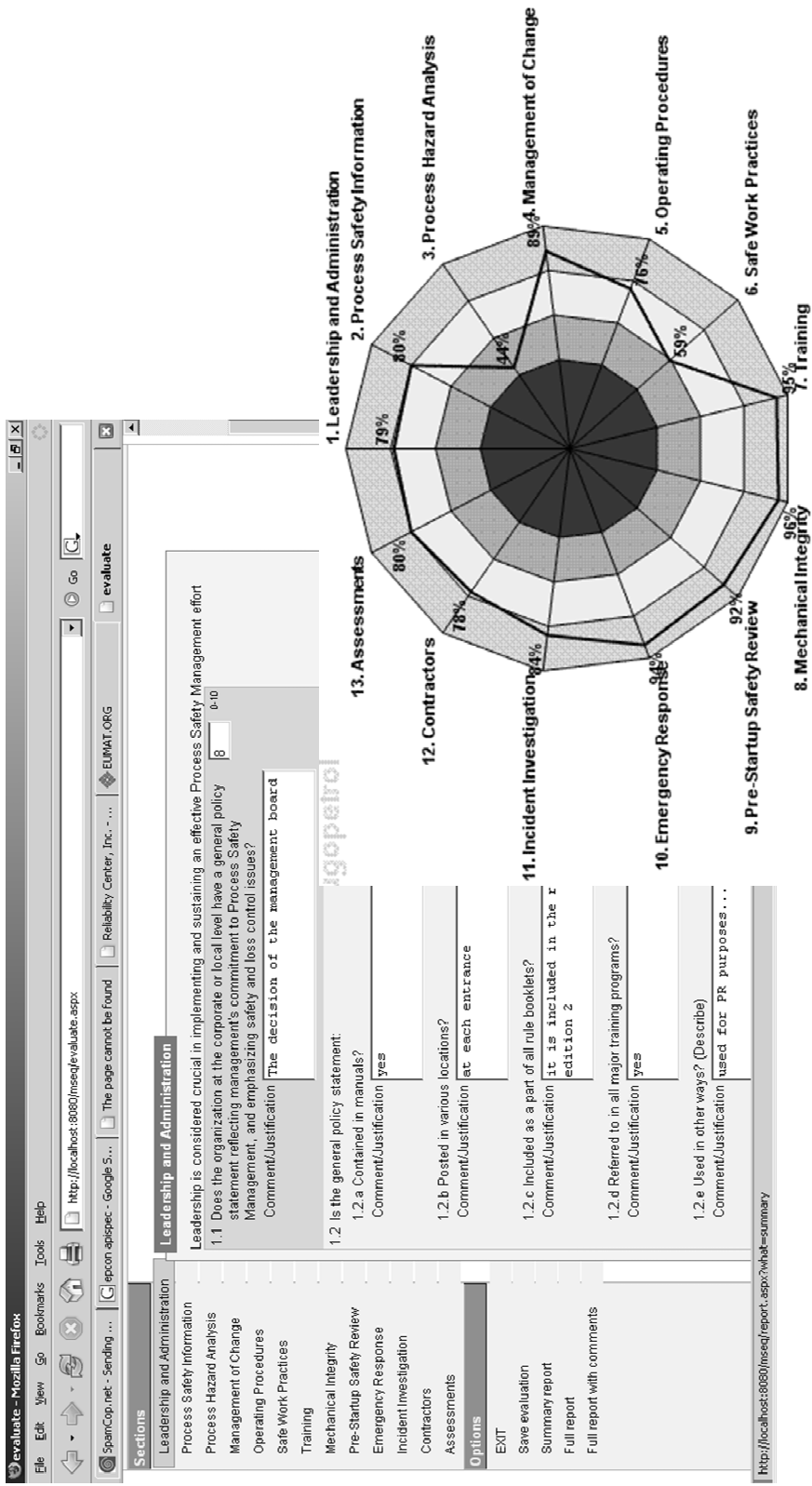


Figure 6. The MSEQ module.

2.2.3 RCM

RCM (Reliability-centered maintenance module) covers all the aspects of the classical RCM approach: Failure Mode and Effects Analysis (FMEA), Failure Classification (FCn), Failure Characteristics Analysis (FCA) and Maintenance Strategy Selection (MSS). Furthermore, the RCM application allows definition of equipment templates where all the data for all four phases of the analysis can be predefined, thus allowing fast and efficient data entry. The module is completely web-based and integrated with other elements of the system.

The RCFA module (Fig. 8) identifies an organization's most significant annual losses and supplies the knowledge to identify the causes and possibly eliminate their recurrence in the plant in the future. RCFA relies on the comprehensive and effective data collection which is absolutely needed in order to manage the knowledge about failures and their (root) causes. RCFA should provide better insight both in what could go wrong and in what has gone wrong, using Basic Failure Modes & Effects Analysis (FMEA) and Opportunity Analysis. The end result is the analyses build a business case for which events are the best candidates for Root Cause Analysis based on the Return-On-Investment.

2.2.4 HSE – HSSE

Occupational safety and health is the discipline concerned with protecting the safety, health and welfare of employees, organizations, and others affected by the work they undertake (such as customers, suppliers, and members of the public). HSE Module is based on current European and American standards in the area (i.e. Seveso II, ATEX, EPA requirements), and is designed as a checklist against the requirements in order to identify critical equipment and show compliance with protection/mitigation measures. The security related part of the system (HSSE) is currently always done on the ad-hoc basis, as a data base of security related scenarios. One of the reasons for such a solution is the lack of norms or de-facto standards in this area, hence, customers requirements are applied.

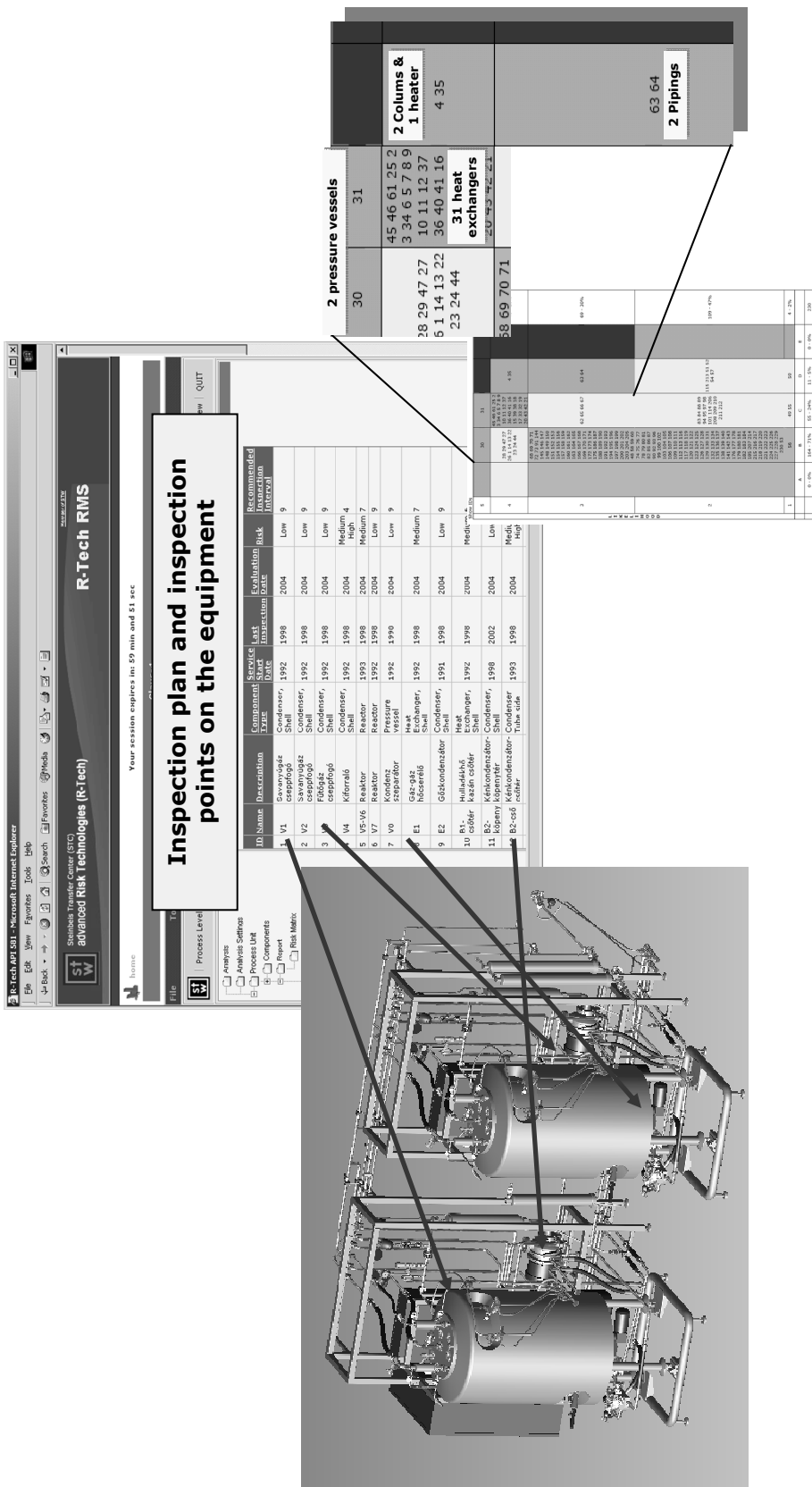


Figure 7. RBI – Inspection plan in iRiS.

2.3 Modules of iRiS Power

iRiS Shell (Fig. 9) includes several packages including plant data management, material database, case histories and documentation base, as well as the modules “iRiS-Power On-line Monitoring package” applied to on-line monitor creep and fatigue damage using the TRD and EN code. The Package “iRiS Basic Life Assessment” (II) is applied to administrate plant data, to use well established methods for the evaluation and analysis of the situation of the plant, and for basic life management purposes. In the “iRiS Advanced Life Assessment” Package (III), material data is provided, as well as methods for creep and fatigue analysis. The most advanced techniques include risk modeling and inspection planning, Reliability Centred Maintenance, and Root Cause Failure Analysis (RCFA), used in the “iRiS Risk Based Life Management” Package (III).

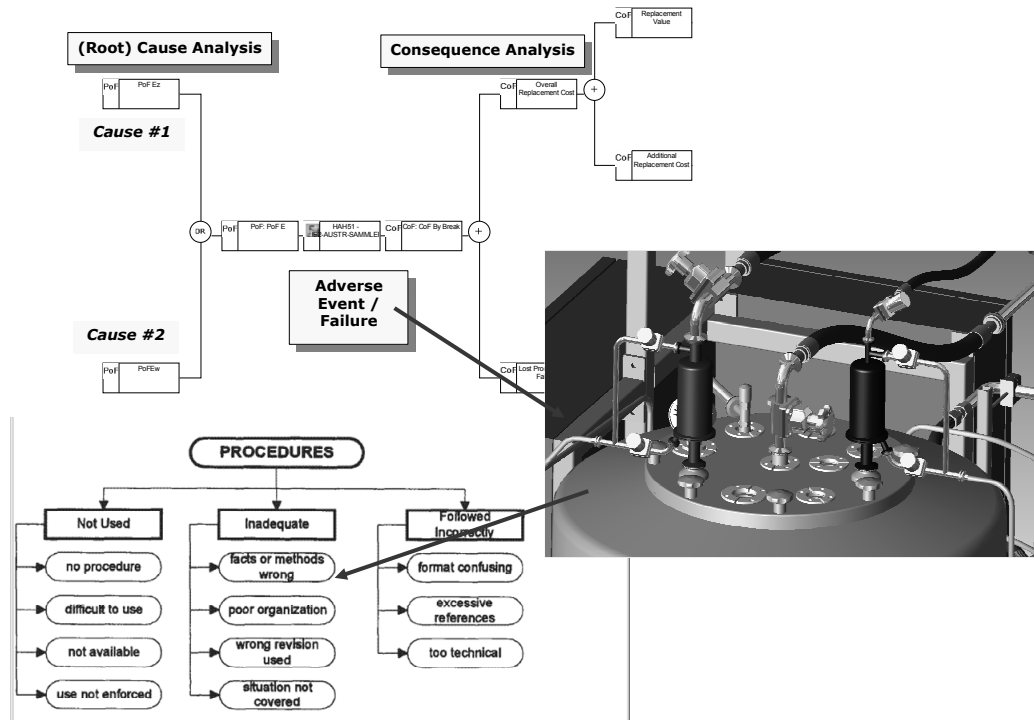


Figure 8. The RCFA module of iRiS.

The modules for handling technical information can be broadly classified into calculation modules and data and documentation modules. The calculation modules comprise modules in the field of damage calculation due to creep and fatigue, optimization of decision-making, replica analysis and others. The data and documentation modules include databases to store data such as component data, analysis data, material data, case histories, NDT data, and standards.

iRiS Risk module (Fig. 10) allows multi-criteria decision-making for ranking of components for the next inspection, according to different predefined (e.g. costs,

remaining life, safety) and/or user's defined criteria. This module is closely linked to other modules in the risk-assessment suite. It allows the user to model the possible effects of an adverse event (i.e. leak or break of a piping component) on one side (consequences) and on the other side to model the possible causes of the event. Using the results of the remaining life assessment as the basis for the probability of the event calculation, as well as the typical effects of the inspections on the probabilities of failure, it is possible to perform risk ranking and quantify the effects of the future inspections in function of risk reduction.

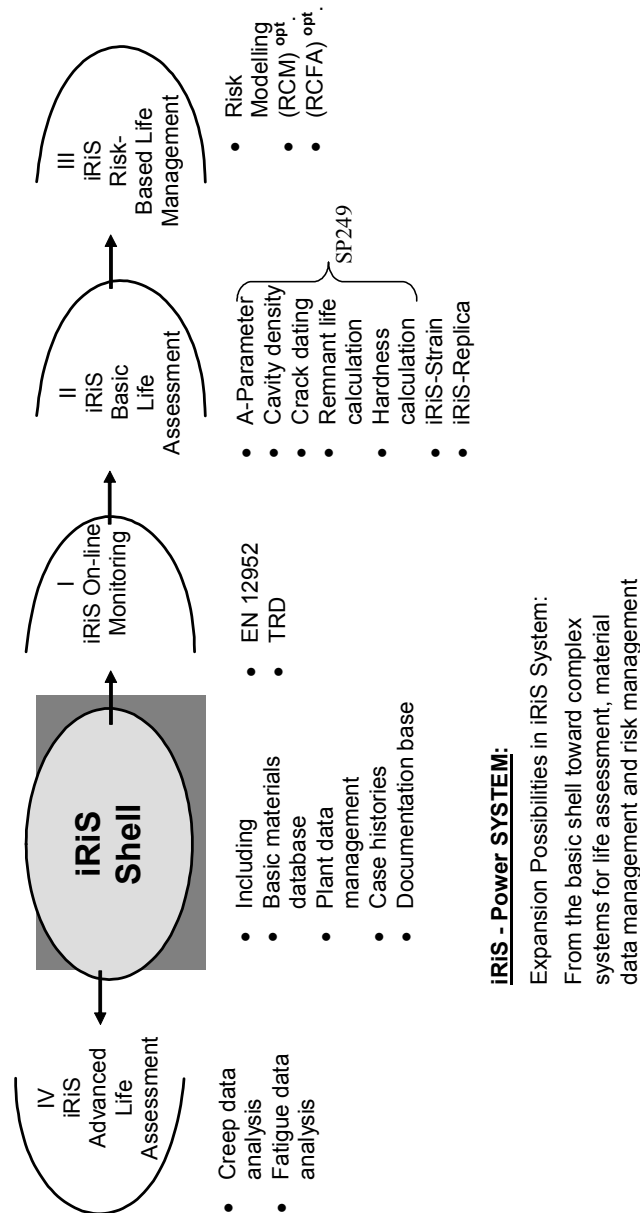


Figure 9. Main modules of iRiS-Power.

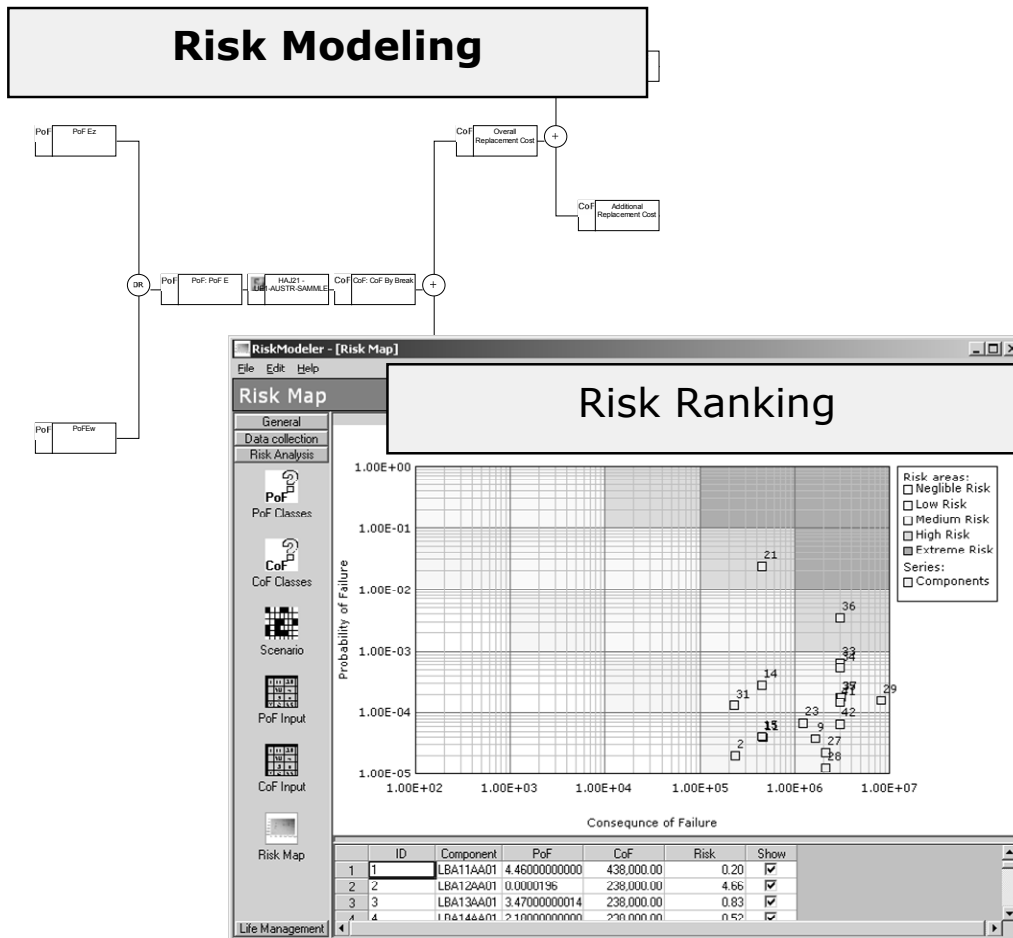


Figure 10. Main steps in risk analysis in iRiS-Power.

To ensure that high usability of the software, R-Tech provides training seminars in addition to adapting iRiS-Power to customer’s specific needs by programming new additional tools. Furthermore, maintenance and hotline support are available. A full range of services in the field of material and component testing, analyses, computation and quality assurance is also offered.

3. Applications of iRiS

iRiS has been developed and applied following the market demand. It responded to the increasing need to have flexible solutions in the new and relatively complex area of risk-based approaches in maintenance and inspection. The system is addressing primarily users introducing these approaches and not necessarily having large own teams to do it alone. It is, therefore, no wonder, that among successful applications one has countries like Hungary, Slovakia, Serbia (for iRiS Petro) or India and Malaysia (for iRiS Power).

The applications in both petrochemical and power industry have shown that substantial improvement can be obtained in inspection optimization (Fig. 11) and inspection and maintenance planning (Fig. 12).

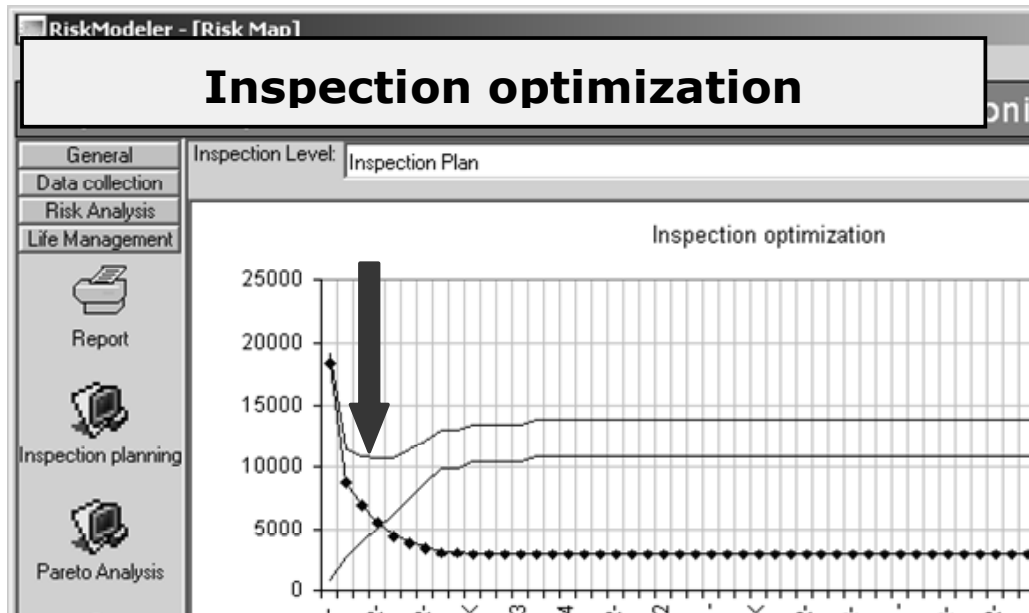


Figure 11. Defining optimized scope of inspection.

4. Advantages of the iRiS-based integrated solution

iRiS-System (both the “petro” and the “power” part) is a tool for plant engineers working in the fields of remaining life assessment, R&D as well as in maintenance and inspection. As a solution it has the following main characteristics:

- “Open”
to allow the customer’s favorite self-made tool to be included. It is adaptable to specific user’s needs, e.g. with respect to data storage and/or integration of customer-specific programs, special interfaces or the monitoring system.
- “Integrated and Intelligent”
to grant effective work by ensuring that i.e. data is typed only once, the system suggests default values etc.
- “Intranet and internet-oriented”
as nowadays data exchange takes place over the network sharing the same data with the effect that sources of errors are minimized; it means that all user may share the same information whenever needed with customer-depending security levels which means that different customer groups see only their information and that they may have different write/read/change rights.

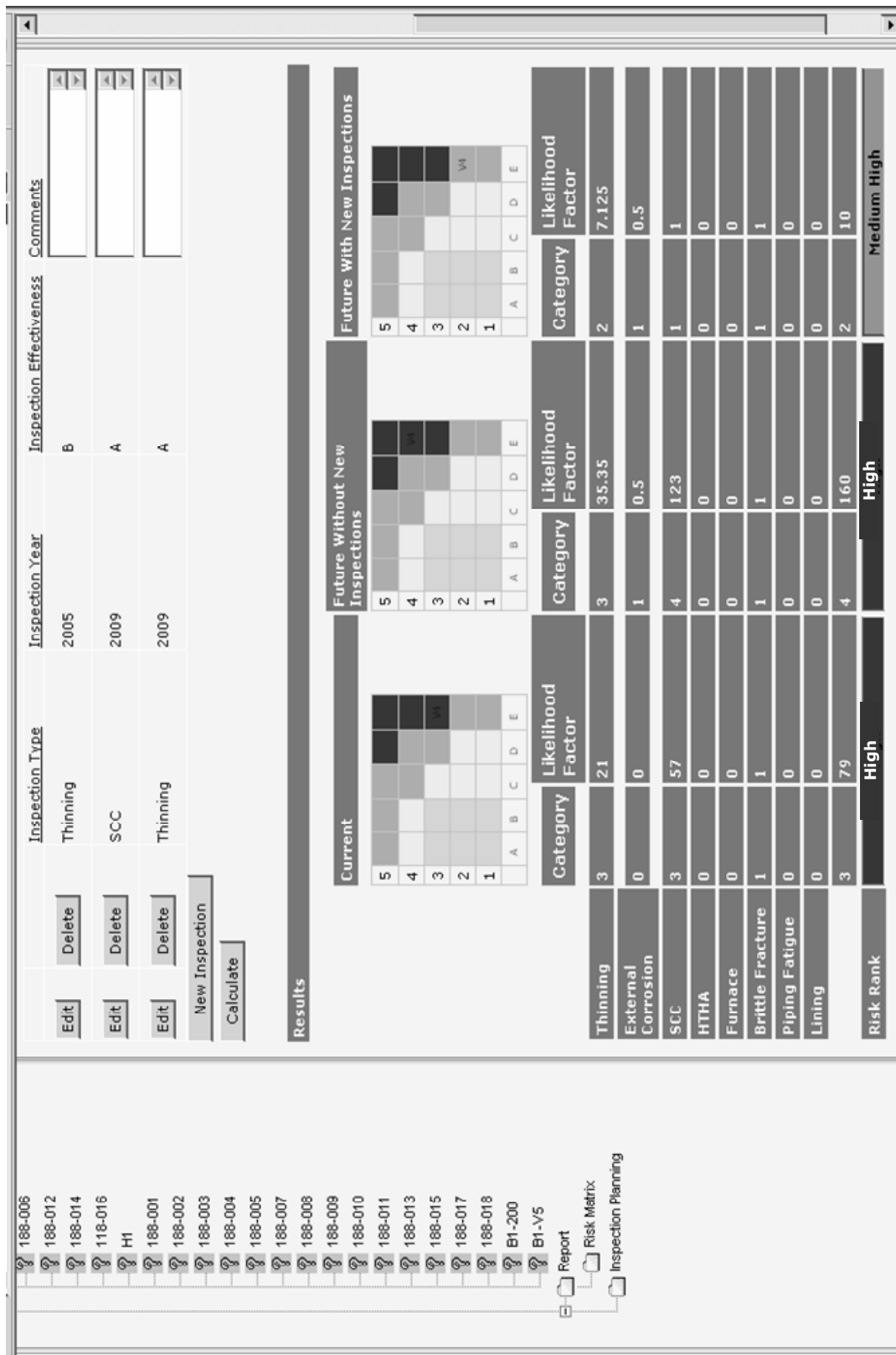


Figure 12. Planning inspections based on risk: Knowing risks before and after, knowing the risk in the case of not-performing an inspection.

Economic advantages of iRiS-Power are:

- Increased effectiveness through the reuse of, and a faster access to collected knowledge
- Decreased costs owing to improved decision-making on the basis of new techniques
- Optimal price-performance through the modularity of a fully scalable solution.

5. Conclusions

By introducing integrated solutions like the one in iRiS, significant improvement can be achieved. Among them are primarily:

- more effective satisfying legal requirements,
- improving overall business practice and
- achieving savings on e.g. losses prevented or reduced insurance costs.

The form of the integrated solutions must be adapted to the particulate user's needs, i.e. one cannot, for instance, say that "integrated must be big". Such solutions must, therefore, span from small, ad-hoc consulting actions for on-going activities and pilot-projects, to large projects covering large nets of plants or whole countries, and they should include the on-the-job and academic training and certification if so desired by the client.

References

- [1] Preliminary Research and Development Roadmap for Protecting and Assuring Critical National Infrastructures Transition Office of the President's Commission on Critical Infrastructure Protection, Washington, D.C., July 2002.
- [2] ETPIS – European Technology Platform Industrial Safety – www.industrialsafety-tp.org.
- [3] Jovanovic, A. et al. (2004). Concept of Risk-Based Monitoring and its Application for high-temperature components in power plants. Proceedings of the PSAM7 Conference (7th International Conference on Probabilistic Safety Assessment and Management), June 14–18, 2004, Berlin, Germany 2004.

- [4] Jovanovic, A. (2004). Overview of RIMAP project and its deliverables in the area of power plants. Elsevier 2004. International Journal of Pressure Vessels and Piping 81, pp. 815–824.
- [5] RIMAP CEN Workshop Document, CEN Workshop 24 “Risk-Based Inspection and Maintenance Procedures for European Industry”, Jovanovic A., Main Editor, Final Draft Document in 60 days public discussion at CEN, April 2007.
- [6] ASME CRTD, Vol. 41, Risk based Methods for Equipment Life Management, ASME International, New York, 2003.
- [7] API 581 – Base resource document on risk based inspection, American Petroleum Institute, US, (1996).
- [8] API 580 – American Petroleum Institute; Risk-based inspection – recommended practice, American Petroleum Institute, US, 2000.
- [9] EEMUA Publication #206 – Risk Based Inspection: Guide to effective use of the RBI process, ISBN 0 85931 150 3, Engineering Equipment and Materials Users Association (2006), <http://www.eemua.co.uk>.
- [10] Health and Safety Executive; Best practice for risk based inspection as a part of plant integrity management – contract research report 363/2001, Health and Safety Executive, (2001).

Coating integrated optical fibres for monitoring of boiler heat transfer surfaces

S. Sandlin, A. Hokkanen and T. Varis

VTT Technical Research Centre of Finland, Espoo, Finland

Abstract

High temperature corrosion is often a problem in biomass combustion and waste incineration boilers. Critical components are heat transfer surfaces, such as water walls and superheaters. Instead of using more corrosion resistant high alloy steels for critical components more economical low alloy steels can be protected by coatings. These coatings can be applied by thermal spray techniques. This work investigates the possibility of integrating thin copper jacketed optical sensing fibres in this kind of coatings during the spray process. This kind of sensing fibres would provide new methods for managing boiler life and controlling the combustion process. The coating embedded fibres can be used for example to locate hot spots and places where corrosion and erosion are destroying the coating. In this work the cheapest possible method (direct spraying) for embedding the fibre was chosen even if it was known that this is close to the limits of what the fibre can sustain in order to retain its optical and mechanical integrity. The results of the direct spraying method are presented and some more advanced methods will be discussed. Methods for monitoring the state of the sprayed coating can extend from simple on-off methods to advanced distributed sensing methods. On-off methods mean monitoring the light transmission of the embedded fibre; when the corrosion or erosion reaches the fibre and destroys it the light transmission will cease. Using optical time domain reflectometry (OTDR) also onset of fibre destruction can be observed as well as the locations of these critical points. More advanced techniques are the use of in-fibre Bragg gratings for temperature and strain monitoring and the use of distributed temperature sensing (DTS) for hot spot detection. Both OTDR and DTS techniques will be presented in this work. The work presented was mainly done in the CEC funded Craft project PROCOMO (Protective coatings with combined monitoring system to control process conditions in boilers). The DTS demo shown in this work was carried out within the STYX project, which was a part of the Finnish nuclear safety research

1. Introduction

Fibre optical sensors have existed for a few decades. A simple introduction to the topic can be found for example in the book by Krohn [1]. Metal embedded in-fibre Bragg gratings for temperature and strain sensing have been presented in two earlier Baltica-conference papers [2, 3]. This time we concentrate on the distributed fibre optical measurement techniques. This unique feature of the fibre sensing technology is the ability to determine temperature and/or strain of the fibre at discrete intervals (usually about one meter) along its entire length. In the following we use the DTS for distributed temperature sensing and DTSS for distributed temperature and strain sensing. Optical time domain reflectometry (OTDR) is a simpler but similar technique used to estimate the optical light attenuation along the fibre. This technique is used to detect fibre breakage and points of undesired high losses in optical fibre telecommunication networks. In this work OTDR is used to measure the attenuation of light in fibres embedded in thermal spray coatings. All these techniques relay on analysing the “echoes” i.e. backscattering of light pulses launched into the fibre. In OTDS it is enough to record the intensity of the backscattered pulses as function of time of flight at a single wavelength, whereas spectral analysis of the backscattered pulses is needed to extract the temperature and strain distributions along the fibre. DTS and DTSS techniques have been used to monitor for example dams, tunnels, railways, power lines, pipelines, mines etc [4, 5].

2. Distributed fibre optical monitoring techniques

Distributed fibre optical sensing is either based on Raman- or Brillouin backscattering of laser pulses launched into the optical fibre. As a result, some anti-Stokes and Stokes photons are generated. A fraction of these propagate backward along the fibre and can be collected at launching end i.e. the measurement can be done with access to only one fibre end. The two scattering processes are illustrated in Fig. 1. In Raman scattering the amount of anti-Stokes photons produced in the scattering process is temperature dependent while the amount of Stokes photons is almost temperature independent (see Fig. 1). Therefore the ratio of the intensities of the anti-Stokes and the Stokes peaks can usually (not necessarily always) be taken as an intensity independent measure of temperature along the fibre. In Brillouin scattering both the wavelength of the anti-Stokes and Stokes peaks as well as the intensity of the peaks are strain and temperature dependent, as shown in Fig. 1. Both the temperature and strain can therefore be determined simultaneously and independently at every 1 m along the fibre [5]. The spatial distribution of strain and temperature along the fibre is given by the time-of-flight of the light pulses as in Raman technique. The Raman based distributed temperature monitoring technique is the older, cheaper and more well-known of these two. The Raman technique was therefore chosen as

the potential temperature monitoring technique to be used together with fibres embedded by thermal spraying. In the following we therefore concentrate on the Raman based DTS.

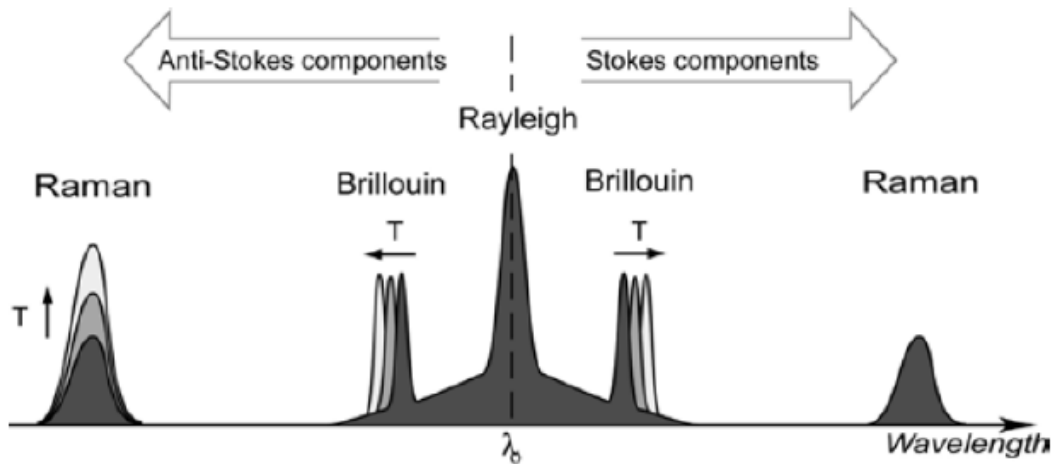


Figure 1. Three different light scattering mechanisms in an optical fibre. The behaviour of the Stokes and anti-Stokes peaks due to temperature in Raman- and Brillouin scattering. The strain dependence of the Brillouin peaks is not shown. The relative peak heights are not to scale. The picture is from a paper by Inaudi & Glisic [6].

2.1 High temperature applications

The sensing fibre jacket is of vital importance for high temperature applications. For temperatures up to 400°C fibres with polyimide jacket can be used; for higher temperatures fibres with metal jacket are needed. In commercial high temperature applications the fibre is inserted in a small (diameter 3 mm) tube and nitrogen purging may be used to avoid oxidation of the fibre jacket. A rigid and hermetic embedding would eliminate the oxidation problem but avoiding high attenuation caused by microbending is a very challenging task, as seen later in this paper. Further, the low thermal expansion of the silica fibre may cause problems.

The greatest benefit of a DTS system over other temperature monitoring systems is the possibility of recording the temperature distribution along the whole fibre “instantaneously” (in practice seconds to minutes). Due to the limited spatial resolution (about 1 m), a DTS system is more suited for detecting local temperature extrusions and extremes than for measuring accurate temperatures. Protecting and installing the fibre (fibres) is a main problem in high temperature applications.

2.2 DTS specifications

The technical performance of a typical DTS instrument is given by Downes and Leung [7] as:

- Range 10 km
- Positional resolution 1 m
- Temperature resolution 1°C
- Accuracy $\pm 1^\circ\text{C}$
- Measurement time for 2°C resolution < 10 min.

Most DTS manufacturers report considerably better temperature resolution (0.01–0.05°C) and shorter measurement times than above. There are also very special and expensive DTS instruments with spatial resolution of 0.1 m, which are based on photon counting. These are still prototypes. However, the performance of a DTS is very application dependent. Fig. 2 illustrate the definition of spatial resolution and Fig. 3 gives the response of the DTS signal to a local hot spot [8]; the size of the hot spot has to be larger than the spatial resolution in order to get a temperature reading close to the actual temperature at the centre of the hot spot.

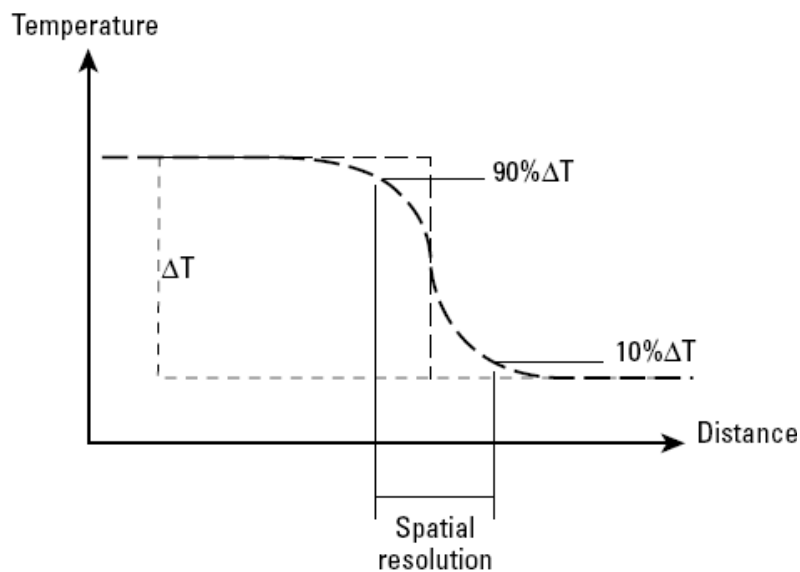


Figure 2. Definition of the spatial resolution of a DTS system [8].

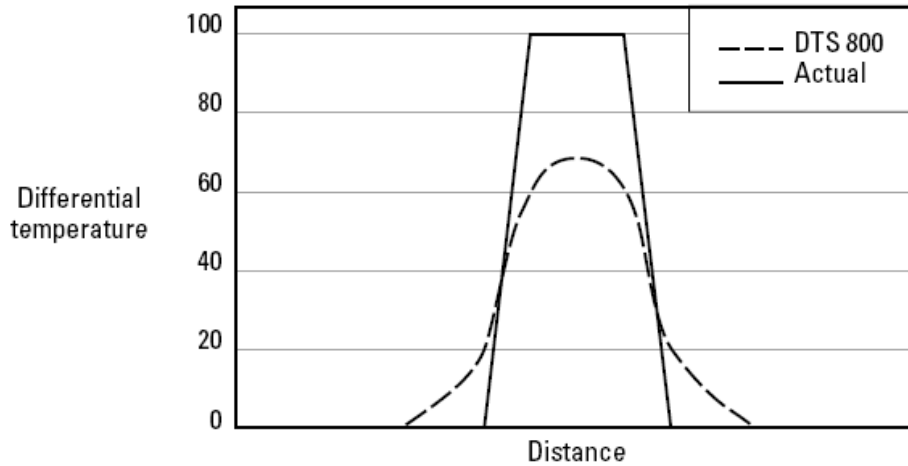


Figure 3. Response of a DTS to a local hot spot. The dashed curve shows the instrument response to the actual temperature [8].

3. Embedding of optical fibres using thermal spray

The laboratory specimen used for the fibre embedding was a steel tube with a diameter of 30 cm and a length of about 60 cm. A length of 33.5 m of copper jacketed fibre was wound around the tube (32 turns) as shown in Fig. 4. The tube surface was sandblasted before the fibre was installed. The thickness of the optical fibre including the copper jacket is 175 μ m. The fibre type is graded index 50/125. The fibre ends, by which the embedded fibre was connected to the measurement instruments, are protected by small stainless steel tubes, which can be seen to the left and to the right in Fig. 4. At the points where the fibre leaves the coating and enters the small protecting stainless steel tubes the fibre was fixed by ceramic adhesive to avoid fibre breakage due to accidental movement. The thermal spray process is shown in Fig. 5. The steel tube on which the fibre is wound is rotating during the spray process. The thickness of the applied Ni20%Cr coating is about 300 μ m. The final sprayed coating with the embedded fibre can be seen in Fig. 6. The embedded fibre can still be seen as a banded structure around the spray coated surface. Based on visual inspection the coating seems to be of good quality. The optical properties of the embedded fibre, however, need to be evaluated using OTDR technique or by light transmission measurements. Fig. 7 shows an optical microscopy image of a cross-section of one of the first successfully embedded fibres. In this case an arc sprayed ferrous base amorphous alloy coating (0.9%C; 2.8%B; 22%Cr; 1.5% Mo; 1–2%W) was used.

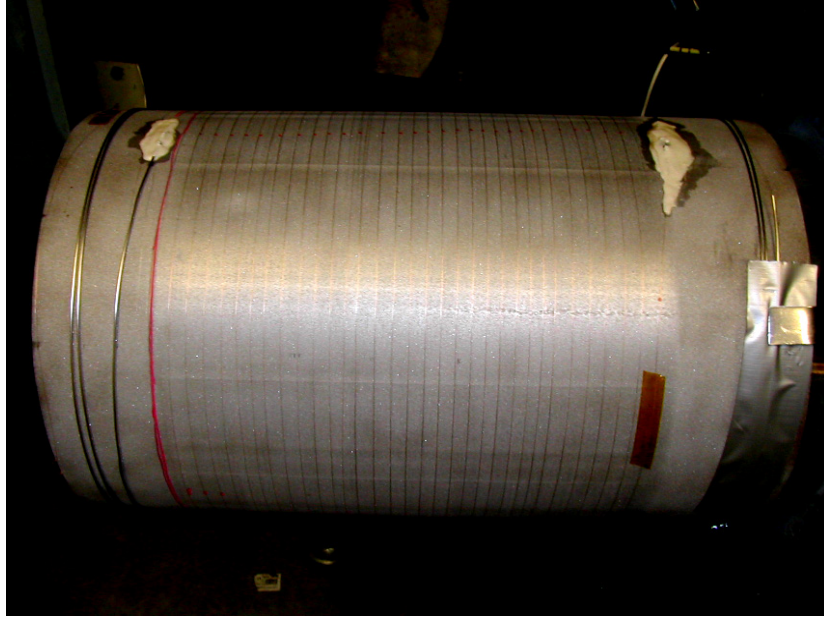


Figure 4. A steel tube with a diameter of about 30 cm and a length of about 60 cm was used in the evaluation of the fibre embedding using thermal spray coating. This picture was taken before spray coating. 32 turns of copper coated optical fibre are wound around the tube. The diameter of the fibre, including the copper jacket, is 175 μm . The fibre pigtailed used to connect the embedded fibre to the measurement instruments are protected by small stainless steel tubes which are seen to the left and to the right.



Figure 5. The thermal spray process. About 33.5 m of fibre was embedded in an about 300 μm thick layer of Ni20%Cr coating. The lead-in and lead-out fibres in small stainless steel tubes to the left and to the right are protected by aluminium foils during spraying.

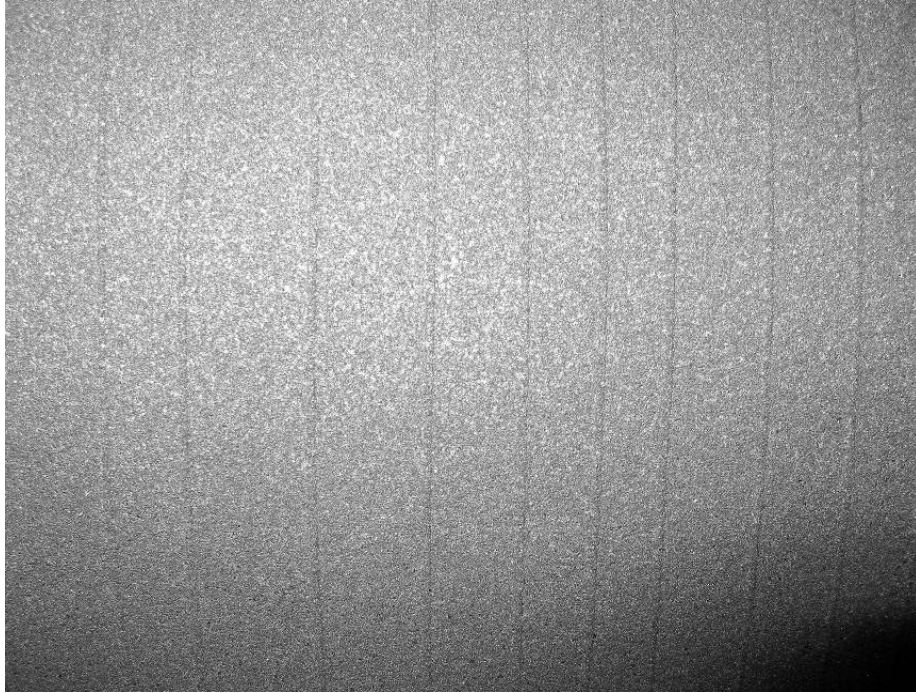


Figure 6. The sprayed Ni20%Cr coating. The embedded fibre can still be seen as a banded structure around the steel tube.

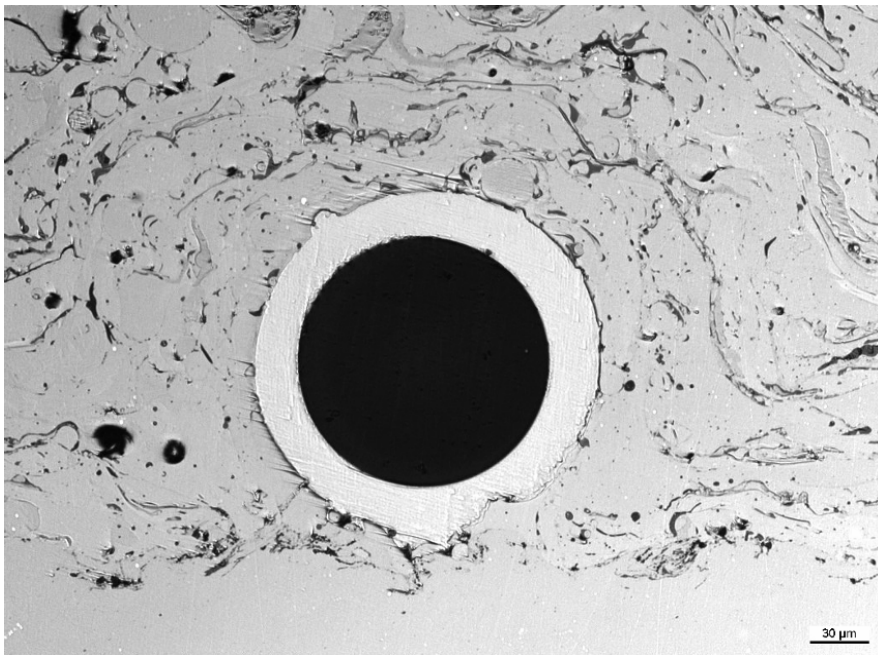


Figure 7. A cross-section of an optical fibre embedded in arc sprayed ferrous base amorphous alloy coating. The diameter of the fibre the (the black circular area) is 125 μm. The gray ring around the fibre is the metal jacket.

4. Optical measurements

The embedded fibre described above was intended for demonstration of the DTS measurements during thermal cycling. However, to evaluate the condition of the embedded fibre both OTDR and light transmission measurements were made. These attenuation measurements were performed from both ends of the fibre both at room temperature and at elevated temperature.

4.1 Light attenuation in the embedded fibre

Fig. 8 illustrates the room temperature attenuation measurements on the embedded fibre using OTDR-technique. The measurements are taken from both ends of the embedded fibre by launching light pulses into the fibre and measuring the backscattered “echoes”. Green and yellow refer to the fibre cables used to connect the embedded fibre to the instrument (OTDR). Curves measured with 1 and 5 minutes signal averaging are shown. In the middle of Fig. 8 a steep decrease in reflected power is seen. The strong attenuation starts from the points where the fibre enters into the sprayed coating. As can be seen, the reflected signal drops to the noise level when the pulses have travelled about three meters in the coating. The behaviour is similar as measured from both ends although the signal from the green end ends up at a higher noise level. The total length of the embedded fibre is 33.5 m. The vertical lines in Fig. 8 show the place where the copper jacketed fibres enter the sprayed coating. The transmission properties of the embedded fibre were also measured using a HP 8153A power meter. These measurements showed that less than a 0.0001 part of the incident light was transmitted. Due to these results no attempts of trying to do DTS measurements were made as the temperature measurements would have been corrupted.

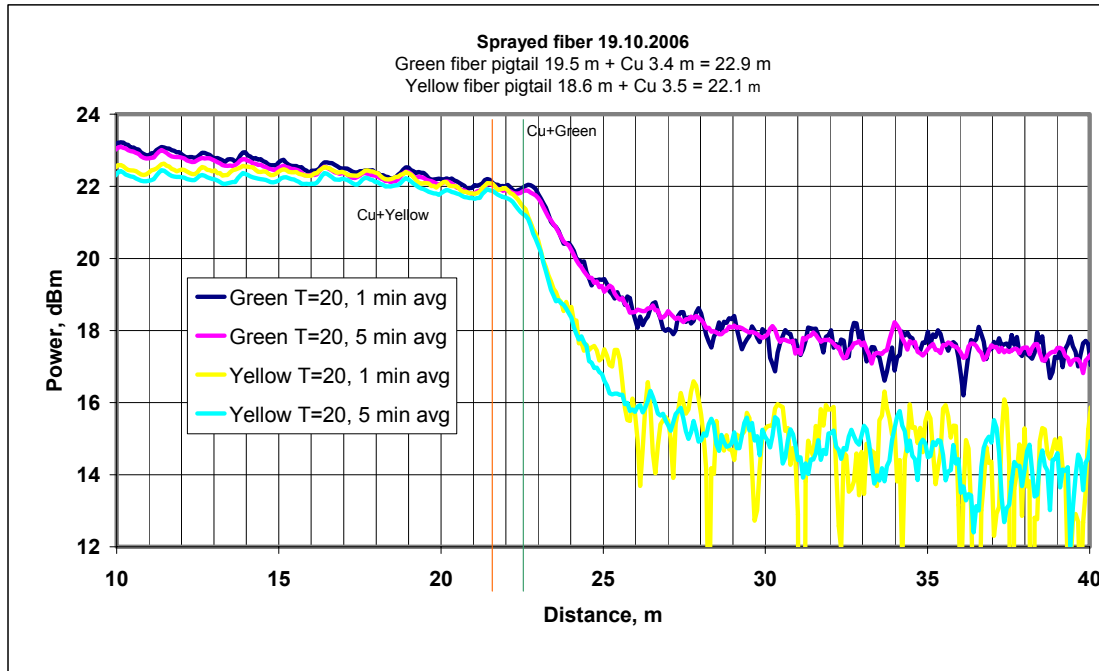


Figure 8. Light attenuation in the embedded fibre; the measurements are taken from both ends at room temperature. Green and yellow refer to the fibre cables connecting the embedded fibre to the OTDR instrument. The almost horizontal curves to the left show the attenuation in the connection fibres. A steep increase in attenuation can be observed from the points where the fibre enters the sprayed coating.

The next step was to measure the attenuation at elevated temperatures. It was assumed, that the reason for the high attenuation might be microbending due to impact of the molten metal droplets on the fibre during the spray process. Possible pores in the sprayed material close to the embedded fibre may also contribute to the amount of microbending. Because of the low thermal expansion of the fibre material (fused silica) the degree of microbending should decrease upon re-heating the fibre and the thermal spray coating assembly. Some degree of recovery of the light guiding properties of the fibre was therefore expected upon heating. Fig. 9 shows the test object in a bogie hearth furnace before closing the door. The two fibre pigtails protected by small stainless steel tubes are coming out from the furnace in the lower part of the picture. Fig. 10 shows the OTDR response of the fibre during heating. No sign of recovery was observed and unfortunately a strong reflection peak (Fig. 10) suddenly appeared when the temperature was around 400°C. At this moment the measurement was switched to the other fibre pigtail (yellow) and unfortunately a similar reflection peak had also appeared from this end as can be seen in Fig. 11. These reflection peaks made further measurements useless because there is always an about 10 m long dead zone after such strong reflections. This dead zone covers the whole length (3 m) of embedded fibre from which backscattered signals were earlier received (see Fig. 8). The reflections seem to originate from the points where the

fibre enters the sprayed coating. The possibility of dealing with a ghost signal due to multiple internal reflections (from connectors, splices etc) was eliminated by introducing an extra fibre link between the OTDR and the fibre pigtails. A reflection from a splice would indicate that the splice is of bad quality, however, both splices were found to be good. This extra fibre link can be seen as a shift in the scale on the x-axis in Fig. 11 as compared to Fig. 10. If the reflections were ghost signals their positions should have shifted due to the extra length of fibre. No such effect was observed. It is therefore concluded that the fibre broke, due to heating, at the points where it enters the sprayed coating. The breakage may be due to pulling forces caused by thermal expansion of the protecting stainless steel tubes. Although this embedding experiment cannot be considered very successful, a positive aspect should be noted. In an earlier similar embedding test no signal from the embedded fibre was received at all; in this case signals from the first three meters of the embedded fibre was observed from both ends. This embedding method may well be functional for some applications other than DTS, for instance Bragg gratings that does not need very long embedded fibres. However, the use of suitable prefixing methods may considerably decrease the attenuation in embedded fibres and hence, make it possible to use much longer embedded fibres than three meters. The prefixing should protect the fibre from direct contact with the thermal spray droplets. It is also evident that no part of an un-embedded fibre should be exposed to high temperatures. Further, monitoring methods relaying on wavelength measurements (such as Bragg gratings) should be preferred instead of intensity based methods as the wavelength based methods are less sensitive to intensity variations in the returning light signal.



Figure 9. The test object with the embedded fibre is ready for elevated temperature tests in a bogie hearth furnace. The fibre pigtails protected by small stainless steel tubes are seen in the lower part of the picture.

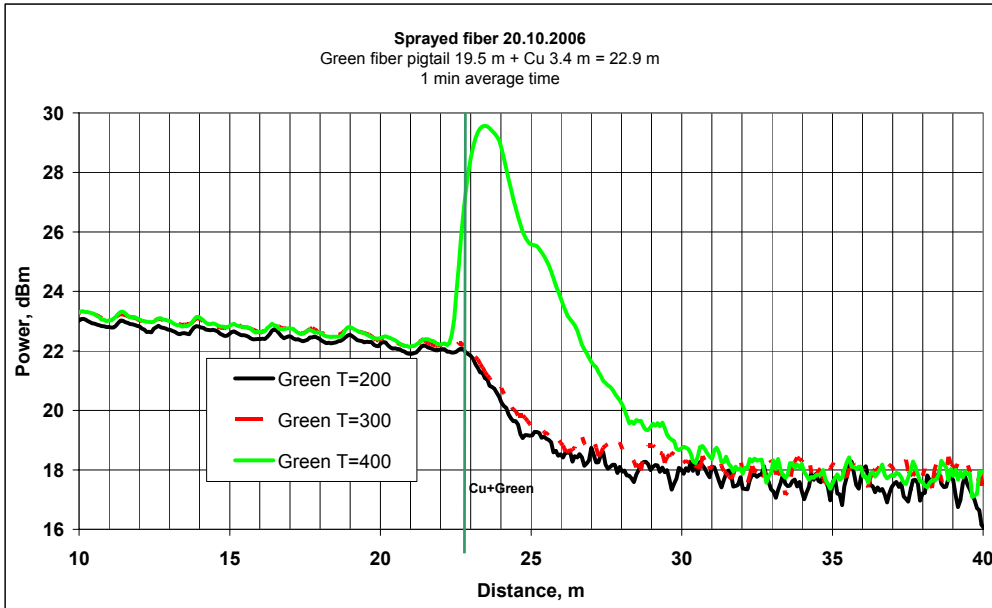


Figure 10. The light attenuation in the embedded fibre from the green end due to heating. Up to 300°C the OTDR-trace is similar to that seen at room temperature (Fig. 8). However, when the temperature approaches 400°C a strong reflection peak appears. The reflection comes from the point where the copper jacketed fibre enters the sprayed coating.

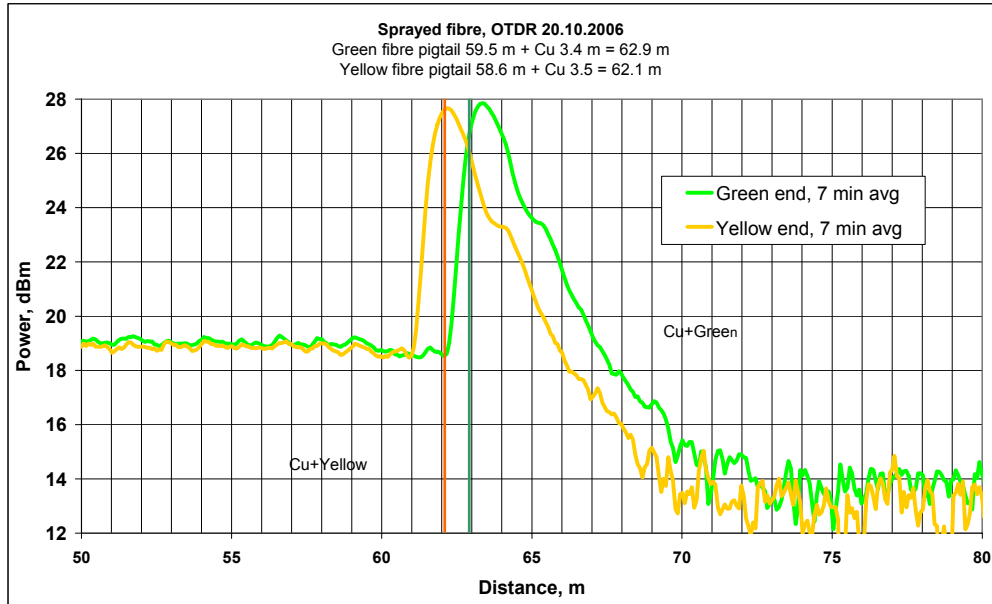


Figure 11. In this picture the OTDR response from the yellow end has also been included. A similar reflection as from the green end has appeared also here. This reflection also comes from the point where the copper jacketed fibre enters the sprayed coating. Notice the shift in distance as compared to Fig. 10 due to the introduction of an extra fibre link.

4.2 Distributed temperature measurement

Due to heavy light attenuation in the thermal spray embedded fibre no distributed temperature (DTS) measurement could be done on specimen shown in Fig. 9. The DTS measurement is therefore illustrated by another application. In the STYX project the coolability of a nuclear reactor core debris after a core melt accident was investigated. The core debris is simulated by a mix of sand and water which is heated by heating elements embedded in the sand. The appearance of local dry-outs is monitored as function of heating power and pressure by 48 thermocouples situated at different places in the sand. A rapid local temperature rise is an indication of a beginning dry-out. These measurement data were intended for further theoretical modelling of the coolability of the reactor debris after a core melt down accident. The DTS instrument used was a FTR-030 from Hitele Systems Ltd in UK. The vessel (diameter 30 cm) containing the sand, thermocouples (not installed when the picture was taken) and the heating elements is shown to the right in Fig. 12. The outside surface of this vessel is instrumented by 50 meters of optical fibre placed in a stainless steel tube with a diameter of 3 mm. The fibre is placed in 10 zones with 5 turns in each as can be seen in the Figure. For the measurements this inner vessel was inserted in the pressure vessel seen to the left in Fig. 12. This type of tube mounting is the classic way of doing high temperature DTS measurements. The fibre is wriggling inside the tube; an arrangement called “overstuffing”. This means that upon heating the fibre will straighten more or less instead of being stretched (due to the low thermal expansion of silica). For temperatures up to 400°C fibres with polyimide jacket can be used, but for higher temperatures metal jacket is needed, possible in combination with nitrogen purging to avoid corrosion. Unfortunately, a 3 mm diameter tube cannot be embedded in thermal spray coating; at least the tube should be flattened and prefixed to the substrate. No such approach was attempted. In the DTS demo presented here the maximum temperature was about 160°C. In this experiment a total length of 75 meters of fibre is monitored from one end of the fibre. There is about 52 meters of fibre inside the pressure vessel, whereas the rest of the monitored fibre length (23 m) is outside the pressure vessel. In Fig. 13 the temperature of each of the 75 one meter long parts of the fibre has been plotted against time. The curves showing temperatures close to room temperature are from the fibre parts far away from the heated pressure vessel, while the curves showing intermediate temperature are from the outer fibre parts which already are affected by the heat from the vessel. The uppermost (overlapping) curves represent the 52 meters of fibre inside the pressure vessel. The steep temperature increases at about 11:30 and 13:12 are due to increases in heating power and pressure in the vessel. During constant temperature periods the temperature given by the DTS usually stays within $\pm 1.0^\circ\text{C}$, which is well in agreement with the specifications given in section 2.2.



Figure 12. The STYX vessels. The inner vessel is shown to the right with ten zones of fibre (in a stainless steel tube of diameter 3 mm), five turns in each, wound on its outer surface. For the measurements the inner vessel was inserted into the pressure vessel shown to the left. The inner vessel contained sand, heating elements and 48 thermocouples.

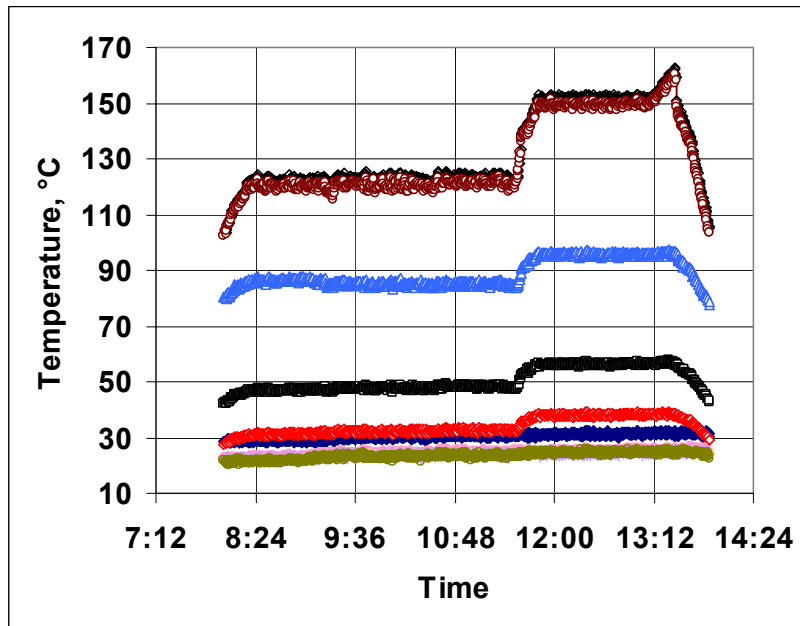


Figure 13. Distributed temperature measurement on the surface of the inner vessel shown in Fig. 12. Each curve represents one meter of fibre and there are 75 curves (most of them overlapping). The lower curves represent the parts of the fibre which are outside the pressure vessel and therefore subjected to less or no heating. The steep temperature increases at about 11:30 and 13:12 are due to increases in heating power and pressure in the vessel.

5. Conclusions

It was shown that a microscopically sound looking embedding of optical fibres can be achieved by thermal spray technique. Backscattered OTDR-signals from an embedded fibre with a copper jacket was observed from a distance of about 3 meters in the sprayed coating. This is, however, a too short length of fibre for the intended DTS application. Further, the points where the fibre enters the sprayed coating were once again considered to be problematic because the OTDR results indicated that the fibre broke at these points during heating. It was also concluded that the thermal spray process is a too violent process for a bare metal jacketed fibre. A prefixing process should therefore be used to protect the fibre before the spray process. No parts of an un-embedded fibre should be exposed to high temperatures. There may be two ways of improving the design:

1. The metal jacketed fibre is, coated by a thin metal foil, brazed or soldered into a small groove machined into the surface of the component. The foil with the fibre underneath should withstand gentle sand blasting before applying the thermal spray coating.

2. The fibre (or preferably two or more fibres) is attached to a metal foil in advance. This foil is then attached to the component using for instance soldering or brazing techniques. The attached foil should withstand gentle sand blasting before applying the thermal spray coating.

A similar technique to that mentioned in point 2 above has been used by Inaudi and Glisic [6] for attaching sensing fibres to composite coiled tubing in the oil & gas industry. Inaudi & Glisic first attached the fibre to a thermoplastic foil as shown in Fig. 14. This foil is then further embedded in the composite structure. However, manufacturing of a similar metal foil with embedded fibres for high temperature applications is of course a very challenging task. Further, the use of single mode fibres may be beneficial because these have a much smaller light guiding core than multimode fibres. The smaller core should be less prone outside mechanical disturbances.

Because of the high light attenuation in the fibre embedded by thermal spray technique the DTS-technique was illustrated by another application where the fibre was mounted in a protective stainless steel tube of diameter 3 mm. The system performance was shown to agree with given specifications. The FTR-030 instrument used for DTS-measurements has a spatial resolution of one metre; however, according to the definition of spatial resolution (Fig. 2) and the response to a hot spot (Fig. 3), there will be some cross-talk to the adjacent one metre fibre elements. In some applications the spatial resolution can be improved by coiling the fibre on the component surface. If this is not practical, an instrument with higher spatial resolution is needed.

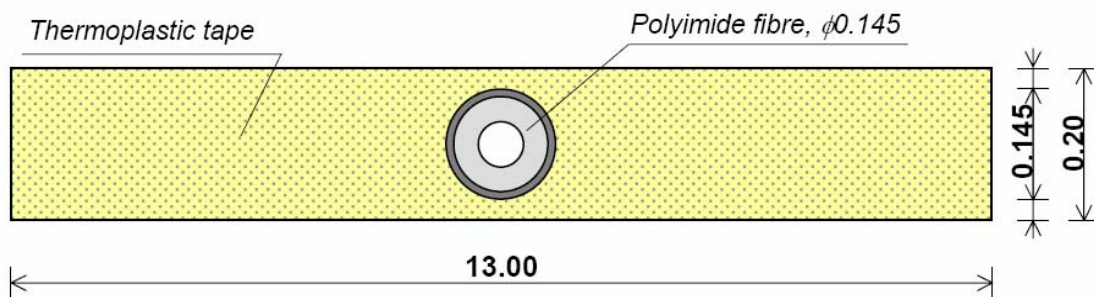


Figure 14. A thermoplastic foil with an embedded polyimide jacketed sensing fibre for further attachment to composite structures [6].

References

1. Krohn, D.A. 1988. Fiber optical sensors, fundamentals and applications. Instrument Society of America, ISBN 0-8777664-997-5. 239 p.
2. Sandlin, S. and Heikinheimo, L. 2001. Evaluation of a new method for metal embedding of optical fibres for high temperature sensing purposes”. Baltica V Conference. Condition and Life Management of Power Plants, Vol. 2, pp. 547–557.
3. Sandlin, S., Jeskanen, H., Li, X.C. and Björklöf, A. 2004. “Manufacturing and quality evaluation of component integrated fibre optical sensors for condition monitoring”. Baltica VI Conference. Condition and Life Management for Power Plants, Vol. 2, pp. 659–679.
4. Johansson, S. 2005. Distributed sensing of seepage and movements using optical fibres – Results from some embankment dams in Sweden. Internet address 2007-03-12:
<http://www.sensornet.co.uk/industries/dams/DamMonitoringArticle.cfm>.
5. Kluth, R., Watly, D., Farhadiroushan, M., Park, D.S., Lee, S.U., Kim, J.Y. and Kim, Y.S. Case study on distributed temperature and strain sensing (DTSS) by using optic fibre. Internet address 2007-03-12:
<http://www.sensornet.co.uk/download.cfm?type=document&document=118>.
6. Inaudi, D. and Glisic, B. 2006. Integration of distributed strain and temperature sensors in composite coiled tubing. SPIE Smart structures and materials conferencer in San Diego, March 2006. 10 p.
7. Downes, J. and Leung, H. Y. 2004. Distributed temperature sensing worldwide power circuit monitoring application. International Conference on Power Systems Technology – POWERCON 2004, Singapore, 24 November. Pp. 1804–1809.
8. Schlumberger. 2002. SENSEA Fiber optic monitoring systems. An overview of distributed temperature sensing. 20 p.

Method of small samples for assessment of properties of power plant components: sampling devices and stress concentration in dimples

A. Dedov, I. Klevtsov, T. Lausmaa and D. Neshumayev

Tallinn University of Technology (TUT), Tallinn, Estonia

Abstract

Long term exposure at elevated temperatures results in a deterioration of short-time mechanical properties of metal. Therefore the direct measurement of mechanical properties of power plant in-service components significantly increases the confidence in assessments of their remaining life. This requires the removal of metal samples big enough for mechanical testing and small enough that does not require the further repair of the sampled area.

Two devices for extracting samples from outside and inside component surfaces were designed and manufactured in Thermal Engineering Department of Tallinn University of Technology. The description of these sampling devices and experience in metal sampling as well as FEM analysis of stress distribution in dimples remained in components after sampling are presented in this paper. It was found that dimple in turbine rotor bore increases stresses about 1.2 times and on the external surface of steam pipeline about 1.5 times but absolute values of stresses in sampled area are low enough to allow further component operation without any restrictions.

1. Introduction

In order to increase the durability of power equipment and to make reasonable 3R decisions (run, repair, replacement) and, hence, to avoid unscheduled outages it is highly significant to be able to estimate the remaining life of the components as accurate as possible. The main criterion of life consumption assessment for components operated at the range of creep conditions is microstructure of metal [1]. Besides changes of metal structure however the deterioration in mechanical properties of metal occurs during service time that causes the decrease of power equipment reliability [2]. Thus the estimation of component durability and allowable life till the next mandatory inspection is based on the results of structural analysis and mechanical properties testing.

So-called non-destructive methods of metal sampling for further remaining life estimation of the power equipment were quite strongly developed in recent two

decades. The definition “non-destructive” is relative concept, since actually the metal is extracted in minimum amount that is enough to provide the data for remaining life assessment on the basis of structural analysis and mechanical properties testing results. The spherical dimple, remained after metal sampling, does not cause the inadmissible increase of stresses and does not require repair of the sampled areas. At the same time the sampling allows significantly improve the accuracy of remaining life assessment. It should be also mentioned that in respect to metal structure analysis this method has considerable advantage in comparison with method of replica because it is more representative and adequate and in complicated cases provides opportunity repeatedly perform analysis.

A detailed review of metal sampling methods and machines could be found in [3–6] both for based on mechanical sample extraction and on the electro-discharge machining.

Tallinn University of Technology (TUT) long-term experience in design and manufacturing of sampling devices, in metal extraction from external and internal surfaces of power plant components as well as FE modeling to confirm the convenience of sampled components for further operation without repair or restrictions are presented in this paper.

2. Sampling devices for metal extraction of small samples

2.1 General information

Two devices for metal sampling, one from external surfaces of power components and the second one from internal surface of turbine rotor bore were designed and manufactured in TUT.

Mechanical sampling machine MSM-1 for metal extraction from external surface was designed and manufactured in 1997. Mechanical sampling machine for metal extraction from internal surface MSM-2 was made later after getting experience in sampling with MSM-1 as well as in testing of samples. Operation principle of designed devices is based on mechanical extraction. The cutting element is hemispherical shell saw with diameter of 60 mm and wall thickness of 0.4–0.5 mm. The cutting edge of the saw is coated with abrasive coating (natural diamond or CBN bits). The hemispherical saw rotates around its axis of symmetry and at the same time moves round the axis, which is normal to rotation axis (and parallel to Y axis, Fig. 1). The maximum thickness of the extracted sample is about 2.2 mm. The geometry and size of sample are formed as intersection of sampled area and sphere with diameter about 58.7 mm (Fig. 2).

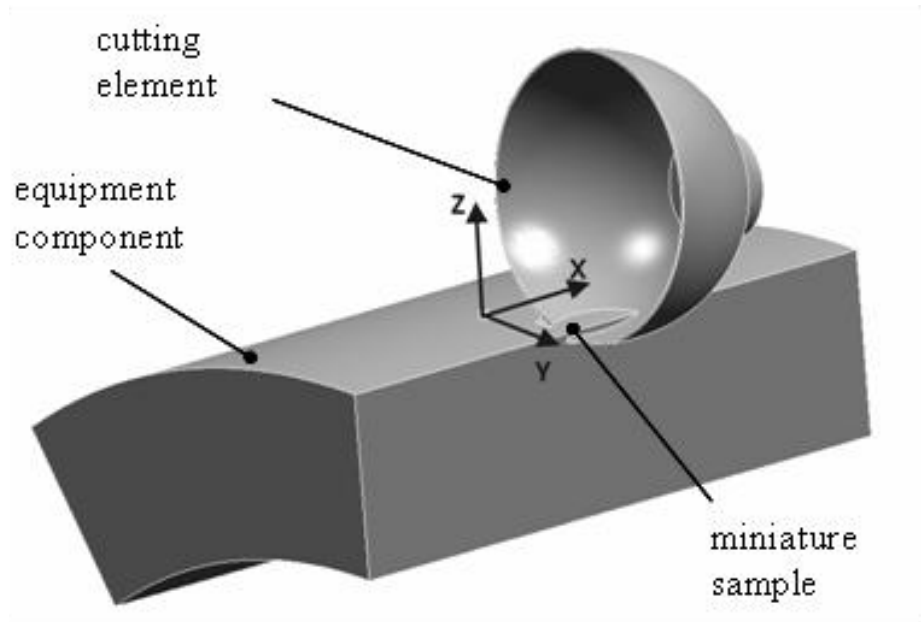


Figure 1. Principle scheme of sample extraction.

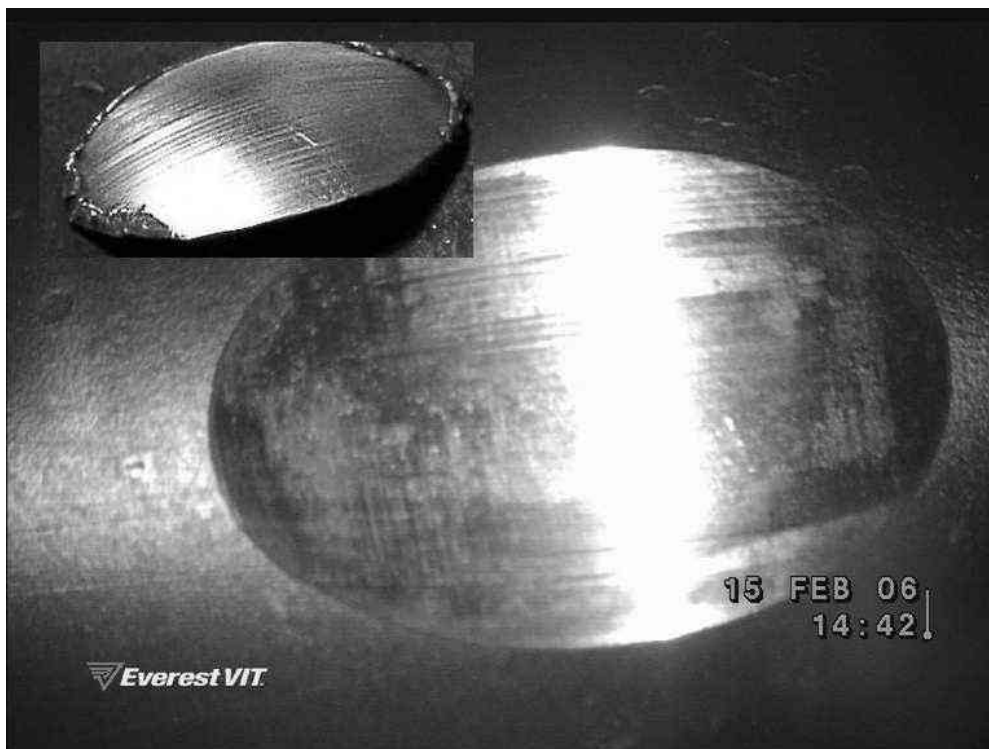


Figure 2. Metal sample and remained spherical dimple on the internal surface of the turbine K-200-130 high pressure rotor bore.

The depth of the dimple after sample extraction could be up to 3.0 mm and it is defined by the thickness of abrasive coating and by the accuracy of the hemispherical shell saw manufacturing. The latter is important to guarantee the

success of extraction process. Poor quality of the saw could cause jamming and emergency outage of cutting tool before the extracting process is completed. If the sampling is performed from the external surface of the component where the access to sampled area is easy, the uncompleted extraction leads only to the lost of the sample. In this case the area of unsuccessful sample extraction could be simply mechanically treated to minimise stress concentration. In the case of uncompleted extraction of the sample from internal surface of turbine rotor bore removing of the formed stress concentrator is rather difficult. It means that the accuracy and reliability of sampling machine should be very high.

Thermal Engineering Department (TED) experience shows that maximum number of samples which could be extracted by one hemispherical shell saw usually alters from 8 to 20. It generally depends on the following factors: accuracy of the saw, conditions of cutting area cooling, quality of abrasive coating, velocity of hemispherical shell rotation and feeding, properties of sampled material, sampling area location.

During sample extraction the area in the vicinity of cutting is cooled by mixture of water and concentrate of standard emulsion for mechanical cutting in the ratio according to recommendations of emulsion producers.

2.2 Sampling device for metal extraction from external surface of the components

Sampling device for metal extraction from external surface of the components (MSM-1) is presented in Fig. 3. The hemispherical shell saw is rotated by electromechanical drive (in MSM-1 is used angle grinder with a working shaft, which is normal to rotor). MSM-1 is additionally equipped with controller of the saw rotation speed.



Figure 3. Device MSM-1 for sampling from external surface of power plant components.

The system of electromechanical drive with a cutting tool is mounted on the working frame that provides the saw drive rotation around the Y axis (Fig. 1). The distance between working frame and sampled area is adjusted by means of four screws located in the corners of the frame. This distance and the shape of the surface of the sampled area define the thickness of the sample. Four magnet holders are used to hold sampling device on the component.

The system of feeding consists of stepping-motor and gear sector on which cutting tool is firmly fixed. The speed of stepping-motor rotation, which defines the speed of feeding, is remotely controlled through the microstepping driver (IM483I). The program of cutting parameters is saved in NVM (non-volatile memory) of microstepping driver. The system allows also remote control of cutting process in online regime (through RS232 interface) and tracking the location of cutting tool (if an encoder is present). Theoretically the speed of cutting/feeding could be variable during sampling process: at the initial and final stages the speed could be higher because the contact area between cutting tool

and surface of the component at these stages is smaller. Therefore, for the intensification of the cutting process the speed of feeding could be changed, depending on the position of cutting tool. However, the program of constant feeding speed, which is optimal for maximum area of contact surface, is realized in presented sampling device because the effect of changing the feeding speed is small (relating to total consumption for sampling and initiation of additional risks).

The speed of rotation of hemispherical shell saw of presented device is about 8 000 RPM. According to TED experience the optimal duration of extraction of one sample (leaving out of account the time of adjustment and setting of the device) is about 45 minutes. Totally more than 200 samples have been extracted from external surface of steam pipes, turbine casings, and drums by this device since it was designed.

2.3 Sampling device for metal extraction from internal surface of turbine rotor bore

Sampling device for metal extraction from internal surface of turbine rotors bores (MSM-2) is presented in Fig. 4. Cutting tool of this device is driven by air turbine through flexible shaft. The speed of rotation of hemispherical shell saw is about 10 000–15 000 RPM.

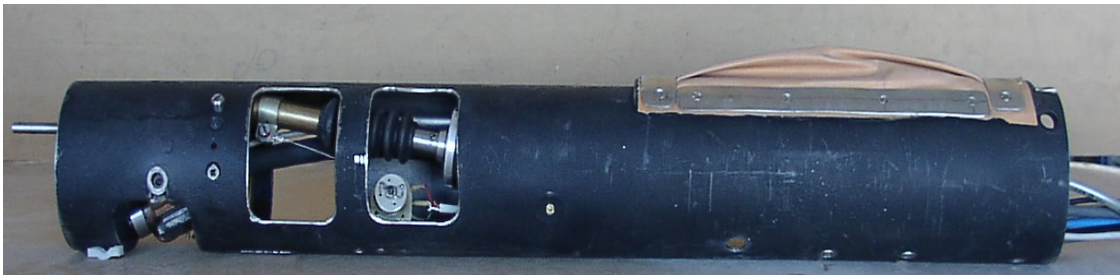


Figure 4. Sampling device (MSM-2) for sampling from bores.

Feeding system is also based on using of stepping-motor and microstepping driver (IM483I). The systems of driving, feeding and auxiliary systems are located inside the tube of 88 mm in outside diameter and 620 mm in length. This tube is hinged with another auxiliary tube of less diameter and 1600 mm in length, which serves as a holder of sampling device. All cables and hoses are placed inside this auxiliary tube. The total length of both tubes allows extract samples at the significant distance from the end of the bore.

Prior to sample extraction the device is fixed inside the bore in two sections, which are normal to the axis of the device. In the first section, near the cutting area (front edge of the device), fixation is realized by means of two rods, which are equidistant (45 degrees) from the vertical plane, passing through the tube axis

and lower support point of the device. In inoperative position these rods are hidden inside the device frame and for the fixation of the device they are pulled out by the drive of pneumatic cylinders. Rear of the device is fixated by air bag. The thickness of the metal sample could be also adjusted and the maximum thickness is about 1.9 mm. The minimal diameter of sampled bore is 95 mm.

Extraction without direct eye contact requires beside high quality of cutting tool some extra equipment to control the sampling process. Therefore, the device MSM-2 is additionally equipped by auxiliary systems. They are the system of rotational speed measurement and indication, the sensor of cutting tool position and limit stop, which turns on the saw reverse to the initial position. Cutting process could be also remotely controlled in online regime as well as in case of MSM-1. Duration of one sample extraction is about 90 min. Design and technical composition of MSM-2 as well as control panel are protected by Estonian utility models [7, 8].

Samples from 10 turbine rotors (rotors of high and intermediate pressure of units No. 1–3 and 5–6 at Eesti Power Plant) were extracted in TED using sampling device MSM-2. In accordance with demand of turbines manufacture (LMZ) metal samples were extracted from places located in 100 mm from axis of the first turbine stage toward front sealing.

3. Stress concentration in dimples

3.1 Stress distribution in the turbine rotor

The impact of the dimple to stress distribution in pipes and turbine rotor is analyzed applying finite elements (FE) method. The commercially available packets ANSYS and COSMOS/M were used.

Two 3-dimensional models of turbine rotor disc were used to analyze the affect of sampling on the stress concentration in dimple. The dimples in both models have the same sizes corresponding to the size of real dimple in the rotor bore. To minimize the calculations (limiting factor is maximum number of elements) only a quarter of rotor disc was simulated. Two 2-dimensional models were used to analyze the impact of circumferential groove and a notch in plane disc on stress distribution. All turbine rotor models were loaded only with centrifugal force due to rotation at 3000 RPM. The axisymmetric elements were applied. To reduce the amount of calculations only one stage of rotor was analyzed. It is justified because the dimple affects on the stress distribution only in the vicinity of its location. The shape and size of circumferential groove profile correspond to the shape and size of dimple cross-section along rotor longitudinal axis. The maximum calculated stress on the undamaged surface of turbine bore in the

middle of the first HP disc was 105.2 N/mm^2 . The maximum stress on the bottom of circumferential groove was 102.3 N/mm^2 .

A notch in rotating plane disc simulates the infinite long longitudinal groove on the surface of turbine rotor bore or rotating cylinder. The inner radius of annular disc was chosen 0.05 m , which corresponds to the radius of turbine rotor bore. A circle with radius 0.03 m simulated the dimple. The external radius of annular disc was 0.3 or 0.5 m .

For determination of the stress concentration factor the stress distribution in the undamaged annular plane disc with the same size was calculated. The stress concentration factor in the middle of the notch, where the maximum stress occurs, was calculated as the ratio of maximum stress and stress on the inner surface of annular plane disc without notch, where the stress does not change along inner perimeter. The stress distribution along the inner perimeter of notched annular disc is shown in Fig. 5. The stress concentration factor equals to 1.27 for the annular disc with outer radius of 0.3 m and equals to 1.29 for the annular disc with outer radius of 0.5 m .

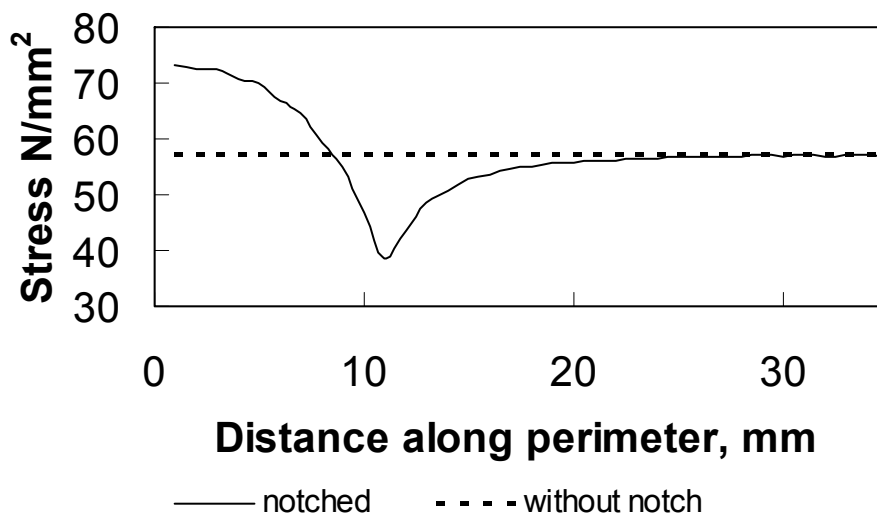


Figure 5. The stress distribution along the internal perimeter of annular disc (in mm) starting from the center of the notch.

The stress concentration factor in the middle of notch in plane annular disc slightly increases with the increasing of the disc size. The stress concentration in the case of longitudinal groove is maximal. The stress concentration on the bottom of elliptical dimple on the surface of turbine rotor bore does not exceed 1.3 .

The hypothesis that two diametrically located dimples on the surface of rotor bore decrease the stress concentration was also examined. The stress concentration factors for both dimples equaled to 1.28. Consequently cutting of two symmetrical samples from rotor bore practically does not change the stress concentration.

The stress concentration factors on the bottom of dimple in the 3-dimensional disc model with different disc mass were found equal to 1.2 and 1.19 where the less value corresponds to the more massive disc. The stress distribution in turbine K-200-130 rotor in the vicinity of dimple is presented in Fig. 6.

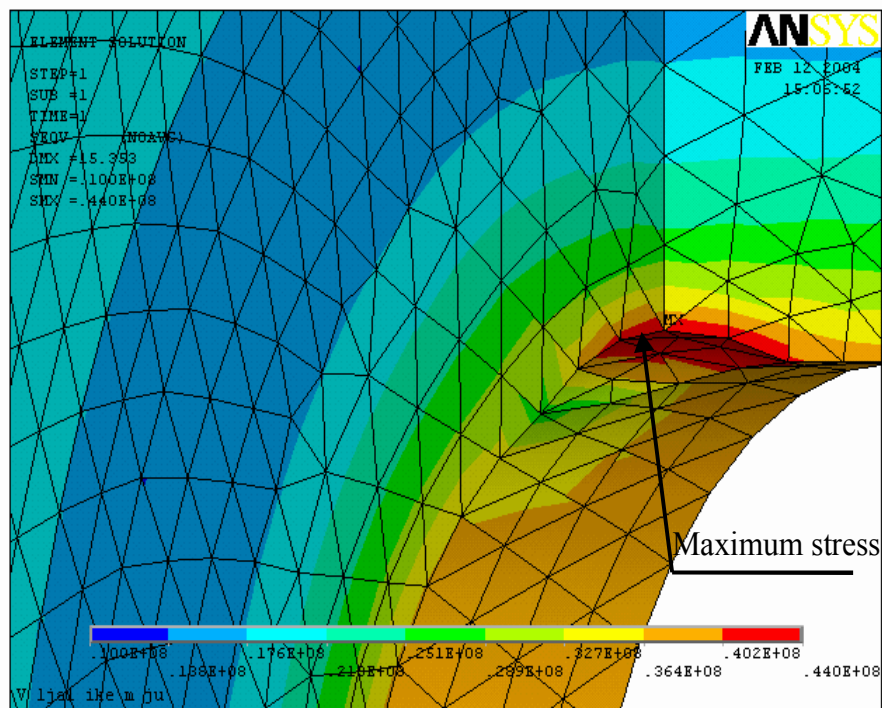


Figure 6. 3D stress distribution in turbine rotor in the vicinity of dimple.

3.2 Stress distribution in pipe wall

The impact of sampling on the stress distribution in pipe wall was analyzed by means of model of straight pipe under internal pressure. The first set of calculations was made for pipe $\text{Ø}325 \times 30$ mm. The depths of dimple was in the range 1–4 mm. The von Mises stress on the external surface of undamaged pipe is 49.4 N/mm^2 and on the internal surface is 73.4 N/mm^2 . The stress distribution in the vicinity of dimple on the external surface of pipe is similar to the case of turbine rotor. The maximum stress is located on the bottom of the dimple. The stress near the edge of dimple is significantly smaller, Fig. 7. The stress distribution along wall thickness for different depth of dimple is presented in Fig. 8.

The deeper is the dimple the greater is the maximum stress on the bottom of the dimple. In the case of small depths of dimple (1 and 2 mm) stress on the bottom of the dimple does not exceed the stress on the internal surface of undamaged pipe.

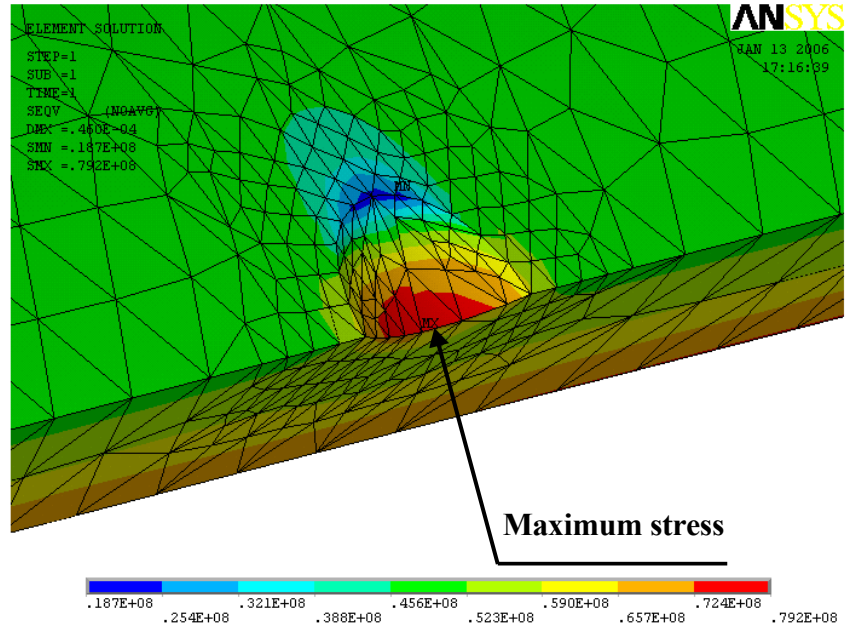


Figure 7. Stress distribution in pipe wall after sampling.

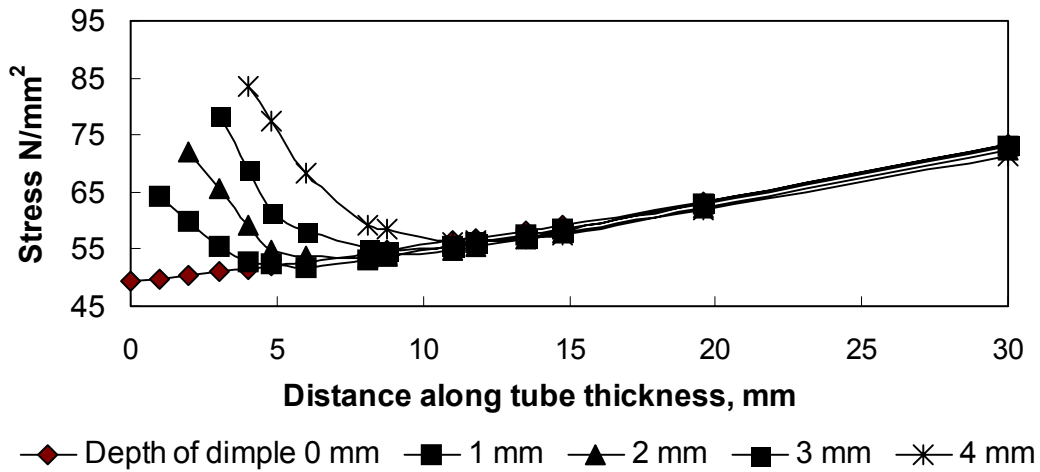


Figure 8. Stress distribution in pipe wall depending on the depth of the dimple.

The stress concentration factor calculated as ratio of the stress on the bottom of dimple to the stress on undamaged pipe wall in the same depth from pipe external surface is shown in Fig. 9.

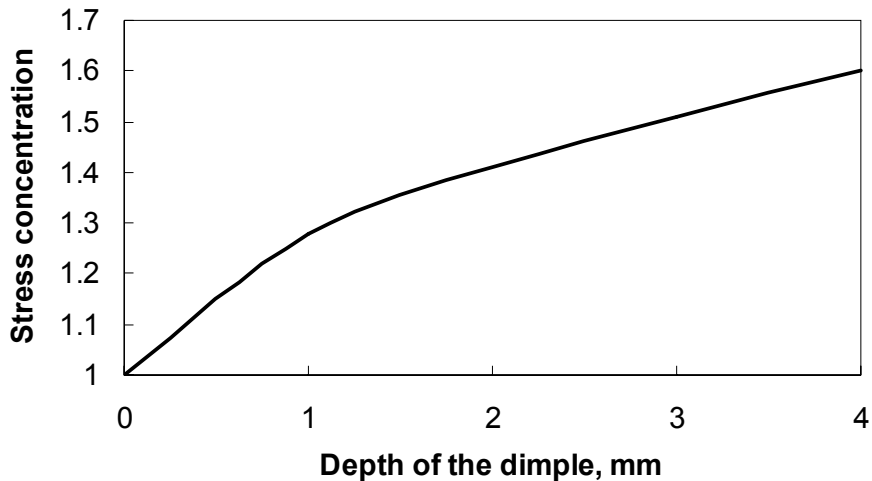


Figure 9. Stress concentration depending on the depth of the dimple for a pipe $\text{Ø}325 \times 30 \text{ mm}$.

In practice the depth of dimple does not exceed 3 mm. The impact of dimple with this depth on the stress concentration in pipes with various diameter, wall thickness and internal pressure (14 MPa and 2.3 MPa) was analysed. The greatest wall thickness corresponds to the TP-67 type boiler drum. The results have shown that the stress concentration factor for pipe wall thickness greater than 30 mm is approximately 1.5. Decrease of the pipe wall thickness leads to increase of the stress concentration factor, see Fig. 10).

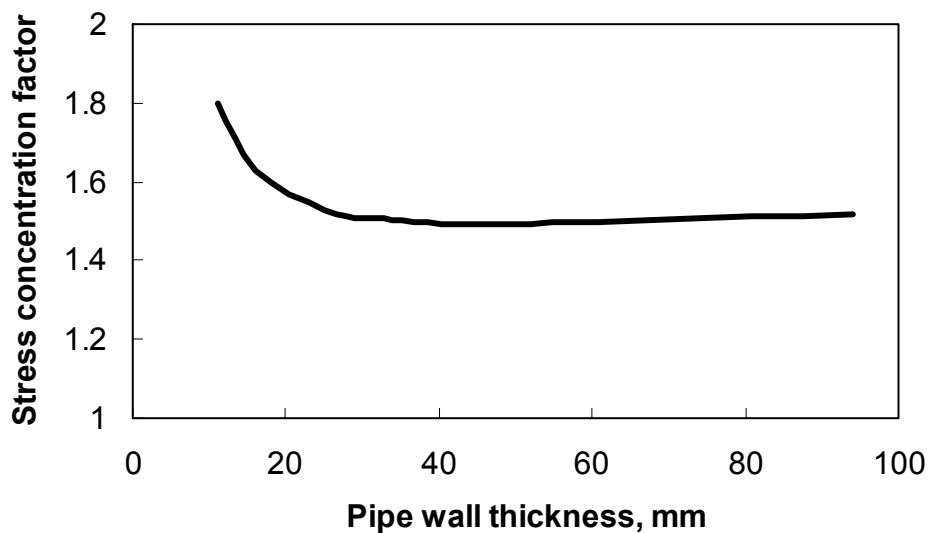


Figure 10. Stress concentration depending on pipe wall thickness for dimple of 3 mm in depth.

The modelling has shown that the stress concentration factor for the dimple on the internal surface is less than one on the external surface. For example, the stress concentration factor for dimple of 3 mm in depth on the internal surface is 1.44 and on the external surface is 1.5 for pipe $\text{Ø}325 \times 30$ mm and 1.27 and 1.49 for pipe $\text{Ø}325 \times 45$ mm.

Modeling of sampling with saw diameter of 50 mm was also performed. The results have revealed that smaller diameter of the cutting hemisphere causes higher stress concentration but in most cases maximal stresses in dimples do not exceed allowable stress value.

4. Conclusions

Two sampling devices for extraction of miniature metal samples have been designed and manufactured in Thermal Engineering Department of Tallinn University of Technology. The first of them MSM-1 has been designed for sampling from external surface of pipes, boiler drums and turbine casings. The second one MSM-2 has been designed for sampling from internal surface of turbine rotor bore. Totally more than 200 samples from external surface of steam pipes, turbine casings, drums and internal surface of turbine rotors have been extracted.

The stress concentration factor on the bottom of the dimple on the surface of turbine rotor bore is approximately 1.2. Two diametrically located dimples on the surface of rotor bore do not decrease the stress concentration on the bottom of these dimples. The stress concentration factor on the bottom of the dimple on the external surface of pipe depends on the depth of the dimple and on pipe wall thickness. The dimple on internal surface causes less stress concentration than dimple with the same depth on external surface. The stress concentration factor for dimples of 3 mm in depth does not exceed 1.5. In the most cases maximal stresses in dimples do not exceed allowable stress value.

The method of miniature samples does not cause the initiation of inadmissible stress concentrations or significant increase of stresses so it could be considered as non-destructive.

References

1. Kumanin, V., Kovalyova, L. and Aleksejev, S. Durability of Metal in the Conditions of Creep. Moscow, 1988. (In Russian.)
2. Berezina, T., Bugay, N. and Trunin, I. Diagnosis and Prognosis of Power Equipment Metal Life. Tehnika, Kiev, 1991 (In Russian.)
3. Purmensky, J. and Kupka, V. Stanoveni užitnych vlastnosti hutnich a strojirenskych vyrobku pomoci metod velmi malych vzorku. Hutnichke listy, 48, 1993, pp. 65–69.
4. Data acceptability criteria and data generation: recommendations for creep testing of post exposed (ex-service) materials, ed. by E Gariboldi and S Brett, ECCC recommendations – Vol. 3 part III [issue 3], 2003.
<http://www.ommi.co.uk/etd/eccc/advancedcreep/index.htm> (21.05.05).
5. Srivastav, S. et al. Unit-specific evaluation of steam turbine rotors using miniature sample removal and safer-pc.
<http://www.exponent.com/about/docs/esia2000.pdf> (21.03.06).
6. Torsello, G. Cesi ct elettrotecnico sperime, Apparatus for taking samples of conducting material, patent number: EP1413872, 2004.
7. Sarandi, J., Tallermo, H., Klevtsov, I. and Uus, M. Device for cutting samples from metal surface, Estonian Utility model EE00492, IPC B24B 19/00, B23B 47/18, Published 17.02.2005.
8. Klevtsov, I., Neshumayev, D. and Uus, M. Control panel for the device for cutting samples from metal surface. Estonian Utility model EE00527 U1, IPC B23Q 15/08, B24B 19/00, Published 15.07.2005.

NIMS structural materials databases and cross search engine – MatNavi

M. Yamazaki, Y. Xu, M. Murata, H. Tanaka, K. Kamihira and K. Kimura

National Institute for Materials Science, Tokyo, Japan

Abstract

Materials Database Station (MDBS) of National Institute for Materials Science (NIMS) owns the world's largest Internet materials database for academic and industry purpose, which is composed of twelve databases: five concerning structural materials, five concerning basic physical properties, one for superconducting materials and one for polymers. All of these databases are opened to Internet access at the website of <http://mits.nims.go.jp/en>. Online tools for predicting properties of polymers and composite materials are also available. The NIMS structural materials databases are composed of structural materials data sheet online version (creep, fatigue, corrosion and space use materials strength), microstructure for crept material database, Pressure vessel materials database and CCT diagram for welding.

1. Introduction

Forty-two years have passed since NIMS (former National Research Institute for Metals, NRIM) started to collect creep and fatigue strength data for domestic structural materials in a neutral setting¹⁻⁴. In Japan, the socioeconomic situation changed drastically and heavy-industry technologies were subject to major changes in environment. However, efforts to develop creep and fatigue data sheets have been continued with strong support from industry, and these data sheets have now become the world's biggest and reliable source of published data on the creep and fatigue strength of structural materials. In addition, NIMS has been developing a data sheet for corrosion and space-use materials strength since fiscal 2001. These structural materials data sheets are publicly available on the Internet as one of the NIMS materials databases as well as printed matter.

The structural materials database of NIMS consists of the above-mentioned creep, fatigue, corrosion and space use materials strength data sheets, which are publicly available on the Internet as PDF files. In addition, factual data regarding creep and fatigue have also been publicly available since April 2004 so that users themselves can produce a graphic representation by choosing each sort of data available using the system. Also, as high-temperature plants are aging in recent years, their

remaining life needs to be accurately predicted for life extension, maintenance and repair, and replacement of structural components used in those plants. In response, not only existing data on time to creep rupture but also data and information on creep deformation, change in microstructure, etc. are necessary. Therefore, NIMS is published as 'Metallographic Atlas Long-Term Crept Materials', parallel with the NIMS Creep Data Sheets⁵⁻¹⁷⁾.

This paper focuses on the NIMS materials databases, especially on the microstructure database for crept materials.

2. NIMS materials databases

Having the largest-scaled materials database of the world, the missions of Materials Database Station of NIMS is world-wide materials information provider and navigator, which serves our user with the best solution of materials selection, materials development and materials application. The NIMS Materials Database is composed of twelve databases: five concerning structural materials, five concerning basic physical properties, one for superconducting materials and one for polymers. All of these databases are opened to Internet access at the website of <http://mits.nims.go.jp/en> (Fig. 1).



NIMS DMI MDBS NIMS Materials Database NEWS LINK		
		National Institute for Materials Science / Materials Database Station
MITS Materials Information & Technology Solutions		 NIMS Materials Database
Keyword Search MatNavi Help <input type="text"/> <input type="button" value="search"/> <input checked="" type="radio"/> AND <input type="radio"/> OR <input checked="" type="checkbox"/> Contain Tree Search <ul style="list-style-type: none"> Material <ul style="list-style-type: none"> Element Alloy Ceramic Polymer Mineral Property 	Basic Properties Database <ul style="list-style-type: none"> Polymer [PoLyInfo] Login Basic Crystal Structures Login Electronic Structures Login Nuclear Reaction Database for Materials Login Diffusion Login 3D Demo System for Ternary Phase Diagrams Login Superconducting Materials Login Metals & Alloys Database <ul style="list-style-type: none"> Nuclear Materials Tensile , Creep Login Pressure Vessel Materials (Cr-Mo Steels) Login CCT Diagrams for Welding Login Application system <ul style="list-style-type: none"> Thermophysical Property Prediction System for Composites Login Polymer Properties Estimation Login Material Risk Information Platform (Japanese only) Login Weld Thermal History Simulator Login Joint Performance Simulator Login Unit Conversion 	NIMS Structural Materials Datasheet Online <ul style="list-style-type: none"> Creep Login Microstructure for Crept Materials Login Fatigue Login Corrosion Login Space Use Materials Strength Login <p>[Availability of Printed Copies]</p> Other database in NIMS <ul style="list-style-type: none"> High Magnetic Field Engineering and Cryogenics Database SANZEN NIMS Thermodynamic Database Materials Sciece Outlook 2005[PDF] Research Activity Information System Cooperation organization (MOU) <ul style="list-style-type: none"> Matdata.net(Granta Desqin) MatWeb(Automation Creations Inc.) Springer Link(Landolt Bornstein)
Notes on Use <ul style="list-style-type: none"> System Requirement (Plug-in) Copyright Reference Feedback CONTACT US Number of registered user Registrated users:25088, Locations:100, Organizations:7879 (at:Oct.31,2006)	What's New ! <ul style="list-style-type: none"> ● [Mar. 13, 2006] Polymer [PoLyInfo] has been UPDATED. ● [Feb. 22, 2007] NIMS Thermodynamic Database was added. ● [Feb. 15, 2007] MITS meeting 2007 was added. ● [Nov. 22, 2006] Polymer [PoLyInfo] has been UPDATED. <p style="text-align: right;">[Details]</p>	Registration [Details] (Free of Charge) <input type="checkbox"/> These db can be registered at once. <div style="background-color: orange; text-align: center; padding: 2px;">Registration</div> <ul style="list-style-type: none"> ● Change(Modification) ● Forqot Your Password? ● Withdraw(Seession) ● FAQ ● Privacy Policy
This system is using SSL. Your information is safe.		

Figure 1. Top page of NIMS materials database (<http://mits.nims.go.jp/en>).

3. Structural materials databases

The NIMS structural materials databases are composed of structural materials data sheet online version (creep, fatigue, corrosion and space use materials strength), microstructure for crept material database, Pressure vessel materials database and CCT diagram for welding. Number of published structural materials datasheets shown in Table 1.

Table 1. Number of structural materials data sheets.

Structural materials data sheets	Number of published
Creep	53
Metallographic Atlas Long-Term Crept Materials	6
Fatigue	103
Corrosion	6
Space use materials strength	10

Note: March 31st, 2007

3.1 Structural materials data sheet online

Forty-two years have passed since NIMS (former National Research Institute for Metals, NRIM) started to collect creep and fatigue strength data for domestic structural materials in a neutral setting²⁾. In addition, NIMS has been developing a data sheet for corrosion and space-use materials strength since fiscal 2001.

The structural materials database of NIMS consists of the above-mentioned creep, fatigue, corrosion and space use materials strength data sheets, which are publicly available on the Internet as PDF files. In addition, factual data regarding creep and fatigue have also been publicly available since April 2004 so that users themselves can produce a graphic representation by choosing each sort of data available using the system (Fig. 2). Also, as high-temperature plants are aging in recent years, their remaining life needs to be accurately predicted for life extension, maintenance and repair, and replacement of structural components used in those plants. In response, not only existing data on time to creep rupture but also data and information on creep deformation, change in microstructure, etc. are necessary. Therefore, NIMS is published as 'Metallographic Atlas Long-Term Crept Materials', parallel with the NIMS Creep Data Sheets⁵⁻¹⁶⁾.

3.2 Microstructure database for crept material

We have been publishing 'Metallographic Atlas of Long-Term Crept Materials', for JIS SUS 304H TB (18Cr-8Ni), 316H TB (18Cr-12Ni-Mo), 321H TB (18Cr-10Ni-Ti), 347H TB(18Cr-12Ni-Nb), STBA 24, SCMV 4NT, ASTM

A542(2.25Cr-1Mo) and ASTM A470-8(1Cr-1Mo-0.25V) heat resistant steels, using specimens tested in NIMS Creep Data Sheet Project (Table 2). The Metallographic Atlas contains a number of optical, scanning electron and transmission electron micrographs showing the change in microstructure during creep for up to about 200 000 h at 450–750°C. The Metallographic Atlas of

austenitic heat resistant steels are opened to Internet access at the website of the NIMS materials database. User can choose from a wide variety of micrographs for creep testing conditions in stress rupture curve of microstructure database for crept material (Fig. 3).

Creep Datasheet				Fact Data				MatWeb	Landolt-Bornstein
Material	Form	Standard	DS No. PDF	Tensile	Creep	Stress relax	Microstructure Image		
4. Austenitic stainless steels									
18Cr-8Ni-steel	18Cr-8Ni (Tube)	JIS SUS 304H TB	4B	●	●	-	●	●	●
	18Cr-8Ni (Plate, Welded joints)	-	32A	●	●	-	-	●	
18Cr-12Ni-Mo steel	18Cr-12Ni-Mo (Tube)	JIS SUS 316H TB	6B	●	●	-	●	●	●
	18Cr-12Ni-Mo (Plate)	JIS SUS 316-HP	14B	●	●	-	-	●	
	18Cr-12Ni-Mo (Bar)	JIS SUS 316-B	15B	●	●	-	-	●	
	18Cr-12Ni-Mo (Plate) (Stress Relaxation)	JIS SUS 316-HP	42	●	●	●	-	●	
	18Cr-12Ni-Mo-middle N-low C	JIS SUS 316-HP	45A	●	●	-	-	●	
18Cr-10Ni-Ti steel	18Cr-10Ni-Ti (Tube)	JIS SUS 321H TB	5B	●	●	-	●	●	●
18Cr-12Ni-Nb steel	18Cr-12Ni-Nb (Tube)	JIS SUS 347H TB	28B	●	●	-	●	●	●
21Cr-32Ni-Ti-Al steel	Fe based 21Cr-32Ni-Ti-Al (Tube)	JIS NCF 800H TB	26B	●	●	-	-	●	●
	Fe based 21Cr-32Ni-Ti-Al (Plate)	JIS NCF 800H-P	27B	●	●	-	-	●	
	Fe based 21Cr-32Ni-Ti-Al (Bar)	JIS NCF 800H-B	47	●	●	●	-	●	
25Cr-12Ni steel	25Cr-12Ni-0.4C (Casting)	JIS SCH 13	37A	●	●	-	-	-	●

Figure 2. Web page of creep data sheet on-line.

Table 2. Metallographic atlas of long-term crept materials.

No	Materials	Atlas (Printed)	On-line
M-1	18Cr - 8Ni	○	○
M-2	18Cr - 12Ni - Mo	○	○
M-3	18Cr - 10Ni - Ti	○	○
M-4	2.25Cr-1Mo	○	-
M-5	18Cr - 12Ni - Nb	○	○
M-6	1Cr-1Mo-0.25V	○	-

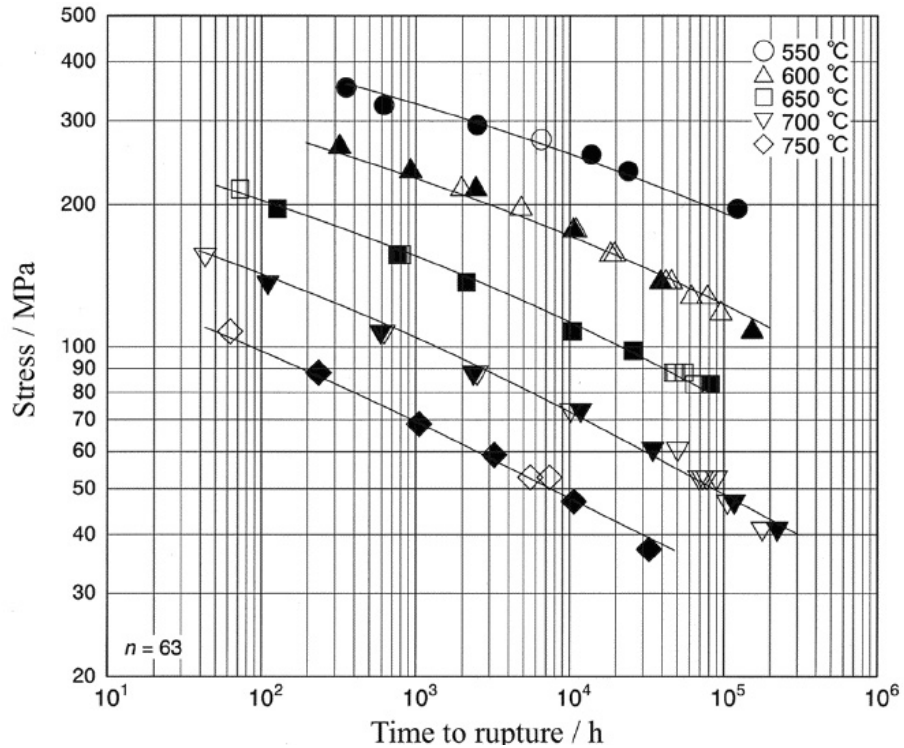


Figure 3. Stress versus time to rupture for 18Cr-12Ni-Mo Steel in Microstructure database (Choose from creep test condition: Click solid symbol).

Fig. 4 shows information of crept specimen and image data; time to rupture, elongation, reduction of area, hardness and location of microstructure examine etc.

Microstructure Data Base (Creep ruptured)			
Test Material	Material	SUS316HTB	Details
	Heat	AAL	
	Specimen number	AALk+	
Creep Rupture Test Data	Temperature	°C 700	
	Stress	MPa 41	
	Ruptured time	h 222705.3	
	Elongation	% 14	
	Reduction of area	% 22	
	Fracture mode 1)	σ	Fracture mode
Optical Micrographs	Near fractured surface 2)		
	Gauge portion		Summary
	Head portion		
	Surface		
Transmission Electron Micrographs	Head portion		Summary
Hardness	Gauge portion	HV5 162.0	
	Head portion	HV5 167.1	Hardness change
Precipitates	Type of precipitate	M23C6 carbide	Laves phase
	Precipitation site	grain boundary	within grain
Identification	Chemical composition 3)	(G) Fe:13, Cr:68, Mo:11, Ni:5	(G) Fe:38, Cr:12, Mo:39, Ni:6
TTP diagram	Area fraction	%	(G) Fe:52, Cr:32, Mo:7, Ni:5
	Number density	mm ⁻²	
	Size	μm	
Supplements	1) T: Transgranular creep fracture W: Wedge-type cracking C: Creep void formation σ : Cracking at σ phase/austenite interface S: Surface cracking 2) Locations of microstructural examinations in creep ruptured specimens 3) G: Gauge portion H: Head portion		
Return			

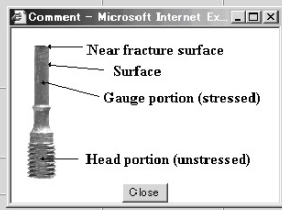


Figure 4. Information of crept specimen and image data.

3.2.1 Micrographs of crept austenitic heat resistant steels

NIMS Microstructure Database is available not only for estimating materials degradation and remaining life but also estimating the operating conditions, such as operating temperature and time, of high-temperature components.

Scanning electron micrographs of 18Cr-12Ni-Mo steel shown in Fig. 5. Micrographs showing the formation of creep voids in specimen interrupted under conditions; 650°C – 88 MPa, 700°C – 61 MPa and 750°C – 37 MPa. Creep voids form at the interface between Sigma phase and austenite matrix and grow along grain boundaries.

Fig. 6 shows optical micrographs of typical surface cracks in specimen gauge portion of 18Cr-12Ni-Nb steel. The surface crack was observed by the crept specimen of 18Cr-12Ni-Nb steel and 18Cr-8Ni-Ti steel. The surface crack of the specimen by high temperature and a long time condition is growing along with grain boundaries.

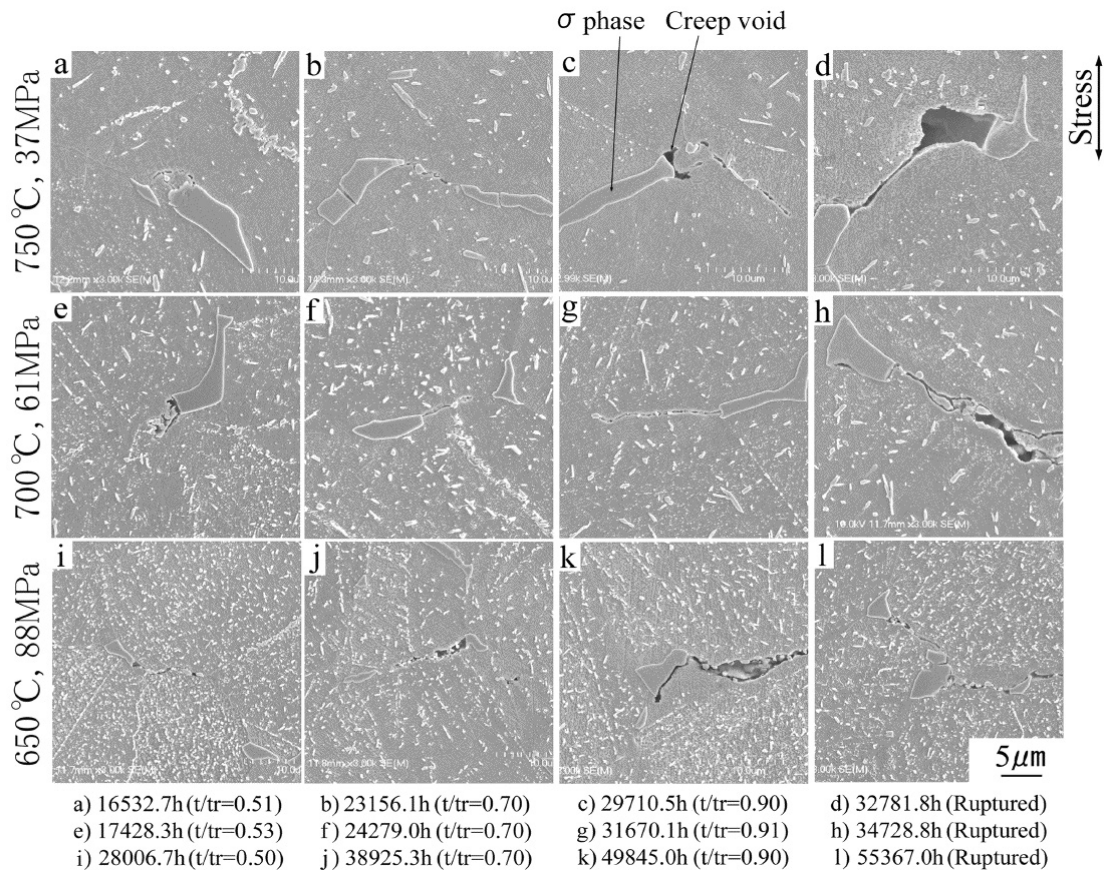


Figure 5. Scanning electron micrographs of 18Cr-12Ni-Mo steel.

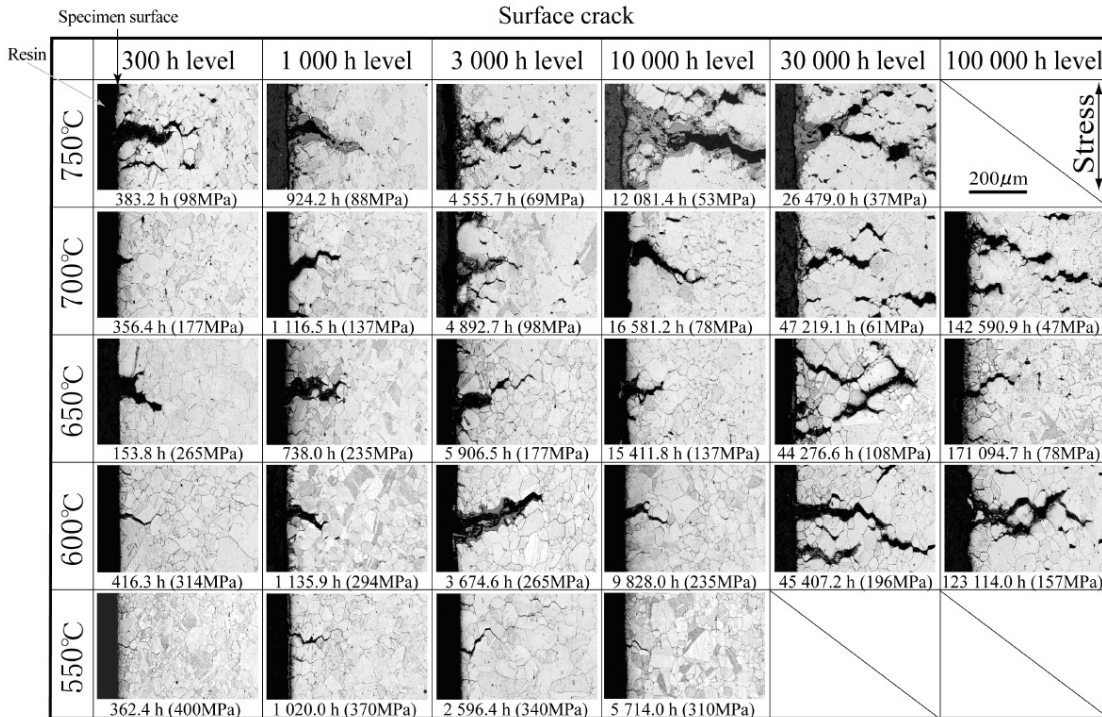


Figure 6. Optical micrographs of typical surface cracks in specimen gauge portion of 18Cr-12Ni-Nb steel.

3.2.2 Time – temperature – precipitation (TTP) diagram

The difference in microstructure between the specimen gauge portion under stress and head portions under no stress disappears at long times.

We prepared the time – temperature – precipitation (TTP) diagram, precipitates in the specimen head portion and the aged specimens under the unstress were examined. The presence of precipitates was determined by transmission electron microscopy at a magnification of 50 000. A variety of second phases, such as $M_{23}C_6$ carbides, G phase, Laves phase, σ phase and χ phase, precipitate at grain boundaries and within grain of 18Cr-12Ni-Mo steel. (Fig. 7-(a)). Most G phase are adjacent to $M_{23}C_6$ carbides on grain boundaries. χ phase precipitates at long times at temperature of 750°C or higher. The other hand, NbC, $M_{23}C_6$ carbides and σ phase precipitate at grain boundaries and within grain of 18Cr-12Ni-Nb steel. (Fig. 7-(b)).

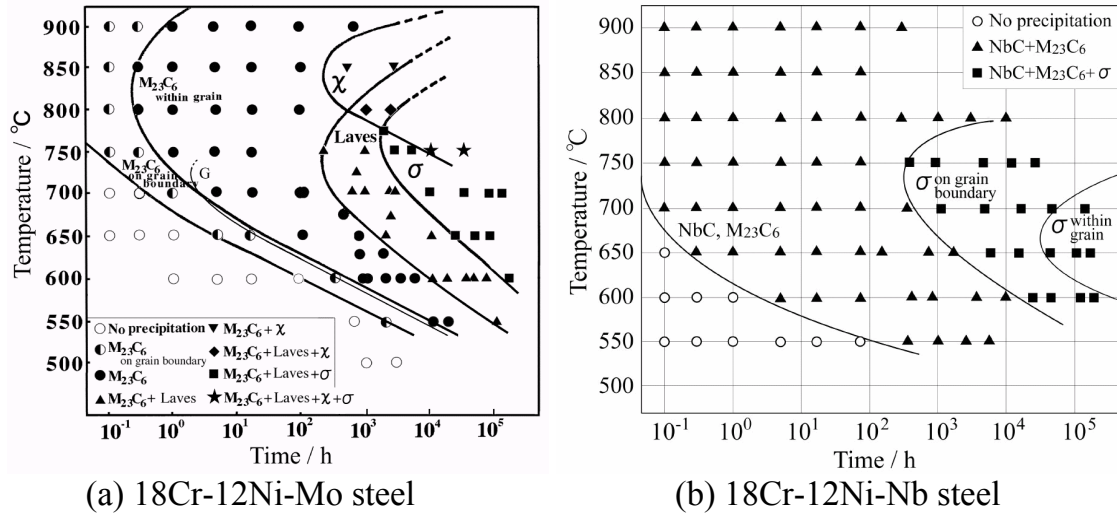


Figure 7. Time – temperature – precipitation diagram of (a) 18Cr-12Ni-Mo steel and (b) 18Cr-12Ni-Nb steel.

3.2.3 Vickers hardness of crept specimens

The Vickers hardness of the gauge and head portions of crept specimens was measured, using the specimen polished on buffing cloths but not etched. The hardness was measured with a load of 5kg for 5 points at random in the center portion of specimen. After eliminating the maximum and minimum values, the average of the remaining 3 points was plotted as shown Fig. 8. The hardening behavior during creep depends on stress levels as well as the precipitation of $M_{23}C_6$ carbides and σ phase. The hardening during creep is determined substantially by the precipitation hardening due to the $M_{23}C_6$ carbides at short times and due to the σ phase at long times above 10 000 h.

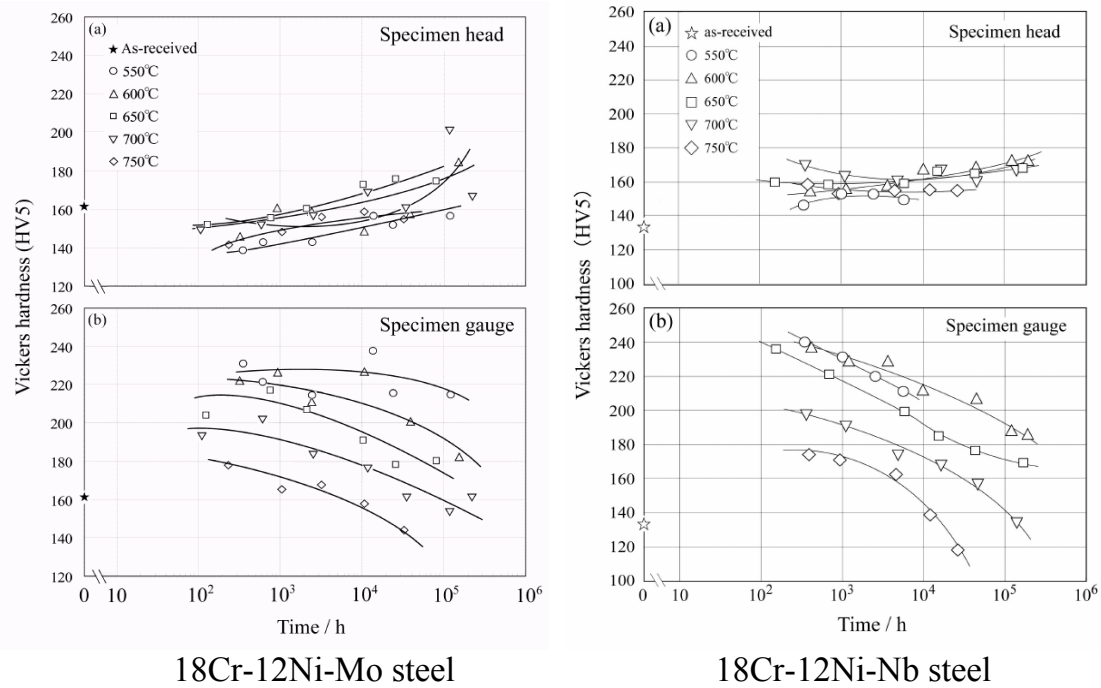


Figure 8. Comparison of Vickers hardness versus time for specimens tested at various temperatures, (a) specimen head and (b) gauge portions of 18Cr-12Ni-Mo steel and 18Cr-12Ni-Nb steel.

3.2.4 Sigma phase of crept austenitic heat resistant steels

The amount of precipitated σ phase is much larger in the gauge portion than in the head portion, indicating an acceleration effect of stress and or strain on the σ phase precipitation. In the head portion under no stress, the number of σ phase significantly increases with time, while the size increases only slightly. In the gauge portion under stress, on the other hand, the number of σ phase decreases or is constant with time, while the size significantly increases with time.

The operating temperature can be estimated by evaluating the total amount of precipitates. Then, the operating time can be estimated from the amount of σ phase.

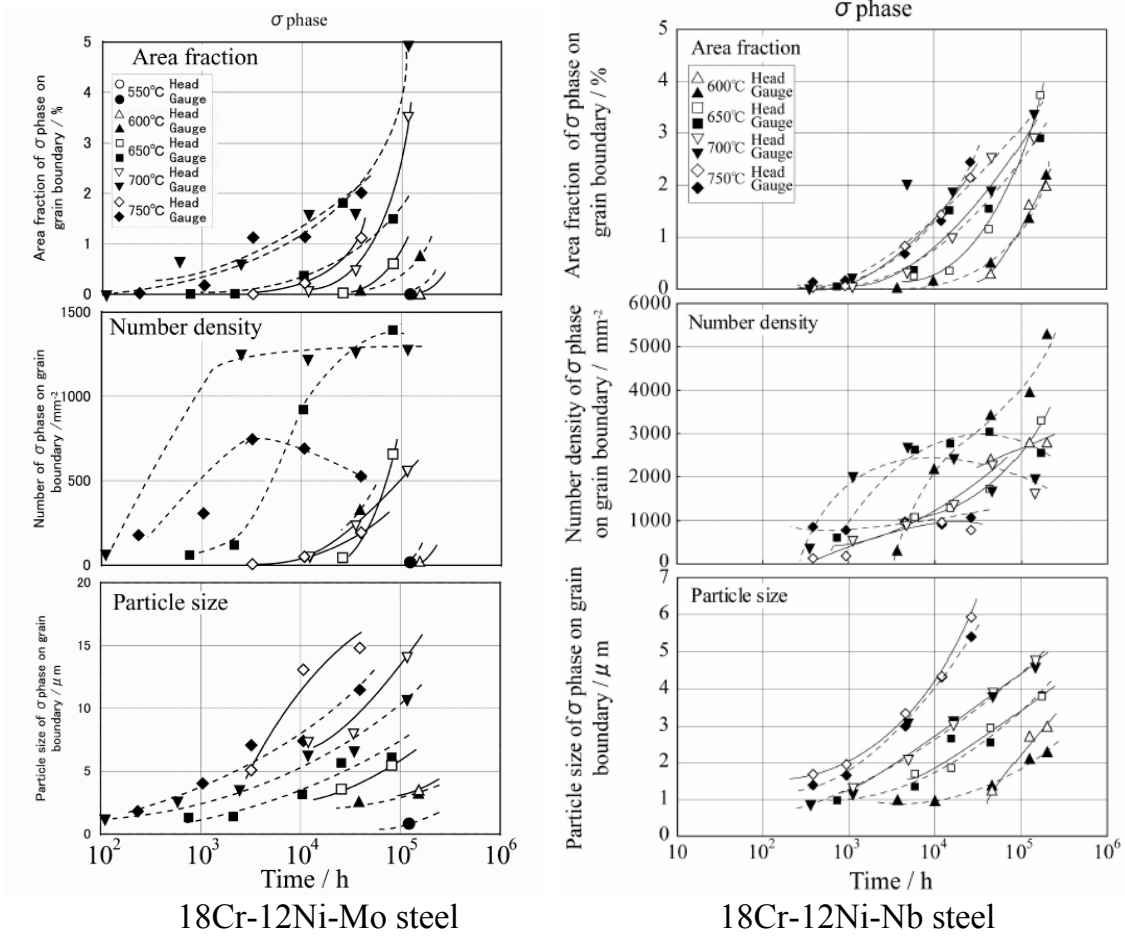
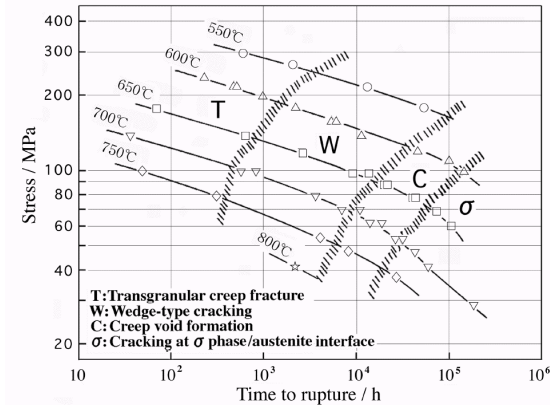


Figure 9. Change in area fraction, number density and particle size of sigma phase at grain boundaries in specimen head and gauge portions as a function of time for 18Cr-12Ni-Mo steel and 18Cr-12Ni-Nb steel.

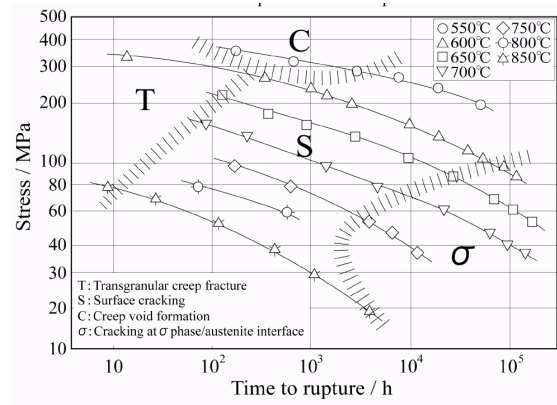
3.2.5 Creep fracture mode map of crept austenitic heat resistant steels

The creep fracture modes for the 18Cr-8Ni and 18Cr-12Ni-Mo steels are divided to one transgranular fracture (denoted by T) and three types of intergranular fracture; the wedge-type cracking (W), the creep cavitation associated with $M_{23}C_6$ carbides at grain boundaries (C) and the σ / matrix interface cracking along grain boundaries (σ). 18Cr-8Ni-Ti and 18Cr-12Ni-Nb steels are no wedge-type cracking, and the surface crack (S) were observed by large range of the stress and temperature (Fig. 10).

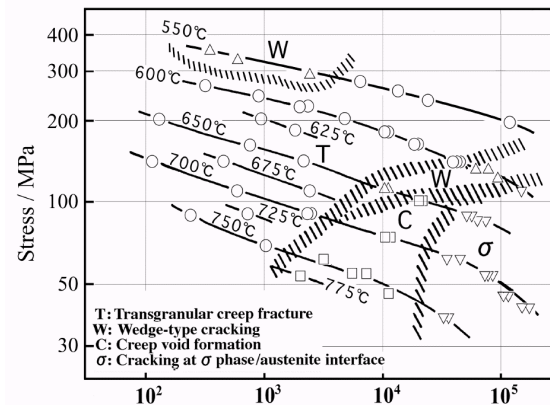
The present results suggest that the creep fracture modes at long times above about 10 000 h are closely connected with the precipitation behavior of $M_{23}C_6$ carbides and σ phase.



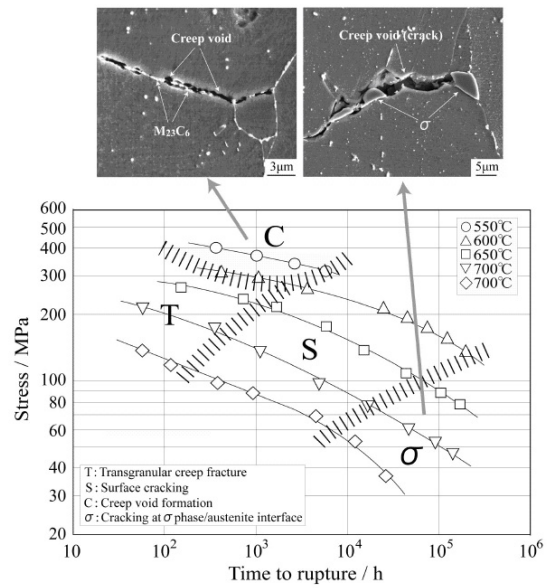
18Cr-8Ni steel



18Cr-8Ni-Ti steel



18Cr-12Ni-Mo steel



18Cr-12Ni-Nb steel

Figure 10. Creep fracture mod maps for 18Cr-8Ni steel, 18Cr-12Ni-Mo steel, 18Cr-8Ni-Ti steel and 18Cr-12Ni-Nb steel.

4. Cross search engine – MatNavi

A user-friendlier database environment has been established with this system in that users can easily obtain pertinent data and the information for material development and for optimal material usage by retrieving information from the databases in the U.K. and the U.S. in addition to the information on the NIMS Materials Database. Further increase in the users of the NIMS Materials Database is expected to lead to a higher degree of material data contributions provided by NIMS to the society.

The Materials Database Network (MDN) was developed by Professor Ashby of Cambridge University by setting up Granta Design Ltd. The MDN not only links the databases which release the material properties of metals, ceramics, and plastics in the U.K. and the U.S. through the network, but also is capable of instantaneously retrieving, by the integrated retrieval system, the same material property information that exists in several databases. Uniting the NIMS database with MDN has led to a quantum increase in the amount of retrievable material information for NIMS database users. The integrated retrieval system is capable of category retrieval by material and ambiguous retrieval through keyword input.

Tree : [Material](#) > [Alloy](#) > [Ferrous Alloys](#)
(Total 3829)

NIMS Structural Materials Datasheet Online	Hit 1218	Preview
Pressure Vessel Materials	Hit 427	Preview
CCT Diagram for Welding	Hit 214	Preview
Nuclear Materials (Data-Free-Way)	Hit 31	Preview
Superconducting Materials	Hit 0	
Polymer (PolyInfo)	Hit 0	
Basic Database for Crystal structures (Pauling File)	Hit 1227	Preview
Diffusion Database	Hit 717	Preview

If you click the following data, it will move to data of database system.
In order to view data, it is necessary to register user.

(Pressure Vessel Materials) Material : 0.5Mb, Product form : Plate, Hit : 2 Property : Tensile,	(CCT Diagram for Welding) (English) (Japanese) Material : Fe-0.1C-0.5Ni-1Cr, SPA-H (JIS G3125), HT50 Property : CCT Diagram, Hardness (Hit 9), Micro-Structure (Hit 4), Tensile
(Pressure Vessel Materials) Material : 0.5Mb, Product form : Plate, Hit : 2 Property : Tensile,	(CCT Diagram for Welding) (English) (Japanese) Material : Fe-0.18C-0.5Si-1.5Mn, SM520 (JIS G3106), HT60 Property : CCT Diagram, Hardness (Hit 6), Micro-Structure (Hit 4), Tensile
(Pressure Vessel Materials) Material : 0.5Mb, Product form : Plate, Hit : 2 Property : Tensile,	(CCT Diagram for Welding) (English) (Japanese) Material : Fe-0.18C-0.5Si-1.5Mn, SM520 (JIS G3106), HT50 Property : CCT Diagram, Hardness (Hit 7), Micro-Structure (Hit 4), Tensile
(Pressure Vessel Materials) Material : 0.5Mb, Product form : Plate, Hit : 2 Property : Tensile,	(CCT Diagram for Welding)

Figure 11. Cross Search Engine – MatNavi.

5. Summary

1. NIMS materials database have been available its website (<http://mits.nims.go.jp/en>) since April, 2003.
2. NIMS microstructure database for crept austenitic heat resistant steels open public since May, 2006.

3. The hardness and the size and number density of σ phase can be used for the assessment of material degradation for austenitic heat resistant steels at long time conditions over 100 000 h. By comparing the hardness or the size and number density of σ phase of high-temperature components with the present data, we can estimate the operating conditions, such as operating temperature and time, for the components.
4. NIMS microstructure database in combination with NIMS Creep Data Sheets and creep strain data can contribute to more reliable assessment of high-temperature components.

References

- [1] NIMS Materials Database. <http://mits.nims.go.jp/en>
- [2] Yagi, K. et al. NRIM Material Strength Data Sheet, Technical Document, No. 10, Testing Plan and Testing Procedures for NRIM Creep Data Sheets Project, 1996.
- [3] Xu, Y. et al. "Development of Materials Knowledge Base with Structured data Format", Journal of Japan Society of Information and Knowledge, Vol. 15, No. 3, 2005, pp. 3–10.
- [4] Yamazaki, M. and Xu, Y. et al. "Developments of Internet Materials Information and Search System", Journal of Japan Society of Information and Knowledge, Vol. 15, No. 3, 2005, pp. 3–10.
- [5] NIMS Creep Data Sheet No. 4B, 18Cr-8Ni (tube), 1986.
- [6] NIMS Creep Data Sheet No. 5B, 18Cr-10Ni-Ti (tube), 1987.
- [7] NIMS Creep Data Sheet No. 6B, 18Cr-12Ni-Mo (tube), 2000.
- [8] NIMS Creep Data Sheet No. 28B, 18Cr-12Ni-Nb (tube), 2001.
- [9] NIMS Creep Data Sheet No. 3B, 2.25Cr-1Mo (tube), 1986.
- [10] NIMS Creep Data Sheet No. 11B, 2.25Cr-1Mo (plate), 1986.
- [11] NIMS Creep Data Sheet No. 36B, 2.25Cr-1Mo (plate), 1997.
- [12] Metallographic Atlas of Long-term Crept Materials No. M-1, 18Cr-8Ni., 1999.

- [13] Metallographic Atlas of Long-term Crept Materials No. M-2, 18Cr-12Ni-Mo, 2003.
- [14] Metallographic Atlas of Long-term Crept Materials No. M-3, 18Cr-10Ni-Ti, 2004.
- [15] Metallographic Atlas of Long-term Crept Materials No. M-4, 2.25Cr-1Mo, 2005.
- [16] Metallographic Atlas of Long-term Crept Materials No. M-5, 18Cr-12Ni-Nb, 2006.
- [17] Kasugai, T. and Fujita, M. Atlas of CCT Diagram for welding(1), NIMS, 1999.

Visualising creep exhaustion in a P22 girth weld

Stefan Holmström, Anssi Laukkanen and Kim Calonius

VTT Technical Research Centre of Finland, Espoo, Finland

Abstract

For pipings creep damage will be localized to locations with degraded microstructures aggravated by triaxiality constraints. These unfavorable conditions are known to be found in the heat affected zone of welds. The influence of triaxiality in a girth weld has been studied using a new “creep exhaustion” filtering technique named Λ -filtering. It has been developed for FEM analysis purposes to localize critical regions for creep exhaustion in components. The creep ductility expression for rigid plastic deformation has been used for visualizing the level of creep exhaustion in a P22 girth weld. The creep response of a 3 zone girth weld was modeled with the logistic creep strain prediction method and Λ -filtered in Comsol software. For comparison some calculations were performed with the Norton law implemented Abaqus software. Preliminary results of the Λ -filtering show that the regions in the weld that are critical according to experience (interface between heat affected zone and parent material) are indeed highlighted by the filtering method.

1. Introduction

FE modeling of girth welds in the creep regime has been studied extensively [1]–[10]. Creep stress and strain distributions are mostly studied without taking the impact of the triaxiality constraints on local creep ductility into account. This can lead to difficulties in pinpointing the true critical locations of the assessed structure. The influence of creep ductility exhaustion under multiaxial conditions is studied in [11] and by recent work on stainless steels [12]. The creep ductility exhaustion approach is also applied for creep-fatigue in the R5 [13] procedures. Triaxiality constraint is applied in other design codes like ASME III [14] and RCC-MR [15] using a time fraction approach.

This work studies the multiaxiality and multiaxial constraint effects on the P22 girth weld previously studied in [1], implementing both the new logistic creep strain prediction (LCSP) approach [16] and also a new filtering technique (named Λ -filtering) for pin-pointing critical locations of the girth weld. The technique is assuming a classical relation [17] for creep ductility ratio (uniaxial vs. multiaxial fracture strain) under complex stress loading.

2. The uniaxial strain model

The logistic creep strain prediction method (LCSP) is a creep strain model based on time to rupture and shape functions. It introduces a transition in a time as a function of creep strain. The function is a non-linear asymmetric transition function with a steepness regulated by the shape variables p and x_0 .

The LCSP model states that the full strain curves at specified temperature and stress can be acquired from knowing only the time to rupture and the material specific (temperature and stress dependent) shape parameters p and x_0 .

The LCSP strain at specified time is defined as

$$\log(\varepsilon_t) = \left(\frac{\log(t_r) + C}{\log(t_\varepsilon) + C} - 1 \right)^{1/p} \cdot x_0 \quad (1)$$

where t_ε is time to strain ε , t_r is time to rupture and x_0 , p and C are fitting constants (for each creep curve).

By differentiating Eq. 1 with respect to time, the resulting strain rate as a function of stress and temperature can be written as

$$\dot{\varepsilon} = -\varepsilon \cdot k_1 \cdot k_2 \cdot x_0 \quad (2)$$

where ε is given by Eq. 1, and

$$k_1 = \frac{(LTF - 1)^{\frac{1}{p}}}{p} \quad (3)$$

and

$$k_2 = \frac{\log(t_r) + \beta}{(\log(t_\varepsilon) + \beta)^2 \cdot t_\varepsilon \cdot (LTF - 1)} \quad (4)$$

$$LTF = \frac{\log(t_r) + \beta}{\log(t_\varepsilon) + \beta} \quad (5)$$

An example creep strain rate curve is shown in Fig. 1. The creep shape function of P22 parent material is given in Table 1.

Table 1. LCSP fitting factors for parent P22 (10CrMo9-10) steel. For the heat affected zone (HAZ) the same shape equations apply after dividing the stress σ with a strength reduction factor 0.8.

$x_0(\sigma, T)$	$p(\sigma, T)$	C
$-0.391 + 0.696 \cdot \log(\sigma) - 3392.5 / (T + 273)$	$4.363 - 2.271 \cdot \log(\sigma) + 3874.9 / (T + 273)$	3.49

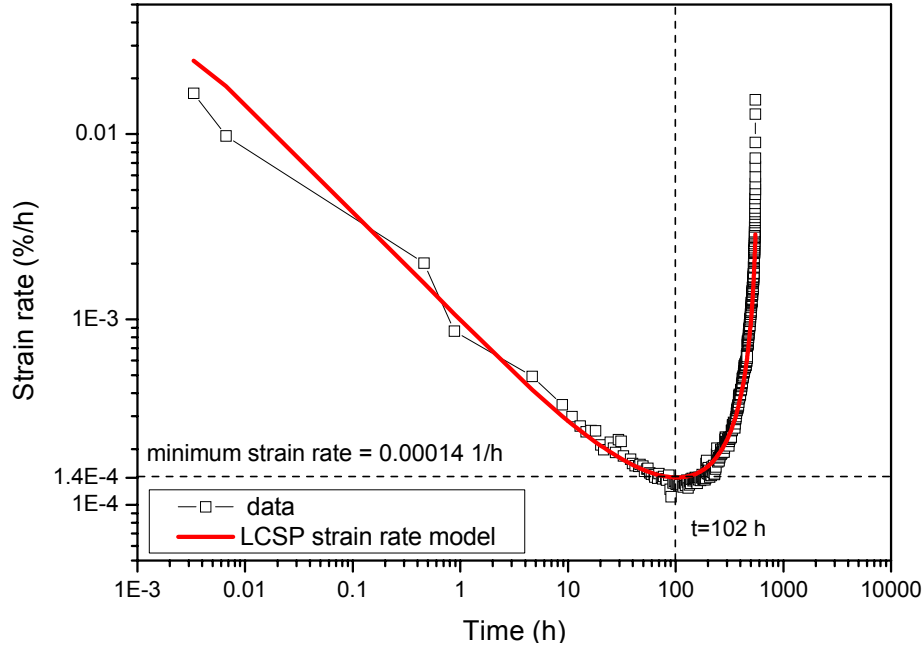


Figure 1. Creep strain rate presentation of uniaxial LCSP model.

3. The multiaxial models

The two multiaxial models implemented in this work are the new multiaxial LCSP coded into Comsol software and the classical Norton law that follows as a standard feature in Abaqus software.

3.1 The LCSP

The multiaxial LCSP generalization originates from the uniaxial strain rate equation. By simplifying Eq. 2 the expressions and redefining the variables for clarity, we attain:

$$\dot{\epsilon} = k_0 k_1 k_2 \left(p_0 + p_1 \log \bar{\sigma} + \frac{p_2}{T + 273} \right) \quad (7)$$

where the equivalent stress has been introduced along with a new set of constants, p_i . By using a von Mises type flow rule we attain the following strain rate tensor:

$$\bar{\sigma} = \frac{3}{2} \cdot \frac{\dot{\epsilon}}{\dot{\epsilon}_{ij}} \cdot s_{ij} \quad (8)$$

where s_{ij} is the deviatoric stress tensor. Substituting to the expression for equivalent creep strain rate, we finally attain the multiaxial LCSP creep strain rate expression:

$$\dot{\epsilon}_{ij}^c = \alpha \cdot \left(\delta \alpha_1 + \delta \alpha_3 \beta_3 (T) + \frac{3}{2} \alpha_4 \cdot s_{ij} \right) \quad (9)$$

where the first α is a function of the uniaxial LCSP model (Eq. 1–5.), δ , α_i and β_i are constants and functions defined by Eq. 7.

The FE implementation itself is formulated using a mixed FE approach for the strain rate and solution of the balance equations using the weighted Galerkin method. The FE equations are interpolated varying the order of interpolation from 2 to 4. Time integration of the rate equations is carried out using an implicit back differentiation routine, with variable step-size and order.

3.2 Norton law

For comparison some FEA modeling was done using Norton law with Abaqus software. The Norton strain rate model for minimum creep strain rate used in standard Abaqus code is defined as:

$$\dot{\epsilon} = B \cdot \exp\left(-\frac{Q}{k \cdot T}\right) \cdot \sigma^n = A \cdot \sigma^n \quad (10)$$

where $\dot{\epsilon}$ is the minimum strain rate, B is a rate coefficient, Q the apparent activation energy for creep, k the Boltzmann constant and n the Norton creep exponent. Here $B \cdot \exp(-Q/kT)$ is treated as a constant A for given temperature.

in multiaxial form the Norton law takes the form [18];

$$\dot{\epsilon}_{ij}^c = \frac{3}{2} \cdot A \cdot \sigma_e^{n-1} \cdot S_{ij} \quad (11)$$

The Norton law parameters relevant for the calculations for the girth weld is presented in Table 2.

Table 2. Norton fitting factor values and calculated minimum strain rates for weld materials A (creep-ductile) and B (creep-brittle) at nominal 70 MPa stress and 550°C for P22 (10CrMo9-10, [19]) parent material. ε_{Nrupt} is the Norton law strain at rupture (minimum strain rate \times time to rupture).

Material	n	$\log(A)$	$\dot{\varepsilon}_{\min}$	ε_{Nrupt}
PM	4.837	-15.426	$3.149 \cdot 10^{-7}$	3.4%
HAZ	5.855	-16.819	$9.643 \cdot 10^{-7}$	4.4%
A	3.979	-13.259	$1.207 \cdot 10^{-6}$	14.7%
B	3.885	-14.096	$1.182 \cdot 10^{-7}$	1.3%

4. The Λ -filtering technique

It is commonly known that when assessing a tubular component for long term creep the maximum equivalent strains will develop on the inner surface of the pipe whereas the maximum equivalent stresses will redistribute towards the outer diameter due to creep.

The creep ductility expression for rigid plastic deformation (Eq. 12) has been used as a filter for visualizing the level of creep exhaustion in a P22 girth weld. The Λ -filtering technique is unifying creep strain, stress state and local creep ductility exhaustion from FEM.

The filtering technique visualizes the ratio of creep strain (at specified time) in relation to available creep ductility ratio (uniaxial to multiaxial creep ductility). This measure of “creep exhaustion” is defined as;

$$\Lambda = \frac{\varepsilon_{fu}}{\varepsilon_{fm}} \cdot \varepsilon_m = \frac{1}{1.65 \exp(-1.5 \cdot h)} \cdot \varepsilon_m \quad (12)$$

where h is;

$$h = \frac{\sigma_1 + \sigma_2 + \sigma_3}{3 \cdot \sigma_{VM}} \quad (13)$$

These constraint presentations could of course be replaced with any other single or mixed mechanism presentation of creep ductility.

The Λ filtering visualizes the effect of constraint so that when the multiaxial strain ε_m progresses as a function of time towards its maximum (multiaxial creep ductility ε_{fm}) then the Λ value goes towards the uniaxial creep ductility value ε_{fu} .

The filtering technique does not require creep ductility values since it is expressed as ratio dependent on stress and momentary strain only. However if the Λ -values was to be divided by the correct local uniaxial creep ductility a normalized ratio of creep exhaustion would be acquired.

5. The assessed structure (girth weld)

The girth weld simulated was of P22 material under a pressure giving a nominal (Von-Mises) stress of 70 MPa (139 bar, 300 mm inner radius, 28 mm wall thickness). The temperature selected was 550°C for a nominal rupture time of 100 000 h in parent material.

5.1 The creep properties for PM, HAZ and WM

In addition to rupture properties the creep strain models (uniaxial and multiaxial) require shape parameters for the different regions. In this work the following was assumed:

Heat affected zone: The rupture time and shape is given by 20% reduction in strength fittings factors for the heat affected zone can be extracted by the same equations as for the parent material (Table 1) by dividing the stress σ with a stress reduction factor (SRF) of 0.8. The LCSP and Norton fitting factors for the HAZ and the weld materials case A and B are given in Table 3 and shown in Fig. 2.

- A) creep-ductile weld metal with equal creep life as the parent material,
- B) creep-brittle weld metal with equal creep life as parent material.

Table 3. LCSP and Norton fitting factor values and calculated minimum strain rates for weld materials A (creep-ductile) and B (creep-brittle) at nominal 70 MPa stress and 550°C for P22 (10CrMo9-10) parent material.

WELD	LCSP model		Norton law		$\dot{\epsilon}_{\min}$
	x0	p	n	log(A)	
PM	-3.23	4.88	4.84	-15.43	3.15·10 ⁻⁷
HAZ	-3.16	4.66	5.86	-16.82	9.64·10 ⁻⁷
A	-2.67	3.58	3.98	-13.26	1.21·10 ⁻⁶
B	-4.00	5.00	3.88	-14.10	1.18·10 ⁻⁷

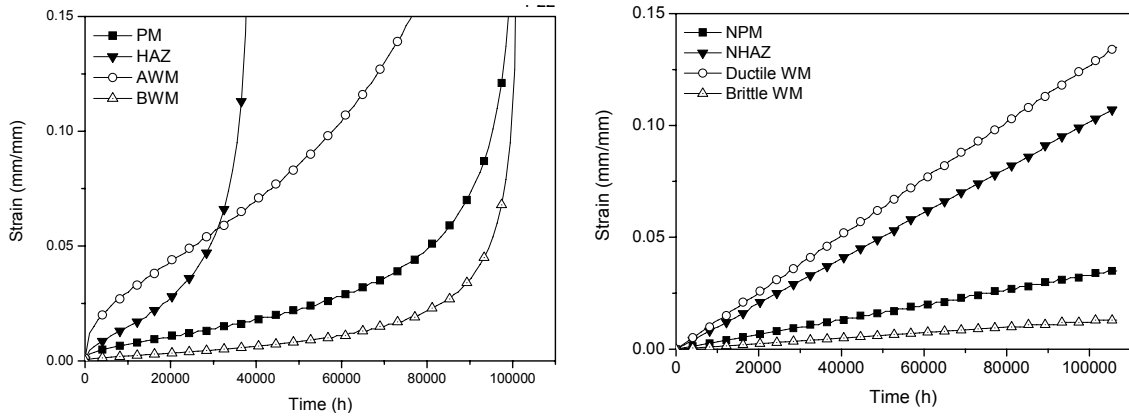


Figure 2. Creep curves LCSP and Norton law for parent, heat affected zone, and simulated weld metals A and B; “ductile” = AWM and “brittle”= BWM.

6. Finite element results

6.1 Creep strain and stresses in the girth weld

The 2D axisymmetric simulations of the cases with weld material being B/brittle are shown in Figs. 3–7 at 100 000 h using both Comsol/LCSP and Abaqus/Norton law FEM simulations. The “ductile” case A was only calculated with Comsol implementation of LCSP, presented in Figs. 8–10. The 100 000 h was selected as a studying point since at this time parent material of the pipe (without weld) would fail if using Von Mises equivalent stress as criterion in the parent rupture master curve.

For the LCSP implementation as for Norton law the stress and strain distributions of the girth weld show concentrations at different locations (ID vs. OD) as shown in the figures below.

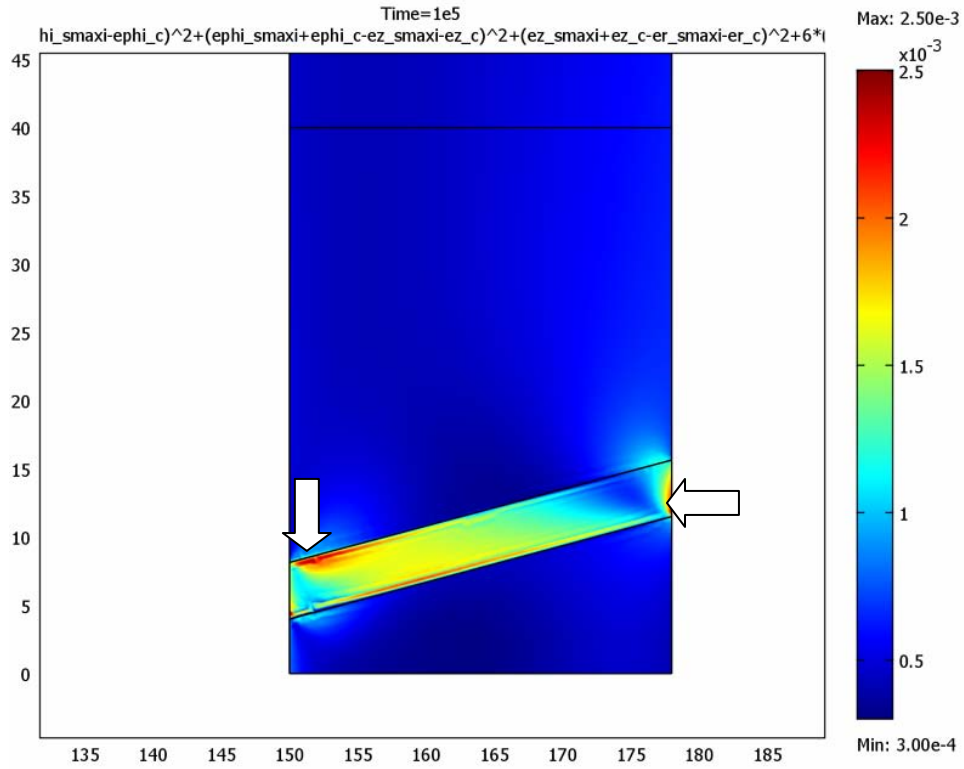


Figure 3. LCSP strain presentation (axial) of case B, brittle at 100 kh. Note maximum strain on the HAZ side of the PM-HAZ interface.

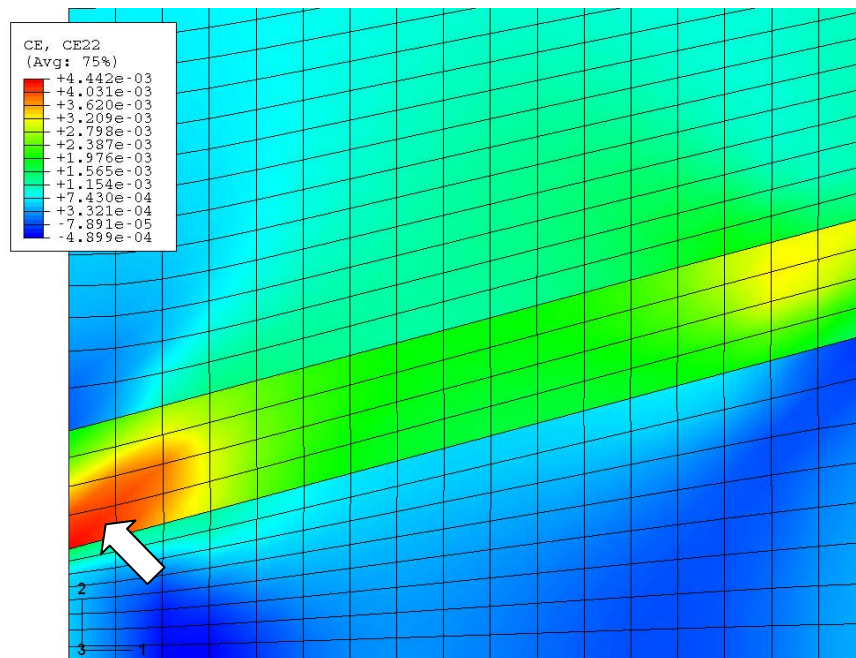


Figure 4. Norton law strain presentation (axial) of case B, brittle at 100 kh. Note maximum strain on the HAZ side of the WM-HAZ interface.

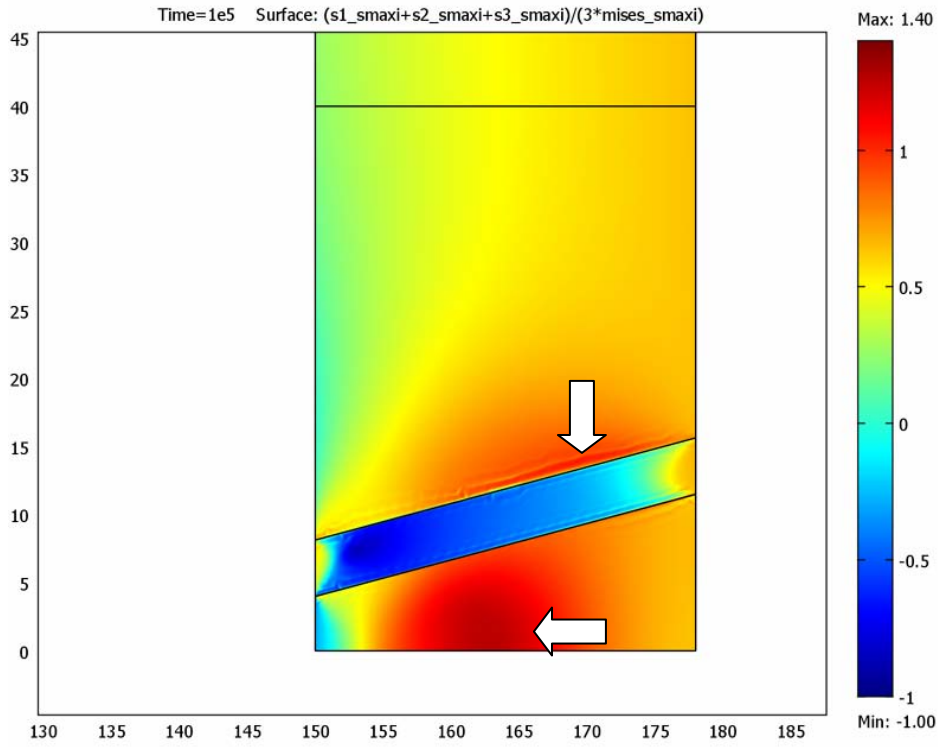


Figure 5. LCSP presentation of hydrostatic stress h for case B (brittle). Note concentration on PM side of PM-HAZ interface and curiously also in the middle of the weld.

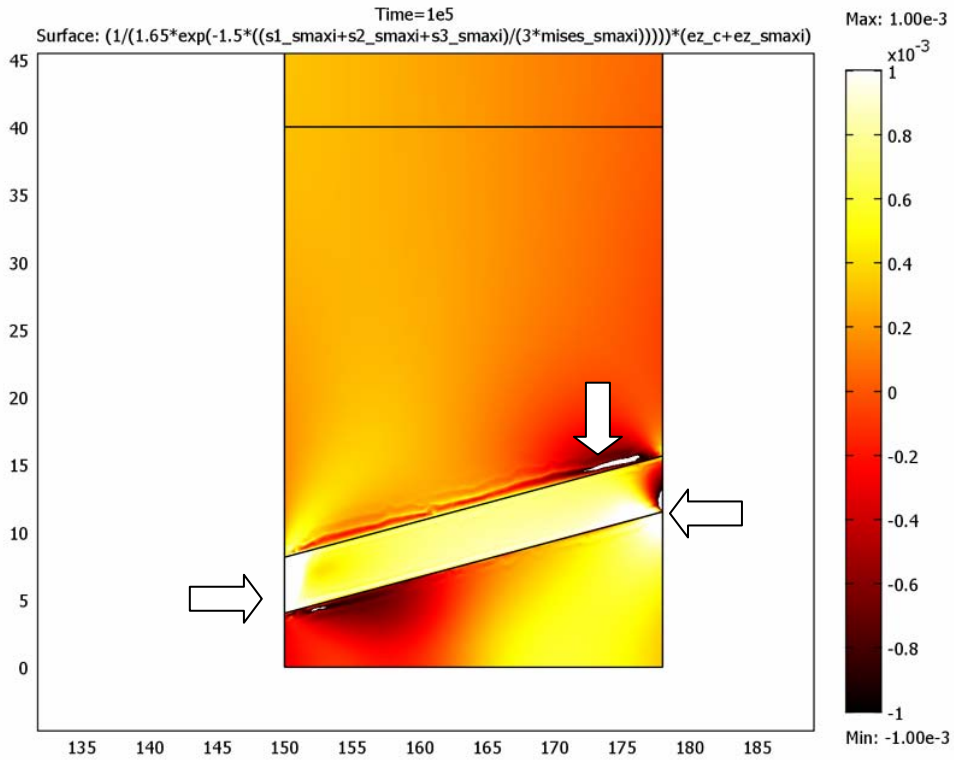


Figure 6. Λ -filtered LCSP presentation (axial strain) of creep exhaustion in case B (brittle). Note critical locations.

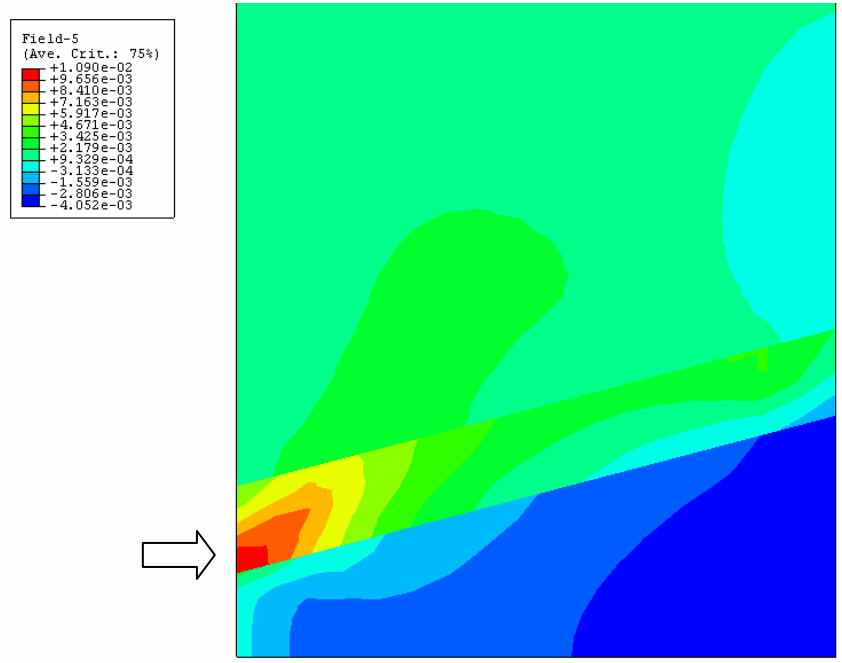


Figure 7. A-filtered Norton law presentation (axial strain) of creep exhaustion in case B (brittle). Note critical location has not changed from strain presentation.

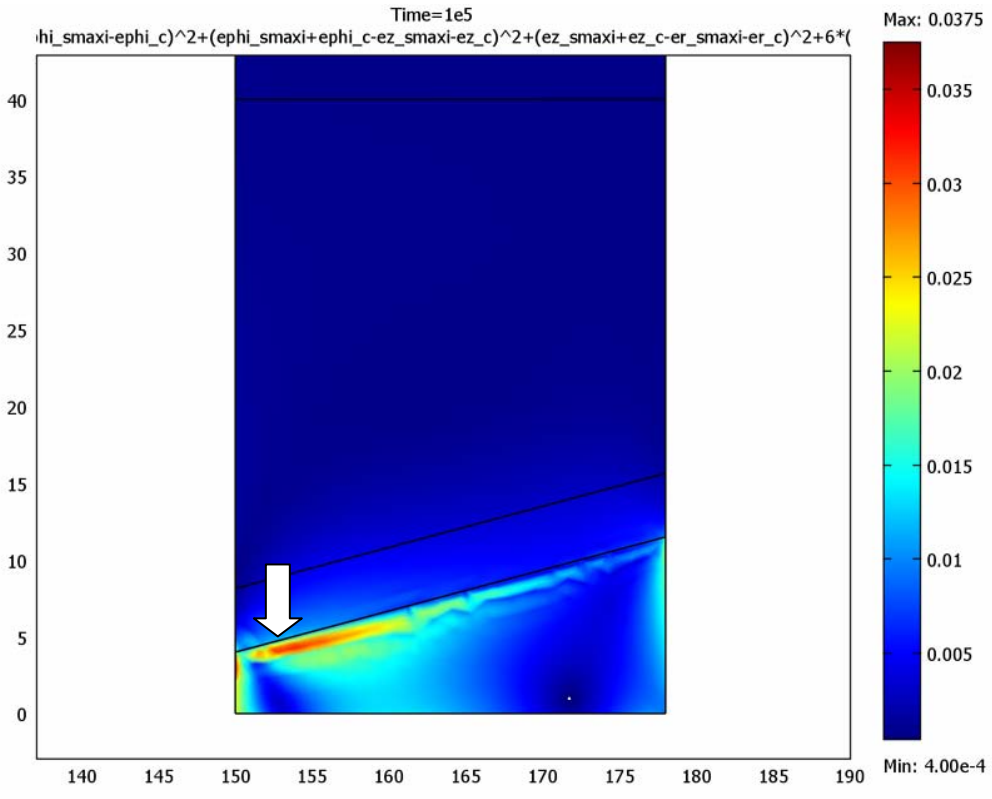


Figure 8. LCSP strain presentation (axial) for case A, ductile at 100 kh. Note maximum strain in HAZ – WM interface (WM side).

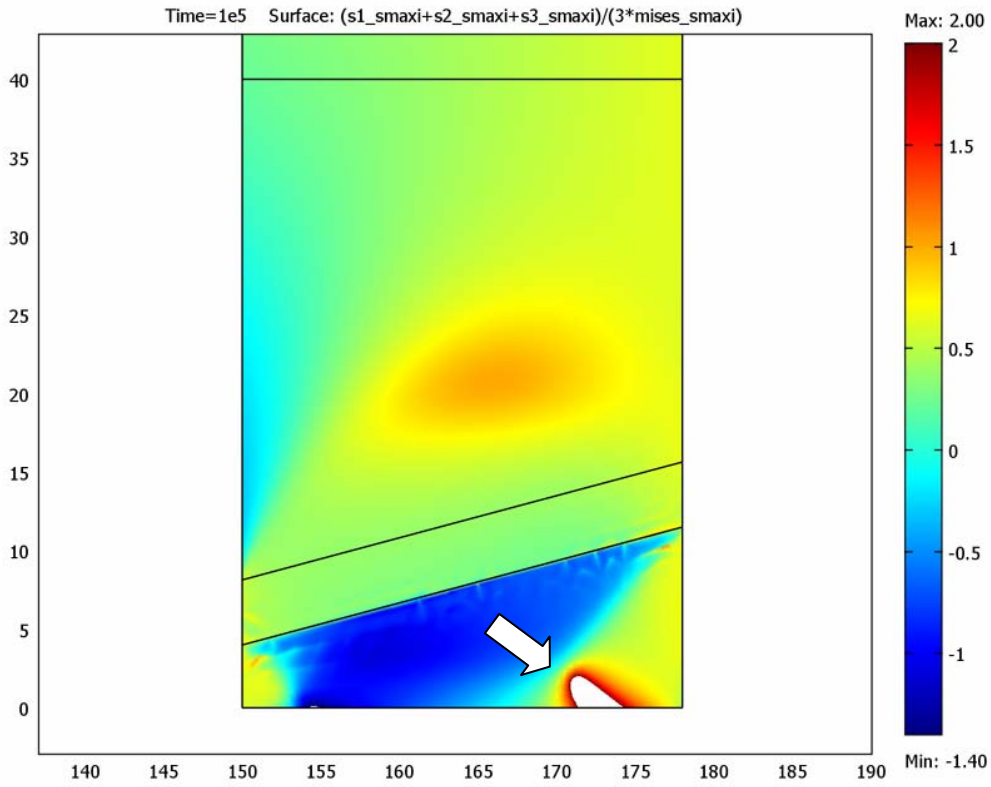


Figure 9. LCSP presentation of hydrostatic stress h for case A (ductile). Note concentration in WM.

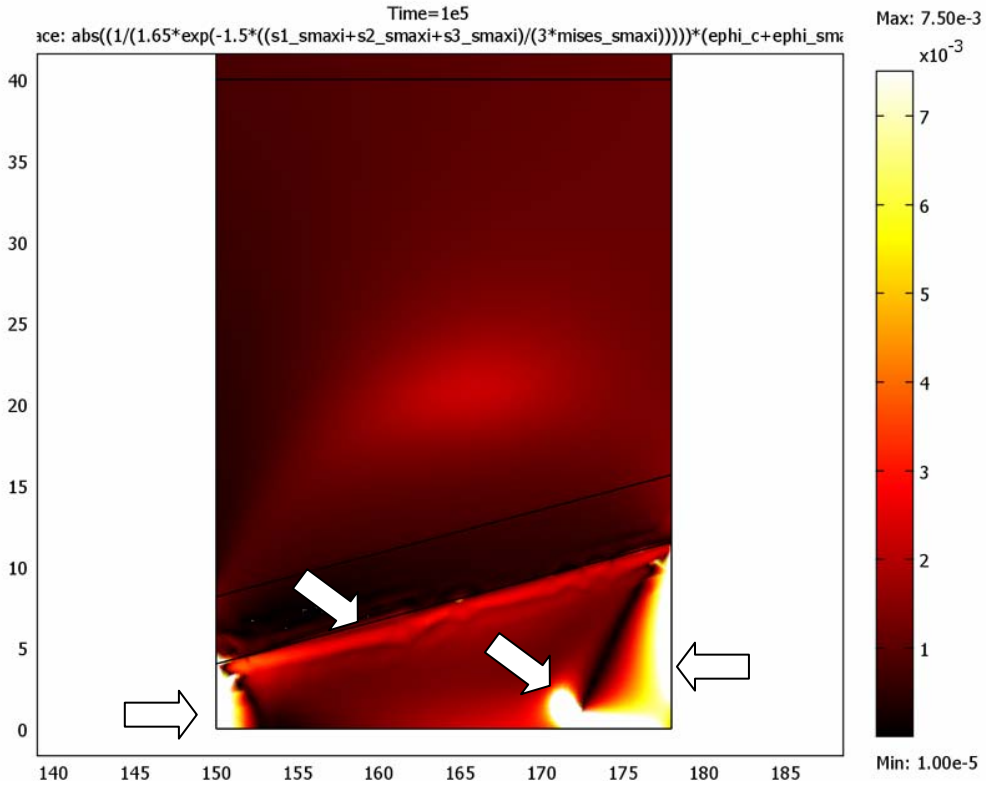


Figure 10. A-filtered LCSP presentation for case A, ductile (h , axial strain). Note critical locations. The interface is still highlighted but not as much as the weld metal.

The highest axial creep strains in the “brittle” case are found on the inner surface of the pipe near the weld root in the HAZ. The strain predicted by LCSP is under 0.25% and for Norton law 0.44%. The location and concentration of strain accumulation varies.

For the “ductile” case the largest axial strains can be found in the weld metal (both Norton law and LCSP) and at the WM-HAZ interface in the LCSP case. Here the LCSP model predicts local strains of over 3.5% in the HAZ-WM interface.

The LCSP results for these particular cases display a higher degree of deformation and Λ -filtered creep exhaustion than the corresponding Norton law simulations.

Quantitative comparison of the results presented show that there are fundamental differences in localizing critical locations between the models. The clearest indication is of course produced with materials showing large primary creep or when the simulation is moving into tertiary creep stage of the LCSP model. The difference is also significant when filtering the data to show creep exhaustion

7. Conclusions and discussion

Numerical analyses were carried out to evaluate the performance of a girth weld with a new “creep exhaustion” filtering technique. The weld was simulated with both a soft “ductile” weld metal and a hard “brittle” weld metal. The creep strain models used were the LCSP model and the Norton law model. The results of the work can be concluded as follows:

The LCSP implementation in Comsol is adequately simple with surprisingly accurate predicted uniaxial strain. The model is based on rupture and shape functions with only a few fitting constants making simulations possible even with very limited strain data. The numerical FEA of the LCSP model was stable and effective. On the simulation of the case girth welds the following conclusions can be made. The creep strength reduction of 20% of PM level performed on the HAZ region together with a creep brittle WM produce maximum strains at the inner diameter in the HAZ on the interface between HAZ and PM. The maximum creep exhaustion again was located below surface on the PM side on the interface PM-HAZ. For the ductile WM case the critical location was pinpointed in the WM. The creep exhaustion filter highlighted the WM-HAZ interface as well. The Λ -filtering with Norton law gave a much more diffuse picture of the usefulness of the filtering technique.

A creep strain model with primary to tertiary creep produces localized maxima of creep strain and “creep exhaustion”. These critical regions are not necessarily in the same location. Norton law predicts maximum creep strain at similar locations as LCSP but in a more distributed manner. The Λ -filtering did not move the creep exhaustion to another location as was the case with filtered LCSP model results.

The filtering technique seems very promising for FEM simulations in pinpointing critical locations in structures under creep. Including mathematical estimates of uniaxial creep ductility would further improve this concept by normalizing the creep exhaustion in a multi-region structure where regional creep ductility might differ remarkably. The impact of other triaxiality constraint parameters should also be further worked on.

Acknowledgements

The support of Academy of Finland (grant 117700) under guidance of prof. Kim Wallin, the VTT project EXTREME, the RFCS project ALoAS, and the ECCC network is gratefully acknowledged.

References

- [1] Holmström, S., Laukkanen, A. and Calonius, K. Weldment matching for creep life of P22 and P91 girth welds. Conf. on Integrity of high temperature welds, 24–26 April 2007, London UK.
- [2] Hayhurst, D. The use of computational creep continuum damage mechanics to optimise materials selection for high temperature weldments. *Modelling Simul. Mater. Eng.* 2, 1994, pp. 421–438.
- [3] Perrin, I. and Hayhurst, D. A method for the transformation of creep constitutive equations. *Int. J. Pres. Ves. & Piping* 68, 1996, pp. 299–309.
- [4] Perrin, I., Hayhurst, D. and Ainsworth, A. Approximate creep rupture lifetimes for butt welded steel pressurised pipes. *Eur. J. Mech. a/Solids* 19, 2000, pp. 223–258.
- [5] Law, M. and Payten, W. Weld performance under creep using finite element modelling. *Int. J. Pres. Ves. & Piping* 72, 1997, pp. 45–49.
- [6] Law, M., Payten, W. and Snowden, S. Creep Modeling of welded joints using the theta projection concept and finite element analysis. *Journal of Pressure Vessel Technology*, ASME Transactions Vol. 122, 2000, pp. 22–26.

- [7] Hyde, T.H. and Sun, W. Life prediction of repair welds in pressurised CrMoV pipe with incorporation of initial damage. *Int. J. Pres. Ves. & Piping* 81, 2004, pp. 1–12.
- [8] Wu, R., Sandström, R. and Seitisleam, F. Influence of extra coarse grains on the creep properties of 9 percent CrMoV (P91) steel weldment. *Journal of engineering and technology, Transactions of ASME Vol. 126*, pp. 87–94.
- [9] Becker, A., Hyde, T., Sun, W. and Andersson, P. Benchmark for finite element analysis of creep continuum damage mechanics. *Computational Materials Science* 25, 2002, pp. 34–41.
- [10] Law, M., Payten, W. and Small, R. Modelling the creep behaviour of reheat header longitudinal weld. *Int. J. Pres. Ves. & Piping* 77, 2000, pp. 99–103.
- [11] Hurst, R.C. and Rantal, J.H. Influence of multiaxial stresses on creep and creep rupture of tubular components. *ASM Handbook, Vol. 8*, 2000.
- [12] Spindler, M.W. The multiaxial creep ductility of austenitic stainless steels. *Fatigue Fract Engng Mater Struct* 27, 2004, pp. 273–281.
- [13] R5 (2001) Assessment procedure for the high temperature response of structures. British Energy, Gloucester UK.
- [14] ASME (2000) Section III Div. 1. Sub-Section NH, ASME, New York, USA.
- [15] RCC-MR (1987) Design and construction rules for mechanical components of FBR nuclear islands, Paris, France.
- [16] Holmström, S. and Auerkari, P. Robust prediction of full creep curves from minimal data and time to rupture. *Energy Materials: Materials Science and Engineering for Energy Systems*. To be published, accepted on 11/01/2007.
- [17] Webster, G.A. High Temperature Component life assessment. Department of Mechanical Engineering, Imperial College of Science, Chapman & Hall. 1994. Pp. 37–38. ISBN 0-412-58520-0.
- [18] Kraus, H. Creep Analysis. A Wiley-Interscience publication, John Wiley & Sons Inc. New York, 1980. ISBN 0-471-06255-3.
- [19] EN 102162, 2002. Seamless steel tubes for pressure purposes. Technical delivery conditions. Part 2: Non-alloy and alloy steel tubes with specified elevated temperature properties. CEN, Brussels. 59 p. + app.

The LICON approach to life management

J.H. Rantala and P. Auerkari

VTT Technical Research Centre of Finland, Espoo, Finland

S.R. Holdsworth

EMPA, Switzerland

R.C. Hurst

EC-JRC-IE, The Netherlands

Abstract

The prediction of long-term high-temperature material properties is difficult when the prediction is based on normal short to medium-term uniaxial creep test results. The test acceleration achieved by increasing either test temperature or stress or both, easily leads to deformation mechanism changes, which makes the prediction unreliable. In a short-term uniaxial laboratory test it is impossible to produce the same type of creep damage as observed in power plant components which have been in operation for more than 100 000 hours.

An alternative method has been proposed based on using multiaxial test specimens. This concept was tested in the LICON project (BE95-3019, 1996–2001), where the theoretical basis of the method was developed and verified experimentally for three steels in base material and welded condition by using several different multiaxial laboratory specimens and full-size test components. A typical test campaign required to apply the methodology is a series of creep crack growth tests on standard CT specimens to 0.5 mm crack extension and test durations between 1.000 and 10.000 hours. A comprehensive Code of Practice document was produced in the project, and this will be published later in 2007.

1. Introduction

High temperature components designed for long term operation at high temperatures are potentially subjected to life-limiting damage. The damage processes include creep straining via strain-dependent damage and geometric effects, thermal degradation as microstructural changes and related redistribution of constitutive elements and phases, environmental effects like internal and external oxidation and corrosion, and development of discontinuities as creep cavities and cracks. Of these mechanisms and signs of overall damage, creep cavitation damage is particularly significant in relatively thick-wall components

where it is also used to indicate the current and future condition in the in-service inspections.

Unfortunately creep cavitation damage and therefore the relevant criteria for in-service inspections are often tedious to obtain in a laboratory environment, because in standard uniaxial creep testing significant creep cavitation can take very long time to appear. This is particularly true for steels with good creep ductility, such as 2¼Cr-1Mo (10CrMo9-10, P22) steel of the low-alloy grades, and many higher alloyed 9–12% Cr steels that are increasingly used for high temperature plant. Consequently, characteristic signatures of creep damage are normally only obtained from very long term creep testing or from long term service experience of the plant. This is inconvenient particularly for new materials for which no long- term testing data or service experience is available. Clearly, a faster laboratory method is needed to establish the characteristic long-term development of creep damage.

Creep and creep failure can be accelerated in principle in three ways, or their combination. The methods of test acceleration with their typical advantages and disadvantages are listed in Table 1.

Table 1. Methods of accelerating creep and creep failure, with characteristic advantages and disadvantages.

Elevating	Advantages	Disadvantages
Temperature	Simple, strong effect on life	Mechanism changes ¹⁾
(Effective) stress	Simple, strong effect on life	Mechanism changes ¹⁾
Stress multiaxiality	Damage enhancement	Control of stress level ²⁾

- 1) with no or little enhancement of creep cavitation damage
- 2) requires appropriate testing geometry with known stress state

Acceleration by elevating temperature or stress level are well known, and particularly the former – the isostress approach – is widely used. However, both methods are ineffective for accelerating creep cavitation damage [1, 2]. The present paper explores the third and more attractive option, which is creep damage enhancement by elevating the stress multiaxiality in creep testing. This approach is a result from the European project LICON (BE95-3019), where the multiaxial testing principle has been applied for parent and welded high temperature steels P91, P92 and E911 as well as some low-alloy steels and dissimilar welds.

2. Damage enhancement under multiaxial creep

In the LICON approach, assuming that the uniaxial time to failure can be described by the inverse Norton law, the corresponding life under constant stress under stress multiaxiality is obtained from

$$t_{u,x} = A(\sigma_0)^{-v'} = A(\sigma_{VM})^{-v'} H^{-\mu v'} \quad (1)$$

where $H = \sigma_1/\sigma_e$, σ_1 is the maximum principal stress, σ_e the relevant effective (Mises) stress, and $\gamma = \mu v'$ varies between 0 (for σ_e control) and v' (for σ_1 control). This formulation is a modification of those used previously on phenomenological and experimental grounds [2], and it can also be deduced from microstructural considerations of creep damage.

Creep life under multiaxial stress is hence affected by the multiaxiality factor H . Increasing H will shorten life, and therefore to accelerate the creep test efficiently requires a testing geometry with a high value of H . A number of specimen types of different geometry have been tested (Table 2). Many of these include notches to increase H , which however also means introducing gradients of local stress. Numerical FE analysis has been used to obtain the stresses and stress states. To support FE, also some uniaxial testing of the same material is needed unless the necessary material parameters can be obtained from elsewhere.

Table 2. Comparison of test types in enhancing creep cavitation damage for PM and XW.

Specimen type	H capability	Inspectability	Testing economy
Uniaxial	1 (for PM)	Possible (surface)	Good
Notched bar	2.15–2.4	Poor	Good
Tubular / ip+tension ¹⁾	> 1 (not assessed)	Possible (surface)	Poor to fair
Tubular notched	2–2.15	Poor	Poor to fair
C-ring	2.8–3	Possible (surface)	Good
Compact tension	3.6	Possible (surface)	Good

1) ip + tens. = internal pressure and axial tension

Although more complex in stress state than many classical multiaxial creep specimens, the CT (compact tension) specimen is a fair compromise to produce high multiaxiality (H), i.e. accelerated development of creep damage, inspectability of the intermediate stages of damage in interrupted testing, and economy of material sampling and testing. However, many other notched specimen types are also possible for the purpose.

3. Creep damage morphology

In order to maintain the capability to predict material behaviour to long times, it would be important in the accelerated laboratory tests to maintain the same damage mechanism as observed in power plant components after service lives beyond 100 000 hours. This is, however, difficult because when the normal test acceleration methods are used by increasing either stress or temperature or both, then the damage mechanism changes and the appearance of damage is clearly different. While the plant conditions with low stresses and long times produce a large density of grain boundary cavities, the laboratory tests tend to produce a smaller density of much larger cavities, which in many cases have not been formed by the same mechanism as the real cavities at plant. In long-term operation the cavities nucleate at the grain boundary as a result of grain boundary sliding and vacancy accumulation and the damage is associated with rather small levels of deformation. On the other hand the short-term damage looks roughly the same in the optical microscope but has been formed as a result of matrix-particle decohesion under fairly high level of overall deformation like in ductile tearing. It is very important to distinguish between these two mechanisms. In the optimal case the laboratory tests should produce the same density of damage by the same mechanism as at plant conditions. The multiaxial testing method developed in the LICON project is believed to have achieved and demonstrated this.

The appearance of observed damage and the importance of it have been reported in two earlier papers on the subject [3, 4]. Therefore in this paper only some examples are shown. Even when multiaxiality enhancement with notched specimens is used, too short a test will result in creep damage that is not representative of expected long-term type of creep cavitation (Fig. 1). Short term creep damage is mostly similar to the cavitation damage preceding ordinary short-term ductile fracture in tensile testing, with relatively large final size and low density of voids, initiating at inclusions, growing within grains and elongating along the main straining direction [4].

Allowing for sufficient testing time under appropriate testing conditions for the material, creep cavitation damage will transform towards the type expected in long term service: smaller cavities initiating at material (grain or other) boundaries, with relatively high final density and transverse orientation to the maximum tensile principal stress (Fig. 2). This trend is independent of material, while the required absolute time as well as the necessary testing temperature are naturally specific for each material and possibly even for the application [4].

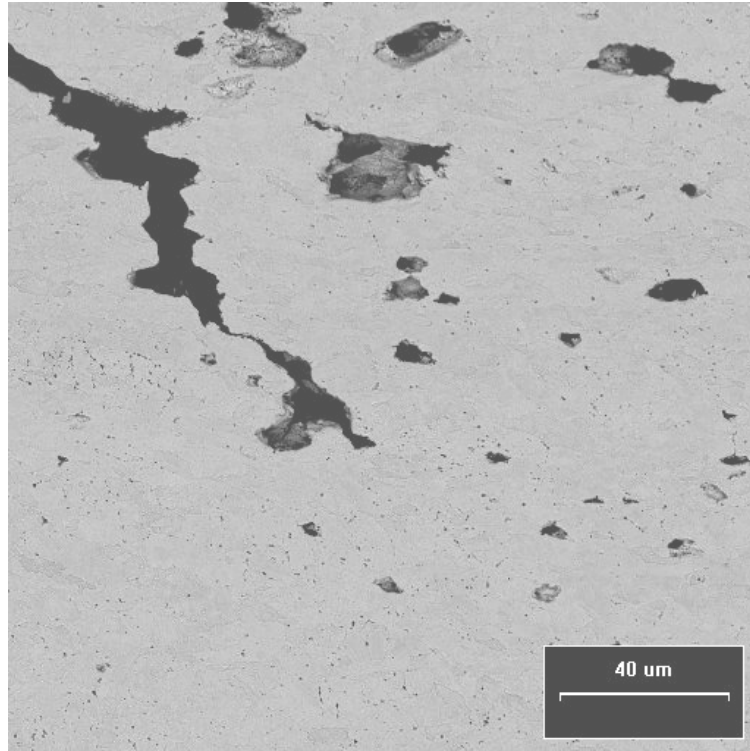


Figure 1. Creep damage in a short-term test: particle-matrix decohesion in welded P91; notched tube test after 900 h at 600°C. [3].

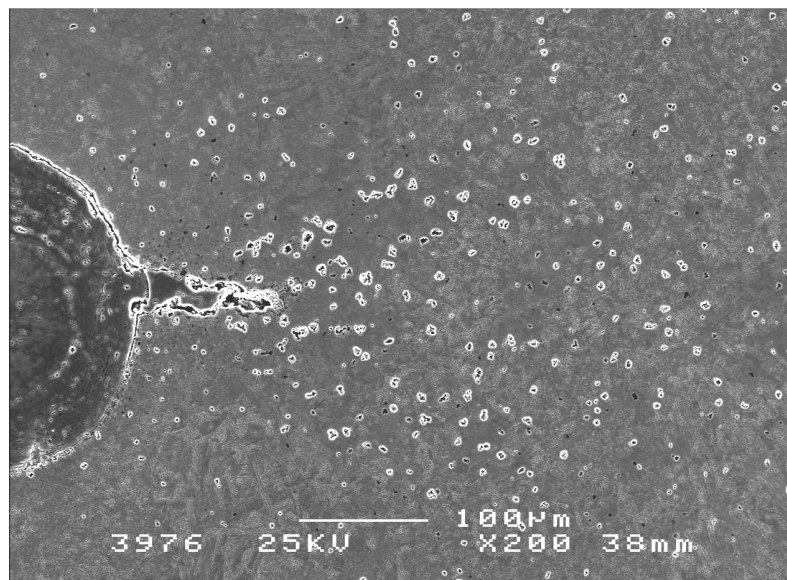


Figure 2. Creep cavitation and crack initiation at the notch tip of a CT-specimen in intercritical HAZ of E911 after 9500 h (625°C). Max principal stress vertical. [3]

A graphical damage mapping technique was developed in the LICON project, and this has been reported earlier [3]. In the same work also cavity densities in front of the crack tip were plotted, which helps evaluate that the target condition

for damage development has been reached. The required cavity density for long term damage should normally well exceed about 1000 cavities/mm² before initiation of a growing creep crack. Testing time of about 10 000 h under appropriate creep testing conditions appears sufficient to show of the typical features of expected long term damage.

4. The principle of multiaxial damage enhancement

The idea of an advanced damage enhancement test is to generate a tri-axial stress state, using testpieces with localised stress concentrations, in relatively short term tests to produce creep property data arising from a damage mechanism consistent with long term behaviour, to thereby enable reliable extrapolation to long durations.

Multi-axiality has been traditionally characterised by the h-parameter, which is the ratio of hydrostatic stress (or mean stress) to effective stress, $(\sigma_1+\sigma_2+\sigma_3)/3\sigma_{VM}$. In the LICON project, the H-parameter was selected to characterise multi-axiality, being the principal stress to effective stress ratio σ_1/σ_{VM} .

The methodology developed in the project referred to as the “LICON Methodology” is based on the model equation shown in Eq. 1. The concept is illustrated in Fig. 3, (a) for unwelded parent steels and (b) for weldments. The initiation criterion, x , in the multi-axial tests is defined as $\Delta a = 0.5$ mm.

Two damage regimes are identified in the $t(T,\sigma)$ diagram, namely Regime-1 and Regime-2. Typically for ferritic steels in Regime-1, the damage mechanism is predominantly void nucleation due to particle/matrix decohesion. Here the constant and exponent in Eq. 1 are referred to as A and v . In Regime-2, damage typically nucleates and develops at grain/lath boundaries and the constant and exponent are referred to as A' and v' . The methodology is not limited to materials exhibiting regimes involving these two mechanisms. The important point is to identify and distinguish between the relevant damage regimes.

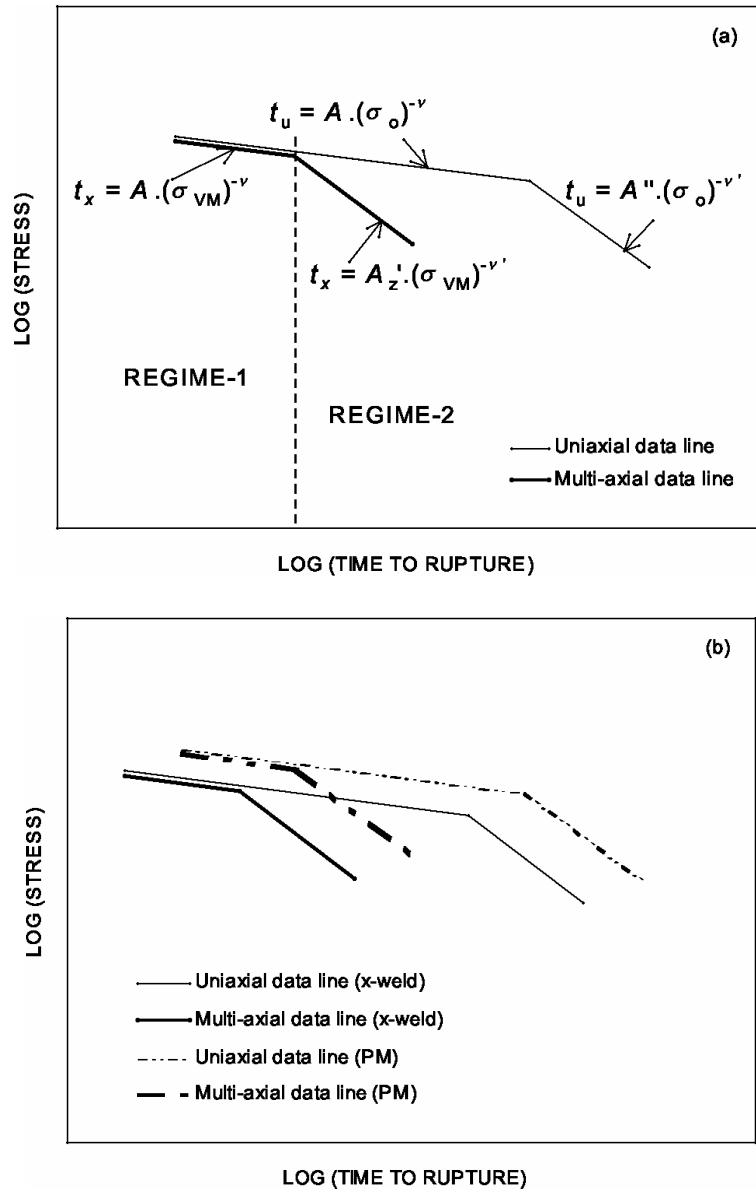


Figure 3. Schematic representation of the LICON ADE concept (a) for un-welded parent steels and (b) for weldments.

5. Steps of the LICON methodology

Material Conditions

The method has been developed for application to components both without and with weldments. In the case of behaviour predictions for unwelded parent steels, the material to be tested should originate from the appropriate product form and meet the requirements of the set specification. Testpieces should be taken from the source product form with an orientation to give the properties required for the target engineering application.

The creep-rupture behaviour of high temperature weldments may be characterised using the results from tests performed on material (i) from actual welds and/or (ii) which has been thermally simulated to give the specific microstructure responsible for long duration fracture. Actual weldment testing is preferred, in particular in the case of new materials when the long duration fracture location is unknown. The successful preparation of material which accurately simulates the specified microstructure is a highly skilled task and, if undertaken in a rigorous way, can require a separate mini-test programme to verify that the target condition has been achieved.

If simulated material is used to characterise the high temperature properties of weldments, it must be demonstrated that simulation has achieved the required microstructure, as a minimum, in terms of transformation product, grain size and hardness.

Actual weld tests should be performed on material taken from weldments prepared according to the same welding procedure to be applied to the target component.

Determination of $t_u(T, \sigma_o)$

The $t_u(T, \sigma_o)$ uni-axial behaviour of a material condition is determined with at least 4 creep-rupture tests with $t_{u, \max} \geq 10$ kh, at each temperature at which long duration predictions are to be made (typically tests to t_u of 1, 2, 5 & 10 kh). Creep deformation properties should be characterised (e.g. using Norton's law).

Determination of $t_x(T, \sigma_{VM})$

The $t_x(T, \sigma_{VM})$ multi-axial behaviour of a material condition is determined with at least 5 creep-rupture tests with $t_{0.5mm, \max} \geq 10$ kh, at each temperature at which long duration predictions are to be made. Typically tests to durations of 1, 2, 3, 7 and 13 kh will be required to give $t_{0.5mm}$ of 0.5, 1, 2, 5 and 10 kh. It should be demonstrated that the required long duration damage mechanism has been generated in ≥ 3 testpieces. For steels, this will be the formation of cavities on grain (and/or lath) boundaries. In the case of weldment tests, it should also be confirmed that crack initiation has occurred in the target weld zone, i.e. that microstructural constituent in which crack initiation is anticipated in long-term failures.

Damage Mechanism

On completion of the uniaxial and multi-axial tests to define $t_u(T, \sigma_o)$ and $t_x(T, \sigma_{VM})$, it should be possible to define Regime-1 and Regime-2 (Fig. 3). It is important to establish that the appearance and type of damage associated with creep crack initiation at the crack starter roots of the multi-axial tests defining Regime-2 is the same as that anticipated in the target component after long term service.

It should also be confirmed that the damage associated with creep crack initiation at the crack starter roots of the multi-axial tests defining Regime-1 is consistent with that observed in the uniaxial rupture test-pieces.

Assessment Input Parameters

Having plotted the $t_u(T, \sigma_0)$ and $t_x(T, \sigma_{VM})$ results in the form of a $\log \sigma - \log t$ diagram and defined Regimes-1 and 2, the A , A' , ν and ν' parameters may then be determined (Eqn. 1, Fig. 3). The A and ν parameters are determined using the uni-axial $t_u(T, \sigma_0)$ data, with reference to the short duration $t_x(T, \sigma_{VM})$ Regime-1 results. The A' and ν' parameters are determined using the $t_x(T, \sigma_{VM})$ Regime-2 data points.

Prediction of Long-term Uni-axial Properties

The prediction of long-term properties for a new material is achieved by extending the uni-axial $t_u(T, \sigma_0)$ data line from Regime-1 into Regime-2. The first step is to extend $t_u(T, \sigma_0)$ into the long-term regime by simple $\log t_u$ (linear- σ_0) extrapolation. Eqn. 1 may be arranged to give:

$$\log t_u - \log t_x = \nu' \log H \quad (2)$$

Knowing μ , μ' and H , it is possible to construct the Regime-2 uni-axial $t_u(T, \sigma_0)$ trend line in the $\log \sigma_0$ versus $\log t_u$ diagram. H -values for various multi-axial testpiece configurations are recommended in the LICON Code of Practice, Table 2.

6. Application of the LICON method

The principle of multiaxial damage acceleration can be used for two main purposes:

- 1) Prediction of the long-term uniaxial properties of new advanced steels
- 2) Prediction of component life time under multiaxial loading conditions.

Many new steel variants like E911, P92, P23, P24 and especially many experimental alloys have recently been developed for high-temperature applications, where good creep strength is required. It has often happened that new steel variants have been introduced into the market on the basis of the results of short-term creep tests, but when long-term results have later become available, the long-term strength values have been lowered. This kind of surprises could be avoided by performing multiaxial tests, which could be used to predict long-term uniaxial properties. This is illustrated in Fig. 4, where the long-term uniaxial behaviour of P92 parent material is predicted on the basis of the multiaxial

LICON tests, which lasted only up to 4000 hours. Two words of caution have to be given here: firstly a recommendation was given in the LICON methodology that the longest multiaxial test durations should be around 10 000 hours, and secondly and more seriously, it is likely that the LICON methodology is not able to take all effects into account which are due to thermal softening of the material and other microstructural changes at long times. This needs to be verified in the future. In the same way the uniaxial behaviour was predicted in the project also for the P91 and E911 base materials.

The plant components are generally cylindrical in shape and are operating under internal pressure. Therefore the loading is multiaxial to a large degree, depending on the thickness of the components. Highest degrees on stress multiaxiality are experienced by thick components with notches or cracks. The capability of the LICON method to predict the behaviour of components under realistic loading conditions was demonstrated in the project for three materials: P91, E911 and P92 in both base material and in welded condition. The result for a welded P92 component is shown Fig. 5, where it can be seen that the component failed prematurely compared to the LICON prediction. The failure in the component was indeed premature, because the main crack appeared in the middle of the weld and not in the Type IV zone as would have been expected.

7. The Code of Practice document

As a result of the development of the testing methodology and the extensive laboratory testing and comprehensive FE analysis in the project a 51 page Code of Practice document was produced, which can be regarded as the main outcome of the project. It has been planned that this document could be made public later in 2007. The document describes the main principles of the proposed testing method in a fairly short main document, but it also contains a set of Appendices where more detailed information and guidance is given. The titles of the Appendices are:

- A – Multi-axial testpiece geometries and stress solutions
- B – Example micrographs
- C – Guidance on material property input data
- D – Recommended h values
- E – Guidance notes on finite element analysis
- F – Worked examples using laboratory test data
- G – Worked examples using component test data.

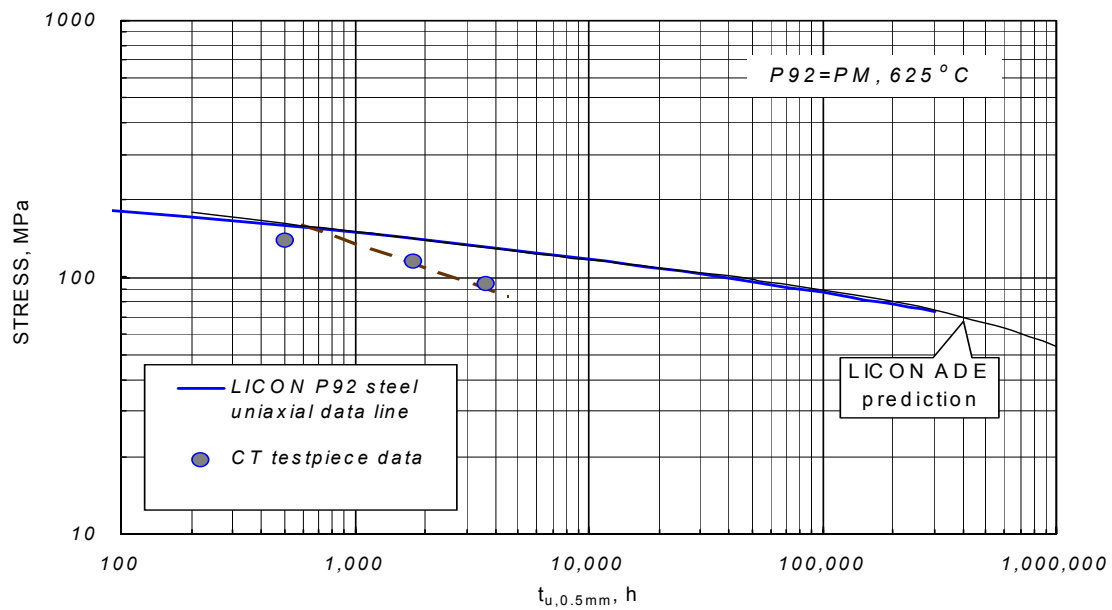


Figure 4. LICON prediction of long term creep rupture strength of P92 parent material at 625°C (broken line based on tests for which damage mechanism is predominantly boundary cavitation) [6].

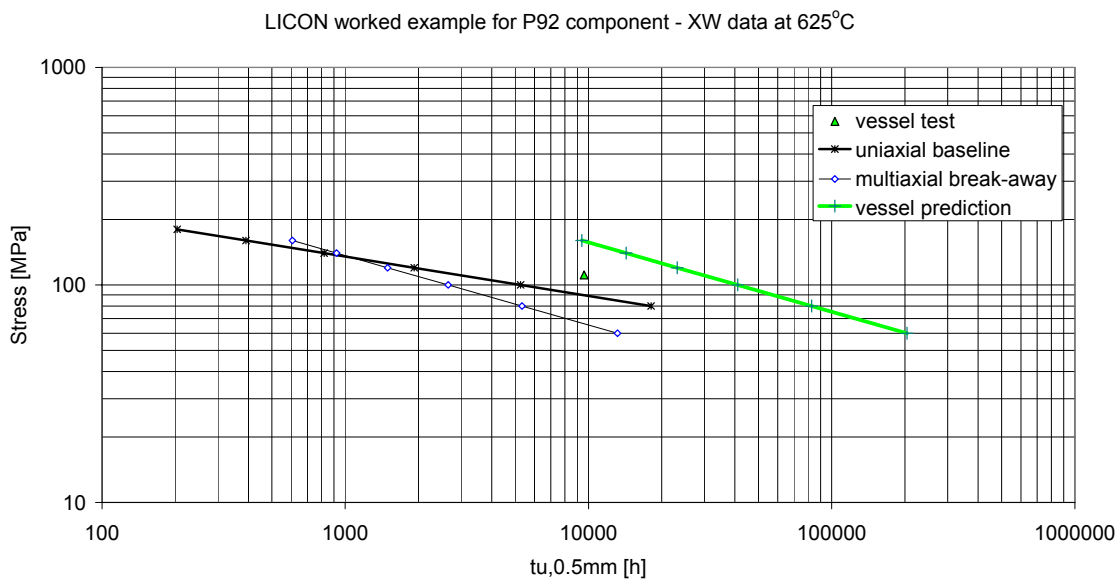


Figure 5. Comparison of predicted component behaviour and actual experimental observation for the P92 welded vessel benchmark test [6].

The recommended test specimen is the standard CT specimen, which is not too expensive to machine, and the test is inexpensive and relatively easy to perform. The CT specimen has the highest degree of stress triaxiality at the crack tip, see Table 2. A recommendation is given that the crack extension of a test series should be at least 0.5 mm and the longest test duration should be around 10 000 hours.

In contrast with the usual practice to calculate the degree of stress multiaxiality by dividing the hydrostatic stress by effective von Mises stress, in the LICON project the multiaxiality was measured in terms of a H parameter, which is defined in terms of the maximum principle stress: $H = \sigma_1/\sigma_e$. Detailed information on how to calculate the H parameter by FE are given in Appendix E and has been reported earlier [5]. Guidance on how the various metallurgical zones in a welded joint should be modeled are given in Appendix C. As a result recommended H values are produced for the various test specimen geometries, see Table 2, and therefore the user of the CoP does not have to do the FE at all as long as he is using the same test geometries given in the table.

Finally the Appendices F and G show the experimental verification of the proposed method by using both laboratory test specimen data as well as results of full-size component tests for three materials in both parent metal and in welded condition.

8. Conclusions

The method of using multiaxial test specimens for life prediction appears to be promising. The method has been initially verified, and with the publication of the code of practice it is expected that the method will be used in many new applications and research projects.

In life prediction based on laboratory specimens there are two fundamental problems: 1) how to maintain the representative deformation mechanism in a short-term test and 2) how to take the long-term thermal softening into account. The LICON method has solved the first problem, but the the question of how to take the thermal softening into account remains open.

References

1. Auerkari, P. 1994. Multiaxial testing. COST 501 Round II, WP5C, Prediction of lifetime under simulated service loads, Vol. 1. CEC, Brussels. Pp. 155–190.
2. Cane, B.J. 1981. Creep damage accumulation and fracture under multiaxial stress. Proc. of the 5th Int. Conf. on Fracture (ICF-5), Cannes, Vol. 3. Pp. 1285–1293.
3. Auerkari, P. Bendick, W., Holdsworth, S. Rantala, J.H., Hurst, R, Coussement, C. and Hack, R. Predicting Long-term Creep Behaviour using the LICON Methodology, Proc. of the Conf Advances in Materials Technology for Fossil Power Plants, Univ. of Wales, Swansea, 1–6 April 2001.

4. Auerkari, P., Holdsworth, S.R., Rantala, J.H., Hurst, R., Coussement, C. and Hach, R. Modelling the development of creep damage: the LICON experience. Proc. Baltica V: Intl. Conf. on Condition and Life Management for Power Plants, Porvoo, Finland, 2001, Vol. 2. Pp. 609–620.
5. Martins, V. Mendes and Holdsworth, S.R. The LICON methodology for predicting the long term service behaviour of new steels, Mater High Temp Vol. 19, Issue 2, 2002, pp. 99–103.
6. Auerkari, P., Bendick, W., Budden, P., Coussement, C., Holdsworth, S.R., Hurst, R., Nikbin, K. and Rantala, J.H. Code of Practice for the LICON Method, LICON project BE95-3019. (Unpublished).

Experience on the ultrasonic inspection of control rod nozzles of reactor pressure vessel

Pentti Kauppinen and Harri Jeskanen

VTT Technical Research Centre of Finland, Espoo, Finland

Raimo Paussu

Fortum Nuclear Services, Helsinki, Finland

Bernhard Elsing

Fortum Power and Heat, Loviisa, Finland

Abstract

The nozzles of control rods to the reactor pressure vessel closure head have caused serious problems worldwide. In the case of VVER440-reactors the special area of interest is to assure the tightness of the austenitic corrosion protection tube placed inside the control rod nozzle. If leakage through the weld closing the protection tube is occurring boric water can penetrate in the narrow air gap between the ferritic nozzle and the tube leading to corrosion damages in the ferritic nozzle. The water can also cause buckling of the tube inwards in the amount that disturbs or even stops the operation of control rod drive mechanism. VTT has developed a special ultrasonic technique to monitor the condition of control rod nozzles during the shutdown period of the plant. The technique has been applied during several years and the results of inspection have led to repair of some nozzles. The principle of the technique as well as its limitations are presented and discussed in this presentation.

1. Closure head of RPV and the nozzles of control rods

The upper part of the closure head with control rod housings is shown in Fig. 1 and a more detailed picture of control rod nozzles in Fig. 2.



Figure 1. Closure head and control rod housings.

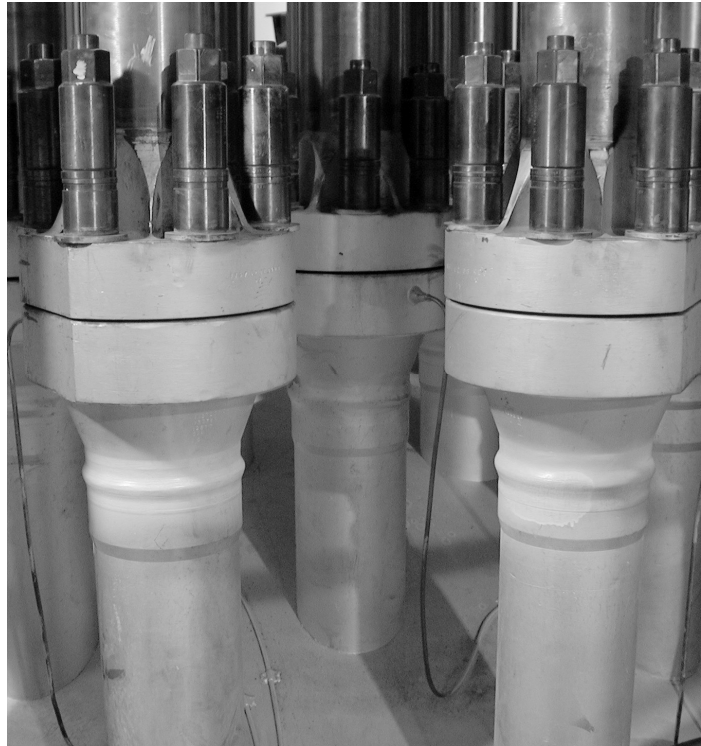


Figure 2. Control rod nozzles. More details of the structure are shown in the middle of Fig. 6.

2. The basics of the ultrasonic inspection technique applied by VTT

To evaluate the integrity of the control rod nozzle a simple ultrasonic inspection technique was developed by VTT and has been applied at Loviisa Power Plant for several years. The technique is based on assumption that in the case of leaking nozzle water has penetrated in the gap between the austenitic corrosion protection tube and the ferritic housing (see Fig. 6) and water exists at the position where the transducer is placed at the time of inspection. Only in this case the leaking nozzles can be revealed.

The basic idea of the ultrasonic measurement is to assure that water is not existing in the narrow gap between the corrosion protection tube and the nozzle. If this is the case the transmitted ultrasonic wave propagates from the ferritic material through water to the austenitic tube and several interface echoes will be seen on the screen of the ultrasonic flaw detector. If there is no water the ultrasonic beam is reflected back from the inside surface of the ferritic nozzle and practically only the thickness of the nozzle is measured. From the existence of water the leakage of the nozzle can be recognized. Because the width of the gap between the tubes is not known the reliability of the method was tested in laboratory by using the arrangement where the thickness of the water layer

between a 15 mm thick ferritic plate and 3.3 mm thick austenitic plate could be varied. The simple arrangement is shown in Fig. 3.

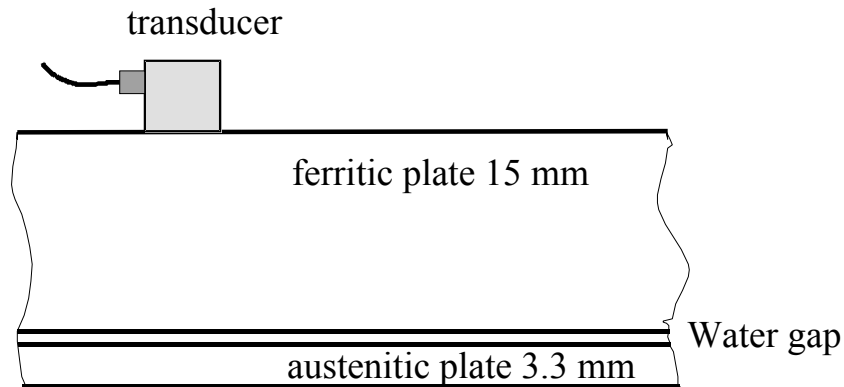


Figure 3. Test arrangement used in laboratory studies.

Fig. 4a shows the ultrasonic signals seen on the screen of UT device during calibration.

The echo amplitude seen on the left is the back-wall echo from the 15 mm thick plate and the signal on the right is the multiple echo from back-wall. The echoes in the measurement gates are echoes from water layer and the distance between these is measured. The device is calibrated on the sound velocity in steel and therefore the distance of echoes measured in gates a and b (2.41 mm) must be divided by:

$$\frac{5920}{1485} \approx 3.98,$$

where 5920 m/s and 1485 m/s are the sound velocities in steel and water. Thus the thickness of the water layer in the case 4a is $(2.41 \text{ mm}/3.98) \approx 0.6 \text{ mm}$.

Fig. 4b shows the ultrasonic signal measured from one control rod nozzle of Loviisa 2.

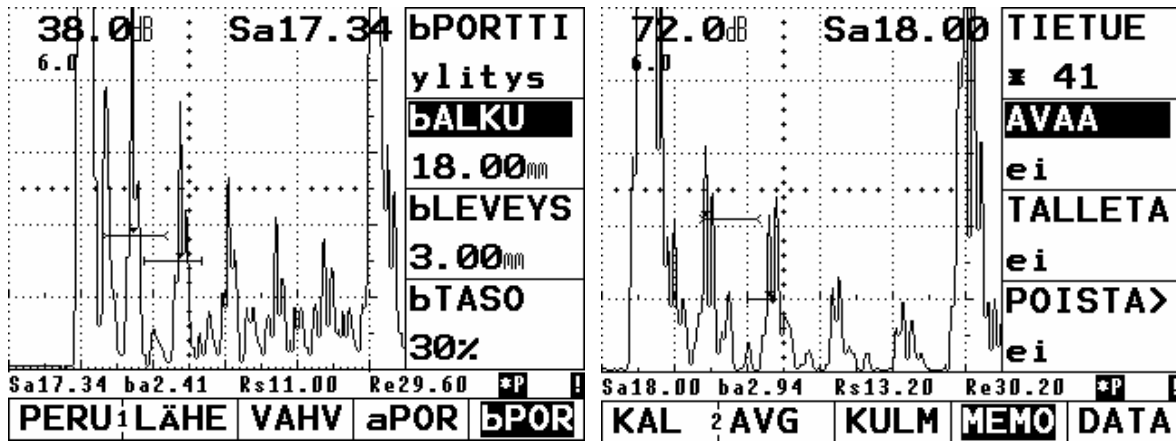


Figure 4a. Ultrasonic signals measured with the arrangement shown in Fig. 1 when the thickness of the water layer is 0.6 mm.

Figure 4b. Ultrasonic signals from a leaking nozzle (06-43). The thickness of water layer is 0 mm and sound propagates in the corrosion protection tube.

On the left ultrasonic signals measured with the arrangement shown in Fig. 3 when the thickness of the water layer is 0.6 mm (4a). On the right signals measured from a control rod nozzle of Loviisa Power Plant Unit 2. Based on the signal this nozzle was estimated as “leaking”.

3. Inspections on site

On site the nozzles are inspected from the outside surface by using a conventional handheld ultrasonic flaw detector Krautkrämer USM 25 S and the normal incidence transducer Panametrics V109, 5 MHz. Ultrasonic gel was used as coupling media. The nozzles on the outer circumference of the head were inspected manually and for nozzles locating on the central area of the head a simple tool was used due to access limitations. This is shown in the lower picture of Fig. 6.

Due to access limitations the complete circumference of the nozzle could not be measured. Therefore the assessment of the result is based on the assumption that possible water has penetrated equally along the circumference. The aim was to measure the nozzle as close to the closure head as possible but the heat insulation material on the head surface was not always removed and the measurement could not be performed at the lowest part of the nozzle. This limited access adversely affects the reliability of the measurement.

One specific problem of the measurement is that the gap between the ferritic tube and austenitic corrosion protection tube is not known. The signal amplitude measured strongly depends on the relation between the ultrasonic frequency

(wavelength) used and the width of the gap. As can be seen from the theoretical example (Fig. 5) calculated for water gap 0.2 mm at certain frequencies very weak signal will be measured from the gap due to the interference of ultrasonic waves. These frequencies should be avoided in the measurement. When the width of the gap is not known relatively low frequencies have to be used in order to be on the safe frequency range. The surface of the nozzle is curved and painted which also make the application of higher frequencies difficult.

One additional uncertainty in the measurement technique is the effect of possible corrosion products in the gap between the tubes.

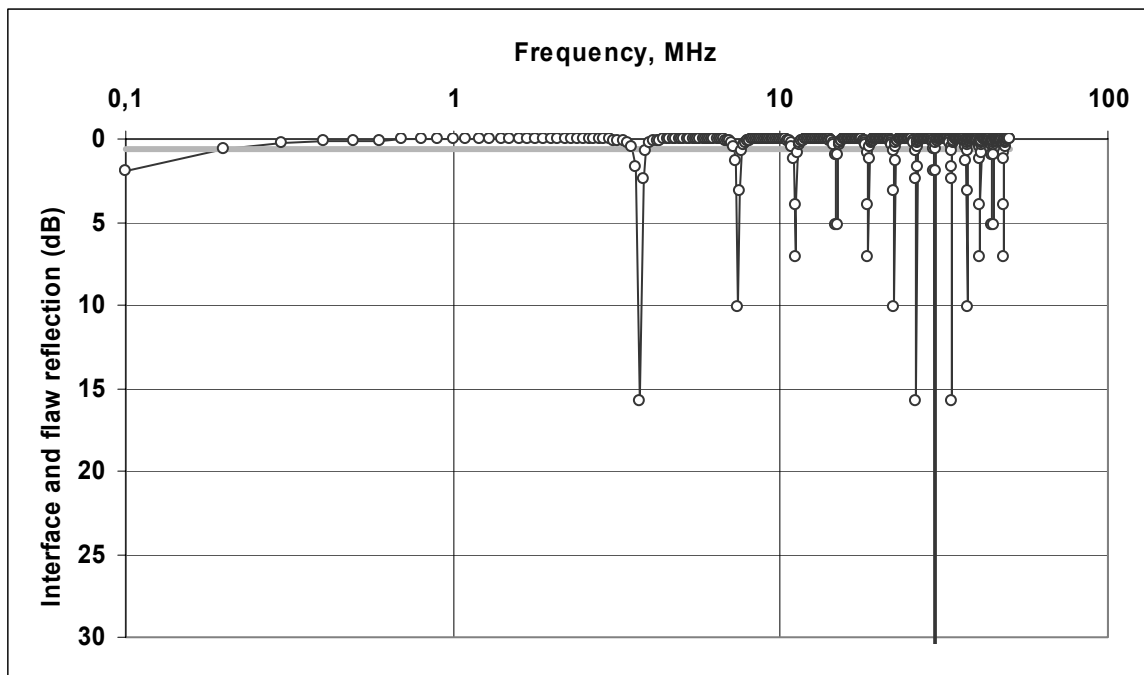


Figure 5. Dependence of the signal amplitude measured on the frequency of the transducer. The water gap is 0.2 mm and the interface echo is measured. The peaks indicate frequencies at which lower signal is measured. The first drop of amplitude occurs at frequency 3.7 MHz.

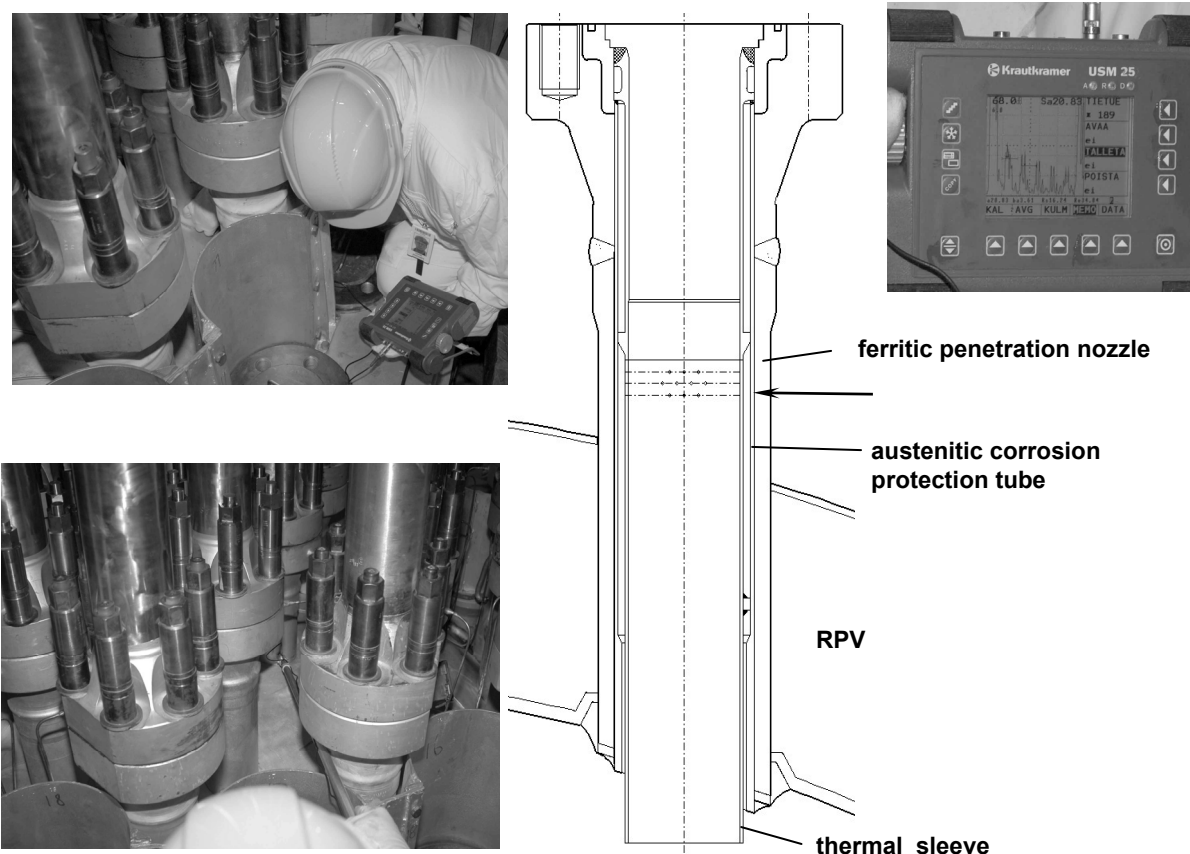


Figure 6. Manual ultrasonic inspection of the control rod nozzle.

Based on the results shown in Fig. 4b the nozzle (06-43) was opened for repair. The liquid penetrant inspection of the interior of the nozzle revealed a crack and thus confirmed the result of ultrasonic measurement. During the repair of the protection tube a crack in the buffering weld of the ferritic nozzle, see Fig. 7 was detected.



Figure 7. Opening of the crack on the inside surface of the nozzle.

4. Discussion

The in-service inspections of Finnish nuclear power plants are performed following the guideline YVL3.8 issued by Radiation and Nuclear Safety Authority (STUK). The technical requirements are based on the ASME Code Section XI. In addition to these ASME-based inspections there are several specific inspections which are performed regularly based on the operational experience, analysis performed by the utility, reports from damages at other nuclear plants worldwide etc. This information has led to the development of ultrasonic inspection technique for the inspection of control rod nozzles of the closure head. The technique itself is a relatively simple application of wall thickness measurement. However, there are certain factors that are limiting the reliability of the technique. The technique can reveal leaking nozzles provided that water has penetrated in the narrow gap between the nozzle tube and corrosion protection tube and water exists at the time of measurement in the position where transducer is placed. As can be seen from the pictures in Fig. 6 the access to the nozzles is very limited especially in the nozzles that are locating in the middle of the closure head. Here the transducer can't be moved along the whole circumference of the nozzle and measurement can be performed only in some positions. In addition, the thermal insulation material on the closure head restricts the access in vertical direction and measurement can't always be performed in the lower part of the nozzle close to the closure head.



Series title, number and report
code of publication

VTT Symposium 247
VTT-SYMP-247

Author(s) Veivo, Juha & Auerkari, Pertti (eds.)		
Title BALTICA VII Life Management and Maintenance for Power Plants. Vol. 2		
Abstract BALTICA VII. International Conference on Life Management and Main-tenance for Power Plants, Helsinki–Stockholm–Helsinki, June 12–14, 2007. This is one of the two volumes of the proceedings of the BALTICA VII Conference. The Conference aims to review recent experience, new technology and views on future developments for supporting successful, safe and productive operation of power plants.		
ISBN 978-951-38-6317-3 (soft back ed.) 978-951-38-6318-0 (URL: http://www.vtt.fi/publications/index.jsp)		
Series title and ISSN VTT Symposium 0357-9387 (soft back ed.) 1455-0873 (URL: http://www.vtt.fi/publications/index.jsp)		Project number
Date June 2007	Language English	Pages 241 p.
Name of project BALTICA VII		Commissioned by
Keywords power plant, maintenance, boilers, machinery, equipment, inspection, monitoring, condition, life, performance, risk, reliability		Publisher VTT Technical Research Centre of Finland P.O. Box 1000, FI-02044 VTT, Finland Phone internat. +358 20 722 4404 Fax +358 20 722 4374

BALTICA VII. International Conference on Life Management and Maintenance for Power Plants, Helsinki–Stockholm–Helsinki, June 12–14, 2007.

This is one of the two volumes of the proceedings of the BALTICA VII Conference. The Conference aims to review recent experience, new technology and views on future developments for supporting successful, safe and productive operation of power plants.

The BALTICA events:

BALTICA I. Materials Aspects in Life Extension of Power Plants, Helsinki–Stockholm–Helsinki, September 19–22, 1988.

BALTICA II. International Conference on Plant Life Management & Extension, Helsinki–Stockholm–Helsinki, October 5–6, together with the International Symposium on Life and Performance of High Temperature Materials and Structures, Tallinn, Estonia, October 7–8, 1992.

BALTICA III. International Conference on Plant Condition & Life Management, Helsinki–Stockholm–Helsinki, June 6–8, 1995.

BALTICA IV. Plant Maintenance for Managing Life & Performance, Helsinki–Stockholm–Helsinki, September 7–9, 1998.

BALTICA V. International Conference on Condition and Life Management for Power Plants, Porvoo, Finland, June 6–8, 2001.

BALTICA VI. International Conference on Life Management and Maintenance for Power Plants, Helsinki–Stockholm–Helsinki, June 8–10, 2004.

BALTICA VII. International Conference on Life Management and Maintenance for Power Plants, Helsinki–Stockholm–Helsinki, June 12–14, 2007.

Julkaisu on saatavana	Publikationen distribueras av	This publication is available from
VTT	VTT	VTT
PL 1000	PB 1000	P.O. Box 1000
02044 VTT	02044 VTT	FI-02044 VTT, Finland
Puh. 020 722 4404	Tel. 020 722 4404	Phone internat. + 358 20 722 4404
Faksi 020 722 4374	Fax 020 722 4374	Fax + 358 20 722 4374
